An essay on the development of an interferometer biosensor integrated with an electro-kinetic technique

A thesis submitted to the University of Birmingham for the degree of DOCTOR IN PHILOSOPHY

Author

Elisabetta Labella

School of Chemistry

College of Engineering and Physical Sciences

University of Birmingham

January 2022

Abstract and thesis outline

A novel optical biosensor is herein presented for label-free analytes detection combining a Young's interferometer and electrophoresis technique employing agarose gel. The interferometer consists of a Fresnel Biprism as beam splitter, a microfluidic chip and the output of this device, an interference pattern, is detected by a CMOS camera. The electric field focuses and actively drives the analytes through a hydrogel-filled channel to the analysis region. As the analytes move, the interference pattern immediately presents a circumscribed shift as a result of the refractive index (RI) modification of the transparent hydrogel. The shift is proportional to the analytes' concentration. In this thesis we describe the theory behind the operation of the instrument and its characterization, highlighting the results about the RI change detection and the correlation between the analytes presence inside the hydrogel and the shift in the interferometer pattern. Finally, to prove the selectivity of our biosensor, the gel has been functionalised with Biotin molecules, which were able to actively attach Streptavidin molecules from a mixed solution. The Streptavidin-Biotin system has allowed us to prove the selectivity of the sensor. The PhD thesis wants to give a full description of the development of a new label free optical biosensor in its initial stage, by describing the challenges met, and the description of the results, which testify the proof-of-concept of our novel optical sensor for the Streptavidin-Biotin system. Through all the thesis the state of art of other optical, and more specific interferometric biosensors will be described, as to guide the reader through the research and the experimental data.

The thesis outline is as followed:

- **Chapter 1 Biosensor**. In this chapter a wide view of the optical biosensors will be illustrated, in particularly by describing the three main parts that characterise a biosensor. It will present the motivation of the choice of an interferometer embedded with electro-kinetic technique.
- **Chapter 2 Interferometry**. The sensing technique will be described in depth in this chapter, by underling the importance of each aspect of the interferometry phenomenon, involved in the instrument.

- **Chapter 3 Electrophoresis**. The technique, which has been used principally as the main force to move the analytes in the sensing area, is the electrophoresis. In this chapter a general description will be given to better understand the advantages and disadvantages of this technique.
- **Chapter 4 Interferometric sensor**. This is the first chapter where the data will be presented, in particularly the interferometer is characterised by using glycerol and bovine serum albumin solutions.
- **Chapter 5 Electro-kinetic characterisation: buffer system and interferometer acquisition.** In this chapter the initial investigation of the combination between interferometry and electrophoresis will be presented.
- **Chapter 6 Selectivity**. As the two main parts of the sensor are described in the previous two chapters, here the focus will be on the chemistry approach and the data analysis of the selectivity of the novel optical sensor.
- **Conclusion and final remarks**. A summary of the project will be presented, highlighting the aspects of the research most remarkable, suggesting new ideas to resolve the problems encountered during the development.

Acknowledgment

Thanks to my supervisor Dr. Ruchi Gupta for the support and for all the ideas proposed along the project and for making me part of this interesting project. Thanks to Dr. N. Goddard for the acquisition software.

I want to thank the University of Birmingham, in particular the School of Chemistry that has helped me through the years to learn and experience a different laboratory setting from the Physics laboratories that I was used to. Besides, thanks to the Engineering and Physical Science Research Council for the funding of my PhD and for the conferences attended.

Thanks for all the members of the group, Thomas, Duilio, Beenish, Firoj, Claire, Sameh, Anil, William, Nicola and Hazel, for the immense support. They have helped me in such different ways, by bringing food, by sharing not only scientific discussion but also a lot of smiles. In particular, thanks Hazel for her advice in writing my thesis.

Thanks to all the members of the Wayfarers Society for introducing me to the natural beauty of the British landscapes. Some of them helped me through my research by giving me their different point of views thanks to their different scientific background.

Thanks to all my friends met through these years, Lucia, WeiWei, Youngju, Nicole, Alex, Dennis, Elena e Valentina for being my “English family”.

Finally, thanks to my parents, my sister, and my brother for their support.

Contents listing

Abstract and thesis outline 3
Acknowledgment 5
Contents listing 6
List of Figures 9
List of Tables 12
Abbreviations 13
List of symbols 14
Declaration 16
Author profile 17
Chapter 1 Biosensors 19
1.1 Label free detection 21
1.2 Recognition signal: Optical sensor 22
1.2.1 Photonic crystal sensor 23
1.2.2 Surface Plasmonic Resonance 24
1.2.3 Waveguide 25
1.2.4 Why choose an interferometer sensor 27
1.2.5 Integration of Optical device with other techniques 28
1.3 Bio-selective material 28
1.3.1 Biotin-Streptavidin 30
Chapter 2 Interferometry 31
2.1 Theory 31
2.1.1 Light and matter 31
2.1.2 Light and light: Interference 35
2.1.3 Sensors based on interferometry 40
2.1.4 Summary and comments 49
Chapter 3 Electrophoresis 52
3.1 Basic principles of electrophoresis 52
3.2 Capillary electrophoresis and concentration techniques 54
3.2.1 Isoelectric focusing 55
3.2.2 Isotachophoresis 57
3.2.3 pH junction 57
3.3 Buffers 58
3.3.1 Tris buffer 59
3.3.2 Phosphate buffer 59
3.4 Supporting media: hydrogels 60
3.4.1 Polyacrylamide 61

3.4.2 Agarose 62
3.5 Microfluidic electrophoresis 63
Chapter 4 Interferometric sensor 69
4.1 Introduction 69
4.2 Instrument description 69
4.2.1 Flow-cell chip 73
4.2.2 Laser 75
4.2.3 Comments on the YI sensor 75
4.2.4 Inhouse software 76
4.3 Characterisation 79
4.3.1 Principle of operation of the YI 80
4.3.2 Baseline 81
4.3.3 Glycerol 83
4.3.4 BSA 89
4.4 Final comments 92
Chapter 5 Electro-kinetic characterisation: buffer systems and interferometer acquisition 94
5.1 Introduction 94
5.2 Hydrogels 96
5.2.1 Choice of hydrogel 96
5.2.2 Polyacrylamide (PAAm) 98
5.2.3 Agarose 104
5.2.4 Why agarose gel 105
5.3 Electrophoresis buffers system and methodology 105
5.3.1 Voltage and porosity 107
5.3.2 Instrumental set-up 107
5.3.3 Data acquisition and representation (counter plot) 109
5.3.4 Data experiments 110
5.3.5 Discussion 113
5.4 pH junction 115
5.4.1 HCl-NaOH junction 118
5.4.2 PBS junction 119
5.4.3 Discussion on the pH junction results 121
5.5 BSA in pH junction 122
5.5.1 Description and materials 122
5.5.2 PBS 123
5.5.3 Tris junction 126
5.5.4 Discussion on the BSA focusing by a pH junction 127
5.6 BSA in one buffer 127

5.6.1 Description and chemical materials 128
5.6.2 PBS 128
5.6.3 Tris 129
5.6.4 Discussion on detection of BSA driven by an electric force 129
5.7 Comparison between two methods 130
5.8 Conclusion 131
Chapter 6 Selectivity 133
6.1 Introduction 133
6.2 Chip designs: Plug and junction configurations. 134
6.2.1 Materials and procedure 135
6.2.2 Fluorescence imaging set-up 136
6.2.3 Results and discussion 137
6.3 Agarose oxidation 138
6.3.1 Materials 139
6.3.2 Reaction 139
6.3.3 Results and discussion 140
6.4 Agarose functionalisation 147
6.4.1 Materials 147
6.4.2 Reaction 148
6.4.3 Results and discussion 148
6.5 Streptavidin-Biotin system 150
6.5.1 Materials 150
6.5.2 Reaction and methodology 151
6.5.3 Electrophoresis buffers system and methodology 153
6.5.4 Experimental steps 153
6.5.5 Results 155
6.5.6 Comments and discussion 169
Conclusion and final remarks 172
References 175

List of Figures

Figure 1 Biosensor components, a schematic representation. 19
Figure 2 *Cross-section schematic of photonic crystal sensor [42]* 23
Figure 3 Light propagation in planar optical waveguide (left). Schematic working principle of label-free planar optical waveguide interferometer biosensor (right) [61]. 26
Figure 4 Representation of Snell`s laws. 32
Figure 5 Schematic representation of Maxwell Garnett theory. 34
Figure 6 Schematic representations of the wave fronts in a double slits experiment (a), and in presence of a Fresnel Biprism (b) [92]. 36
Figure 7 Schematic representation of how a difference in the RI can change the phase difference. 38
Figure 8 A Y junction that creates a Young Interferometer in a waveguide structure [105]. 42
Figure 9 Forces diagram applied on a positively charged molecule. 52
Figure 10 Flow profile in electrophoretic (a) and pressure driven (b) separation columns [170]. 55
Figure 11 Schematic representation of Isotachophoresis technique by *Garcia-Shawa et al.[199]*. 57
Figure 12 Hydrogel network schematic representation. 60
Figure 13 Agarose oxidation reaction ([246]) 63
Figure 14 Hydrazide reaction chemistry [247]. 63
Figure 15 Schematic configuration of the interferometer of this project [284]. 69
Figure 16 Rays diagram for a Fresnel biprism [288]. 70
Figure 17 Rays diagram for the interferometer (side view, distances not to scale). 71
Figure 18 Interference patterns for two D values. As the distance increase, also the number of the fringes increases. 73
Figure 19 Schematic representation of the tree elements of the chip. 3D view of the assembling (a); dimension of three elements (b). 74
Figure 20 Three different designs of the channels for the spacer. 74
Figure 21 Matching between beams area with interference pattern area. 75
Figure 22 Representation of the areas (red rectangles) that divide the interference pattern. 77
Figure 23 atan2(x,y) graph. The red dashed rectangles define the neighbourhood of the two asymptotes. 78
Figure 24 Baseline 80 minutes long. In the channels is being pumped only deionised water. 82
Figure 25 Interference patterns with the boxes used for the acquisition. Phase difference acquisition value in real-time for five boxes area. A is the box nearest to the inlet, while E is the next to the outlet. The errors are not visible since they are of the order of 10^{-3} radians. They have been calculated as deviation standard of the plateau values. 84
Figure 26 Calibration curve and PD values for the glycerol concentrations (light blue line). The black spots represent the model values obtained by calculating the model phase difference from the refractive index of the glycerol solution measured with the refractometer. The errors are not so visible since are of the order of 10^{-5} radians even for the simulation data. 85
Figure 27 Phase difference dependence from the refractive index. 86
Figure 28 Glycerol run of four concentrations, in three different heights channels. The two shades of the same colours represent the measurements along different points of the channels. Blue (A, B) 250 m, yellow (C, D) 1.48mm, green (E, F) 3 mm. The errors in all the measurements are in a range from 0.005 rad to 0.07 rad, so they are not visible in the graph. 88
Figure 29 Average values of the phase difference of the measurement reported in Figure 28. The errors in all the measurements are in a range from 0.005 rad to 0.07 rad. 88
Figure 30 Phase difference real-time acquisition for BSA solution, prepared in buffer pH 7.10 (10 mM) and 0.2% Tween20. The errors in all the measurements are in a range from 0.005 rad to 0.07 rad, for this reason they are not visible in the graph. The errors were calculated as the standard deviation errors 89

Figure 31 Calibration curve of the interferometric sensor for BSA. The errors in all the measurements are in a range from 0.005 rad to 0.07 rad, for this reason they are not visible in the graph. The errors were calculated as the standard deviation errors 90
Figure 32 Correlation refractive index and BSA concentration. The data reported are the RI calculated from the PD of the interferometer and the RI measured with the refractometer. The errors are slightly visible for the RI. The errors from the interferometer were calculated from the propagations of errors of all the values (5 acquisitions) obtained from a single acquisition. 92
Figure 33 Schematic representation of all the parameters from "Handbook of Capillary and Microchip Electrophoresis and Associated landers" [301]. 95
Figure 34 Interference pattern of PAAm (1 mm thickness) (a) and empty chip (b). 97
Figure 35 PAAm inside the channels 200V and 800µA. Beginning and after 3 minutes after the voltage was applied. The red boxes evidence the main differences between the two patterns. 99
Figure 36 Interference pattern of the chip filled with PAAm with protein solution moving inside it under a V=40 V, at 10 and 100 seconds after the voltage was applied. 99
Figure 37 Interference patterns of PAAM using APS and TEMED to crosslink the gel. In some cases, the interference pattern is not visible. 100
Figure 38 Interference patterns of PAAm gel initiated with photo-initiators. 101
Figure 39 Defects hypothesised. Side view for only one channel. 102
Figure 40 Three chip configuration: a. glass, b hybrid, c plastic. 102
Figure 41 Some example of interference patterns of a PAAm gel in a glass, hybrid, and plastic chip. The glass was treated with Chloro(dimethyl)vinylsilane. 103
Figure 42 Some example of interference patterns of a PAAm+allylamine gel in a glass, hybrid, and plastic chip. The glass was treated with Chloro(dimethyl)vinylsilane. 103
Figure 43 Some example of interference patterns of a PAAm gel in a glass, and hybrid chip. The glass was treated with Allyltrichlorosilane. 103
Figure 44 Schematic representations of the top view of the chip to highlight the importance of the distance between the channels. The green areas represent the beams spots. In the beams touch the edges of the channels, while in **b**, the beams are perfectly in the middle of the channels. 104
Figure 45 Schematic representation of migration of charged proteins in the chip. 106
*Figure 46 Microfluidic chip with the electrodes attached and laser beams going through the channels **(a)**. And an image from the top of the chip, to visualise with a camera the movement of solution with dye (black) inside the channels filled with agarose gel **(b)**.* 108
*Figure 47 Schematic representation of channel configuration (it is indicated the axis for the distance) (a) and of the counter plot of the phase difference (b) **distance vs. time**, highlighting the three main steps of the measurement.* 109
Figure 48 BSA velocity. Counter plot distance versus time for three voltages (20, 30, 10 V) and velocity distribution. 111
Figure 49 Phase difference values in counter plot distance vs time of 1% BSA in two agarose concentration 2%, 1%, and 0.5%. The dashed lines identify the time when the BSA has been arrived at the opposite site. The time is higher for 2% than 0.5%. 112
Figure 50 PD values at difference position in the channel, for buffer applied in 1% agarose gel at 20 V for 20 minutes (1200 seconds). Around 850 sec, in some position the PD assumes values quite far from 0 radians. 113
Figure 51 PD values at difference position in the channel, for buffer applied in 1% agarose gel at 30 V for 20 minutes (1200 seconds). Around 600 sec, in some position the PD assumes values quite far from 0 radians. 114
Figure 52 PD values at difference position in the channel, for buffer applied in 1% agarose gel at 10 V for 20 minutes. For all the experiment the PD keep the same value 0.12±0.05 radians. 114
Figure 53 Experimental BSA focusing on a pH junction made with PBS and TRIs buffers. A schematic representation of the pH junction is also reported. The BSA has a blue colour, while acid buffer is yellow, and basic buffer is purple. 115

Figure 54 Apparatus to create a pH junction with the use of a pH sensitive dye (a). In b, the colours, due to the BCP dye, represent the basic (purple), acidic (yellow) pH, and the presence of 1% or more BSA in basic solution (blue). 116
Figure 55 How the PD changes at different regions of the interference pattern along the time of the measurement. 118
Figure 56 PBS junction. agarose in pH 3. The BSA focusing is visible in one channel. 120
Figure 57 PBS junction. agarose in pH 3. The BSA focusing is visible in both channels. 120
Figure 58 PBS junction. agarose in pH 5. The BSA focusing is visible in one channel 121
Figure 59 Schematic set-up of the electric circuit. The voltage is applied only in the sample channel. 122
Figure 60 Counter plots of BSA focused on pH junction for three concentrations (w/v): 23% (a), 12% (b), 20% (c). 123
Figure 61 Distance vs time plot of 0.5% BSA in PBS pH junction. 124
Figure 62 Counter plots of pH junction in PBS, where the agarose gel is prepared in pH 5.3 10 mM, and 10 mM NaCl. 125
Figure 63 An example with the colour images, how the focusing is happening with Tris buffer system. The red circles represent the regions where the BSA has been focused in both channels. 126
Figure 64 Counter plot of three BSA concentrations in a pH junction Tris buffer, and of the background (due only to the two pHs). 126
Figure 65 BSA calibration curve in pH 3.2 environment. 10V applied, 10 mM buffer strength. 128
Figure 66 BSA calibration curve in pH 9.2 environment. 10V applied, 10 mM buffer strength. 129
Figure 67 Chip designs for plug (a) and junction (b) configuration. 134
Figure 68 Schematic representation of the plug configuration channels chip with the dimensions reported. 135
Figure 69 Fluorescence imaging set-up used. 136
Figure 70 Fluorescence image of junction configuration in both channels of the chip. The red dashed lines show where the intersection between the two gels is. 137
Figure 71 Fluorescent image (a) and profile (b) of one plug gel execution. The blue dashed line in image a represents the length of the profile acquired. In image b, the red dashed lines represent the distance value at half height of the plug profile. 138
Figure 72 Hydrazide dye (LY) calibration curve (pH 7.4). 141
Figure 73 Values of the LY calibration curve reported in the graph in figure 72. 141
Figure 74 Fluorescence image (a), Grey scale values in the junction between agarose gel and empty channel (b). 142
Figure 75 Fluorescence image (a), Grey scale values in the channel filled with oxidised agarose (b). 143
Figure 76 Fluorescence image of oxidised agarose (30 min), after 2 hours dye reaction (a), and after the washing (b). 143
Figure 77 Grey scale values after the washing in the oxidised agarose gel (30 minutes) 144
Figure 78 Fluorescence image (a), Grey scale values in the channel filled with oxidised agarose (45 minutes) (no dye inside. The average represents the background value). 144
Figure 79 Fluorescence image of oxidised agarose (45 min), after 2 hours dye reaction (a), and after the washing (b). 144
Figure 80 Grey scale values after the washing in the oxidised agarose gel (45 minutes). 145
Figure 81 Fluorescence image (a), Grey scale values in the channel filled with oxidised agarose (60 minutes). 145
Figure 82 Fluorescence image of oxidised agarose (60 min), after 2 hours dye reaction (a), and after the washing (b). 146
Figure 83 Grey scale values after the washing in the oxidised agarose gel (60 minutes). 146
Figure 84 Fluorescence image of the chip filled with agarose oxidised and LY dye (a), and grey scale values (b). 147
Figure 85 Fluorescence image after the washing (a) and configuration (b) of the plug. 149
Figure 86 Grey values of the plug profile from the fluorescent image (plug configuration) 149

Figure 87 Schematic representation of the experimental steps, for the junction and the plug scenarios. 154
Figure 88 Streptavidin calibration of the interferometric embedded with electro-kinetic. The values and the errors are reported in the table 10. 156
Figure 89 Schematic representation of the junction configuration (a). The Biotin-gel is near the cathode. Counter plot (b) of the Phase Difference variation through the channel as the time going. 157
Figure 90 Schematic representation of the steps to prove the selectivity of the sensor. 158
Figure 91 Schematic representation of the chip (a), contour plot showing 7.5 μM BSA, and 10 μM Streptavidin runs in a gel junction configuration (b). 158
Figure 92 Schematic representation of the chip (a), contour plot showing 8 M Streptavidin runs in a gel junction configuration (b). 159
Figure 93 Schematic draw of gel configuration (a) and counter plot of the mixed solution (3.75 μM BSA, 5 μM streptavidin) in gel junction. 160
Figure 94 Schematic draw of gel configuration (a), 3.75 μM BSA, 5 μM streptavidin in gel junction (b). 161
Figure 95 Two possible orientation of the plug configuration. 161
Figure 96 Control measurement. 20 μM Streptavidin in agarose gel in plug chip. 162
Figure 97 Schematic representation of the chip (a), contour plot showing 8 μM Streptavidin runs in a gel plug configuration (b). 162
Figure 98 Schematic representation of the chip (a), contour plot showing 7.5 μM BSA, and 20 μM Streptavidin runs in a gel plug configuration (b). 163
Figure 99 Schematic representation of the chip (a), contour plot showing 15 μM BSA, and 20 μM Streptavidin runs in a gel plug configuration (b). 164
Figure 100 Schematic representation of the chip (a), contour plot showing 20 μM Streptavidin runs in a gel plug configuration, 2mM Biotin gel plug (b). Interference pattern in the plug configuration at **pH 3.**2. On the left is also reported the interference pattern recorded. 165
Figure 101 Schematic representation of the chip (a), contour plot showing 15 μM BSA, and 20 μM Streptavidin runs in a gel plug configuration (b). 166
Figure 102 Schematic representation of the chip (a), contour plot showing mixed solution (7.5 μM BSA, and 10 μM Streptavidin) runs in a gel plug configuration (b). 167
Figure 103 Schematic representation of the chip (a), contour plot showing 20 μM Streptavidin runs in a gel plug configuration, 1mM biotin plug gel (b). 167
Figure 104 Schematic representation of the chip (a), contour plot showing 2 μM Streptavidin run in a gel plug configuration (b). 168
Figure 105 Schematic representation of the plug chip (a), counter plot of 20 μM streptavidin run in 2 mM Biotin gel plug followed by a wash of pH 3.2 and a wash of pH 7.4. 169
Figure 106 Schematic representation of the electric circuit of the channels system, where R_1 and R_2 represent the electric resistance of the sensing and reference channels, respectively. While i_1 and i_2 are their currents. 170

List of Tables

Table 1 List of some optical biosensors....26
Table 2 Interferometric sensors 47
Table 3 List of microfluidic sensors 65
Table 4 Conditions on the distance D (microfluidic device-camera).....72
Table 5 BSA concentration and Refractive index and Phase difference calculated (average). 91
Table 6 Composition of the PBS buffered for the pHs used in the experiments. The composition refers to 100 ml solution of 100 mM strength.....119
Table 7 Calibration curves of BSA in two instrument configurations. 130

Table 8 Quantities used in the preparation of pHs 5.5; 6.4, 7.4 PBS, for 100 ml, 100 mM strength.....139
Table 9 Quantities used in the preparation of pHs 3.2; 6.4, 7.4 and 9.2 PBS, for 100 ml, 100 mM strength......151
Table 10 Phase Difference values for the streptavidin concentrations used in the calibration curve. .156

Abbreviations

- 2D-PAGE Two-dimensional polyacrylamide gel electrophoresis
- APS Ammonium Persulfate
- B Magnetic field
- BGE Background electrolyte
- BSA Bovine Serum Albumin
- CE Capillary Electrophoresis
- CMOS Complementary metal–oxide–semiconductor
- Diamine 4,7,10-Trioxa-1,13-tridecanediamine
- E Electric field
- ELISA Enzyme-Linked Immunosorbent Assay
- EM Electromagnetic field
- EMA Effective Medium Approximation
- EOF Electroosmotic flow
- FB Fresnel Biprism
- FFT Fast Fourier Transform
- FITC Fluorescein isothiocyanate
- IEF Isoelectric electrophoresis
- IgG Immunoglobulin G
- ITP Isotachophoresis
- LE Leading Electrolyte
- LIF Laser induced fluorescence
- LOD Limit of Detection
- LY Lucifer Yellow hydrazide dye
- MCE Microchip capillary electrophoresis
- MED Microfluidic electrophoresis devices
- MZI Mach-Zehnder interferometer
- NAPMAAm n-(3-aminopropyl) methacrylamide hydrochloride
- OPD Optical Path difference
- PAAM Polyacrylamide
- PBS Phosphate Buffered Solution
- PC Photonic Crystal

- PD Phase Difference
- PDMS Polydimethylsiloxane
- PEG-DA Poly(ethylene glycol)-diacrylate
- pI Isoelectric Point
- PI1 2-hydroxy-4-(2-hydroxyethoxy)-2-methylpropiophenone
- PI2 2,2'-Azobis[2-(2-imidazolin-2-yl)propane] Dihydrochloride
- PMMA Poly(methyl methacrylate)
- POC Point-of-care
- QCM Quartz Crystal Microbalance
- RI Refractive Index
- RIU Refractive Index Unit
- SDS Sodium Dodecyl Sulfate
- SPR Surface Plasmonic Resonance
- TE Terminating Electrolyte
- TEMED N,N,N`,N`- Tetramethylethylenediamine
- WG Waveguide
- YI Young Interferometer

List of symbols

- ω ..... Angular frequency
- η ..... Viscosity
- α ..... Apex angle
- μ ..... Magnetic constant in the medium
- φ ..... Phase of the wave
- χ ..... Phase of the wave
- ν ..... Velocity
- $\Delta\varphi$ ..... Phase Difference
- θi, θr, θt ..... Snel's angles
- ϕ, ϕref, ϕsen ..... Phase of one wave of reference, and sensing waves
- Λ..... Spatial fringes spaces
- λ..... Wavelength
- ε_0 ..... Permittivity in vacuum (8.85x10-12 F m-1)
- μ_0 ..... Magnetic permittivity constant in the vacuum
- β_c ..... Coherent length
- μ_E ..... Electrophoretic mobility
- Δf..... Wavelength band width
- Δn ..... Difference of refractive indexes
- λ_n..... Wavelength in the medium

- ε_r …… Relative permittivity of the solution or medium
- A_{ref}…….. Amplitude of the reference wave (V/m)
- A_{sen}…….. Amplitude of the sensing wave (V/m)
- *d* …… Distance of the two light sources (m)
- *D*……Distance from the light sources and the screen (m)
- *f*…….. Frequency of the wave (Hz)
- f_c…… Focal length of the cylindrical lens (m)
- F_e …… Electrostatic force (N)
- F_f…… Frictional force (N)
- *h*, h_{ref}, h_{sen}…… Interaction length, in the reference, and in the sensing
- n …… Refractive index
- n_F, n_C, n_S …… Refractive indexes of middle layer, cover, substrate
- $p\kappa_a$…… Dissociation constant
- q …… Charge of the ionic species (C)
- t …… Time (s)
- V …… Applied voltage (V)
- *x, y, z*…… Coordinates of the space
- L_{FB-CL}…… Distance between Fresnel Biprism and a cylindrica lens (m)

Declaration

I declare that no portion of the work referred to in the thesis has been submitted in support of an application for another degree or qualification of this or any other university or other institute of learning.

Author profile

SCIENTIFIC PUBLICATIONS

- A.K. Pal, E. Labella, N.J. Goddard, R. Gupta, "Photofunctionalizable Hydrogel for Fabricating Volume Optical Diffractive Sensors", Macromolecular Chemistry and Physics, 2019, 220, 1900228. DOI: 10.1002/macp.201900228.
- R. Gupta, E. Labella, N.J. Goddard, "An Optofluidic Young Interferometer Sensor for Real-Time Imaging of Refractive Index in μTAS Applications", Sensors and Actuators B, 2020, 128491. DOI: 10.1016/j.snb.2020.128491.

PRESENTATIONS

- E. Labella, R. Gupta, *Essay Development for an Optical Biosensor,* Analytical Research Forum 2018, 21 June 2018, London, UK (***Poster*** communication).
- E. Labella, N. Goddard, R. Gupta, *Fast-Response Optical Biosensor for Early Diagnosis,* STEM for Britain 2019, 13 Mar 2019, London, UK (***Poster*** communication).
- E. Labella, N. Goddard, R. Gupta, *Interferometric optical biosensor integrated with electrophoresis*, Royal Society of Chemistry Tokyo International Conference 2020 (webinar), 15-16 December 2020 (***Poster*** communication).

GRANT AND FELLOWSHIP

2018 Grant for free registration and for travel to international conference "Analytical Research Forum 2018", London, England UK, by Royal Chemistry Society.

2019 Grant for travel for the event "Showcasing Physical Sciences Impact Event 2019", 6 December 2019, London, UK by EPSRC.

Chapter 1 Biosensors

A biosensor is "a device that uses specific biochemical reactions mediated by isolated enzymes, immunosystems, tissues, organelles or whole cells to detect chemical compounds usually by electrical, thermal or optical signals", as defined by IUPAC [1]. Or more generally, we can refer as "biosensor" to all the devices whose aim is to detect a biological target molecule. The main application for a biosensor is in the Point-of-Care (POC) sector, where it is important recognise various antigens rapidly to give a fast and accurate diagnosis and treatment to the patient. Particularly in the diagnostic field, the capability of a device to identify disease biomarkers at the initial stages (in a quite low concentration) is attractive since this could increase the probability of the patient to heal or to survive [2]. As figure 1 shows, a biosensor is usually composed of three parts: a bio-selective material, a recognition signal, and a transducer.

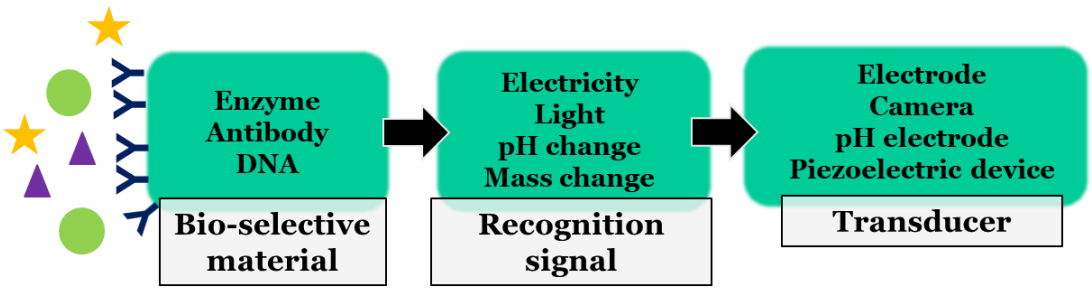

Figure 1 Biosensor components, a schematic representation.

The bio-selective materials generally used are enzyme, antibody or DNA which are the elements that react with the target analyte. As the reaction occurs, a change in the recognition signal is recorded in the transducer. Light (absorbance spectrum for example), pH change or mass change are the recognition signals most used. Accordingly, the transducer, a recorded device, is selected. A large number of possible different transducers can be proposed, including mechanical [3], ellipsometry [4], acoustic [5, 6], Impedance Spectroscopy [7], Quartz Crystal Microbalance (QCM) [8]. In all these different transducers, optical techniques are the most widely used in the development of biosensors, due to their fast response essential for real-time measurements, and multiplexed sensing capability, which make possible the realisation of a number of selective sensors [9, 10].

Typically, a biosensor is characterised by its limit of detection (LOD), the smallest variation in concentration/mass that the sensor is capable to detect in the output signal. The unit of measure of LOD also expresses which aspect of the biosensor the authors want emphasised. There are three units generally used; the first one is the surface mass density (or total mass) $pgmm^{-2}$ (or *pg*), which represents the sensing capability to detect change mass density on the surface. This reflects an intrinsic sensing capability of the biosensor and it is usually used to compare the performance of different biosensors [11]. The second unit that has been used is *ng/ml* which denotes the sample concentration and is easier to determine experimentally. However, by choosing this unit the LOD has to be indicated for each biomolecule as its value depends on the target analyte and its affinity with the biorecognition element [11]. Finally, the third unit is the refractive index unit (RIU), which is typically used for optical sensors. This is generally used to compare different optical phenomena and instruments.

In this perspective, the general properties that a biosensor should possess are good reproducibility and stability, and a high capacity of selectivity and specificity between different analytes. Reproducibility refers to the aptitude to obtain an identical signal for repetitive experiments, while the stability regards the influence that the environmental noises, such as vibrations or temperature gradients, may have on the accuracy and the performance of the instrument [12]. Finally, the selectivity represents the ability of the biosensor to detect the analyte in a mixture and its effect is proportional to the affinity reaction selected [12]. In practical terms, a biosensor for POC applications should be simple and easy to use for a non-skilled person [13]. This is because it should never be forgotten that the biosensor in its final stage (commercial, patent cover) will be used by doctors, nurses or possibly the patient, who are not meant to receive difficult instructions for using the sensor. The biosensor market is expected to grow from USD 21.2 billion in 2019 to USD 31.5 billion by 2024 [14] due the high request at the point-of-care level for fast and trustworthy biosensors, which can explore a new sensing application and update the commercial platforms already available or developing new ones [15].

1.1 Label free detection

Historically, biological research has used labelled techniques, such as fluorescence, to study molecules/cells [16]. For example, for over forty years, Enzyme-Linked Immunosorbent Assay (ELISA) has been the gold-standard method in biological detection with a detection limit of 1 pM [17]. However, this approach is time-consuming due to the laborious and costly labelling processes which may prevent the analyte binding and interfere with the results [18]. Generally, the tests are being executed in laboratories and requires from several hours to days, as it is the case for the cell culture technique [19]. Further difficulties with labelled approaches are the perturbations in molecular interactions caused by label molecules that can lead to false-positive or negative signals [20]. Moreover, the demand in the health care sector for compact devices, which can be used directly by the patient or non-skilled person at home, has pushed the research to find innovative ideas to develop a portable and reliable biosensor. In fact, in the last two decades in parallel with the progress of the nanotechnology approaches, label-free biosensors have emerged through the years obtaining in some cases the same sensitivity of their labelled predecessors [21]. In contrast with their predecessors, label-free devices directly measure a physical property of the analytes [22], such as the refractive index (RI), the electric charge or the molecular weight , and have the unique advantage of providing real-time quantitative information on the progress of the biochemical reaction without any risk of undesired effects [10]. Due to their detection methods which greatly simplify the time and effort required for evaluating detection, label-free biosensor are so desirable and highly attractive [23] in the POC sector. Nevertheless, as with other detection approaches, the label-free techniques are not without any flaws; if previously the labelling step was described as the one that can alter the signal, in the label-free approach the same “antagonist” role is played by the substrate. More precisely, the specific-binding sites are or on the surface or inside the support; if the non-specific binding is not sufficiently low, the measurements can be affected by those interferents, especially in some applications as with low molecular weight analytes, or where the binding affinity is not strong enough [17]. Even with these drawbacks, the label-free approaches are more attractive than their counterparts in the POC sector since the overall measurement is faster and in real-

time. Therefore, the sensitivity of the sensor increases accordingly with the density of the binding sites in a smaller platform, which makes the label-free techniques so appealing for the next generation of portable POC devices [2] [24]. Among all the label-free biosensing platforms that have been investigated in literature, the optical biosensors are the most versatile with one of the higher sensitivities [25], and for that, here the excursus will continue to highlight this group of biosensors. Other label-free sensors, such as the electrochemical [26] [27], will not be discussed in this thesis.

1.2 Recognition signal: Optical sensor

As it has been said at the beginning of this chapter, the recognition signal represents the characteristic technique that is selected for the biosensor. In this thesis, the optical biosensors are described more in-depth since one of them has been adopted in the present project. Furthermore, the optical sensors are the most widely used group of biosensors and are showing an extraordinary potential in healthcare and biotechnological industries [28, 29]. They provide a robust real-time monitoring of the RI changes connected to the target-molecules bide on the bio-receptors platform [30]. The RI change modifies the properties of the incident light, which are manifested in the transmission, reflection and absorbance signals or interference patterns, and are collected by a transducer [25] [31]. Furthermore, most of the biological molecules do not absorb in the visible spectrum, so this simplify the study of the RI [19]. The optical signal is non-destructive and allows an *in situ* measurement [32]. In addition, most of the applications are reversible and allow a multi-reuse of the sensing platform [15], so that their economical cost is been reduced. A direct comparison between different optical sensors is very difficult to undertake, because there are different aspects, such as LOD or sensitivity, that depend on the application [33]. The most advanced aspect of this category of biosensors, is that they have been demonstrated to work using a smartphone, for example by Cunningham B. group [34], or as other examples which can be found in Zarei M.'s review [35]. Below a general description of the most used optical biosensors is reported, showing their aspects and the reason why in this thesis project the interferometric sensor is being adopted.

1.2.1 Photonic crystal sensor

A Photonic Crystal (PC) is a periodic dielectric structure with a periodicity in the order of nanometres where not all the wavelengths of the visible spectrum can pass through it due to the presence of the photonic band gap [36]. However, a photonic "defect" in the PC's periodic structure leads the light resonating with the defect mode, to propagate in the PC [37]. In turn, a centred wavelength peak λ_0 and bandwidth $\Delta\lambda$ is observed in the reflection or transmission spectrum and recorded with a camera [19]. As the refractive index changes near the defect, the λ_0 peak moves accordingly, in this way the PC has some potentialities to be used as a biosensor [21]. The PCs are defined based on how many directions (one, two or three) the variation is placed [10]. Examples of gas [38] and pH sensors [39] can be found in the literature, and in Figure 2 is illustrated an example of PC sensor. In the past ten years, PCs have attracted a lot of attention in the biosensor development. The first example of a PC biosensor was provided in 2002 by Cunningham and his group [40], who fabricated the PC on a glass substrate and showed the shift of λ_0 peak accordingly to each step of the PC bio-functionalisation; the lowest refractive index change of this PC biosensor was 3.4 x 10^{-5} RIU. More recently, Pal *et al.* have proposed a two-dimensional PC sensor combined with a waveguide structure for virus detection with a LOD of 1.4 nM for buffer and sample solutions and an experimental sensitivity of the peak shift of 0.1 nm/nM [41].

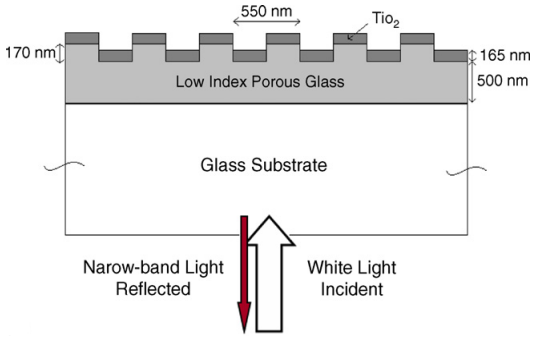

Figure 2 *Cross-section schematic of photonic crystal sensor [42]*

In order to improve the commerciality of their sensor, Scullion *et al.* [43] have integrated their sensor with PDMS microfluidics. They have achieved a limit of detection of 1 μm/ml for dissolved avidin and a surface mass density of 60 pg/mm^2. Finally, in the last decade with the introduction of the smart materials in the PC, such as hydrogel, the PCs have seen an additional interest as biosensor [44], because by incorporating the analyte, they

show an enhance of sensitivity. For example Choi et al. [45] have proposed a PC biosensor with a 3D poly(ethylene glycol)-diacrylate (PEG-DA) matrix that is able to measure the immunoglobulin G (IgG) antibody; the results showed a correlation between the analyte concentration and the shift, but no detection limit is reported. Similarly, Maeng *et al.* [46] also adopted a PEG-DA hydrogel as a backbone of the PC structure to detect Rotavirus with a concentration from 6.35 mg/ml to 1.27 mg/ml without pre-treatment of the sample. They have also shown that their results are comparable or superior to the ELISA instrument in commerce. In conclusion, only few examples of PC biosensors are reported as to compare it with the sensor adopted in this project. Further information on PCs sensors can be found in the literature, such as the review by Inan *et al.* [47] .

1.2.2 Surface Plasmonic Resonance

The surface plasmonic resonance is a phenomenon that occurs at the metal-dielectric interface when an electromagnetic wave interacts with the metal. If the wavelength of this beam is the same as the resonance oscillation of the free electrons in the metal, then their oscillation generates an electromagnetic field that arises from the metal layer. The resultant field decays exponentially in the dielectric material in the ranges of few hundred nanometres, and this distance is called penetration depth. In other words, an evanescent field travels through the dielectric material and is extremely sensitive to the refractive index variation of the second medium. Thanks to this characteristic, this phenomenon can be adopted for sensing purpose. For example, if the incident light is a white source, a peak in the absorbance spectrum can be observed and its shift is related to the change of the refractive index due the presence of the target molecule [28]. The main limitation of a SPR sensor is that it is mainly a surface sensor, because the evanescent field decays within 400 nm in the material, so that measuring the cells can be problematic [33], since their dimension exceed the sensing region of a SPR sensor. For this reason, most of the reported SPR sensors present strategies to bind the analyte over the metal surface, obtaining a successful result in biological interaction analysis [48], as for example BIAcore system (Biacore AB, Uppsala, Sweden). To obtain multiple light beam interactions with the metal surface, a coupling structure is commonly used [44], since freely propagating light is not able to couple to the surface plasmonic modes

[49], a wavevector matching scheme, such as a prism or waveguide, will, in fact, fix it. If the coupling structure in one way improves the sensitivity (by causing multiple light beam interactions), in the other one reduces the possibilities to miniaturise the sensor [25] [21]. In conclusion, not only the absorbance peak, but also the resonance angle can be monitored, and the sensitivity resolution has been reported to be between 10^{-5} to 10^{-7} refractive index units RIU [21]. The principle development and applications of SPR biosensors have been well described by Homola *et al.* [50]. Overall, the SPR has a good solidity and reproducibility, but it is more complicated to obtain a compact designed to be able to use for multiplexing detection purposes and POC [51].

1.2.3 Waveguide

A waveguide (WG) is an optical sandwich-like device where the middle layer (F) has a RI higher than both the cover (C) and substrate (S) ($n_F > n_C, n_S$). The light is "entrapped" in the middle film by means the total internal reflection (TIR) and travels inside it via a zig-zag motion, Figure 3. The incident angle requested for TIR is:

$$\theta_i \geq \theta_{cri} = \arcsin\left(\frac{n_c}{n_F}\right)$$

Changes in the effective RI in a WG biosensor are due to two possible adjustments in the cover layer: a formation of an adlayer of adsorbed or attached molecules, or a modification of the RI [22]. As with the SPR sensor, also the WG sensor can be classified as a surface sensor, because the detection principle is based on the attenuation on the cover layer of the evanescent field [52]. The RI of the cover layer changes when the analyte is binding on the bio-selective material; the changing of the RI provokes a modification on the reflected beam, which is usually recorded by a camera in order to detect a shift in either resonance angle, wavelength, or change in intensity [53].

If for the SPR the penetration depth of the evanescent field is within 400 nm, in the last years, it has been demonstrated by Gupta R. group that for a Leaky Waveguide the decay happens up to a few microns [54] [53], so that the WG can be more versatile than the SPR sensor. Furthermore, the WG has been integrated with other techniques, such as interferometry [55] [56], or SPR [57], for its characteristic to "guide" the light beam in a definite direction. The sensitivity resolution of the RI for the WG have been reported to vary within 1.28×10^{-4} to 2.37×10^{-6} RIU [53], and it has been reported for different uses,

such as a biosensor[55, 58], a device for characterisation of dielectric material [59], and for environment applications [60].

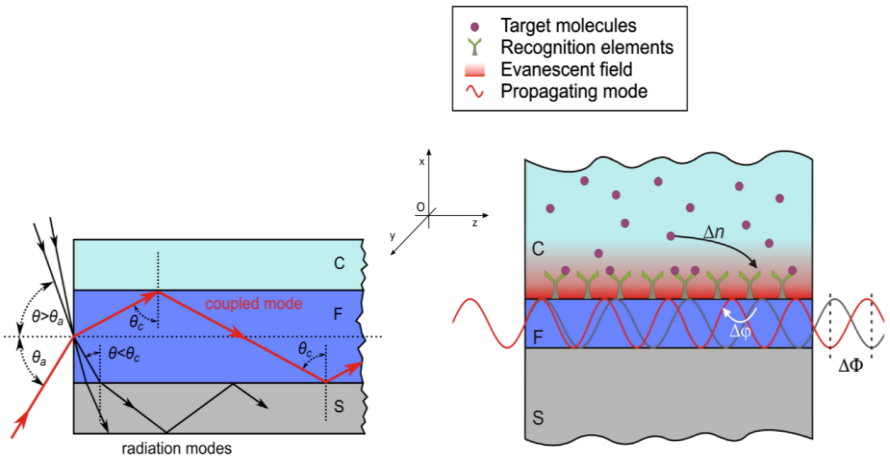

Figure 3 Light propagation in planar optical waveguide (left). Schematic working principle of label-free planar optical waveguide interferometer biosensor (right) [61].

A historical perspective of the WG sensors evolutions has been presenting by Gupta R. and Goddard N. [53]. Some significant disadvantages for the WG are the coupling light in to the structure [62] which reduces the possibilities to miniaturise the sensor, and the need for precise temperature controller [53].

Table 1 List of some optical biosensors

Optical	Integrated with	Analytes	Sensitivity	paper
Waveguide	Grating coupled planar WG	Escherichia coli K12	1.65 X 10^{-6} (deg/cell)/mm2	[63]
Waveguide	Bimodal WG	Bovine Serum Albumin (BSA)	2.5 X 10^{-7} RIU	[55]
SPR	WG	hCG	1.2X10^{-6} RIU	[57]
SPR	WG	Aldehydes of benzaldehyde	1.6X10^{-6} RIU	[64]
SPR	Microscopy	Aβ42 (Alzheimer's disease)	(DL)1.5 pM ~2.9 nm LSPR-peak shift	[65]
Photonic crystal	2D	protein	10 µg/ml	[66]

Interferometry	Multichannel Young Interferometer	Glucose solution	8.5 X 10^{-8} RIU	[67]
SPR	interferometry	DNA synthetic	~pM	[68]
Photonic crystal	/	/	1,3 nM, 0.1 nm/nM	[41]

1.2.4 Why choose an interferometer sensor

Not all the optical biosensors present in the literature are being described in this thesis so far. The group still missed is the interferometric sensors, one of which has been chosen for this project. Interferometric sensors allow the monitoring of the RI change of the sensing layer across all its volume [33] [69], whereas the other optical sensors are not able to do this due to their nature of surface techniques. This feature allows the interferometric sensor to be chosen for multi-detection purposes, aspects also relevant in the POC point of view. Comparing the RI change sensitivity with other optical sensors, it is important to note that the interferometer approaches are reported to be able to detect an order of magnitude from 10^{-6} RIU down to 10^{-8} RIU [30] [70]; on the other hand the interferometric sensors show a smaller sensitivity for low molecular mass analytes [31] as it happens with the SPR [51]. From the literature, it is evident that a transducer *per se* is not able to achieve the sensitivity or the selectivity required for an optimal biosensor. In other words, it is not so crucial which technique has the higher sensitivity or the faster time measurement, but it is a key point how much the selected sensor is adaptable by being integrated and improved with other optical devices, measurement techniques or chemistry strategies. In this perspective, the interferometry shows a good versatility, as Zhou *et al*. [71] have showed by adopting a WG structure to reduce the chip dimension. Finally, another aspect to be considered is the noise factors, for example the temperature drift in the measurements. The interferometry signal from its nature is due to the interaction between two beams, usually referred as reference and sensor beams, so, as long as the two beams are near enough in the device, the possible drift caused by a gradient in temperature should be negligible. For other optical instrument it happens that the comparison with a reference signal is made at the analysis stage, like in the case of Guo *et al.* [72]. In conclusion, an

interferometer has a lot of potential as a biosensor, which will be described in more details in the chapter 2.

1.2.5 Integration of Optical device with other techniques

In the last two decades, the label-free detection methods are being integrated with more than one techniques, such as fluorescence assays or liquid chromatography, to reduce the dimension of the instrument and to be able to characterise biomolecules with more information parallelly [16]. Another way to reduce the cost and the dimension of an optical biosensor has been the integration of passive and active optical elements in a single chip [73]. So far, the integration with fluidics has been widely explored [52], as to rise a new discipline called “optofluidic”, which push the development of new microfluidic microchips, using for example different materials from polymer hybrids to silicon. Utilising a microfluidic microchip consents the implementation with electrophoretic techniques [31], such as isoelectric focusing (IEF) or isotachophoresis (ITP), and allows a reduction in sample volume required, so desirable for POC devices [74]. In conclusion, the integration between two or more techniques seems to be a pivotal passage for the development of new POC devices, even though it is not a straightforward process [18]. In this project, electrophoresis has been integrated with the interferometer, for its capacity to separate molecules in a solution (in base of their isoelectric point or velocity) and to speed up the transport of the target molecule. Further aspects will be explained in chapter 3.

1.3 Bio-selective material

The second property that denotes a biosensor is the bio-selective material, which is selected based on the analyte of study; it defines the specificity and selectivity of the biosensor [75]. It is a biomolecule on the surface or in the matrix which is responsible for the analyte immobilisation. As the result of the immobilisation, the analyte is separated from other molecules in the mixer solution [31] and is concentrated in a limited space on the surface/volume of the platform. The main quality that a good immobilisation should possess is the stability, not only for storage and reuse aspects, but furthermost during the measurement, when the bioreceptors may be easily removed by the environment conditions, such as pH or buffer nature [25]. The stability of the biomolecule immobilisation is the most challenging and crucial part in the

biosensor development process and it should be noted that in many articles this aspect is not so well explained or presented [31]. In turn, a bioconjugation reaction design is the key point to succeed in biosensor production [74]. Generally, there are four attachment strategies so far used in the literature [25]:

- Covalent binding.
- Chemical crosslinking.
- Physical entrapment in a matrix, such as hydrogel.
- Physical absorption.

For the interferometric sensor, two strategies have been mainly reported for surface functionalisation: physical absorption and covalent bonding. Physical adsorption is controlled by electrostatic interactions between the surface and the receptor [25], while the covalent bond is more stable and strong linkage. The functional groups that are generally used to form a covalent bond with proteins are amino, carboxylic or thiol groups [44], which have been also entrapped in hydrogels. In the cases where the target analyte is a protein, it is strongly advised to create an environment that can preserve the activity of the protein [44], and the hydrogel seems to facilitate the right condition. On this aspect Charles P.T. *et al.* have demonstrated that a three-dimensional structure has more capacity for molecules immobilisation, since the target molecules are free to move through it, and so the possible interaction is multiplied compare to a two-dimensional surface [76]. On the other hand, using a matrix such as a hydrogel, the signal detected is influenced not only by the affinity of the target molecule, but also from the analyte dimension, the viscosity of hydrogel, the flow rate and the transport system adopted [33].

Another difficulty, when undertaking the immobilisation of the molecules, is the nonspecific interaction of other molecules that results in a compromised signal. In order to overcome this problem, competitive or binding inhibition processes can be used [33] or anti-fouling agents, such as other proteins (Urea o Bovine serum albumin), may enhance the analyte detection accuracy [47]. A surprising fact is that, despite all the knowledge on biofunctionalisation approaches evident from the literature, a lack of techniques to preserve the activity of the functional groups of the involved molecules is

present [30], or in other words a lack of standardised approaches. This may be due to the wide applications involved in the biosensor development, which use different conditions, such as pH or type of buffer or other experimental parameters, which may influence the results. In conclusion, is important to highlight that to obtain the highest possible sensitivity of a biosensor, it is fundamental for the recognition element choice to have the highest affinity with the target analyte, or utopianly speaking, the unique affinity with it. The sensitivity of a biosensor will result in the combination between the transducer technique and the affinity between the analyte and the bio-recognition element. Below, the main strategy for the biorecognition is presented.

1.3.1 Biotin-Streptavidin

Generally, the first strategy of biorecognition adopted in biosensor development is the Biotin-(strept)avidin system [30] [33]. The interaction is between a protein and a ligand, as the egg white (avidin) for vitamin B7 (biotin) in nature. Their affinity is among the strongest interaction with a dissociation constant of 1.3×10^{-15} M; this means that any other environmental variations, such as buffer, pH or temperature will not inhibit the interaction [77]. Some examples of optical biosensor adopting this strategy are presented by Hoffman *et al*., who have achieved the biorecognition by covalent attachment [78] in 2007 and by Schneider *et al.*, who studied the biotin-(strept)avidin system by direct coupling of avidin [79]. The sensitivity achieved with this system is quite remarkable, but it is always useful to remember that the sensitivity recorded with one target analyte does not represent the sensitivity for all the other molecules [33]. Stamm *et al.* have presented interesting research on this aspect; they have been monitoring with their optical sensor the biotin-avidin affinity using diverse avidin molecules. The absorption of three different avidin was not comparable among them, due their different physical properties, such as the isoelectric point (pI) [80]. In the majority of the experiments, it is the Streptavidin to be used, instead the avidin (glycoprotein), because it has a lower isoelectric point (circa 5.2 against 10), and so is less reactive to unspecific binding due to ionic interaction, and it is also less costly [31]. The streptavidin has a bacterial origin and derives from Streptomyces avidinii [77]. Further applications that involve the Biotin-(Strept)Avidin system are protein purification and immunoassay.

Chapter 2 Interferometry

2.1 Theory

The interferometry is a quite versatile technique, and it has been used in various fields of science, such as exploiting the gravitational waves with VIRGO or other astronomical studies, or also as a seismograph. But in this thesis, the interferometry is presented as a powerful tool for much "smaller" explorations such as detection of proteins, which require a more compact and portable dimension of the instrument. In this section the light interaction with the matter and with another light source are described to present a wide and complete description of the phenomenon and described its potentiality as sensor.

2.1.1 Light and matter

Light is an electromagnetic (EM) wave composed of an electrical field (E) and a magnetic field (B) perpendicular to each other, which in turn are also perpendicular to the wave vector ***k***. In the case where the EM wave propagates in the vacuum along the *z* direction, the solutions of the wave equations (obtained from Maxwell`s equations [81]) are:

$$E_Z(z,t) = E_0 \exp\left[i(t - kz + \phi)\right] \qquad (\mathbf{2.1.1})$$

$$B_Z(z,t) = B_0 \exp\left[i(t - kz + \chi)\right] \qquad (\mathbf{2.1.2})$$

The wave propagates to a fixed direction, which is defined by wave vector ***k***, with period *T* and wavelength λ. The parameters in the expressions above, ϕ and χ, are the phases of the E and B waves, ω (angular frequency) and ***k*** are defined by $\omega = 2\pi/T$; $k = 2\pi/\lambda$, while the velocity of the EM wave is defined as:

$$c = \frac{1}{\sqrt{\varepsilon_0 \mu_0}} = \frac{\omega}{k} \qquad (\mathbf{2.1.3})$$

If now we consider the case in which the EM wave interacts with the matter, we find some variations with the previous case. One of the main differences from the vacuum case is that the light changes some of its characteristics (speed and wavelength) inside other media, decreasing its **velocity** and wavelength by following the formulae:

$$v = \frac{c}{n} \quad ; \quad \lambda_n = \frac{\lambda}{n} \tag{2.1.4}$$

Where v and λ_n are the velocity and the wavelength of the light inside the medium respectively, while n is the **refractive index (RI)**. The last is a dimensionless number which defines the electrical/optical properties of all materials.

In this context when an EM wave comes from a medium and incises on a second one, a reflected beam and transmitted (refracted) beam are generated, Figure 4. In this discussion the two media are homogeneous and isotropic, and they are characterized by their RI n_1 and n_2 respectively. The incident beam intensity is in part reflected and in part absorbed in the second medium.

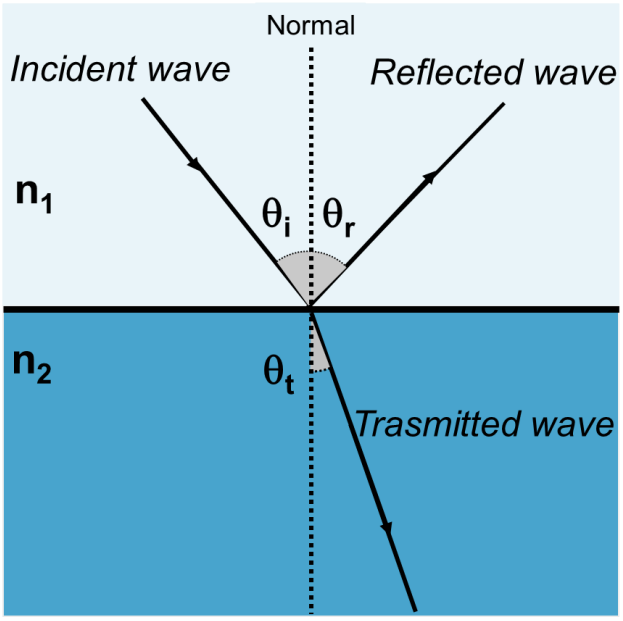

Figure 4 Representation of Snell`s laws.

The formulas **2.1.5** which describe the EM behaviour at the interface between two media, are the Snell`s laws [66]. They are the following, where θ_i, θ_r and θ_t are the incident, the reflective and the refractive angle respectively.

$$\sin\theta_i = \sin\theta_r \rightarrow \theta_i = \theta_r \quad ; \quad \frac{\sin\theta_i}{\sin\theta_t} = \frac{n_1}{n_2} \tag{2.1.5}$$

In the specific case of the incident beam perpendicular to the surface, from the Snell's formulae it can be deduced that the incident, reflective and transmitted beams are collinear (formulae **2.1.6**).

$$\theta_i = 0 \rightarrow \ \theta_r = 0 \ and \ \theta_t = 0 \qquad \textbf{(2.1.6)}$$

2.1.1.1 Refractive index

To better explain the importance of the RI, the most interesting aspects of the RI will be presented. The RI is dimensionless number and represents the optical but also the electrical properties of all the materials, due to the electromagnetic nature of the light. The RI can be calculated indeed not only from the formula **2.1.4**, but also using the permittivity ε and the permeability μ of an optical material from the formula **2.1.3** obtaining the following relation, where the connection between the RI and the permittivity is explicit.

$$n = \sqrt{\epsilon\mu} \rightarrow \text{for no-magnetic material } n = \sqrt{\epsilon} \qquad (\textbf{2.1.7})$$

Since ε strongly depends on the wavelength, it follows that also the RI depends on it too, which is the main cause of the dispersion of the light when it interacts with a material. Moreover, if the light propagates through such dispersive medium, it can lose energy due to the absorption and scatter mechanism of the material. Therefore, the RI of a lossy material is a complex function of the wavelength of the light, where the real part, *n*, follow the Snell's laws, while the imaginary part, κ, called extinction coefficient, describes how the energy will be absorbed by the material.

Furthermore, the RI of a heterogenous material becomes more elaborate to study. For example, if the medium of interest (solution) is composed by two materials, "A" (the solvent) and "B" (the analyte), to describe the RI function the concentration and the RI functions of the two components are pondered. This approach is called *effective medium approximation (EMA)*, where instead of studying the system at microscopic level, the method focuses the attention on the macroscopic variable, such as the permittivity [82]. It follows that the great potential of investigating the RI variation instead of the other quantities (molecular weight) is exactly the possibility of studying a

microscopic system, using its macroscopic properties [83]. There are different EMA approach, such as the Lorentz-Lorenz description or the Bruggemann theory [84] .

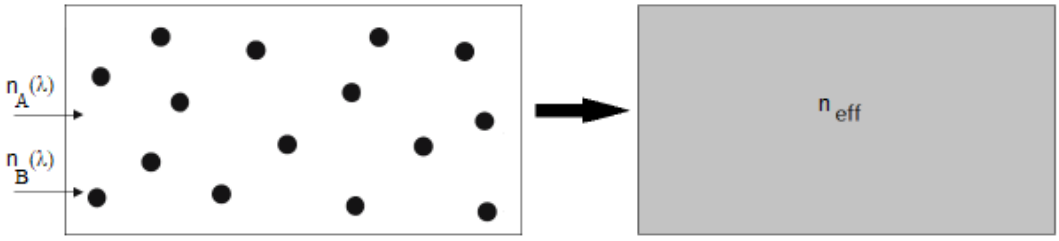

Figure 5 Schematic representation of Maxwell Garnett theory.

The approach that better describes the example previously proposed is the Maxwell-Garnett theory (MG) [85] [86], because it analyses the case where one component occupies a bigger volume than the other one; the space occupied by the analyte is indeed far smaller than the volume occupied by the solvent. In particular, this method recognises an unlimited homogeneous matrix, host medium, and spherical inclusions, in which RI functions are $n_A(\lambda)$ and $n_B(\lambda)$ respectively; a schematic representation can be observed in Figure 5. Adopting the MG theory, the effective refractive index of the solution n_{eff} is the following:

$$\frac{n_{eff}^2 - n_A^2}{n_{eff}^2 + 2n_A^2} = f_b \frac{n_B^2 - n_A^2}{n_B^2 + 2n_A^2} \qquad \textbf{(2.1.8)}$$

Where the f_b, represents the volume fraction occupied by the *B* component. In addition, observing the formula **2.1.8** and considering a case of a defined wavelength, an alteration of the n_{eff} is only caused by a variation of f_b, or in other words by a concentration variation of the analyte. This is the case which will be considered in this thesis, to evaluate the sample concentration. The wavelength used is in the visible range, where most of the molecules do not absorb the light, so the RI can be considered a real number. The EMA methods are a good approximation and as such they have to be considered, but they do not describe all the aspects of the system.

The major challenge in RI detection is the temperature drift that alters the RI value [87]; for most liquids, the fluctuation of refractive index units (RIU) is 10^{-4} RIU/°C and such sensing system is usually require a sensitivity of 10^{-6} RIU [88]. Consequently, a temperature control or the adoption of a reference (such as the one used in this project)

are essential for a valid RI measurement. Lastly, an important aspect that should always be kept in mind is that it is not possible to have a direct measurement of the RI, but its valuation is always calculated from a formula (Snell's laws for example [89]) that connects the RI to a measurable quantity, such as the phase, the wavelength, the angle, and the intensity of the reflected or transmitted beam [90].

2.1.2 Light and light: Interference

After the discussion about the interaction between light and matter, now it will be presented the case when the light interacts with the light. More precisely, when two or more waves are superposed to each other in one point in space, the resultant wave can have a lower or greater amplitude respect to the initial wave sources. The interference can be constructive if the amplitude is the sum of the interacting waves, or destructive if the resultant wave amplitude is zero. The explanation reported below, gives a mathematical description of this phenomenon.

2.1.2.1 Double slit experiment

The first person who performed this interaction purposely was Thomas Young [91], with his well-known experiment of the double-slits, Figure 6.a. In this setting, a monochromatic light source passes through two slits (positioned at a distance *d*), which in turn act as two light sources with the same phase. Then, a sequence of white (bright) and black (dark) fringes which form the interference pattern appears on the screen, positioned at a distance *D* from the slits. The bright and the dark fringes represent the constructive and deconstructive interference of the two waves respectively. Bright fringes (constructive interference) occur when the two waves are in phase, while the dark fringes (destructive interference) occur when the two waves are out of phase. The intensity (*I*) and the **phase difference $\Delta\varphi$ (PD)** depend not only on the position on the screen *y*, but also from geometrical parameters, as evidenced in the equations.

Optical path difference (OPD) $$OPD = d\sin\theta \underset{\theta\to 0}{\sim} d\frac{y}{D} \qquad \textbf{(2.1.9)}$$

Phase difference (**PD**) $$\text{PD} = \Delta\varphi = \frac{2\pi}{\lambda} OPD \qquad \textbf{(2.1.10)}$$

Intensity $$I = I_0 \cos^2(\Delta\varphi)$$ **(2.1.11)**

Observing formula **2.1.11**, the nature of the intensity is cosinusoidal square behaviour of the phase difference ($\cos^2(\Delta\varphi)$), which causes the periodical sequence of bright and dark bands, fringes, of the interference pattern. Furthermore, the intensity is related to the phase difference $\Delta\varphi$, which in turn is influenced by the optical path difference (OPD). *m* is the order fringe number.

Bright fringes positions $$y = m\frac{\lambda D}{d}$$ **(2.1.12)**

Dark fringes positions $$y = (m + \frac{1}{2})\frac{\lambda D}{d}$$ **(2.1.13)**

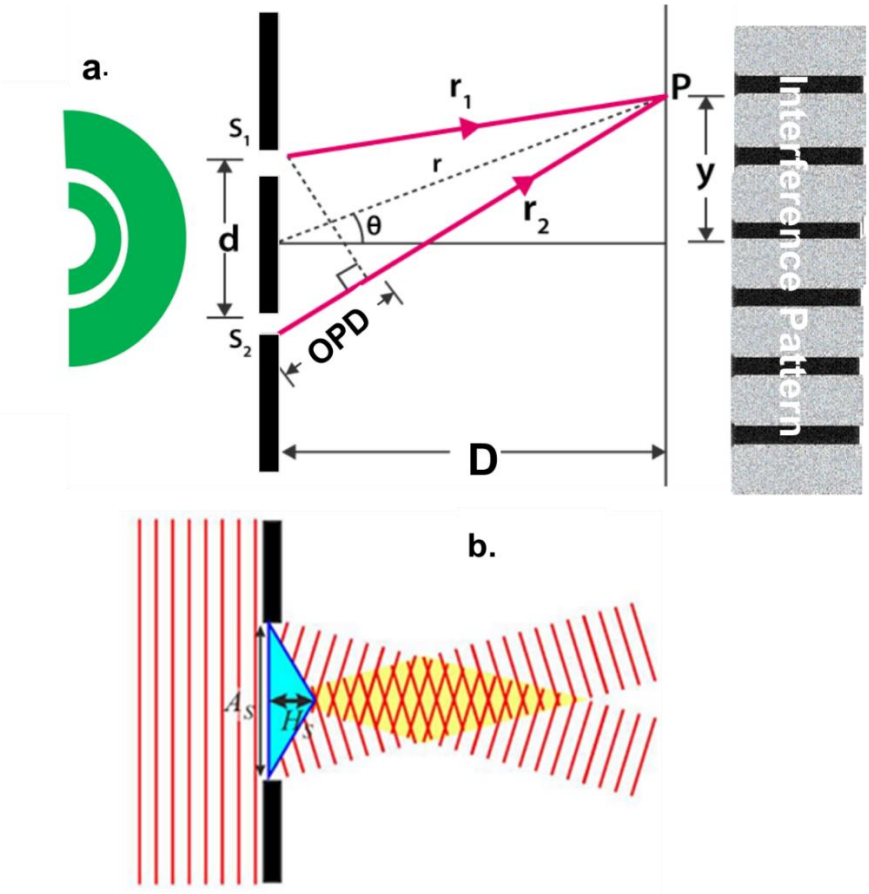

Figure 6 Schematic representations of the wave fronts in a double slits experiment (a), and in presence of a Fresnel Biprism (b) [92].

Bright fringes occur when the two waves are in phase, or in other words when the OPD differs by an integer number of wavelengths, while the dark fringes occur when the two waves are out of phase, or the OPD differs by a half-integer number of wavelengths. The main features that both waves must possess are having the same wavelengths and being coherent (having a constant phase for a length longer than the experiment setting dimensions). For those reasons the laser is the optimal light source having those properties. Young's double slits experiment is still the most famous teaching example in optics courses [92], used to introduce the interferometry and to describe the light as a wave [93].

2.1.2.2 Phase Difference

As just described, in the interference pattern the fringes represent the sum of the amplitudes of the two waves [94] and their positions are related to the phase difference. To highlight the key aspect of the phase difference (PD) and the role it plays in the interferometry sensor measurements an excursus is now presented. In this description, it is still assumed, like in the Young experiment, that the two waves, now named the reference (*ref*) and the sensing (*sen*) beams, are propagating in the same direction with the same frequency [94] and, most importantly, they are originated from the same light source, and consequently the waves have also the same phase. The amplitudes of the two waves are $A_{ref} = a_{ref}\exp(-i\phi_{ref})$ and $A_{sen} = a_{sen}\exp(-i\phi_{sen})$, and when they overlap to each other, the amplitude of the interference is then:

$$A = A_{ref} + A_{sen} \qquad (\mathbf{2.1.14})$$

Consequently, the resulting intensity is:

$$I = |A|^2 =$$

$$= \left(A_{ref} + A_{sen}\right)\left(\tilde{A}_{ref} + \tilde{A}_{sen}\right) =$$

$$= \left|A_{ref}\right|^2 + |A_{sen}|^2 + A_{ref}\tilde{A}_{sen} + \tilde{A}_{ref}A_{sen} =$$

$$I = I_{ref} + I_{sen} + 2\sqrt{(I_{ref}I_{sen})}\cos^2(\Delta\varphi) \qquad (\mathbf{2.1.15})$$

where I_{ref} and I_{sen} are the intensities of the two waves acting separately and $\Delta\varphi = \phi_{ref} - \phi_{sen}$ is the phase difference between them [95].

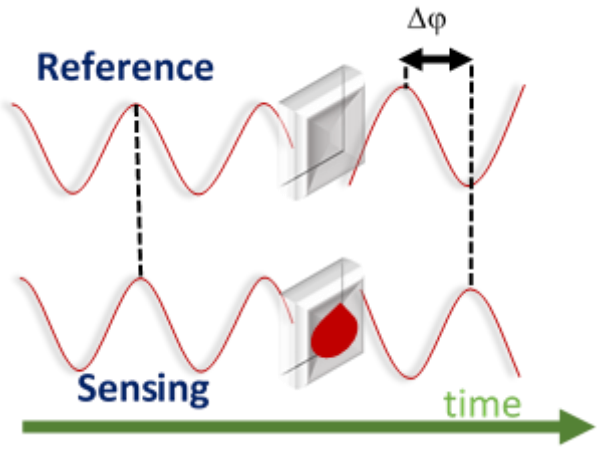

Figure 7 Schematic representation of how a difference in the RI can change the phase difference.

Another aspect to be evaluated is how the formulae presented before, change when the two beams go through a medium and not only in the vacuum. The OPD then can be rewritten as formula **2.1.16**, where h_i (i= *ref* and *sen*) represent the thickness of the two media, called also interaction length, while n_i are their effective refractive indexes.

$$OPD = d\frac{y}{D} + |n_{ref}h_{ref} - n_{sen}h_{sen}| \qquad \textbf{(2.1.16)}$$

In order to reduce or compensate for wavelength and temperature fluctuations, an important assumption is to have the same interaction length [96] (h_{ref} = h_{sen} = h), then the OPD and PD(**2.1.10**) obtained after the last assumption are:

$$OPD = d\frac{y}{D} + h|n_{ref} - n_{sen}| = d\frac{y}{D} + h\Delta n \qquad \textbf{(2.1.17)}$$

$$\Delta\varphi = \frac{2\pi}{\lambda}\left(d\frac{y}{D} + h\Delta n\right) \qquad \textbf{(2.1.18)}$$

In the formula **2.1.18**, it is evident that the PD of a interferometer is due to two contributions: the geometrical (dy/D) disposition of the interferometer and the responsiveness of the interferometry to the refractive index difference ($h\Delta n$). To evaluate the RI, and the concentration of the analyte, in our project, the formula **2.1.18** has been simplified in:

$$\mathrm{PD} = \Delta\varphi = 2\pi\frac{h}{\lambda}\Delta n \qquad \textbf{(2.1.19)}$$

since the same geometrical dispositions are maintained the same through the experiment. Consequently, a change of PD can only be due to a modification of the RI. The phase difference is expresses in radians and its values are an integer of 2π, which gives the periodicity behaviour.

2.1.2.3 Coherence

To get through to interference phenomenon, an indispensable wave characteristic is the *coherence*. In optics the term coherence refers to the property of an electromagnetic wave to maintain a constant phase relation with itself through all its propagation in the space [97]. Consequently, two waves are considered coherent if their relative phase is constant in time/distance. The partial coherence between the two waves limits the possibility to obtain the interference in any part of the space, where the interaction occurs. It is possible to identify two aspects of the coherence: the temporal and the spatial coherence. The first one, the temporal coherence, describes the duration, or length, of the electromagnetic wave package emitted by the light source, whereas the spatial coherence is linked to the dimension of the light source. As a more in-depth description considering a monochromatic light source, the temporal coherence is determined by the wavelength band width ($\Delta\nu$) of the light source in the vacuum as $t_c = 1/\Delta\upsilon$; it follows that the smaller the band width, the longer the time and distance that the two waves can be considered coherent. The coherent length is defined as $\beta_c = ct_c = \frac{\lambda^2}{\Delta\lambda}$ [97]. An example of a light source with this feature is the laser, whose temporal coherence is equivalent to a distance in kilometres, typically 3/4 km. Whereas the second property, the spatial coherence, is referred to as two waves originated from two points positioned perpendicularly to the direction of the wave propagation, whose phase difference, $\Delta\varphi$, is constant in time; the wider the region where this occurs, higher is the spatial coherence. The interferogram of the Young experiment perfectly represents the region where the two waves are spatially coherent. Therefore, the term coherence is directly associated with the interferogram, and *vice versa*; the higher the coherence, the higher the fringes contrast [98]. Furthermore, with an extended light source the fringes position on the screen corresponds to the precise locus points on the light source [94]; the advantages for this feature are reported in the following chapter, where the instrument is described. A more recently description of the correlation

between coherence and interferogram has been conducted by Pearson et al. [99], where they have studied how the size of the light source influences the final result of the interference.

To obtain two coherent light waves, the starting point is to use one light source and divide into two equal parts. More precisely, two main techniques can be individuated:

- Wavefront division. The two point sources are obtained by two small apertures on a plane, such as pinholes, or by using optical element, such as Fresnel Biprism, which creates two virtual sources. In this case the wavefront is equally divided, as with the double slits experiment.
- Amplitude division. In this technique, the initial wave amplitude is halved using optical elements, such as beam splitter and diffraction grating [94]. An example is the Mach-Zehnder interferometer, in the "classic" disposition, where a beam splitter is normally used, instead of a waveguide structure.

The light source normally used in interferometry is the laser. The invention of the laser was a boost for the interferometric techniques, removing the limitations, such as low coherence, of the other light sources. Along the years, different laser sources have also been created, such as the gas laser, or laser diode systems, such as the one used in this project. A drawback with the laser is the high degree of coherence itself, because random scattered light, or spatial noise, can cause interference both literally and optically, with the main beams [94].

2.1.3 Sensors based on interferometry

As it has been already mentioned in the previous chapter, the interferometric sensors display the highest sensitivity to the variation of refractive index compared to the other optical sensors [96] and are more attractive compared to the fluorescence techniques [100], which are labelled methods adding further cost and complexity that can conflict with the measurement itself [51], such as artefacts. Furthermore, Lukosz *et al.* [101] compared the theoretical sensitivity of the surface plasmonic resonance with one of an waveguide interferometric sensor, asserting that the interferometer-based sensor has potentially the utmost sensitivity to the refractive index changes. The optical elements disposition for interferometry is quite simple, albeit their alignment can be tedious.

Below various interferometric instruments are reported, accentuating their main aspects. Some common configurations among all the following interferometric sensors can be established, such as the halving of the primary light source in reference and sensor beams, where a local change of refractive index occurs [24], or the refractive index change is also proportional to the interaction length. Another similarity, that emerges from reading the previous works, is that the majority of those biosensors presents an instrument where two or more techniques are embedded together in order to improve the sensitivity and the selectivity of a target analyte. Further advantages to embed two or more measurement techniques are the robustness, the downsizing of the sensor dimension and of the sample volume, as Zinoviev *et al.* reports [102], features which are essential for a biosensor development. The most common set-ups used for interferometric sensing measurement are the Young (YI) and the Mach-Zehnder interferometers (MZI) [12]. Both have also been developed in parallel and despite the fact that the YIs has shown the highest refractive index sensitivity among the optical sensor [103], the MZI results to be the most used among the interferometers.

On contrast, the major sources of uncertainty in interferometry are the signal periodicity, as was already described in the phase difference section, and the intensity fluctuation of the laser [96], which both can be easily removed by a software that is able to recognise the difference, and finally the other source of uncertainty is the thermal fluctuation [30]. Further descriptions on the phase ambiguity are described in this chapter at paragraph 2.1.4.1 and in chapter 4, section 4.2.4. Usually, the thermal fluctuation is reduced by adopting a chip where the two arms are spaced by only a few μm (internally referenced), in such way the temperature gradient can be eliminated [30]. With such geometrical disposition, the temperature is theorised equal in the reference and in the sensing arms. Although the interferometric sensors are the oldest method adopted in sensing, they still contain hidden potential for further applications, such as biosensors [104], as the following list will show.

2.1.3.1 Young Interferometer

The first interferometer sensor to be described is the Young interferometer. In the most common configuration, the light source beam is halved using a Y junction, as it can be observed in Figure 8, in a waveguide (WG) chip, where the reference and the sensor

branches lay on the surface. After the beams travel through the two arms, they overlap on a camera and the fringes of the interference pattern are recorded.

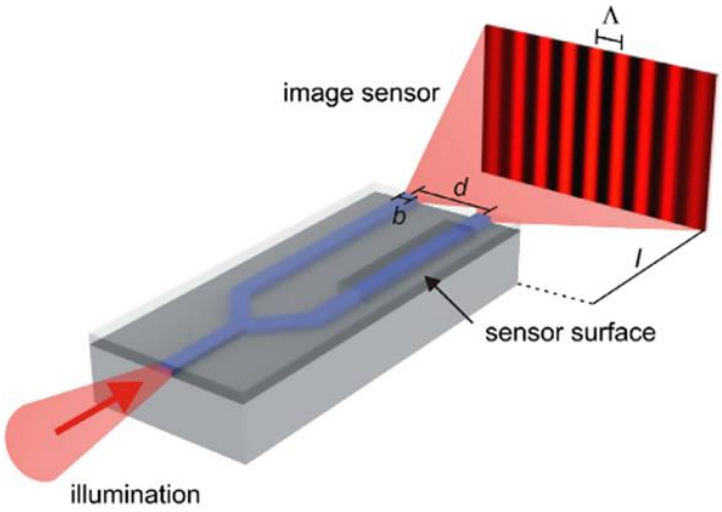

Figure 8 A Y junction that creates a Young Interferometer in a waveguide structure [105].

The lengths of the two arms are identical and as close as possible; the phase difference is the quantity that is usually measured using an appropriate software, which the Fast Fourier Transform (FFT) uses to identify the PD from the fringe shift on the screen. The first reported YI sensor was reported by Brandenburg and Henninger (1994) [106], who suggested this new instrument for refractometry and chemical sensing and tested it with different sugar solutions. After few year (1997), Brandenburg achieved a sensitivity of the refractive index of 10^{-9} refractive index unit (RIU) [107]. In 1999 Cross *et al.* introduced a YI with multiple layers based on optical waveguide system, having the two channels disposed vertically [108] for humidity sensing and obtained a LOD of 1ppm. In 2000 Brandenburg *et al.* presented the first YI for measuring the immunosensing [96] with a sensitivity of 9.0×10^{-8} refractive index unit, RIU, and a lower detection limit (LOD) of Γ= 750 fg/mm^2. Whereas, Cross et al. demonstrated a further possible use of the YI: the possibility of studying the protein structure and function [109]. Moreover, almost in the same year, Ymeti *et al.* (Heideman's group) started to implement the YI two-channel sensing waveguide chip [110] [67] (2001) towards the realisation of the YI multichannel in 2003 [111], with a sensitivity of 8.3×10^{-8} RIU and in 2007 the same group managed to detect different analytes from the same interferogram using the multichannel YI [112]. In this system one channel is the reference while the other three

ones are being used to measure different analytes by treating the channels with appropriate antibodies and lastly using a peristaltic pump to flow in the solutions. In the same years, Schmitt *et al.* (also Brandenburg's group) determined binding rate constants k_a and k_d by evaluating the initial binding rate $\Delta n_{eff}/dt$ and analysing the Biotin–streptavidin system and the immunoreaction protein G–immunoglobulin G kinetic analysis [113]. In the same period of time, Hradetzky *et al.* used the YI to prove the suitability of this sensor as a biosensor, by coating the surface of the sensor channel to immobilise DNA [114]. The following years have seen the research more focused on changing chip material [115] [116] and on different coupling methods for the light and the waveguide chip [117] [71], rather than on the explicit and effective use of YI as a biosensor. Furthermore, YI have been investigated with surface plasmon resonance by Wong *et al*. [118] and Divitt *et al.* [119], or by using double polarisation of the light source [120] [121] in order to eliminate the phase difference ambiguity. Our own group has developed the first YI embedded with electrophoresis [122], towards the realisation of a biosensor that benefits from the high sensitivity of the YI and the rapidity and selectivity of the electrophoresis, as it will be described through this thesis. Lastly, in the last ten years, only three papers have been reported so far for using a YI as a biosensor to the author's knowledge. In 2012, when Wang *et al.* [123] [124], who adopted the vertical disposition and obtained a LOD of 10^{-5} RIU and 4 pg/mm^2 . In the same articles, they also reported a phase difference smaller for bovine serum albumin (BSA) concentration than for IgG molecules, indicating the difference in the length/molecular weight (Mw), 66kDa for BSA and 150 kDa for the IgG molecule, as the reason. On the 2016, Aikio et al. used the 4-channels proposed before, with two reference channels and the other two for sensing with a sensitivity that is between 10^{-5} and 10^{-6} RIU [125]. The analytes used for testing were C-reactive protein (CRP) and human chorionic gonadotropin (hCG) on a surface patterned with antibody-based receptor, which were patterned by inkjet printing; with this technique the group wanted demonstrate the analyte specific chemical- and biosensing with a disposable polymeric chip and possibly reduce the cost of (bio)chemical sensors [125]. In conclusion, it appears quite surprisingly that only a few research groups are investigating YI as a biosensor, instead of temperature sensor [126] or for studying atomic effects [127] , considering that from a Young interferometer pattern it is possible to measure both the intensity and the

phase difference, whereas with a Mach-Zehnder interferogram only the intensity can be extrapolated. Consequently, more information can be evaluated at the same time with a Young interferometer.

2.1.3.2 Mach-Zehnder Interferometer

The second interferometer presented is the Mach-Zehnder interferometer (MZI), which takes its name from the two inventors, Ludwig Zehnder and Ernst Mach, who thought of the new setting based on the YI [12]. In this configuration, the monochromatic light source is divided in two equal beams, one then travels through the reference and the other through the sensor part, which causes a change in phase of the beam. After traveling the same distance, the two beams are recombined in the same beam, that is characterised by a field intensity, which in turn is related to the refractive index difference [44]. The pioneer of the MZI as a biosensor is Heideman *et al.* [128] [129], who in the first years of the 1990's, measured the thickness of an adsorbed thin layer on the surface of a cuvette placed and coupled in the middle of a SiO_2 waveguide, together with the reference cuvette in the other arm of the interferometer. The analyte was human Chorionic Gonadotropin (hCG) that was binding on the anti-hCG antibody-modified sensor, with a limit of detection of 2.5 ng/ml or 50 pM (2×10^{-5} RIU) in 20 minutes. Finally in 1999 Heideman and Lambeck [130] managed to improve their MZI biosensor to obtain the highest sensitivity 10^{-6} RIU, for this interferometer configuration, which has not yet been surpassed [30]. Besides, other groups adopted the MZI using a WG chip, trying to reduce the dimension (from cm^2 of Heideman to mm^2 or μm^2) and improve the antigen binding such as Brosinger *et al.* who detected 2,4-dichlorophenoxyacetic acid (2,4-D) using a competitive immunoassay with a LOD of 1 µg/ml [131]; whereas Schipper *et al.* modified the sensor surface with an anti-hCG antibody, detecting hCG with a concentration of 60 and 80 nM, but without reporting the LOD [132]. In the following years the research was focused on improve the performances of the waveguide such as Prieto et al. [133], who after few years improved their MZI for biosensing [134], measuring in real-time the covalent immobilisation and hybridisation of DNA on the surface without using any label with a limit of detection of 300-10 pM. Then, the research was focused on adopting different materials for the waveguide layers, such as polymers, to improve the selectivity and decrease the

productive cost as Tung et al. showed in 2005 [135]. Some examples of polymer chip for biosensing application in MZI are the works reported by Bruck et al. [136] and Bastos et al. [73]. Other ways that have been exploited are the magneto-optic modulation [137] and the integration with surface plasmonic resonance (SPR) [138] [139]. An example of MZI combined with microchip capillary electrophoresis (MCE) (see the chapter Chapter 3 for more information) has been promoted by Crespi A. et al. [18]; they have adopted a commercial MCE device and have obtained a sensitivity of only $1.5x10^{-4}$ RIU and a limit of detection for peptides of 9mM . Most recently, a MZI sensor for protein separation has been developed by Yang X. *et al.* [140], who have combined the interferometer with optical fibres using SDS electrophoresis for the separation of Bovine serum albumin (BSA) and Chicken egg albumin (CEA). In this paper, the group manage to identify the separation through the interferometer pattern, however they have only reported quality data and they have not suggested any way to quantify the analyte concentration. A good example of miniaturising MZI for point-of-care applications can be found in Misiakos *et al.* work [141], where the limit of detection is only 10^{-5} RIU. More recently they have reported an improvement of the selectivity of this biosensor [142], where they have described all the passages of the surface treatment required, underlining the importance of the procedure step-by-step [143] and efforts that are required in the development of a biosensor. The MZI has also been used to monitoring reactions [144] and gelation processes [145].

In conclusion, MZI is still the most used interferometer sensor nowadays, in particular for biosensing applications, having the simplest signal acquisition using a photodetector, but at the same time this interferometer requires high stability for the light coupling [55]. For further descriptions and discussions on how a MZI interferometer works the following papers are suggested [138] [12].

2.1.3.3 Back-scattering interferometer

The last interferometer here reported is the “youngest” interferometer sensor that is called the back-scattering interferometer (BSI). The working principle can be attributed to the interferometry of a multilayer. In summary, a single wavelength laser source incises on the surface of a capillary and the beams are reflected by the internal and external surfaces of the capillary, where the sample flows. Then the reflective beams

interference between each other's and the interference pattern, similar to the YI, in recorded in the camera [33]. The interference pattern is related to the thickness and the refractive index of the layers and can locally change, so that this technique is also able to detect a local change of the refractive index [146]. The BSI is a label-free technique which has been promoted by Bornhop and his research group, quite intensely in the last decade, although Bornohop and Dovichi published the first article in 1986 [147], where they declared the ability to measure the analyte concentration using a nanolitre sample volume, in contrast with the other analytical techniques, normally used in a Chemistry laboratory, such as chromatography.

Along the years, they have tried different configurations, such as collecting the transmitted beam in the beginning to switch to the reflective beams more recently, and the limit of detection has been improved achieving 10^{-7} to 10^{-8} RIU [100, 148] after years and adopting more sophisticated algorithms for the acquisition software. Nevertheless, a temperature control has always been adopted [51], to reduce the temperature perturbation of the room. Having a capillary of 210 µm × 100 µm radius dimension, the alignment of the laser beam has been reported as tedious [148]. The BSI has been adopted not only for measuring small refractive index changes in capillaries, but also to obtain the rate and affinity of biomolecular interactions in a microfluidic device [146] [51]. More recently, Dunn have been adopting the BSI as an alternative method to mass spectroscopy or other analytical techniques [149] [88]. Overall, all the groups before cited have presented the BSI as a good alternative to the "classic" analytical methods in a laboratory environment, but they have not yet shown the potential as a biosensor and in particularly as point-of-care device. The reason that the BSI is here reported is because it is a technique that combine the capillary characteristics with an interferometric method, and can be compared with the project presented here, as it is useful to underline the differences between those two techniques.

In the following table, Table 2, some of the interferometric sensors previously described, are reported, by highlighting the chip materials, the detection limit, the analytes and most importantly the interaction length and if the instrument is integrated with another sensing techniques.

Table 2 Interferometric sensors

Interference	Chip	Interaction length	Integrated with	Analytes	DL	Articles
MZI	di-ureasil film	5 mm	WG	E. coli	$2*10^{-4}$ RIU, 2 pg/mm^3	[73]
MZI	PDMS	15 mm	microfluidic	Hydrochloric acid solutions	2×10^{-7} RIU	[150]
MZI	SiO_2 and Si_3N_4	1 cm	WG and grating	immunoassay	$3x\ 10^{-6}$ RIU, 10^{-2} nM (hCG)	[129]
MZI	silicon	600 μm	/	K-casein solution	63 ng/mL	[143]
MZI	PDMS	1 cm	WG	Streptavidin-Biotin binding	0.1 μm/ml	[136]
MZI	7	9.5 mm	Optical fibre, electrophoresis	BSA, CEA	3580 nm/RIU	[140]
MZI	PDMS	15 mm	microfluidic	Hydrochloric acid solutions	2×10^{-7} RIU	[150]
BSI	glass capillary	0.1 mm	/	nematic liquid crystals	0.008 mM	[151]
BSI	glass	100 μm	/	Glycerol, ConA–mannose binding	7.0×10^{-7} RIU (0.11 mM glycerol)	[148]
BSI	glass	550 μm	/	glycerine	4.73 μM glycerine, 6.17×10^{-8} RIU.	[100]
YI	Silicon support	No reported	grating coupler	Blood plasma	/	[152]

YI	planar Ta_2O_5	5 mm	WG	protein G–immunoglobulin G	9*10-9 RIU, 0.013 pg/mm^2	[113]
YI	/	1.65 mm	SPR and WG	Sample solutions	10^{-6} RIU	[118]
YI	hybrid material on Si substrate, Flow cell is made of PMMA	13 mm	Dual slab WG	Glucose, IgG solutions	10^{-5} RIU, 4 pg/mm^2	[123]
YI	SiON	4 mm	WG	HSV-1 virus	6×10^{-8} RIU, 20 fg mm^{-2}	[112]
YI	molecularly imprinted polymers	1,5 cm	WG	melamine	1251 rad RIU-1	[153]
YI	Ormostamp/ glass	5 mm	WG	Glucose	6.0 10^{-6} RIU	[115]
YI	Al2O3/TiO2	800 µm	WG	ethanol-water solutions	10^{-6} RIU	[116]
YI	PMMA	250 µm	microfluidic	Glycerol solution	2x10^{-6} RIU	[122] (This project)

2.1.4 Summary and comments

In conclusion, the comparison of the current state-of-art interferometric biosensors reveals a more orientated integration attitude between the interference and the other optical methods, more specifically with the SPR, perhaps because it is more industrially available, rather than to improve or incorporate the interferometric sensor with other analytical techniques, such as the electrophoresis, as this project aims to deliver. Since the majority of the optical biosensors are based on evanescent field optics [103], usually the presence of the analyte changes the optical properties of the surface, while the peculiar characteristic of our instrument is that the analyte modifies the optical properties for the entire volume. There are only few examples in literature, such as Heideman *et al.* [154] and Lenferink *et al.* [155], where they have determined the concentration of the analyte from a model which describes the complexity of the bulk refractive index difference (RID). This project wants also to emphasise the advantages of modifying locally and in the entire volume the refractive index, giving the sensor more versatility and potential to detect different analytes focused on different regions, since only two previous works, has reported a multitracking feature (Ymeti's and Aikio's groups) with an interferometric biosensor. The majority of the chips of the interferometers reported are a waveguide structure [156], which restricts the choices for the materials and the geometrical dimensions that can be adopted, and also required special equipment for coupling the light into the structure [24]. In the last few decades, instead to using a Si wafer, polymer-based chips have been developed in order to decrease the cost and improve the mass production, reducing their instability when in contact with protein and buffer solutions which can cause a perturbation in the measurement of the refractive index [19]. Unlike the other optical sensors, an interferometer by its nature has a reference signal, which is fundamental to reduce external noise, such as temperature drift [105].

In conclusion, despite all its potentialities, the employment of an interferometric transducer in biosensors applications is still rare and relegated to laboratory research [24]. It seems that the main disadvantage is to reduce the dimension of the instrument, which must be addressed in order to obtain a compact biosensor that can be utilised for

point-of-care applications [24]. Few interferometric sensors have been reported in **Table 2**.

2.1.4.1 Software

The final aspect that is relevant to be discussed is the delicate part that the software plays in the phase acquisition. As previously discussed, the high sensitivity to a small change in the refractive index and the phase ambiguity of the interference pattern can cause a misinterpretation of the final value. So a desirable software is one that is capable to nullify the phase ambiguity, discriminating two values which are differing for a multiple integer of 2π [157]. For example, it is only Heideman *et al.* who have achieved one of the highest sensitivities after they have started to apply an active phase modulation [130]. Even other groups have reported that after investing in upgrading the software, they have been observing an improvement of the RIU of the order of one or two order [158], such as Kammer *et al.* by applying a low pass filter [148] or compensated interferometric reader [159]. Analysing in depth the case of the Young interferogram, normally the phase difference is extrapolated by the software that regularly acquiring the position of the fringes in the interference pattern and applies the Fast Fourier Transform (FFT)[74], relative to the position [109]. A problem that can arise at this point is if the software is tracking the positions of all the fringes or tracking only the darkest/brightest fringe. The image processing results to be one of the key aspects in the acquisition, as it is the first step needed to translate an image to a signal or data. If it is the latter case, a possible disturbance is a variation intensity due to the interaction with the chip which can lead to a misinterpretation of the fringe shift [100]. In other words, the FFT can required a more sophisticate and fast microprocessor to be able to deliver the measurement in real-time [160]. For further reading, Dante S. *et al.* works are suggested [157, 161].

In conclusion, the phase ambiguity has been approached by other researchers by combining different methods, such as image processing, statistical approaches, local or global optimisations [162], as reflection of the diverse setting that have been created. Since the main target of the our project has been to demonstrate a proof of concept of the interferometric sensor by using an inhouse software, an improvement of the software and a greater deepening in the literature are suggested as next steps in the

developing. During all the PhD duration the software has never been modified or upgraded. A description of the software used in the project is reported in chapter 4 paragraph 4.2.4.

Chapter 3 Electrophoresis

3.1 Basic principles of electrophoresis

The movement of charged particles relative to a fluid under the influence of a spatially uniform electric field is called electrophoresis. The charged particles are subjected to a frictional force $\boldsymbol{F_f}$ due to the fluid and to an electrostatic Coulomb force $\boldsymbol{F_{el}}$ exerted by the electric field, both reported in the formulae **(3.1.1)** . For free solution the $\boldsymbol{F_f}$ follows the Stokes' law where η, r and $\boldsymbol{v}$ are respectively the viscosity of the fluid, the radius, and the velocity of the particle; while in the formula for the $\boldsymbol{F_{el}}$ the charge of the molecules is represented by q and E is the electric field applied.

$$\boldsymbol{F_f} = 6\pi\eta r\boldsymbol{v} \; ; \; \boldsymbol{F_{el}} = q\boldsymbol{E} \qquad \textbf{(3.1.1)}$$

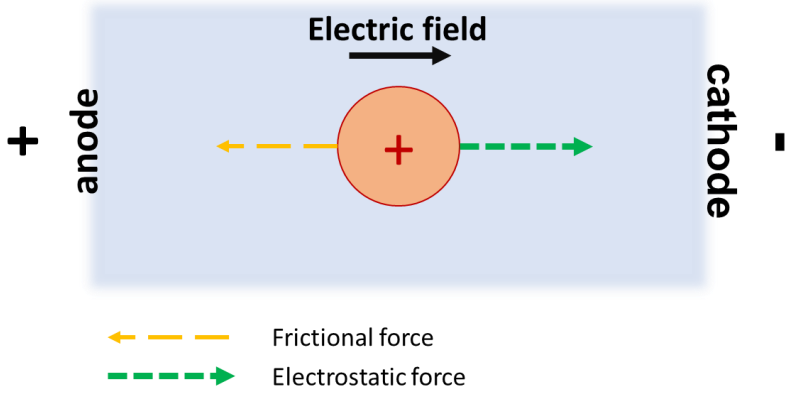

Figure 9 Forces diagram applied on a positively charged molecule.

At the steady-state the net force $\mathbf{F_{tot}} = \boldsymbol{F_f} + \boldsymbol{F_{el}}$ is zero, so the constant velocity of the charge will be given by the formula **(3.1.2)** , while the direction of the movement depends from the charge, if it is positive or negative, it will move to cathode or anode respectively, Figure 9.

$$v = \frac{qE}{6\pi\eta r} \qquad \textbf{(3.1.2)}$$

A property which represents how easily the molecules move in the presence of a uniform electric field is the electrophoretic mobility μ_E. Its value is defined as the velocity v, or also as the distance d travelled in time t, by the electric field applied E.

$$\mu_E = \frac{v}{E} = \frac{d}{t\,E} \qquad \textbf{(3.1.3)}$$

Since the spatial uniform electric field *E* is given by $E = -V/L$, where *V* is the voltage applied and *L* is the distance of the two electrodes, formally if the voltage applied is doubled, the velocity will in turn be doubled (directly proportional) so that the molecule will travel the same distance in half time. However, even with the same voltage applied, the velocity, for example, may be different, because other factors, such as Joule's effect (heat generated by the current) [163]. Even so, the formulae remain a good model to predict the molecules migration. If in the formula **(3.1.3)** we substitute the *v* from equation **(3.1.2)**, then it is evident that the electrophoretic mobility is influenced by the dimension, the charge and the shape of the molecule, such as the formula **3.1.4** suggests.

$$\mu_E = \frac{q}{6\pi\eta r} \qquad \textbf{(3.1.4)}$$

Consequently, electrophoresis can be used to separate the molecules in a solution according to their electrophoretic mobility. The type of molecules most used in electrophoresis have both anionic and cationic groups, such as proteins, and are called zwitterions, which have an equal number of positive and negative groups and are therefore overall neutral. For this group of molecules, the pH environment plays an important role in the electrophoresis because it influences the net charge of such molecules and accordingly their electrophoretic mobility [163]. Furthermore, the pH environment can neutralise the molecules net charge at a specific value called *isoelectric point pI*, which is specific for each molecule. This is possible because, at that specific pH, the positive and negative charges of the protein are titrated by the acids and bases present in the surroundings [164]. For instance, if the solution has a pH below the isoelectric point, a protein will move toward the cathode, the negative electrode, because it will be positively charged. On the contrary, if the pH of the solution is above the *pI*, the protein will be negatively charged and will move toward the anode, the positive electrode [164]. Due to the impact that this has on the protein mobility during

electrophoresis experiment, the pH environment has to be preserved; this is the main challenge as the water is the main, if not the only, solvent used in biology and a deeper insight will be explored further in this chapter. Therefore if protein are being studied, a buffered solution is more desirable, in order to contrast the formation of the ions H^+ at the anode and OH^- at the cathode, formed during the electrolysis of water [164] [165]. In particular this is important if a hydrogel has been adopted as a separation medium [166]. In the latter case, further factors have to be evaluated, such as the porosity of the hydrogel, to better define and achieve an accurate and defined separation of the proteins from the other components in the solution [163]. For example, for the proteins their migration velocity is proportional to the ratio between their mass and their charges and their structure is not as predictable, unlike in the case of nucleic acids [167]. There are other examples where the water in not the principal solvent such the Duarte`s review presents [168] , but herein they will not be discussed.

Below the most used focusing techniques are described, with an in-depth view on the small capillary methods, since they describe the physical processes used in herein project.

3.2 Capillary electrophoresis and concentration techniques

Capillary electrophoresis (CE) is an electro-kinetic method which performs the separation in micro/nano-channel, where the sample constituents are separated based on their different electrophoretic mobility when an electric field is applied. The main advantages of the CE are fast measurements, small sample volume required and the selectivity can be obtained by modifying the buffer and its components [169]. Inside a narrow capillary, the electroosmotic flow (EOF) influences the sample mobility to a greater extent than in other set-ups. The EOF is, indeed, the liquid motion induced by the charged particles on the surface of the capillary tube; to neutralise the EOF, a charged double layer on the surfaces of the tube is made, where the electric potential decreases as the distance between the liquid and the surface increase and consequently its influences on the general motion. The electric potential on the tube surface is called zeta potential (ζ) and causes a smooth velocity distribution across the tube diameter. The typical CE profile is the flat one in Figure 10, while the parabolic profile is common in other separation techniques [169]. Furthermore, if the zeta potential is due to a

positive charges, cations will be moved by the EOF and form sharp peaks, while the anions will be driven against the main flux, having a longer migration times [170]. In order to reduce the EOF, which may decrease the quality of separation, in most cases the capillary surface is treated so the zeta potential is neutralised, or buffer components are modified, such as changing the pH and also the background electrolyte (BGE) composition [171]. The CE, at beginning of 1990's [172], was the first electrophoresis technique to be miniaturised, reducing the time analysis and sample volume [173].

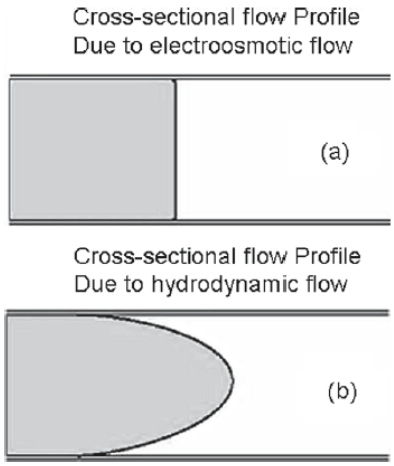

Figure 10 Flow profile in electrophoretic (a) and pressure driven (b) separation columns [170].

The sensitivity of the CE techniques can be improved by applying further electrophoretic pre-concentration methods, such as in-situ procedures which are considered the most favourable ways, since they require only small changes and a small amount of time [174]. Below, the most used pre-concentration in-situ techniques are reported, highlighting the aspects most related to this project, such as the miniaturisation. As it will be clear, the specific properties of the chosen analytes tailor the applications and conditions of the pre-concentration technique [175], so it is always challenging finding the perfect balance between all these elements.

3.2.1 Isoelectric focusing

The first concentration method here presented is the isoelectric focusing (IEF), used in particularly for proteins detection; the pH-dependent mobility of proteins is the key property used in this separation technique, where the protein are separated by their isoelectric points [164]. In this application, the electric field is applied parallel to the pH gradient and as the protein are electrophoresed into a pH gradient, they are focused at

different positions, corresponding to their **pI** [164, 176]. Kolin A. was the first researcher [177] who in 1954 documented the haemoglobin separation from cytochrome in a glycerol solution by adopting a pH gradient [178], and from that time a huge amount of attention has been focused on this method so that IEF is now one of the main tools used in the study of proteins [176]. The reason of this interest relies on the peculiarity of **pIs** for ampholytes: as the **pIs** identify the molecules and so their position in the pH gradient. The main challenge for this technique is to design a pH gradient that is stable during the measurement and can separate molecules with similar **pI** values. Along the years, starting from the 1950's, in the literature it is clear how this procedure has evolved; from adopting a mixing zone between two or more different buffers, called artificial pH gradient (APG) [179] [180], to a more recent development using ampholyte solutions (compounds that can act either as acid or as a base, like the amino acids) to create an immobilised pH gradient gel (IPG) [181] [182]. In APG the sample is injected directly into the zone where buffers with different pH values are mixed. Therefore, such approach needs a considerable effort in the selection of the buffers in order to acquire sufficient stability of the pH gradient [183]. The electric field applied causes an electric migration of the ions present in the buffers, and in turn the pH gradient can change and the focusing can be ruined.

Consequently, the key point is to control the ions migration so that the components to be separated are faster than the pH gradient. Buffers containing the same ionic species are preferable and a system of pairs one which include the pI of the sample is more indicated [183]. On the other hand, the use of ampholytes has predominated giving the possibility to create a custom and more stable pH-gradient range [184]. The introduction of the Immobiline (compounds with functionalised groups that act similarly as the ampholytes) in the 1988 [185] has increased the stability of the pH gradient (IPG) [186] [187, 188]. While IEF is an efficient and successful method in many approaches, it has some limitations in micro-systems [189] and multichannel platforms [190], such as casting the gel with a pH gradient can be a quite problematic task [191] due chemical preparation required the rigid electric condition to satisfy, and finally, the use of isoelectric point markers (usually fluorescent labelled) [192], which required a laborious labelling process. A general drawback of this method is its small capacity to keep focused

the proteins, because at their pI they have the lowest solubility [193], but on the other hand this method permits multi analyte detection.

3.2.2 Isotachophoresis

The second preconcentration method in electrophoresis is the isotachophoresis (ITP) and it is typically executed in free solution in small diameter tubes [194]. The technique has also been improved with the time and was known by multiple names and was only in 1970's, with Haglund's work [195], that it started to be defined as Isotachophoresis, name of Greek origins that underling the aspect that at equilibrium the ions zones migrate at the same velocity. In ITP, due to different ionic mobilities, the sample is concentrated between two electrolytes: the leading electrolyte (LE) and the terminating electrolyte (TE) [196]. When a voltage is applied, the difference in mobility between the LE and TE creates a non-uniform electric field, which in turn entraps ions with a mobility between leading and terminating electrolytes [197, 198], resulting in a focusing effect of the sample, if it is present with enough amounts. At the steady state, all the ionic components will move separately as a well-defined band [194]. The conditions for this method are shown in Figure 11.

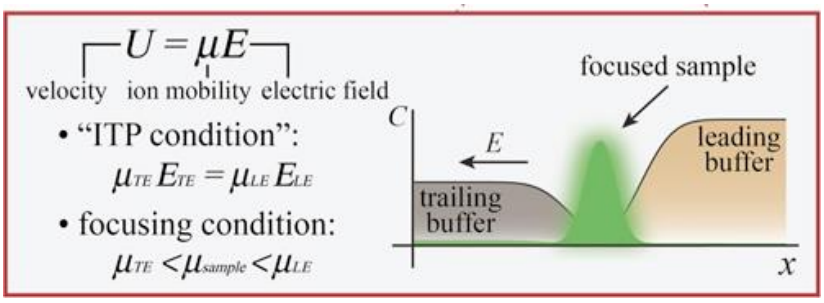

Figure 11 Schematic representation of Isotachophoresis technique by *Garcia-Shawa et al.[199]*.

In biological sample a fold concentration between 1000 to 15000 fold can be achieved ITP [200]. ITP is a technique which is adaptable with different microfluidic platforms [201].

3.2.3 pH junction

The last in-situ concentration technique presented is the pH junction, also called pH-mediated stacking by its pioneers Aebersold and Morrison [202] and also called by other names [197], but here will be always defined as "pH junction", as defined by Britz-McKibbin [203]. Two main principles have been suggested in order to describe the

mechanism of this method [204] [205]. The first one is that the neutralization of H^+ and OH^- ions, which migrate in opposite direction, create a stacking region of low-conductivity. The second mechanism is the velocity reduction of the analyte across the pH junction which allows the concentration of a sample in a small zone. In both cases, the required key is determining some electrophoretic parameters, which cause concentration of the analyte in the border between the two regions, where it drastically changes velocity [198]. Further research is required to fully understand and found the right conditions [203]. As a consequence of the mechanisms previously described, the pH junction is not suitable for neutral and strong acidic analytes, because their mobility is independent from pH environment [175]. The presence of high salt concentration does not seem to interfere with the pH junction procedure, unless that no influence the pHs values [206] [207]; furthermore a wide pH discontinuity, such as a step-gradient, seems to be responsible for an increase in focusing [208]. This method can achieve a 10-to a 2000-fold sample concentration detection limit [209], where last limit was obtained by Nesbitt *et al.* [210] [211]. The majority of the works uses a pH junction applied to a capillary, which requires specific surface treatments [212], that can be time-consuming [213] [214].

The present PhD project has adopted the pH junction to increase the limit of detection of the biosensor by focusing the target analyte. Furthermore, to the author's knowledge, there are only few papers which report this technique at microscale, one example is reported by the Sonker *et al.* [215] in 2017, but never together with hydrogels, nor using an optical detection instrument, such as the interferometry, instead of fluorescence microscopy or electropherogram.

3.3 Buffers

In all the previous electrophoresis techniques the buffers play a crucial role in the results of the analyte detection. A buffer consists of an acid and its conjugated base, and the relationship between its components is express by the Henderson-Hasselbalch equation.

Given the reaction: $$AH + H_2O \rightleftharpoons A^- + H_3O^+ \quad (3.1.20)$$

$$pH = pK_a + \log_{10}\frac{[A^-]}{[HA]} \quad (3.1.21)$$

Where $[A^-]$ and [HA] are the concentrations of the acid in the dissociated and no-dissociated forms respectively; whereas the pH =-log$[H^+]$ is the negative logarithm of the proton concentration and, finally, pK_a=-log(K_a), the negative logarithm of K_a, is the dissociation constant of the buffer components [216]. The pK_a indicates the value at which the buffer has the highest buffer capacity; beside at this value the buffer components are just half dissociated. It is generally accepted that a buffer with a pH value above or below the pK_a by one unit will start to lose its buffer capacity. Furthermore, when an electrophoresis technique is used, the water will be electrolysed, so the buffers must have a buffer capacity that can contrast the water ions to keep a stable buffer system. The more the buffers are concentrated, higher the buffer capacity will be [217]. Consequently, a high buffer capacity will generate high current which, in turn, will cause heating effects to the system and compromises the electrophoresis results. Moreover, in order to keep the protein structure stable, a buffer with moderate capacity, such as 0.05 to 0.2 M, is preferred [216].

In this project, two types of buffers have been used in the electrophoresis experiments. Below are reported their general descriptions.

3.3.1 Tris buffer

Tris(hydroxymethyl)aminomethane, or Tris, is an organic compound with the formula $(HOCH_2)3CNH_2$. It is used in biochemistry and molecular biology as main component of buffer solutions [218]. It has a primary amine which can react with other molecules, such aldehydes, and is known to chelate with metal ions, so this buffer is not suitable for enzyme experiments [216] [219]. Tris has a pK_a of 8.07 at room temperature (25 °C).

3.3.2 Phosphate buffer

Phosphate-buffered solution (PBS) is a buffer commonly used in biological research. It contains monosodium phosphate and its conjugate bases. PBS is non-toxic to most cells, although is highly conductive so it should be used at low concentrations [208]. The PB has three pKa values of 2.16, 7.21, and 12.32 [220], which offer more versatility on the application and analytes [208].

3.4 Supporting media: hydrogels

One of the benefits of adopting a gel as the supporting media in electrophoresis is to be able to cut-off molecules according to their size, just by tailoring the porosity of the gel accordingly. As the applied voltage forces the molecules through the gel, only the ones smaller than the gel network will move almost like in a free solution, while on the other hand the larger molecules will be stalled [164]. In the electrophoresis separation, the gel can also act as a thermal convector by reducing the heating due the electric current [221]. Furthermore the gel is preferred to be chemically inert [166], because the presence of fixed charges will also cause the electroendosmosis (flow of water toward one electrode) which damages the quality of separation [164]. Nevertheless, having fixed charged groups in the gel can allow for selectivity of the analyte, in a way that charged groups such as a Schiff base can functionalise the gel and actively react with a specific analyte. Gel electrophoresis (GE) is therefore a more appropriate approach when the sample is made by molecules with different sizes and charges, like proteins and nucleic acid [222].

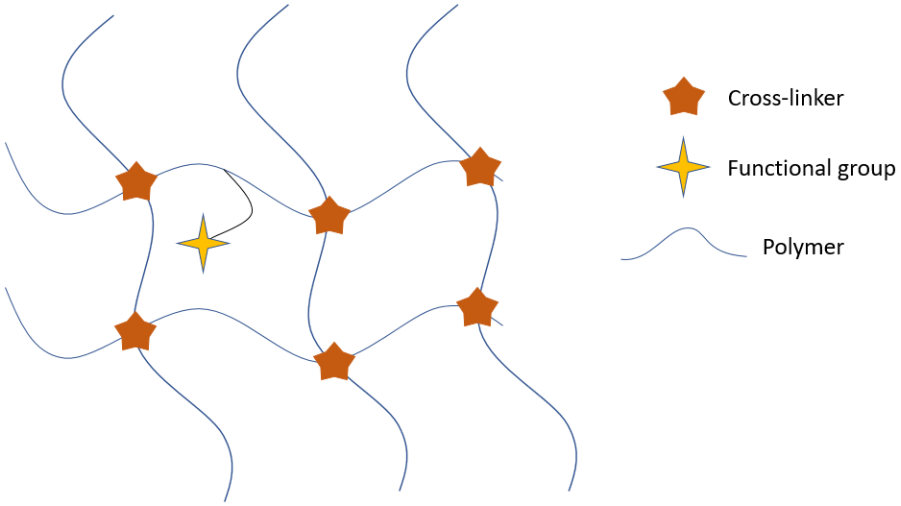

Figure 12 Hydrogel network schematic representation.

Hydrogels are polymeric sponge-like networks, which resemble natural living structures due to their high water content, porosity and soft consistency, more than any other biocompatible materials [223]. Furthermore, hydrogels are nontoxic and water-soluble polymers so they are the most recommended for various pharmaceutical and biomedical applications, such as contact lenses [224] [223] and wound dressing [225] [226]. As responsive "smart materials," hydrogels with functional groups usually reveal

changes in swelling or optical properties by a wide range of external factors, such as pH environment and temperature alteration, electric field [223] [227] and light [228]. Therefore due to their versatility, hydrogel-based sensors have attracted the attention of researchers and industry for the design of novel detection system for different diagnostic applications [229]. In particular, the hydrogel has the function to filter the molecules based on their dimension and to actively attach a specific analyte present in low concentration, since the three-dimensional nature of the gel network consents a considerable amounts of bio-recognition elements [230]. More specifically, in electrophoresis, the hydrogels most widely used are the agarose and the polyacrylamide gels (PAAM), because they embody all the requisites, such as being electrochemically neutral and having an easily controllable porosity due to their cross-linked nature.

3.4.1 Polyacrylamide

Polyacrylamide (PAAM) is a polymer (-$CH_2CHCONH_2$-) formed from acrylamide monomers. It can be synthesised as a simple linear-chain structure or cross-linked, typically using N,N'-methylenebisacrylamide (Bis), usually via free-radical polymerisation [231], which makes the gelation more complicated than in the agarose [164]. The acrylamide concentration determines the average polymer chain length while the Bis concentration determines the segment of cross-link formation. The ratio between those two concentrations determines the PAAM gel properties such as density, elasticity and porosity [163]. The choice of crosslinker and copolymer allows more functionality to the gel [232], such as acrylic acid give thermo-[233] and metal responsive [234] gels, while an -allylamine copolymer can give a pH sensitive gel [235]. A study about of the effect the pore structure and pH-sensitivity was made by Zhao et al. [236]. The multifunctional PAAM gels offer a wide range of benefits for the microfluidic platform, such as removal of unwanted hydrodynamic flow [237]. PAAM is the gel most widely used in biology and particular in electrophoresis, but, as monomer is toxic and carcinogenic while the polymerisation results in a non-toxic gel, wearing gloves and washing of the gel to remove any unreacted monomer is always advisable. The PAAM gel has been tested in the herein biosensor and its result can be found in the chapter 5.

3.4.2 Agarose

Nowadays agarose is the polysaccharide gel matrix most popular in electrophoresis. Agarose derives from agar and it is a polymer which consists of a repeating agarobiose unit having a galactose and 3,6-anhydrogalactose [166]. Agarose is soluble only in boiling water and, as the solution starts cooling down, at 37 °C the gelation process will be initiated [238]. This polymer is neutral and non-toxic, and it is used in biotechnological applications [238], such as separation of DNA molecules [166] [239]. Commonly, agarose gels are melted with the desired buffer (Tris, phosphate buffers), which establishes the pH and provides ions to support conductivity, and finally the gel solution is cast in the selected box [166]. The pore size and mechanical properties of the gel are determined by the concentration of the agarose in the solution: the higher the concentration, the smaller the pore size and firmer the gel will be. Generally the concentration used in the literature is in a ranges from 0.4% to 4% [164]. Agarose gels also exhibit high gel strength at low concentrations [217], meanings that a strong force is needed to be applied to break it, although this aspect will degraded with time as the spontaneous hydrolysis of the agarose chain will start [217]. Agarose can be a good alternative to the polyacrylamide, because it is not toxic or carcinogenic and is compatible with many activation strategies [239], such as tissue engineering [240]. Furthermore, agarose gel electrophoresis is a technique that allow the separation of large molecules (over 1 million Da), that cannot be achieved with acrylamide, because it cannot polymerise at the conditions required for the appropriate porosity [241].

3.4.2.1 Agarose functionalisation

Treated polysaccharides, like agarose are often preferred as support media for enzyme immobilisation due to their large availability of active groups [242]. In order to maximise the degree of interaction between the protein and the support, it is advisable to manage the immobilisation conditions [243]. In the agarose case, each agarobiose unit has four hydroxyl groups (-OH), three of which are secondary, and the fourth group is primary [239]. The primary group is the only one that is capable to react, which consequently will be the only site for the functionalisation, and an excessive degree of reaction could deeply modify the favourable properties of agarose gels [239]. In order to activate the primary group, sodium periodate can be used to oxidise it [244] [245], obtaining in turn

an aldehyde group (-C(H)=O), which at a pH environment of 5 to 7 can react with a hydrazide reagent to form a hydrazone bond, Figure 14.

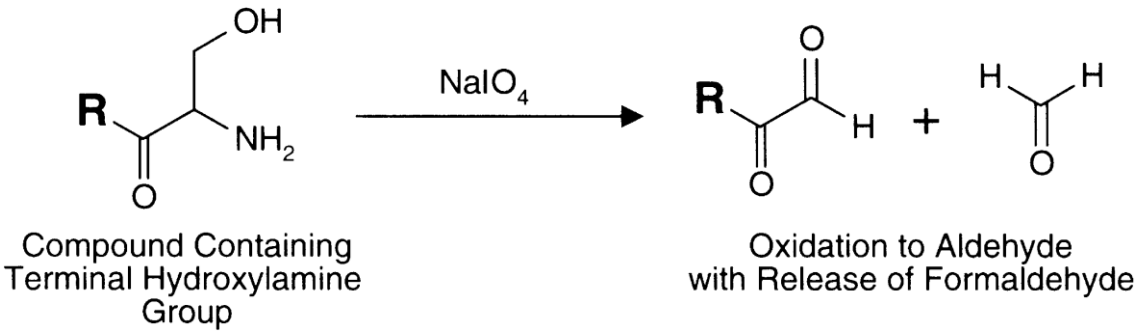

Figure 13 Agarose oxidation reaction ([246])

This bond is sufficiently stable for most applications, but it can be reduced to a more stable secondary amine using for example sodium cyanoborohydride, or the use of a stronger reducing agent can be employed to also reduce all remaining aldehydes to hydroxyl groups on the agarose gel support [246].

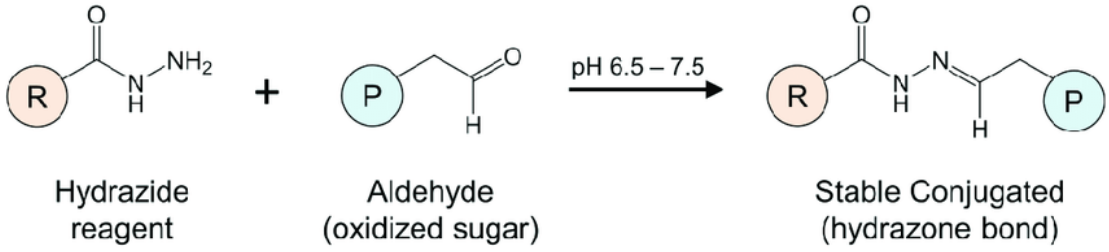

Figure 14 Hydrazide reaction chemistry [247].

The support obtained is a peculiar one and to maintain it stable for long time, the environment conditions are preferably being controlled, such as the pH. For example, some kind of buffers are better to be exclude, like the Tris or the borate buffers, because they can actively interact with this support [243].

3.5 Microfluidic electrophoresis

The last two decades have seen a burst of microfluidic electrophoresis devices (MED), emerging as an excellent platform for rapid biological molecules studies, including high separation efficiency and analysis of proteins and DNA [190] [248]. These systems provide a miniaturisation of the CE and the other electrophoresis techniques described before. They have small dimensions and use small sample volumes allowing for a significant reduction of time [237] and sample quantity, all of which are essential

properties in the point-of-care (PoC) applications [249] which also leads to lower analysis costs [250]. Often the low concentration of analyte in the biological sample can result in a loss of detection, so preconcentration methods have been developed to resolve this problem [251] [252], such as changing the chip layout, allowing for convenient sample introduction in the channel [249]. MED have the huge advantages to provide a whole channel detection and to be easily combined with other analytical steps by improving the channel functionalisation [253], as called by the other name of "Lab-on-chip" (LoC) systems [254]. A wide range of materials, such as silicon, glass [255] [256] [257], polydimethylsiloxane (PDMS) [258] , poly(methyl methacrylate) (PMMA) [259], and cyclic-olefin copolymer resins [260] have been used to fabricate MED [258]. All of them have drawbacks, such as the higher cost for silicon and glass compare to the polymer/plastic-based chip [261], or PDMS that adsorbs proteins in its hydrophobic natural state, interfering with the electrophoretic separation [262]. Furthermore, all the interactions between the surface and the analyte led to a low reproducibility and a loss of signal. Consequently, in most of the cases, the surface has been pre-treated [263] in order to neutralise, for example, electrostatic interactions [264].

Hydrogels are also being utilised as a membrane or plug [265] [186] , functional matrix [199] [266], pH gradient [267] [268] [269], on the basis of their broad chemical and physical properties which can improve the MED [198] performances.

To obtain a real-time monitoring of the analyte, optical methods and electrochemical methods have been integrated. Using optical detection methods provide versatility and a wide range of applications, and benefits due to the vast range of optical techniques available which detect intensity variations, such as fluorescence [270] and absorbance methods, or light properties variation, such as evanescent waves, optical waveguide and interferometry [261]. The first group represents the labelled methods and can be considered as the traditional methods that have been used in the past, while the second one, in most of the cases, are label-free techniques and represents the future of the PoC devices, as highlighted in the previous chapter. For example, the Laser-Induced Fluorescence (LID) is a distinguished optical labelled method for biochemical detection in MES, but it requires fluorescence tags which involve a long synthesis procedure and not all the molecules can be efficiently labelled [222]. Furthermore, the tag presence

can produce artefacts which compromise the separation efficiency [271]. A final reminder is that the estimation of a pure protein concentration is always challenging, as it can depend on the experimental conditions, because the proteins' structure is not so predictable and can interact with the environment. For this reason a calibration is always required and the more pure the protein is, the more repeatable the measurement will be [221].

In conclusion Table 3 shows the resolution or concentration factors obtained by some microfluidic sensors, by connected that to the detection method, the focusing techniques, the materials used for the chip and finally the analyte used. The table can give the idea of the vastity of the growth of this field, and how difficult results to be a comparison among them.

TABLE 3 LIST OF MICROFLUIDIC SENSORS

Chip material/substrate	Focusing technique	Detector	Analyte	Resolution/ concentration Factor	Paper
PMMA	ITP	fluorescent	DNA–aptamer and its thrombin	1100	[272]
poly(ethylenetere-phthalate) (PET)	exclusion-enrichment effect' (EEE)	Fluorescent microscope	Dog serum albumin	10^3–10^5 fold	[273]
glass	CE	LIF (Laser induced fluorescence)	FITC-labeled proteins	Separation	[255]

Five different polymers (PU PET EP PEG PPG)	CIEF	Mass spectrometry	Bovine Serum Albumin	0.9 nmol/ ml,	[274]
PMMA	CGE (acrylamide)	LIF	8-aminopyrene-1,3,6-trisulfonate derivatives, and fluorescein isothiocyanate (FITC)-labeled glycopeptides and glycoproteins.	10^5	[259]
3D printing	CGE	Fluorescent detection	DNA separation	50÷800bp	[275]
Glass (fused silica)	microscale isoelectric fractionation (µIF), IEF	Fluorescent detection	fluorescently labeled proteins	5-25	[186]
Glass/PDMS hybrid	Dielectrophoresis	/	platelets		[276]
Glass	µIF	Fluorescent detection	Mix proteins	50	[267]
Glass	pH junction	Refractive index	proteins	3	[277]
silica	pH gradient electro-focusing	Fluorescent microscopy	RPhycoerythrin Dylight labeled streptavidin	385 and 107	[180]

silica	CGF (concentration gradient focusing)	Fluorescent	RPhycoerythrin	/	[196]
glass	Microfluidic Free-Flow Isoelectric Focusing (µFFIEF).	Fluorescent microscopy	proteins	0.4–2.4 µm spatial separation	[189]
PMMA	Gel electrophoresis	Fluorescent microscopy and Mass spectroscopy	peptides	/	[253]
Glass and photomask (hybrid)	electrophoresis-based immunoassay	Fluorescence microscopy	FITC-insulin	3 nM	[278]
Nafion	cIEF	Mass spectrometry	Plasma (Alzheimer's disease)	/	[279]
PDMS and silica	CE	Fluorescence microscopy	Bovine serum albumin labelled, lysozyme and cytochrome c	/	[262]
Polycarbonate	CGE	Fluorescence camera	DNA immobilization	100 folds	[280]
PDMS/Glass (3 different channel configurations)	ITP (functionalised hydrogel on the surface)	Fluorescence microscopy	DNA sequences	8.2-fold, 100 fM	[281]

/	ITP (functionalised hydrogel on the surface)	Fluorescence microscopy	Nucleic acid	4-fold, 1 pM	[199]
glass	pH junction	Fluorescence microscopy	vancomycin	217-fold, 1.2 μg/mL	[282]
Nanogold peg	electrophoresis	LSPR	thrombin	10 pM	[283]

Chapter 4 Interferometric sensor

4.1 Introduction

The optical sensing has a very long tradition; the first discovery of the properties of the light were illustrated in the XIX century. As the instrumentations have been improving, diverse metrologies have been adopted, such as phase difference detection. In this project we have adopted one of the "oldest" set-ups, the Young interferometer (YI), but we are given to it a fresh and more modern features, which made it capable to spatially detect the analyte with a good sensitivity compared with other instrument in literature (table 2).

4.2 Instrument description

The optical sensor selected for the project is a Young interferometer (YI), Figure 15. As with other interferometer set-ups, the interference is due to the overlap of two beams, being coherent in space and time, being originated from the same light source, a laser.

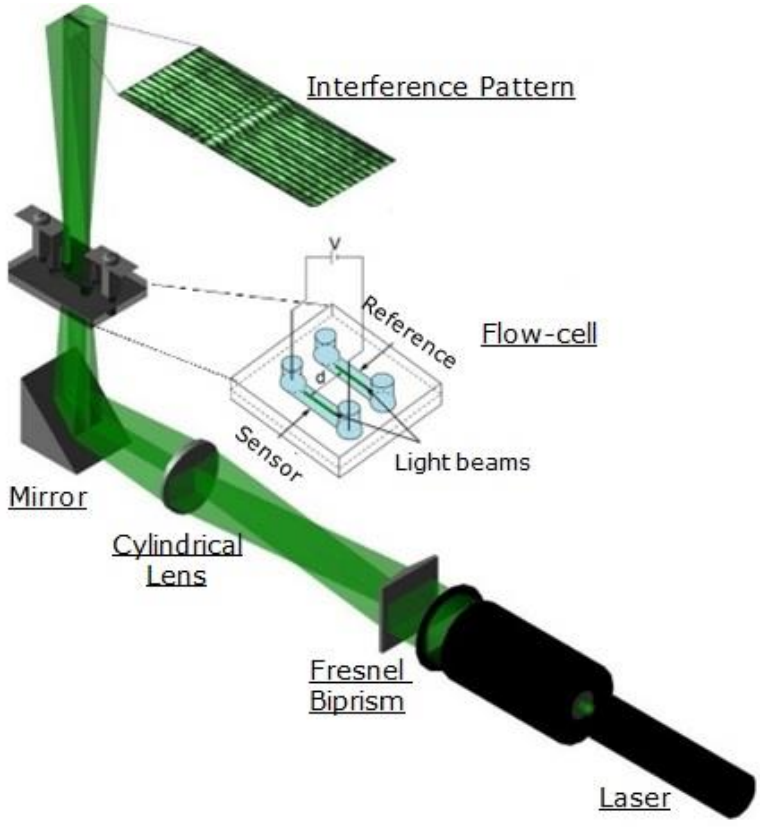

Figure 15 Schematic configuration of the interferometer of this project [284].

The main aspect that characterises the YI is that the two beams are recombined before the detection. The interference pattern is a sequence of white and black fringes, which represent the constructive and deconstructive interference of the two beams, respectively. Here, a detailed description of the interferometer will follow, which is in our paper *"An optofluidic Young interferometer sensor for real-time imaging of refractive index in μTAS applications"* [284]. The laser adopted has a wavelength of λ = 532 nm (LD 532-1-3, Roithner Lasertechnik, Vienna, Austria), and therefore it has a green colour. The beam has a circular aspect, and it is expanded 5 times, from 5 mm to 25 mm diameter by using a beam expander (Comar Optics, Cambridge, UK), that is at 1 cm distance from a Fresnel biprism (**FB**). The latter optical element is used to halve the beam and to obtain the two virtual sources. Historically in the Young interferometer the two distinctive rays were made by creating two small slits in a screen, as in Young's experiments [285], but after that Fresnel (1788–1827) [286] and Billet (1808–1882) [287] proposed two other ways of creating two virtual sources. The Fresnel method has been chosen for this project, since it requires a singular optical element the FB (for a Billet method two lenses are positioned in the two slits [92]). It is showed in Figure 16, where a point source *S* illuminates the FB, which produces two identical virtual sources (S'_1, S'_2) aligned with the real source; on the screen positioned on the x axis it is possible to observe an interferogram.

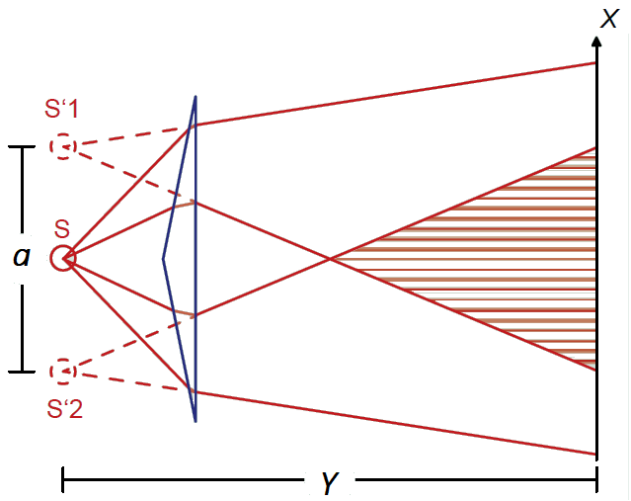

Figure 16 Rays diagram for a Fresnel biprism [288].

A FB has been used in other works to obtain two coherent light sources [289, 290], and further theoretical explanation has been discussed recently by A. Sabatyan and S. A.

Hoseini [291]. In figure 16, it is possible to observe that the FB is composed by two prisms with a common base. The apex angle, α, of the FB used in the project is 179° (3B Scientific, Somerset, UK). As the light passes through the FB, the beam has been split, but after few centimetres a superposition region is visible. So, to obtain two distinguishable wedge-shaped light sources a cylindrical lens with a focal length (f_c) of 120 mm is positioned at 320 mm from the FB. The cylindrical lens redistributes the light rays in a way that at its focal length the two light sources are extrapolated. For this reason, the microfluidic device, held in place using an 3D printed holder, is positioned at 120 mm from the cylindrical lens. At that distance the two beams are two perfectly parallel lines, where each of them passes through one channel in the device. The interferogram is visible again after 120 mm from the microfluidic device, so a 6.6 Mpixel CMOS camera (PL-B781, Pixelink, Ottawa, Canada) is positioned at 680 mm away from the microfluidic chip. The camera area is 10.5 mm by 7.7 mm, and the pixel size is 3.5 µm by 3.5 µm. The long axis of the camera has been aligned to the length of the channel in the chip. A diagram of the light path is schematized in Figure 17. Two mirrors (PFSQ10-03-F01, Thorlabs, Ely, UK) have been used to bend the light path through the desirable directions. They are not reported in Figure 17, since they only "bend" the rays as desired.

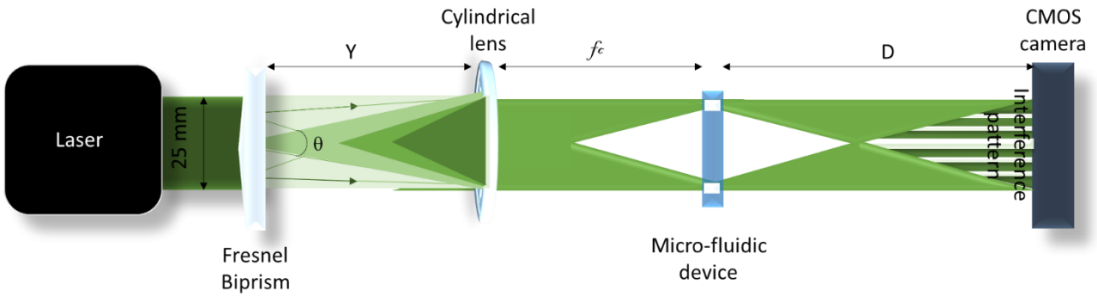

Figure 17 Rays diagram for the interferometer (side view, distances not to scale).

One of the conditions to observe the interference pattern is the reciprocal positions of the FB with the cylindrical lens. In fact, if the distance between FB and the cylindrical lens corresponds to $L_{FB-CL} < 2f_c$ (two time the focal length of the cylindrical lens fc) the beams diverge after the lens, so no interference pattern is visible. On the other hand, if $L_{FB-CL} \geq 2f_c$ the condition is respected and the distance *d* between the two light sources after the cylindrical lens is given by the formula **4.2.1.**

$$d = 2f_c \tan\frac{\theta}{2} = 2.17 \text{ mm} \qquad \textbf{(4.2.1)}$$

So, the distance of the two beams is regulated by the focal length of the cylindrical lens and the geometry of the FB, where θ is expressed by the formula

$$\theta = \alpha - 2\cos^{-1}\left(n\cos\left(\frac{\alpha}{2}\right)\right) = 0.52° \qquad \textbf{(4.2.2)}$$

Where *n* in the refractive index of the FB that is made of glass, so n=1,517. Finally, by having all those conditions and relations, it is possible to calculate the width of the fringes (Λ), of the given instrument, where D is ~ 680 mm.

$$\Lambda = \frac{\lambda D}{\pi d} = 53{,}17\ \mu m \qquad \textbf{(4.2.3)}$$

Further conditions that can be extrapolated from the previous formulae (**4.2.1**; **4.2.2**; **4.2.3**) are linked to the distance between the microfluidic device, where also the two beams are focused, and the camera.

Table 4 Conditions on the distance D (microfluidic device-camera).

$D \leq f_c$	No interference
$f_c < D \leq 2f_c$	Numbers of the fringes are proportional to D
$D \geq 2f_c$	Λ is largely independent from D

In Table 4 are summarised the three conditions of the distance D. If the camera is positioned too close to the microfluidic device ($D \leq f_c$), the two beams are not yet overlapped, so the interference pattern is not observable. Whereas, if the camera is positioned between the f_c and $2f_c$, the number of the fringes will increase with the distance ($f_c < D \leq 2f_c$), Figure 18.

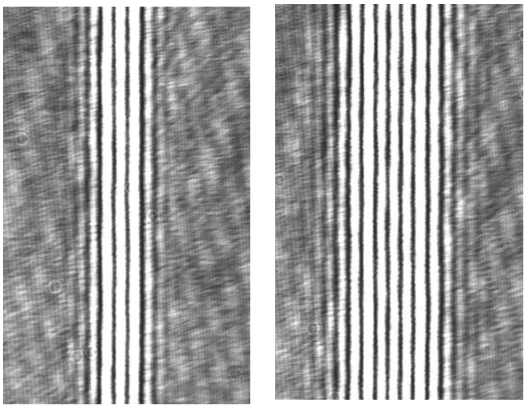

Figure 18 Interference patterns for two D values. As the distance increase, also the number of the fringes increases.

At $D = 2f_c$ the interference pattern has the maximum number of fringes, it follows that, for distance longer than that ($D \geq 2f_c$) the interference pattern will have the same aspect, and so the Λ, spatial fringes space, is constant. In conclusion, the camera in herein project has been set at ~ 680 mm from the microfluidic device, to obtain a steady interference pattern.

4.2.1 Flow-cell chip

To have a better outlook of all the main elements in the sensing instrument, a short excursus of the flow-cell chip will follow. The chip is composed of three part and assembled as a sandwich. It is possible to recognise the substrate, the spacer, and the cover pieces. All of them have the dimension 38.1x25.4 mm and along each shorter side they have a circular hole of 2 mm diameter; through this hole the chip is held to the mount by screws. The material used is thick clear poly (methyl methacrylate) (PMMA) sheets, purchased from RS Components (Corby, UK). The thickness of the substrate and the cover are 3 mm respectively, while three thicknesses have been used for the spacer piece: 250 μm, 750 μm and 3 mm. The spacer thickness also defines the height of the channels (the interaction length). Both surfaces of the spacer are bi-sided adhesive films (3 M 7961 M P) bought from Cadillac Plastics (Swindon, UK). In the spacer representation in Figure 19, the dimensions of the channels are reported. These are 10 mm long with a width of 1 mm; the distance between the two channels is 1 mm.

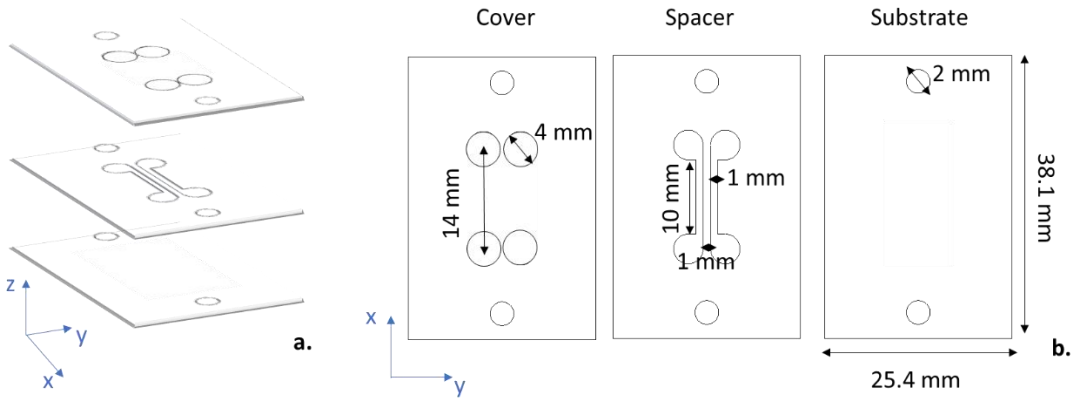

Figure 19 Schematic representation of the tree elements of the chip. 3D view of the assembling (a); dimension of three elements (b).

The three elements are being assembled by manually aligning them and pressing them in a way to remove any air bubbles in the adhesive surface. Through all the PhD project the channels design has been modified for different purposes as will be explained through the thesis. Even the material for the cover, and the substrate has been changed in some experiments with glass; so, chip made all of glass or hybrid (cover in PMMA and substrate in glass) has been also used. Some further design adopted are reported in Figure 20. The channels have different lengths, widths, and distances, but still, they possess three inlets per channel, since that characteristic allows the injection of diverse range of materials (solution, gels) within channels (paragraph 5.2.2.1).

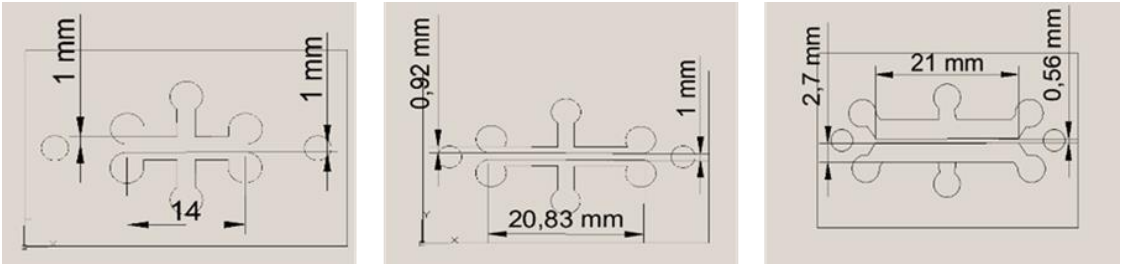

Figure 20 Three different designs of the channels for the spacer.

The channel design used mainly in this project is the one in Figure 19, if the experiment has been performed with diverse design, it will be signalled in the text. Finally, each channel is identified with a name for a specific use; one is the reference channel, the other one is the sensing channel, where the sample will be driven in by means of a peristaltic pump or a power supply in the next chapters.

4.2.2 Laser

The aspect that more identifies the YI of this project is the ability to detect the spatial variation of the refractive index along the channel (10 mm).

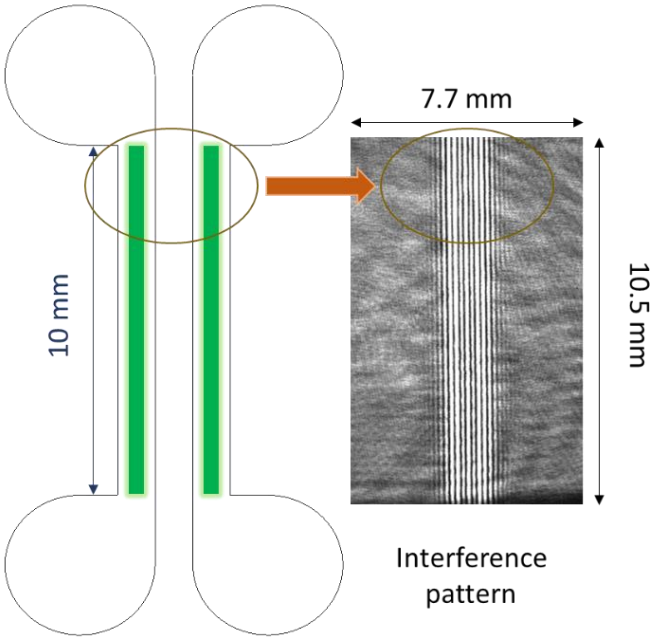

Figure 21 Matching between beams area with interference pattern area.

To obtain an interference pattern, where its dimensions are proportional to the channels length, the light source adopted must be coherent in time and space [292]. This is possible when the light source has a high degree of coherence space and time, consequently the only possible light source with these properties is a laser [293]. Thanks to this unique characteristic of the sensing instrument, it is possible to directly link a localised region in the interference pattern with a specific part of the light source, and in turn, with the channels [293]. The matching is illustrated in Figure 21. A theoretical explanation of the interferometry and the description of the light source have been illustrated in more depth in chapter 2.

4.2.3 Comments on the YI sensor

The advantages of our Young Interferometer configuration are the key aspects of a potential novel biosensor. The YI does not need a sophisticated object to perfectly align the beams though the channel, as in waveguide configuration or surface plasmonic sensors. Another aspect is that the beams illuminate the sensing surface (in both channels) perpendicularly, so that the light dispersion is only due to the transparency of

the materials that have been used. The detection in our configuration is reliant on the transmitted beam, instead along the reflection beam. This facilitates the alignment of the light through all the elements, from the FB to the camera. Furthermore, since the two light sources are not a point source, but they are two extended sources capable to illuminate throughout all the channels length (≅10 mm), the interference pattern obtained has information connected with the variation of the refractive index in the volume of the channels. This is of vital importance for the selectivity and the ability to locate the analyte through the channels, as it will be better shown in the next chapters. A further advantage of an interferometer over other optical sensors is that due its nature the interferogram is a product of the difference in composition between the reference and the sensing channels. This means that noises due to, for example, temperature fluctuations are reduced, since any external noise will affect the sensing channel, as well the reference channel. Consequently, the interferometer does not need other instrumentation to control and stabilise other variables, and it makes the interferometer the most appropriate sensor configuration for a biosensor. The instrument does not present any controller that would have made it more complicated and too bulky for handling. On the other hand, the high sensitivity of the instrument could cause some backlash, since every small difference, such as air bubble in one channel, could then be interpreted as a difference in analyte concentration, rather than noise. For this reason, the software that analyses the image of the camera and extrapolates the measurement, should be able to distinguish between the two cases.

4.2.4 Inhouse software

As with the instrument, the software has a key part in the development of the sensor. The software has been developed in C++ by the collaborator Dr N. Goddard. Briefly, the algorithm by processing the images of the interference pattern can quantify the shift of the fringes by extrapolating the phase difference. In more details, the software can process in real time the images acquired by the camera, and confronts the image acquired with the previous one to detect any difference in the fringe position. To do so, the software divides the interference pattern into evenly spaced rectangles. The numbers of regions and their dimension are selected by the user, and in Figure 22 it is possible to observe an example of the blocks created on the image. To minimise the

noise in the interferogram due to the refraction of the light from the edges of the channels, such as the plastic pipes or the electrodes, a black tape has been used to cover those parts. Unfortunately, this method causes a discrepancy of the exposed length channel, which varies from 8 to 10 mm, as it will be evident in the graphs where the RI variation is reported along the channel. The discrepancy *per se* will not reduce the sensitivity of the interferometer tracking the RI change, but it complicates the extrapolation of correlation between the position of the analyte in the channel with its position in the interferogram. For this reason, to improve the localisation of the analyte, a new chip design has been created (section 6.5.5.3).

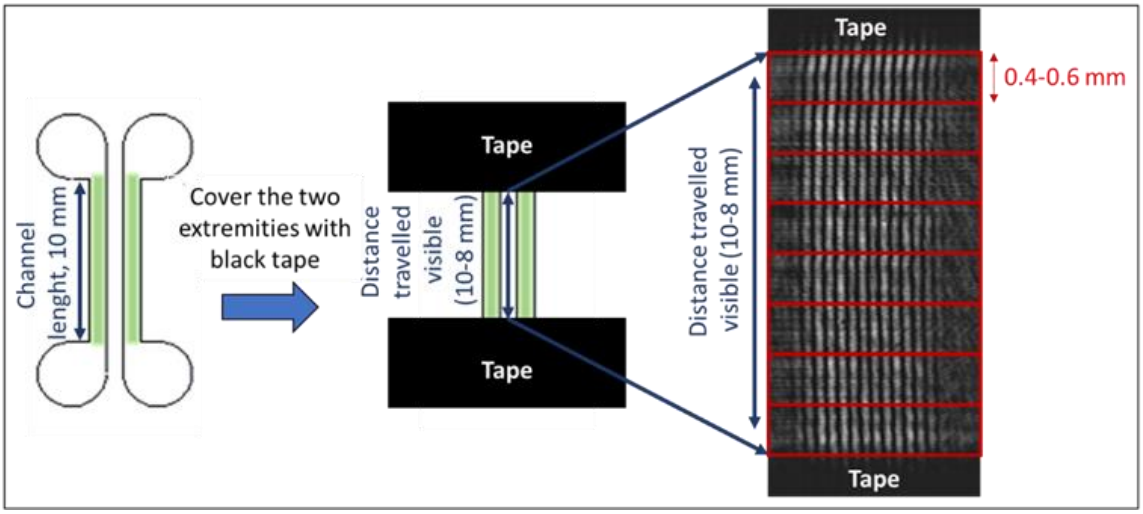

Figure 22 Representation of the areas (red rectangles) that divide the interference pattern.

Returning to how the software extrapolate the phase difference from the interference pattern, the algorithm converts the alternation of white and black fringes, as the maximum and minimum values respectively in the complex spatial frequency. As the maximum magnitude is localised for each rectangle, the spatial frequency is estimated by comparing the maximum with the two nearest maximums. Finally, the phase difference value is calculated by detecting a shift in the fringes. This is carried out by using the Fast Fourier Transform (FFT). The software results are quite fast (between 1-2 seconds), but it has some difficulties in determining the maximus positions, as the intensity of the fringes changes during the measurement. For example, since there are ten or eleven constructive fringes (white lines) in each interference patter, the software does not track the maximum in each fringe, but it tracks only the one with the highest value. Consequently, the highest value detected could not be placed on the same fringe

but can be on another one. It follows that the shift recorded from the software will have a higher variation. For this reason, after a lot of attempts in the years to identify how the acquisition could be improved, a lower exposition time has been identified to reduce this problem. Another ambiguity, that the estimation of the phase difference value causes, is due to periodicity nature of the unit [294]. In fact, the phase difference is obtained by the FFT of the spatial frequency and then the atan2(x,y) of that number gives the final value in radians. This function returns the arctangent of y/x, using the signs of both arguments to determine the quadrant of the return value, which is given in radians within the range -π to π. From the graph of the trigonometric function in Figure 23, it can be observed that for ±π/2 there is an asymptote, around where the value of the function changes completely if is under or over the asymptote. So, it seems reasonable to assume that when the data are extrapolated, there could be an error in identifying the right value in the neighbourhood of the asymptote. In conclusion, every time a jump appears in the measurement, a translation of the data is made manually, in such a way as to respect the trend of the values. Finally, it appears of vital importance to advance the software so to improve the sensitivity of the instrument [158], since reducing the external intervention will make the final analysis faster, but more important, more trustworthy and reliable.

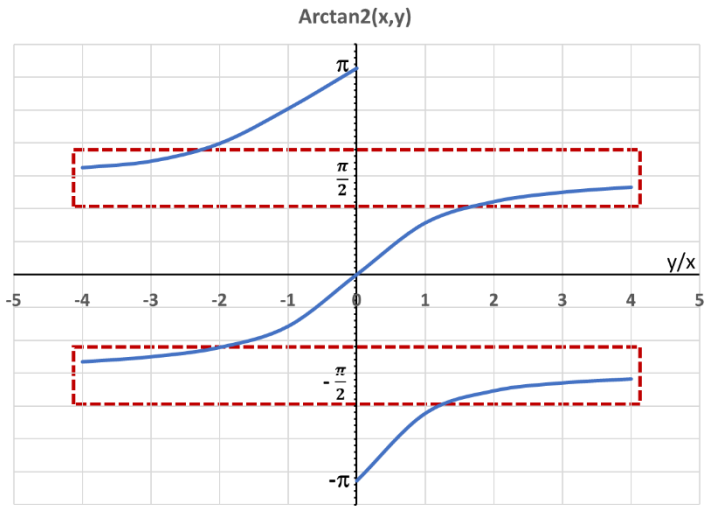

Figure 23 atan2(x,y) graph. The red dashed rectangles define the neighbourhood of the two asymptotes.

Another fundamental aspect to consider is the connection between the camera and the software. The camera trigger allows the software to have full control on the camera so

that it co-ordinates the camera acquisition and the image processing. The settings of the software, but also of the camera are important for an optimal acquisition. For example, the camera frame rate and the exposure time define the image acquisition timing, which should be set in a way to allow the software to process the image acquired, which drastically depends on the number of boxes. In other words, before starting the acquisition, the number of boxes is chosen in a way to balance the definition rate and the processing time of the software; the higher the number of the boxes provides a higher definition of PD along the channel is obtained, but more time will be required for image processing by the software. Consequently, it is necessary to find the right compromise between definition and time processing. For example, for several boxes higher than 15, the processing time required is $\geq$ 2 seconds. This setting will be used in the next chapters, as a higher definition was required to be able to track the analyte movement, whereas for this chapter, where the aim was to characterise the instrument, a smaller number of boxes were used, as the average values through the channels were considered for the purpose of calibration. Consequently, for a smaller number of boxes the time of acquisition was $\sim$ 1 second. In all the cases, the acquisition time of the software was set in a way to allow the processing of the images, and it varies from 1 to 2 seconds throughout the project. The number of boxes defines the small area in which the interference pattern has been divided. Usually, the number of boxes was chosen in a way that for calibration each of them has a height in a range of 600 to 900 μm, whereas for electrophoresis measurements (chapter 5 and chapter 6) the range used was 250 to 600 μm.

4.3 Characterisation

The starting point of this project was to characterise the interferometer. Not only as to determine the sensitivity, but also to test the software for the real-time measurement. Other than the instrument previously described, a Minipuls 3 (Gilson, Bedfordshire, UK) was employed to pump the solution into both channels in the chip. By adopting a pump, the sample and the reference solutions are introduced with a same and constant pressure [148] and their temperature is presumed to be the same, as they are kept at room temperature. The solutions were prepared in deionised water or phosphate buffer (10 mM pH 7.4) prepared by dissolving sodium phosphate monobasic monohydrate,

sodium phosphate dibasic heptahydrate in deionised water and 1 M sodium hydroxide (NaOH) and 1 M hydrochloric (HCl) acid were added to adjust the pH. The analytes adopted in the investigation were glycerol and bovine serum albumin (BSA). All the materials were bought from Sigma-Aldrich (Gillingham, UK), aside from the glycerol which was purchased by Fisher Scientific (UK). The refractive index (RI) of the solutions were measured with a RFM960-T refractometer (Bellingham and Stanley, Kent, UK) with an accuracy of ± 1 × 10^{-5} refractive index units (RIU).

4.3.1 Principle of operation of the YI

From the interferometer and the software descriptions, it is evident that the measurement is based on the position of the fringes. As described in chapter 2, as two coherent beams overlap each other an interference patter is created in that position. It is a periodical sequence of constructive and destructive interference. The intensity distribution is given by the formula

$$I = I_1 + I_2 + 2\sqrt{(I_1 I_2)}\cos\left[\frac{2\pi d}{\lambda D}y + \Delta\varphi(x,\lambda)\right] \qquad \textbf{(4.2.4)}$$

Where the intensities of the two beams are I_1 and I_2, d is the distance between the two beams, D is the distance between the microfluidic device and the camera, y is the distance along the transversal side of the camera (and so the interference pattern), λ is the laser wavelength, and finally $\Delta\varphi$ is the phase difference between the two beams caused by the difference in composition of the two channels. Finally, the x is the distance along the longitudinal side of the camera. The two elements that causes the interference (the phase shift) are:

Geometrical phase difference
$$g = \frac{2\pi d}{\lambda D}y \qquad \textbf{(4.2.5)}$$

Material phase difference
$$\Delta\varphi = \frac{2\pi h}{\lambda}\Delta n(x,\lambda) \qquad \textbf{(4.2.4)}$$

The phase difference (PD) due to the geometrical configuration (g) can be considered as constant during the measurement since no geometrical modification will be done. In other words, the shift of the fringes is caused only by the variation of contents in one channel in comparison to the other one. From the formula 4.2.4, the PD ($\Delta\varphi$) is

proportional to *h*, the height of the channels, and Δn, which is the refractive index variation between the two channels. The last value depends on the wavelength of the light source, since the refractive index of biological molecules is more sensitive to the wavelength, and on *x.* In conclusion, the PD acquired from the software will be only related to the material phase difference, and from this point on the PD will be indicated as only the material phase difference (formula **4.2.4**). From the same equation it is possible to calculate the theoretical value of the slope, or how PD and refractive index variation are correlate. For example, for a height value of 250 μm, it is possible to obtain:

Theoretical $$\frac{\Delta\varphi}{\Delta n} = 2952 \pm 150 \frac{rad}{RIU}$$ **(4.2.5)**

If the height of the channels changes the value will change accordingly. The height of the channels (interaction length) is determined by the thickness of the spacer layer.

4.3.2 Baseline

To test the stability of the interferometer, but also to verify the reliability of the software, baseline measurements were investigated to identify the most appropriate settings (such as acquisition time, numbers of areas) of the software. The baseline measurements were also helpful to identify the time interval stability for the measurement and for the laser, and so to identify the range of the external noises, such as mechanical vibration or change in the room temperature in very long measurement (six/eight hours). For all those reasons, the baseline measurements were indispensable for the deep understanding of the sensing system. One example of baselines was performed with a spacer of 250 μm thickness and is represented in Figure 24. During all this measurement, the same solution, deionised water 250 ml, has been pumped in both channels. The main thing that is visible is the drift of the phase difference. The interference pattern was divided in twelve boxes, where the first series were near the outlet, whereas the last series were near to the inlet. By observing the graph in Figure 24, it seems reasonable to say that for measurement that last hours, the phase difference detection exhibits a drift.

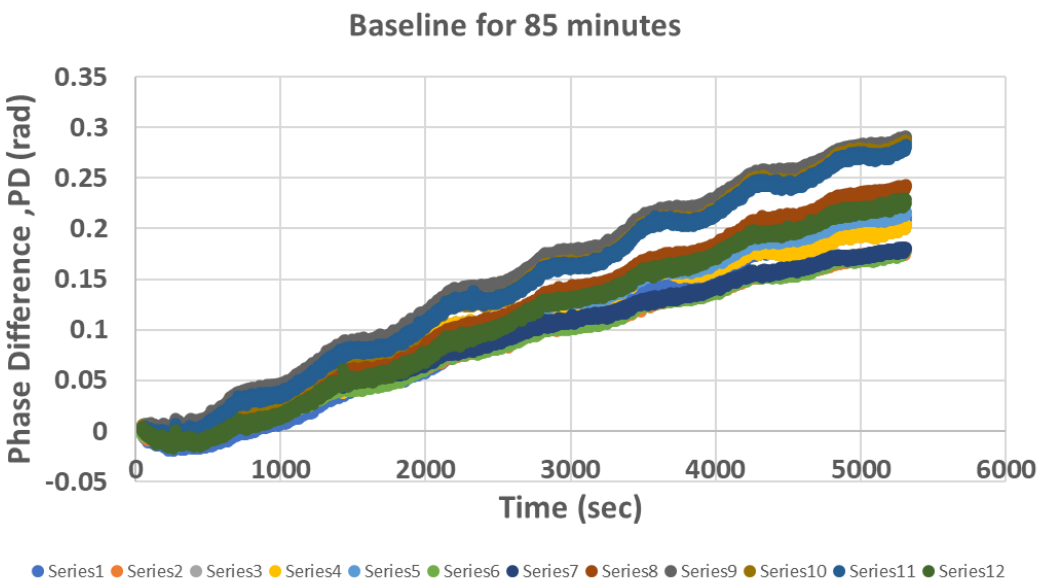

Figure 24 Baseline 80 minutes long. In the channels is being pumped only deionised water.

It is reasonable to link this drift to the temperature changing in the room, it is a small and slow change. Although, the temperature of the room is the same, during a long run the temperature could change and in turn the refractive index of the solution. This causes a slow modification that the interferometer detects as a small change in the phase difference. To reduce the temperature noise, or any other external stimuli/noises, such as air movement, the optical instrument is kept inside a black card-box. The box helps to maintain the temperature by creating a more controlled environment. The thermal drift here reported has been thought to be caused by the change of the temperature in the room for measuring that lasts for hours, which cause a RI change of the air. The laser itself should be considered as a heating source for the plastic chip, as its temperature is reasonable expected to chance for a prolongated exposure. Consequently, all the measurements have been performed using the box. Moreover, the sinusoidal behaviour, more evident for the series 1, 2 and 3, may be due to the laser. In conclusion, for the calibrations presented in the next sections a drift in the acquisition data was still visible, but it has been removed in analysis process as it will be explained next. For long measurement (over one hour long) it seemed that the drift was due to the volume difference between the reference samples (250 ml) and the samples volumes (20 ml for glycerol and BSA solutions). The reference solution volume is bigger than the sample, to minimise any contaminations for example due to the sample pipes.

As the sample volumes is smaller than the reference solution volume, the first could have suffered more the temperature changes of the room.

4.3.3 Glycerol

The first analyte selected to determine the instrument sensitivity and limit of detection (LOD) is glycerol. Glycerol is a common analyte used to characterise most optical sensors [123] [18]. The glycerol was dissolved in deionised water at different concentration (V/V). The measurement was principally performed by alternating deionised water and glycerol solutions in the sensing channel, while keeping constant deionised water flow in the reference channel. Every 15 minutes the pump was turned off to allow the change solution in the sensor channel. This must be performed with care, as carelessness can introduce air bubbles that will damage the measurement.

The final volume for each sample solutions was 20 ml, whereas the reference solution (deionised water) was 250 ml kept in a beaker covered with parafilm, so that the water was not contaminated. The solutions were prepared from a stock solution of 10% glycerol, and for decreasing the errors in the solutions preparation the other solutions were prepared by diluting in sequence the stock solution, so 1 % from 10%, whereas 0.5% were prepared from 1% solution. The interference pattern was divided in five areas (A, B, C, D, E), 1.2 mm along the short side (as it is possible to observe in the interferogram in Figure 25), and the phase difference acquisition values is represented in Figure 25. The errors are not visible in the graph since they are of the order of 10^{-4} to 10^{-3} radians; they have been calculated as deviation standard of the plateau values. In the graph the PD values of all boxes are reported as a proof of the uniformity of the interferometer measurement along the channel. This also proves that the RI change uniformly and at the same time within the channel as the solutions flow inside it.

From the glycerol run, it could be noticed that the phase difference achieves its constant value, a plateau, after eight minutes. This means that the system (pump, solutions, interferometer) requires eight minutes to completely change and differentiate the material, and so the refractive index, inside the channel. The PD value for each glycerol concentration has been determined by calculating the average of the plateau part for the glycerol steps, and the average for the plateau of the deionised water step before the glycerol; in turn the subtraction between the two averages is the value recorded as

the PD of the specific glycerol concentration. The errors, consequently, were calculated as variation standard of those values, and it result in the order of 10^{-5} radians. Adopting this data analysis, we want to reduce the drift of the long run that the system has shown in the baseline measurement. The slope was removed during the analysis process.

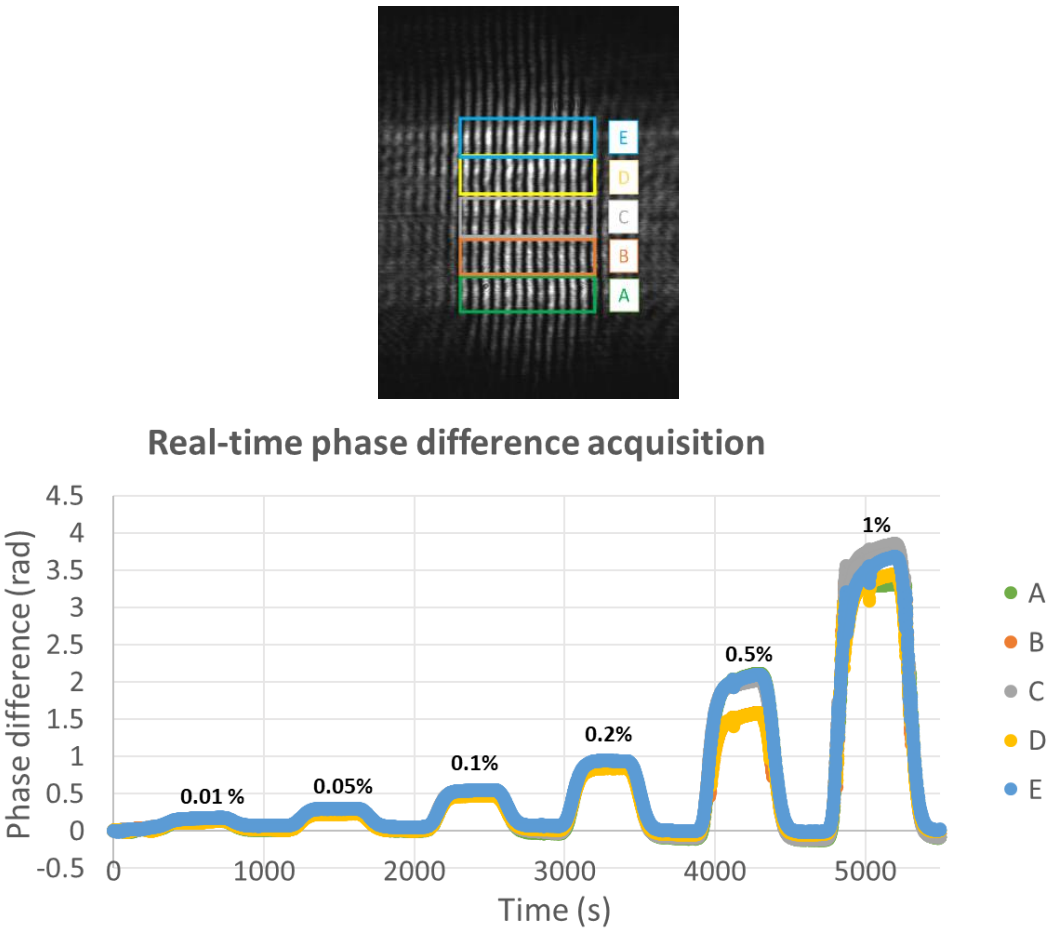

Figure 25 Interference patterns with the boxes used for the acquisition. Phase difference acquisition value in real-time for five boxes area. A is the box nearest to the inlet, while E is the next to the outlet. The errors are not visible since they are of the order of 10^{-3} radians. They have been calculated as deviation standard of the plateau values.

For the steps that identify the 0.5% and 1% concentrations, the software was not able to track constantly the changes, so the plateau is not flat, but shows a slope. For the same concentration it is possible to observe a not so good accordance with the simulation data reported in Figure 26. It could be possible to identify the 0.5% glycerol solution as the concentration beyond the upper limit of detection of the instrument.

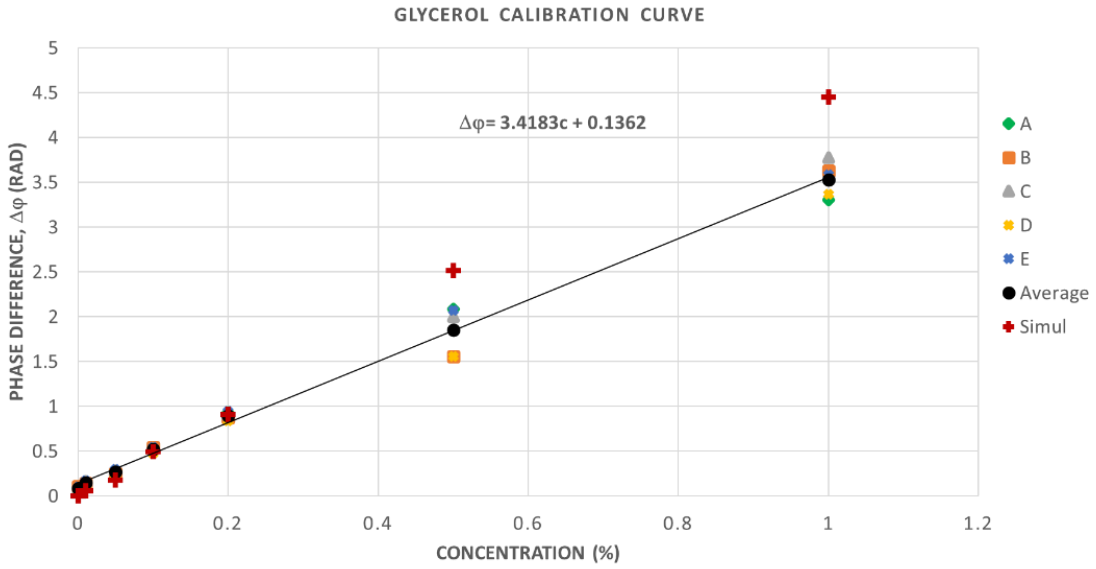

%	A (rad)	B (rad)	C (rad)	D (rad)	E (rad)	Average (rad)	Simul (rad)
0	0.078±0.005	0.108±0.005	0.080±0.006	0.063±0.005	0.103±0.005	0.087±0.005	0
0.01	0.142±0.004	0.141±0.006	0.164±0.005	0.119±0.005	0.168±0.005	0.147±0.005	0.058±0.005
0.05	0.272 ±0.006	0.255±0.006	0.283±0.006	0.231±0.005	0.297±0.005	0.268±0.006	0.175±0.006
0.1	0.514±0.007	0.546±0.006	0.531±0.005	0.473±0.006	0.546±0.006	0.522±0.006	0.497±0.006
0.2	0.929±0.005	0.875±0.009	0.907±0.006	0.843±0.009	0.943±0.009	0.899±0.009	0.907±0.009
0.5	2.08±0.009	1.559±0.009	2.001±0.008	1.556±0.009	2.070±0.009	1.854±0.008	2.518±0.009
1	3.302 ±0.009	3.626±0.009	3.776±0.009	3.366±0.009	3.586±0.009	3.531±0.009	4.452±0.009

Figure 26 Calibration curve and PD values for the glycerol concentrations (light blue line). The black spots represent the model values obtained by calculating the model phase difference from the refractive index of the glycerol solution measured with the refractometer. The errors are not so visible since are of the order of 10^{-5} radians even for the simulation data.

The average for the plateau for both concentrations present a higher error than the other values. The 0.01% glycerol has reported to be the lowest glycerol concentration detectable by the instrument. Once the phase difference acquisition was concluded, the values were reported in the graph correlating to the respective glycerol concentration, as the graph in Figure 26. In the same graph the average values are also presented, among the five boxes for each concentration, indicated in black. From the averages

values the glycerol calibration curve has been determined and it is reported in formula 4.3.6.

Glycerol calibration curve

$$\Delta\varphi = 3.4183\, c + 0.1362 \qquad \textbf{(4.3.6)}$$

The refractive index of the glycerol solutions has been also measured with the refractometer. By substituting that value in **4.2.4**, where the refractive index difference is:

$$\Delta n = n_{water} - n_{refrac} = 1.33299 - n_{refrac} \qquad \textbf{(4.3.7)}$$

From the RI values of the refractometer, by using the formulae we have simulate the PD values, which are reported in Figure 26 as a red cross. The error of the refractometer is $1x10^{-5}$ RIU, which corresponds to an error of ~ 0.003 radians of the phase difference. The accordance between the simulation data with the experimental data is optimal for the smaller concentrations, whereas for 0.5% and 1% the accordance is not evident. This is due to the acquisition data for the two higher glycerol concentration has required an important analysing process, that may have caused an underestimated of the phase difference.

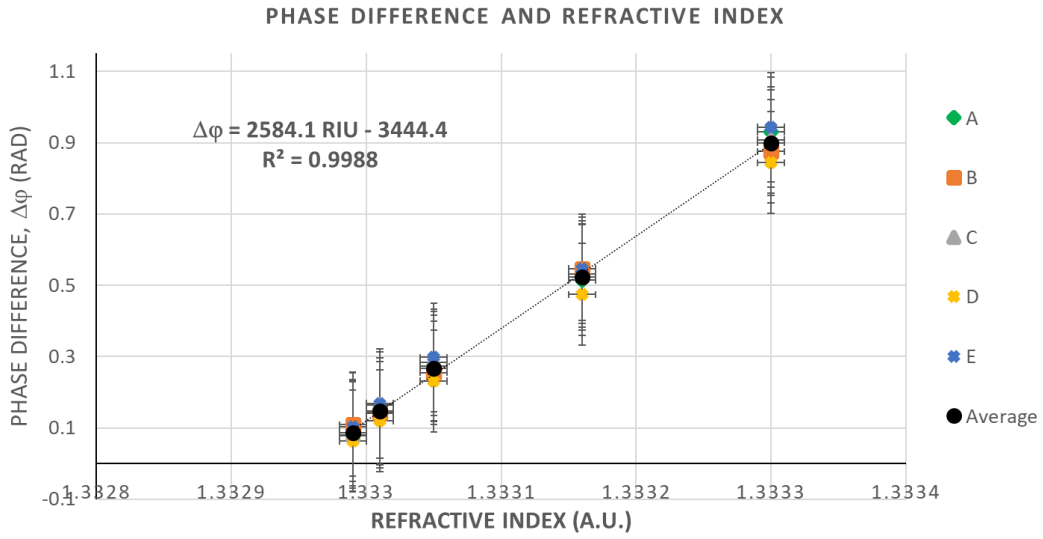

Figure 27 Phase difference dependence from the refractive index.

Now the PD experimental data for the lower concentrations are represented in the graph in dependence to the refractive index measured with the refractometer, *figure 27.* The coefficient of proportionality of those data is calculated and reported in

equation **4.3.8**. There is an agreement between the experimental value expressed by the formula **4.3.8**, with the theoretical value expressed by the formula **4.2.5**.

Experimental $$\frac{\Delta\varphi}{\Delta n} = 2584 \pm 130 \frac{rad}{RIU} \quad \textbf{(4.3.8)}$$

Finally, from the calibration curve, it is shown that the phase difference value is proportional to the glycerol refractive index, as is predicted from in formula **4.2.4**. Moreover, as expected the refractive index values are increasing as the concentration of the analyte increase.

4.3.3.1 Three different heights of the channels

As a further proof of the formula **4.2.4** and, particularly, the direct proportionality of the PD with the thickness of the channels (*h*), four glycerol solutions (0.01%, 0.05%, 0.1% and 0.2% v/v) were measured by using chips with three different channels heights: 250 μm (as in the previous experiment), 1.48 μm, and 3mm. In Figure 28 the measurements are shown. For each height two acquisition are reported that represent different positions along the channels (the start and end of the channel). It is evident from the graph that as the thickness increases, the PD values follow in the increment. If for example, we compare the PD values of the 0.05% concentration reported in Figure 29, it can be observed that between 250 μm and 1.48 mm the PD values are 0.24 rad and 1.6 rad respectively, so their ratio is 6.6 as the ratio between the thickness is 5.9.

Furthermore, if their values are compared with the highest channel, we obtain a ratio of 2.3 between 3mm and 1.48 mm, whose ratio is 2.0, and a ratio of 15.4 between the shortest and the longest height channels, whose ratio is 11. The ratio of the PD values may not be so comparable to the ratio of the height, but even so the trend is tangible. In conclusion, the sensitivity of the interferometric sensor relates to the height of the channels. Sensitivity improves as the height increases, since for smaller concentration a higher phase difference is detected. For example, if we considered the lowest concentration 0.01%, PD detected for 250 μm is 0.13 radians, whereas for 3 mm the phase difference was 0.79 radians. On the other hand, a higher sensitivity causes a drift more notable, as it can be observed for the 1,48 mm and 3 mm heights measurements in Figure 28, where at the end of the acquisitions the phase differences relative to the

reference solution are distant from the zero value, traced instead by the 250 μm height channel.

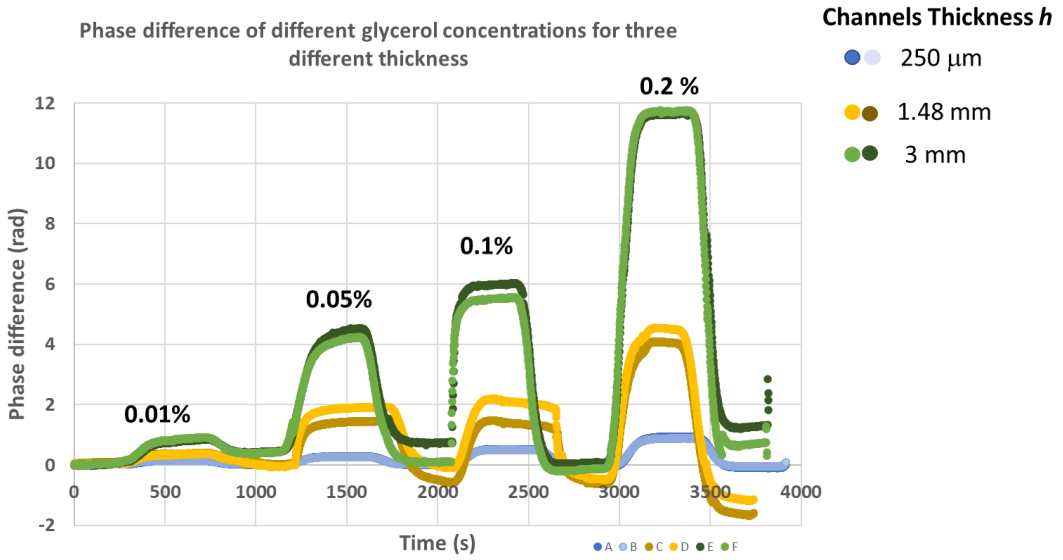

Figure 28 Glycerol run of four concentrations, in three different heights channels. The two shades of the same colours represent the measurements along different points of the channels. Blue (A, B) 250 m, yellow (C, D) 1.48mm, green (E, F) 3 mm. The errors in all the measurements are in a range from 0.005 rad to 0.07 rad, so they are not visible in the graph.

%	Phase difference (rad)					
0.01	0.13	0.13	0.31	0.35	0.76	0.82
0.05	0.26	0.22	1.39	1.91	3.89	3.65
0.1	0.51	0.48	1.91	2.15	5.87	5.60
0.2	0.95	0.86	4.56	4.88	11.5	11.83
	250 μm		1.48 mm		3 mm	

Figure 29 Average values of the phase difference of the measurement reported in Figure 28. The errors in all the measurements are in a range from 0.005 rad to 0.07 rad.

4.3.3.2 Discussion of the glycerol measurements

The glycerol measurements previously reported were fundamental for the characterisation of the software and the instrument, such as its lowest and highest limit of detection of sample concentration. In particular for the software which, since it is a novel, no guidelines were available, but through testing the best conditions were found,

such as the right equilibrium between the definition and the time acquisition mentioned previously in the “Inhouse software” paragraph.

4.3.4 BSA

As the first characterisation was performed with glycerol, the next move was to analyse the instrument response with Bovine serum albumin (BSA), purchased from Sigma-Aldrich. Since BSA can be easily adsorbed on PMMA and other surfaces [295], it was dissolved in a solution made of phosphate buffer (10 mM pH 7.10) and 0.2% Tween®20 (Sigma-Aldrich, for molecular biology, viscous liquid, P9416-25ml). Tween®20 is a viscous liquid, and a non-ionic detergent which is primarily used for preventing surface adsorption and keeping the solubility of the protein [296] [191].

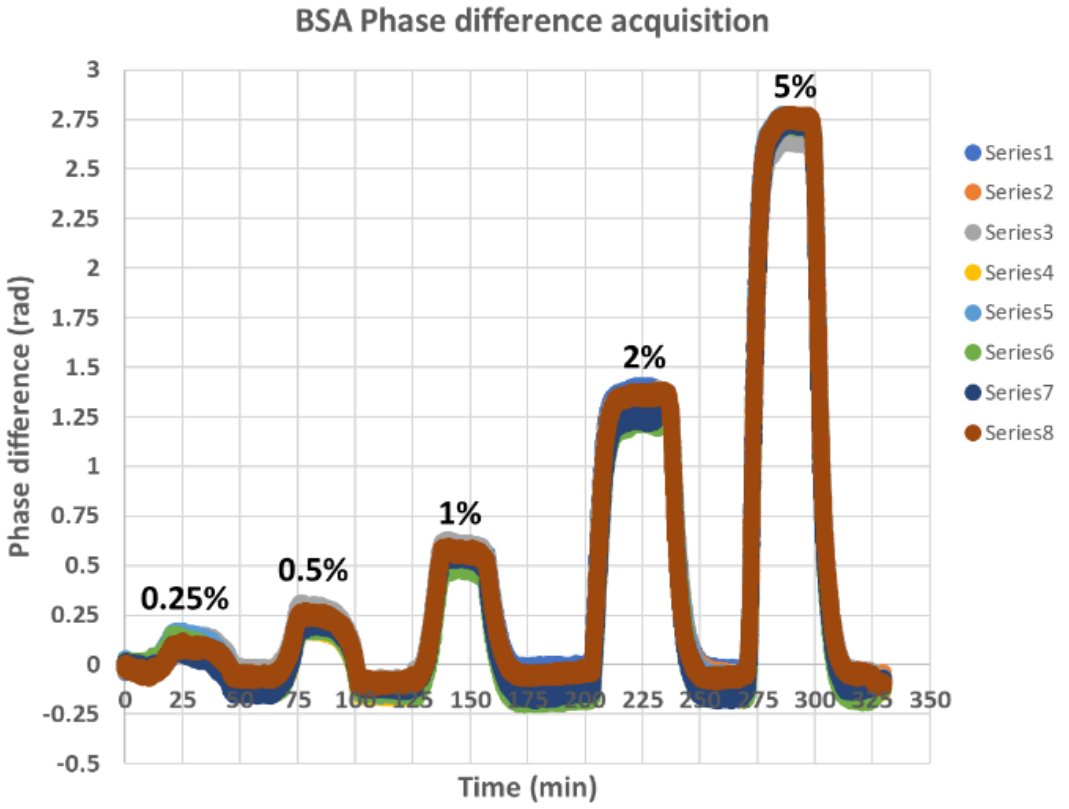

Figure 30 Phase difference real-time acquisition for BSA solution, prepared in buffer pH 7.10 (10 mM) and 0.2% Tween20. The errors in all the measurements are in a range from 0.005 rad to 0.07 rad, for this reason they are not visible in the graph. The errors were calculated as the standard deviation errors

As with the glycerol, five different concentrations of BSA (0.25%, 0.5%, 1%, 2%, and 5% (W/V)) were pumped into the sensor channel by alternating it with the solution buffer and Tween®20, which was consistently pumped into the reference channel; the run is

reported in Figure 30. The five percentages correspond to a molar concentration of 3.75 μM, 7.5 μM, 15 μM, 30 μM, and 75 μM of BSA. They were prepared by preparing a 5% solution, followed by sequential dilutions. The refractive indexes of the solutions are reported in table 5. Differently from the glycerol run, the BSA solution seemed to require a longer flow inside the channels, to stabilise the phase difference; so that the solutions were exchanged every 25 minutes. In this case also, along the channel the phase difference is increasing as the concentration increases. The lowest concentration that the interferometer was able to detect was 0.25% (3.75 μM). For lower concentrations the signal was covered with instrument noise. As it was observed with the highest glycerol concentrations, in the BSA measurement for the smallest concentrations a small drift is visible. This could be due to fact that those concentrations are near to the lower limit of detection of the instrument, or it could be possible that a longer injection could have determined a more stable and recognisable plateau.

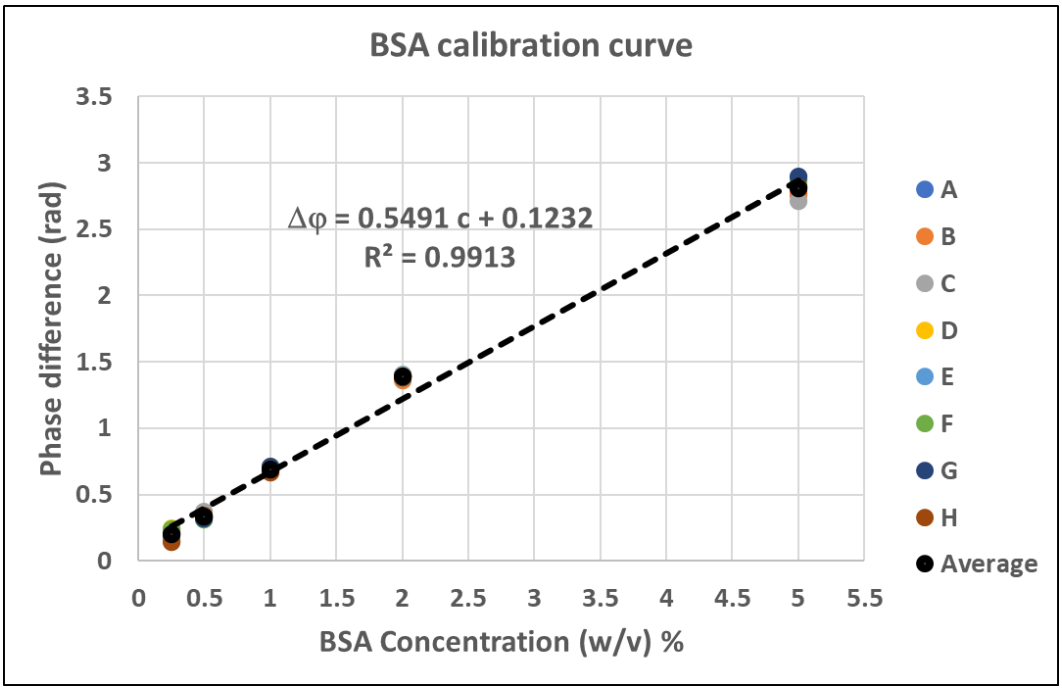

Figure 31 Calibration curve of the interferometric sensor for BSA. The errors in all the measurements are in a range from 0.005 rad to 0.07 rad, for this reason they are not visible in the graph. The errors were calculated as the standard deviation errors

The calibration curve, that has been determined from the graph in Figure 31, shows the proportional relationship between the phase difference detected at each BSA concentration. The errors are not visible in the graph since they are of the order of 10^{-4}

to 10^{-3} radians, but they are reported in table 5. The calibration curve is reported in equation **Error! Reference source not found.9.**

Table 5 BSA concentration and Refractive index and Phase difference calculated (average).

BSA Concentration % (W/V)	Refractive Index (refractometer)	Phase Difference PD (rad)	Refractive Index (calculated from the PD)
0 (Buffer+Tween20)	1.33507±0.00005	0	/
0.25	1.33523±0.00005	0.21	1.33528 ± 1.2E-05
0.5	1.33530±0.00005	0.33	1.335322 ± 6E-06
1	1.33538±0.00005	0.69	1.335443 ± 5E-06
2	1.33559±0.00005	1.39	1.335679 ± 5E-06
5	1.33602±0.00005	2.81	1.33616 ± 2E-05

BSA calibration curve $\Delta\varphi = 0.5491\, c + 0.1232$ **(4.3.9)**

As in the glycerol case, the PD value for each concentration has been determined by subtracting the average values of the analyte steps with the average value of the reference solution (buffer). In the literature since the optical sensor may detect diverse quantities to make a confront among them usually the correlation between the refractive index and the analyte concentration is also reported. For this reason, in Figure 32 it is showed the calibration, where the refractive index has been calculated by using the formula **4.2.4**. The refractive index values have been calculated by determining the average value of the phase difference along the channel, and in turn it was used in the inverse formula **4.2.4**.

The proportional factor value is 0.188 ml/g and this corresponds to the one reported in literature [297, 298]. In other words, the phase difference, and in turn the refractive index measured by our instrument is in accordance with the protein progression reported in literature [297], where for untreated proteins dn/dc varies within 0.18–0.19 ml/g. As the BSA is one of the analytes used for the electrophoresis characterisation in the next chapter, it was important for comparison reason to obtain a calibration curve.

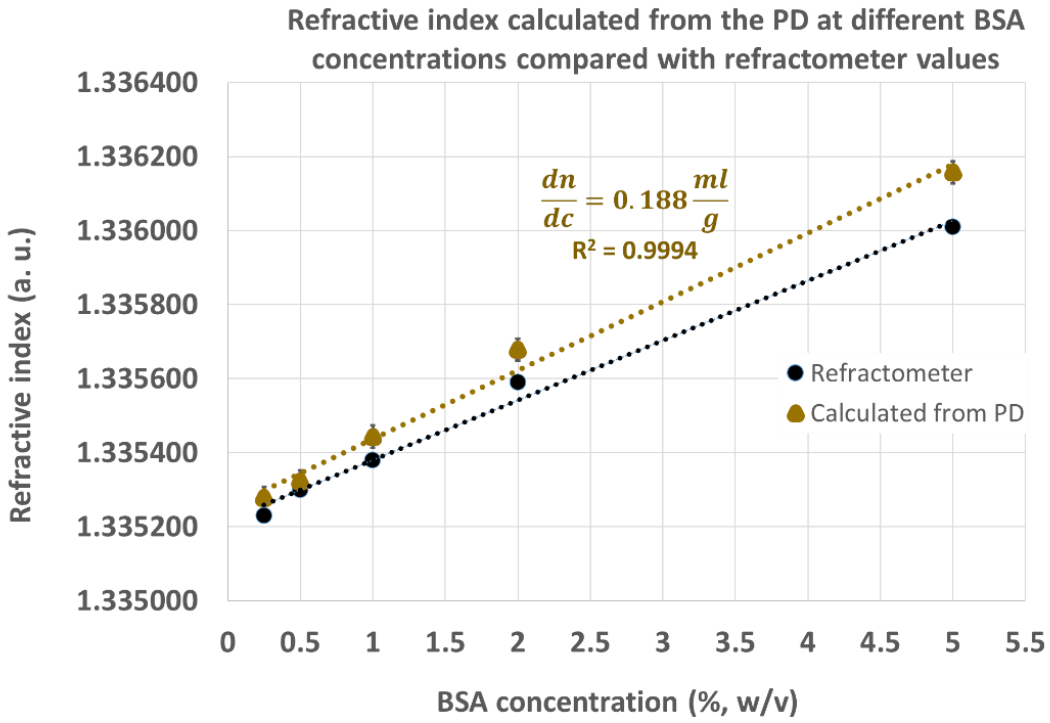

Figure 32 Correlation refractive index and BSA concentration. The data reported are the RI calculated from the PD of the interferometer and the RI measured with the refractometer. The errors are slightly visible for the RI. The errors from the interferometer were calculated from the propagations of errors of all the values (5 acquisitions) obtained from a single acquisition.

4.4 Final comments

In conclusion by confronting the calibration curves of glycerol and BSA, it is possible to say that the interferometer and the software are detecting well the two analytes studied. Regarding the sensor sensitivity, here the Refractive Index Sensitivity (RIS) is reported as more general descriptor since it is better represented the instrument and allows to confront with another optical instruments. From the characterisation the refractive index resolution is 2.04×10^{-6} RIU, which is give quite competitive with other optical interferometric sensors (table 2, chapter 2), as for example [123], whose instrument has a detection limit of 10^{-5} RIU. As it was explained in the "Inhouse software" paragraph 4.2.1, a $\pi/2$ phase difference may cause a spike in the measurements. Such phase difference change results to be for a 250 μm height channel a variation of 5.32×10^{-4} RIU. In turn, if the analyte is a protein, whose refractive index increment with the concentration is $\sim 0.256\ RIU\ ml/g$ at 532 nm light source [297], then that phase difference variation is due to an increase of 0.21 % (w/v) of the analyte concentration. In other words, every concentration increments of 0.21% of the protein,

may cause a jump in the measurement. The standard deviation error due the noise has been found to be in the range of $8x10^{-3}$ to $1.2x10^{-2}$ radians, which, by considering three standard deviation levels, corresponds to RI resolution range of $8.16x10^{-6}$ to $1.22x10^{-5}$ RIU. Given the previous description, the lowest protein concentration detectable is 0.21%, which for BSA correspond to 3.15 μM, which is in agreement with lowest BSA concentration detected experimentally of 0.25% (3.75 μM). From the study of the PD at diverse channel heights, even though the 3 mm height produce the best sensitivity, for all the following experiments and the BSA run a 250 μm height has been adopted, since for electrophoresis studies, a higher channel would have caused more thermal noises (Joule effects) as will be explained in the next chapters. Furthermore, as the LOD of the sensor seems to be higher at the expense of its RI sensitivity, the main cause seems to be the difficulty to recognise the signal from the background noise. An advancement of the software may allow to improve the limit of detection not only for glycerol or BSA, but also for proteins. Parallelly, the use of biorecognition elements in the sensing area, other than give a selectivity feature to the sensor, may also improve the limit of detection, since it will allow to concentrate the analyte in a narrower region as will better discussed in chapter 6.

Chapter 5 Electro-kinetic characterisation: buffer systems and interferometer acquisition

5.1 Introduction

A biosensor is a compact device designed to detect or quantify an analyte using a combination of a bio-recognition species with a physical transducer. The combination of micro-technology, molecular biology and photonics opens the possibility of developing biosensors with a potential for a wide variety of diagnostic and therapeutic uses [299]. One of the main aspects, that emerges reading the previous works, is that most of those biosensors presents an instrument where two or more techniques are embedded together in order to improve the sensitivity and the selectivity of a well-defined analyte. In the present work we have combined the interferometry with the micro-flow-chip electrophoresis, by translating some concepts usually related to bulky system, such as capillary electrophoresis (CE) and Polyacrylamide Gel electrophoresis (PAGE), to a smaller system as the microfluidic channels. This approach consents to miniaturize the chip, reducing the analysis time [251] [237] and, moreover other potential advantages include a lowered sample volume and enhanced mass transfer [300]. For all those reasons the electrophoresis enhanced interferometric sensing offers an innovative design view for chemical and biological sensors, which could proceed further with specific modifications on the hydrogel functionalization (as it will be presented in the next chapter). A similar combination, electrophoresis with interferometry, has also been delineated by Crespi et al. [18] and Yang et al. [140], but in neither cases the instrument has been presented as biosensor. It is important to point out that the interferometer, as with any other optical sensor, is not capable to distinguish by itself the analytes. For those instruments, it is essential to create such conditions which will create a separation or a selection. A further characteristic that distinguishes the sensor presented here from the ones in the literature is the method used for the acquisition of the information. In fact, our instrument acquires an image from where it is possible not only to quantify the analyte (as described in previous chapter), but also to provide spatial information of the refractive index modification in the micro-chip [122]. As it was illustrated in the previous

chapter, the interferometer is capable to measure the Phase Difference (PD) of different sample solutions. It was then essential, considering the development of an optical biosensor, to study separately the electro-kinetic technique since the analyte in our project is pushed through the channel with electrophoresis. Consequently, in this chapter, aspects more related to the electro-kinetic techniques will be presented, by showing the research of the most appropriate hydrogels for the herein sensor, followed by the electric characterisation of the gel and the target analyte.

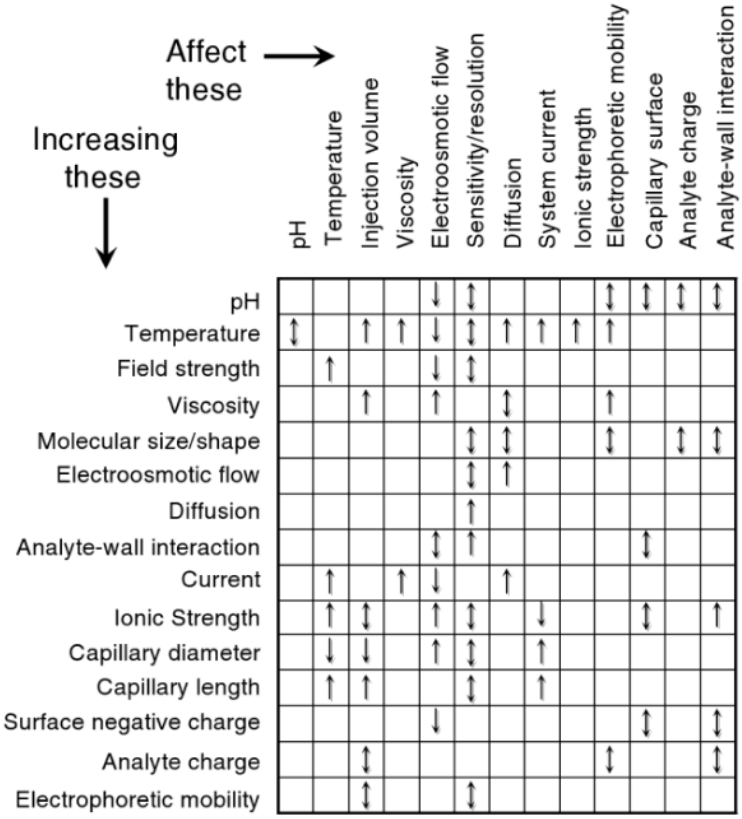

Figure 33 Schematic representation of all the parameters from "Handbook of Capillary and Microchip Electrophoresis and Associated landers" [301].

Since the electro-kinetic technique was thought not only as a driving force for the analyte so that to speed up the measurement, but also as a technique that could focus a small amount of analyte in a narrow region, experiments on pH junction have been performed. Electrophoresis has been widely used as a separation technique for proteins, ionic substances, and peptides [302]. Generally, a matrix is adopted which has a solid support such as agarose or polyacrylamide gels, and paper [301]. Gel electrophoresis includes various parameters, some of them are reported in Figure 33. Finding the right equilibrium among them determines the success of the experiment. It is well known that

the electrophoresis suffer from some problems, whose alternatives are still not so effective [301]. As further proof, in the literature it is possible to find more reviews on capillary electrophoresis (CE) ([205], [303], [304, 305], [198]) by same groups that each two or three years published a new review for gathering innovative information that other groups can have achieved. Those disadvantages are particularly hard to control in separation techniques, such as Isotachophoresis and pH junction stacking [205] [306], where the right balance with all the parameters makes the experiments a successful. Finally, another aspect that should be considered is the way the sample is injected in the sensor area. The most common method is by hydrodynamics, but in this project the sample is electro-kinetically injected [307]. The latter method has been defined as the one with less reliability [308], but in such cases the electro-kinetic injection is applied to a complicated channels structure, whereas in this project the system consists of two reservoirs connected and the electrophoresis is applied in the longitudinal direction of the channel. Lack of reproducibility is a common aspect in the electrophoresis and electro-kinetic techniques [309] [306], so they are methods that require experience and deep knowledge.

5.2 Hydrogels

One of first steps required for the developing of the chip structure was the selection of the matrix which has to suit both purposes: the analyte confinement, and a good interference pattern acquisition.

5.2.1 Choice of hydrogel

To use the interferometric set-up for bio-sensing embedded with electrophoresis, we first studied how the interference pattern is modified by the presence of a hydrogel inside the channels of the chip. Generally, a hydrogel has a porous structure made of monomers and chemical or physical cross-linkers [310] and, like the name suggests, the preeminent substance is water. The hydrogels are so widely used in bio sensing because they have some distinctive features which permit the hydrogel to be sensitive to external stimuli, to interact with molecules and most importantly to incorporate bio-receptors through synthesis methods. Furthermore, some of the hydrogels can be used in interesting methods, such as the electrophoresis, where the analytes are forced through the gel at increased speed achieving a reduction of the acquisition time. The

main challenge is to obtain a well-defined interference pattern, ideally defined as well as the one obtained with only the interferometer, image showed in Figure 34.b. The difficulties in this aspect, as it will be described deeper in the next paragraphs, are due to the existence of irregularities of the hydrogel inside the micro-channels, in part caused by a defective adherence between the hydrogel and the chip surfaces. Besides, another aspect that should be considered in the hydrogel choice is the resilience against a uniform electric field for the electrophoresis purpose. Therefore, it is essential to find the right material that has satisfactory optical and electrical properties for this project. Typically, the gels used in electrophoresis are polyacrylamide (PAAm) and agarose gel. Initially, PAAm polymer, has been tested, since it is optically transparent and its functional group (-NH^2) can be used to give the hydrogel new functionalities. Before filling the channels, 1 mm PAAm coated over a glass slide was tested by depositing a 1 mm thickness gel over a glass slide of 2.5x2.5 cm square. Its interference pattern was recorded and is shown in Figure 34.a

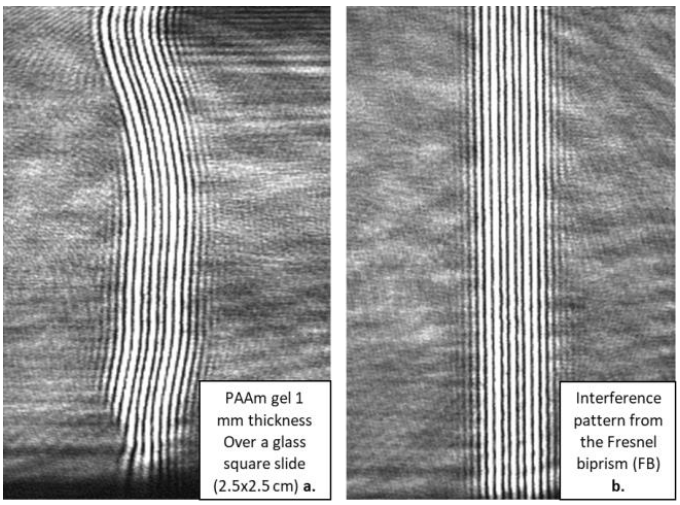

Figure 34 Interference pattern of PAAm (1 mm thickness) (a) and empty chip (b).

From the two interference patterns in Figure 34, it is possible to observe that the definition between black and white fringes is good in both, but the “lines” in figure 33.a are not straight in comparison to figure 33.b. The curves are caused by the imperfections in the surface flatness and uniformity of the hydrogel. However, the PAAm was not the only hydrogel that has been used in this research; poly(allylamine) gel and agarose gel have also been investigated. In the PAAm gel used in the previous images, the monomer, acrylamide, was present in 5% concentration (mol/mol) in the prepolymer solution. The

initiator concentration has been always taken as 10% (mol/mol) of the monomer concentration, while the cross-linkers were 1/30 (mol/mol) of the monomer moles. Similarly, the same proportions were used to prepare the poly(allylamine) gel with the cross-linker poly(ethylene glycol)-diacrylate (PEGD). Completely different is the case of the agarose, that is a thermosensitive hydrogel and so its status depends principally upon the temperature. It polymerises without a crosslinker, but by dissolving the agarose in water at temperatures close to 100 °C and it solidifies at temperature below 30°C. In the next paragraphs, all the hydrogels tested will be described with their advantages, but also disadvantages, to illustrate the steps followed in the beginning of the this project.

5.2.2 Polyacrylamide (PAAm)

As better described in chapter 3, the PAAm is a polymer, whose monomer is acrylamide that is typically crosslinked with bisacrylamide. Two types of PAAm hydrogel have been studied: a cross-linked linear polymer chains, and a cross-linked monomer. The linear polymers that have been used are the polyacrylamide cross-linked with glutaraldehyde. It has been also combined with allylamine and n-(3-aminopropyl) methacrylamide hydrochloride (NAPMAAm) to embody active amino groups in the hydrogel. Those groups are important to make a hydrogel sensitive to the target molecules, such as proteins. The idea to use the linear polymer came from the intention to form a more uniform structure of the hydrogel. The protocols used for their preparation is described below, with their relative interference patterns obtained. The protocol used for the acrylamide polymerisation is well known in the field, since it is a pillar of the gel electrophoresis [311]. Both groups (cross-polymers and linear polymers) possess a voltage limit over which the interference pattern started to change appearance, like figure 35 shows; if for the first group the limit is 30/40 V, for the second group the voltage limit is 80/90 V. Regarding this aspect, all gels were tested to find out its electric limits (voltage and electric current). Furthermore, the interference pattern was not so well define for all the gels prepared, as it will be showed next.

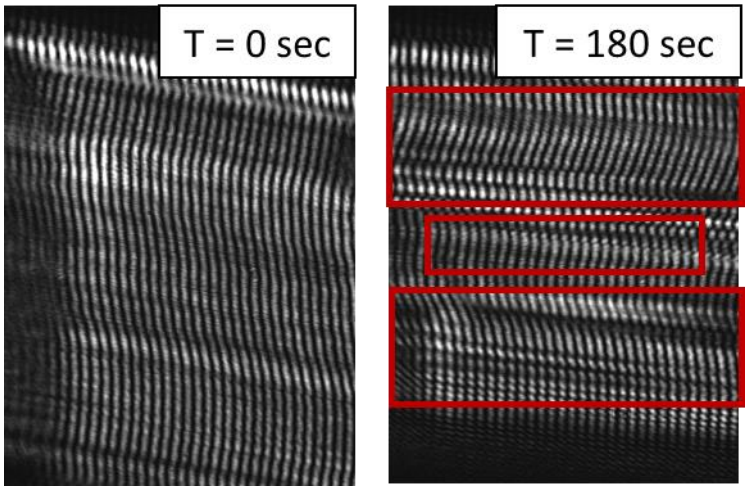

Figure 35 PAAm inside the channels 200V and 800μA. Beginning and after 3 minutes after the voltage was applied. The red boxes evidence the main differences between the two patterns.

In all the electrophoresis experiments a pH 9.2, 1 mM, phosphate buffer solution (PBS) was used, and stainless-steel electrodes were adopted. One of the first images obtained using the electrophoresis technique combined with the interferometric set-up are shown in Figure 36. The channels are filled with polyacrylamide gel, polymerised by TEMED (tetramethylethylene diamine) and ammonium persulfate (APS), then a solution of FITC-Streptavidin 0.067 (mg/ml) in a pH 9 buffer was applied to the sample channel, while the same buffer was added in the reservoir of the reference channel.

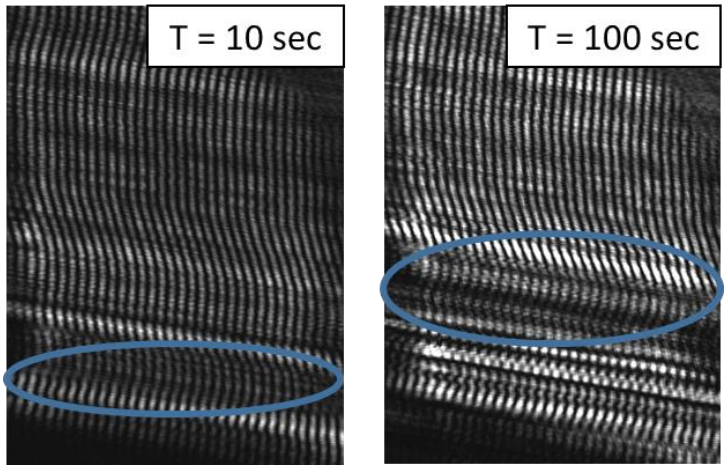

Figure 36 Interference pattern of the chip filled with PAAm with protein solution moving inside it under a V=40 V, at 10 and 100 seconds after the voltage was applied.

In figure 36, we can observe how the interference pattern changes with the sample solution coming inside the channel under a voltage of 40 V and a resultant current of 20 μA. Unfortunately, because the preparation of the chips was not reproducible, it was

not possible to study deeper the movement of the protein inside the channel. The interference patterns in Figure 36 show a qualitative movement that can be extrapolated from the local change in the pattern, as the blue ellipses highlight in the same figure, along the passing of the time. Below the exact preparations for all the hydrogels used are presented with their relative interference pattern.

- Polyacrylamide with APS and TEMED (PAAm)

For 2 ml solution

- 1.75 ml deionised water nitrogen bubbled
- 250 μl acrylamide/bis-acrylamide 30:1 40%
- 25 μl 10% APS
- 2.5 μl TEMED

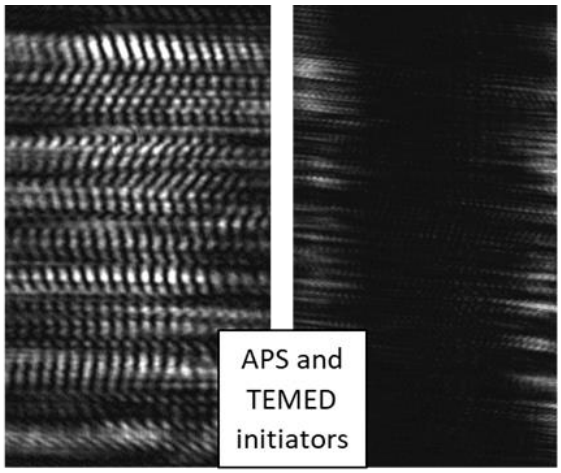

Figure 37 Interference patterns of PAAM using APS and TEMED to crosslink the gel. In some cases, the interference pattern is not visible.

The other polyacrylamide gels had different preparation. Photoinitiators, such as 2-hydroxy-4-(2-hydroxyethoxy)-2-methylpropiophenone **(PI1)**, or 2,2'-Azobis[2-(2-imidazolin-2-yl)propane] Dihydrochloride **(PI2)** were investigated by illumination with a UV light source with a wavelength of 350 nm. The exposure time for the two photoinitiators were of the order of 10 minutes.

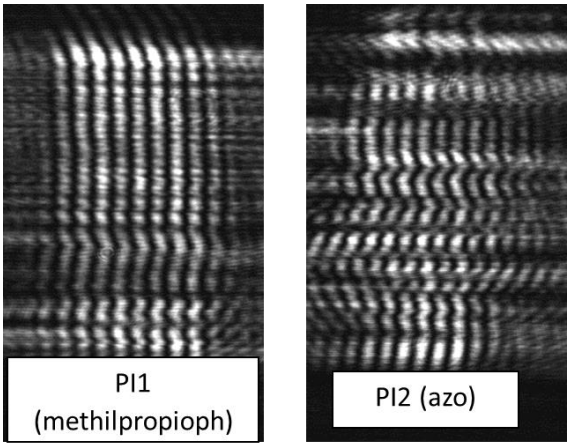

Figure 38 Interference patterns of PAAm gel initiated with photo-initiators.

Another polyacrylamide gel was obtained by use of a synthesized linear polyacrylamide. Although they show an acceptable interference pattern, they seem quite refractory when the voltage is applied. The current inside the hydrogel is quite high (~1-4 mA) applying a voltage of 50-200 V and the structure, looking the interference pattern, seems to be modified and stressed, like the image shows. On the other hand, the other group of hydrogels possess some better electrical properties, having a current of 5-50 μA under a voltage of 50-200 V. These hydrogels are prepared by cross-linking the acrylamide with bis-acrylamide using UV initiators, such as PI1 and PI2, or radical initiators like ammonium persulfate (APS) with N,N,N`,N`- Tetramethylethylenediamine (TEMED). The interference pattern of these hydrogels is visible, but not uniform or completely absent, as can be seen in Figure 37 and Figure 38. To prepare the polymer it is important to purge deionised water under nitrogen for 30 minutes, then add acrylamide (and allylamine) to the purged water. In turn add TEMED to solution and then APS (previously dissolved in degassed deionised water to get 10% (w/v)). Keeping the solution covered, allow it to react for two hours. Finally recover the polymer by pouring the reaction mixture into approx. 200 ml methanol and retrieve the solid via centrifugation, filtration, dialysis, or freeze dry overnight. And finally in order to prepare the gel solution with the polyacrylamide dissolve 50 mg polymer (used also the commercial one *Polyacrylamide* Sigma-Aldrich 738743) in 1 ml of HCl 1 M. Add 40 μl of water to 10 μl of 25% glutaraldehyde. Add 900 μl of the first solution (I) to 100 μl of the second (II) solution. Wait overnight

5.2.2.1 Glass functionalization and channels design

Due to the lack of reproducibility of a good interference pattern from a PAAm gel, a study for the main cause has been explored. One idea was to improve the adherence of the hydrogel on the channels surface, so that a functionalisation of the chip material (PMMA and glass) was undertaken. In parallel, a second way to obtain a reproducible interference pattern was by changing the channels design, in such way that any the imperfections in the gel could be present at greater distance from the area through which the beam passes. For example, the effects of the fast polymerisation (10-20 seconds) of the pre-polymerise in gel definition within the channel. In fact, there are some parts, like the edges, where the gel is compressed or there are some air/water gaps, such as shown in Figure 39, and also if the time required to polymerise (too long or short) will somehow influenced the adherence of the hydrogel on the interface. To improve the attachment between the hydrogel and other surface, the glass for the substrate, and for the cover of the chip, has been functionalised with Chloro(dimethyl)vinylsilane, and Allyltrichlorosilane.

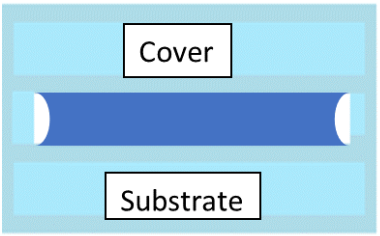

Figure 39 Defects hypothesised. Side view for only one channel.

Different combinations of substrate and cover material has been used. For example, both were made of treated glass, or the substrate with treated glass and the cover of PMMA, or finally a PMMA chip Figure 40.

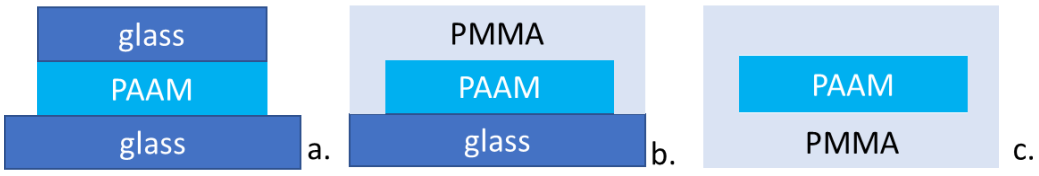

Figure 40 Three chip configuration: a. glass, b hybrid, c plastic.

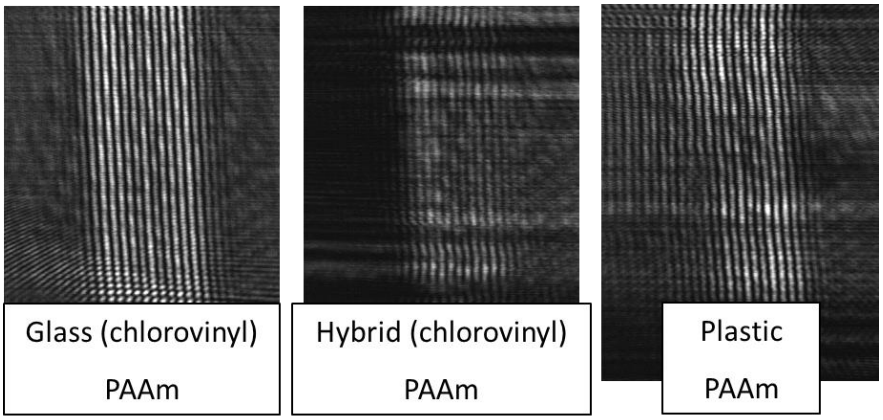

Figure 41 Some example of interference patterns of a PAAm gel in a glass, hybrid, and plastic chip. The glass was treated with Chloro(dimethyl)vinylsilane.

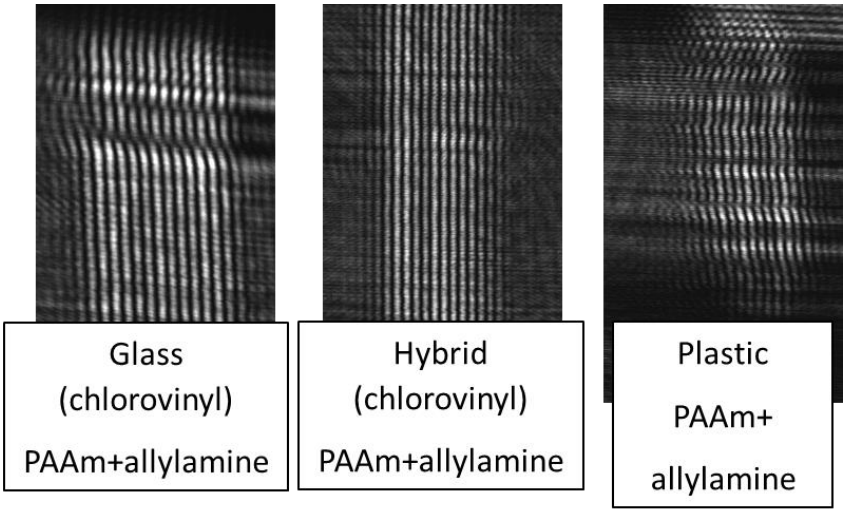

Figure 42 Some example of interference patterns of a PAAm+allylamine gel in a glass, hybrid, and plastic chip. The glass was treated with Chloro(dimethyl)vinylsilane.

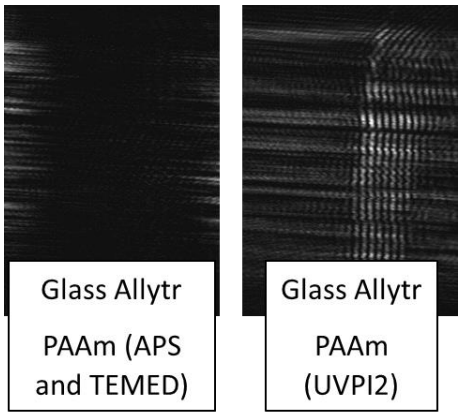

Figure 43 Some example of interference patterns of a PAAm gel in a glass, and hybrid chip. The glass was treated with Allyltrichlorosilane.

The main difference between the glass treated with those two chemicals, was the transparency of the slide. Transparency is better with Chlorodimethyl(vinylsilane) than with Chlorodimethyl(vinylsilane). Regarding the chip design, the main change was to make the channels wider, in a way that the beams will not interact with the defects in the gel around the surface. On the other hand, the volume of the hydrogel is wanted to be as small as possible, to be still able to use a low voltage to speed-up the protein inside the channel. At this state the chip was a rectangular device, whose dimensions are 2.5x4cm (the height change from 4 mm to 9 mm) where the two channels are incised in the centre of the chip. The device consists of three layers, all of them having different thicknesses: the substrate, the channels and finally the cover. Aside from the channel layer which is made by acrylic and poly(methyl methacrylate), the other ones can be made entirely in PMMA, glass or a hybrid between them.

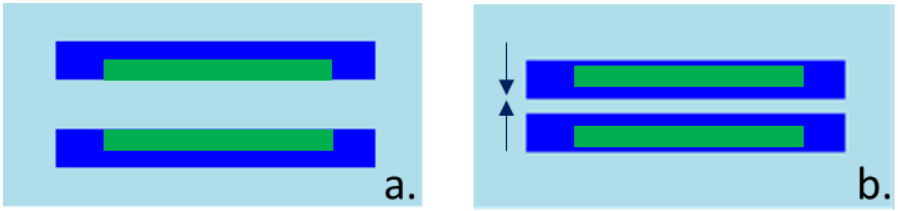

*Figure 44 Schematic representations of the top view of the chip to highlight the importance of the distance between the channels. The green areas represent the beams spots. In the beams touch the edges of the channels, while in **b**, the beams are perfectly in the middle of the channels.*

The channels have different lengths, widths, but still, they have three inlets per channel, because that characteristic allow us to fill them with different gels. A longer length of the channels consents to have more surface interaction with the light, and so a longer interference pattern, while the width and the distance between the two channels are conceived and realised in a way that the two beams do not interact with the edges of the channels, Figure 44.

5.2.3 Agarose

The other gel that has been tested was agarose gel. This gel is a linear polymer, that dissolve in near boiling temperature, and it gels when is cooled down. The porosity of the gel depends on the agarose concentration. Typically, the concentration of agarose gel is in the range of 0.5% to 2% [241] [312], for protein studies. The agarose gel presents

a better adherence than PAAm a PMMA chip, and in turn the interference pattern is always visible and well defined.

The hydrogel selected for all the following experiments is agarose gel (BioReagent, for molecular biology, low EEO, CAS number 9012-36-6, 10 g, Sigma-Aldrich) (**LM agarose**). The agarose powder is thermally sensitive, so it is possible to dissolve it in water at temperatures over 60 °C (a higher temperature than the LM agarose before mentioned). A 1% (w/v) agarose solution in deionised water is dissolved at 120°C (hotplate value) and stirred on a hotplate in a glass vial. As the powder is completely dissolved, the temperature is set on 60°C. At that point, the agarose solution is kept at 60 °C. At that temperature, the solution can be pipetted and used to fill the channel of the chip, in the way to obtain a junction or a plug gel.

5.2.4 Why agarose gel

By observing the interference patterns of the previous gels, it appears clear how the agarose gel gives the most definitive one, and the reproducibility is better than the other gels. Furthermore, the agarose allows to use a PMMA chip, which is easier to handle and make, rather than a glass chip. Besides, for the electrophoresis purpose, a plastic cover is easier to cut to produce the reservoirs for the solution and create a small volume that can contain the solutions. While for the glass, it has been impossible to cut four small circumferences with a diameter of 2 mm each. In conclusion, the agarose was the hydrogel selected mainly for the reproducibility of a good interference pattern of a plastic chip filled with this gel. Since this project was in the initial steps, it was important to characterise the interferometer-electrokinetic system with a hydrogel that was easy and fast to make, so that more experiments were possible to undertake for the characterisation of the system.

5.3 Electrophoresis buffers system and methodology

As it has been stated in chapter 3, the protein charge depends on the solution environment. As the method to drive the analytes inside the gel is the electrokinetic injection, it is important to remember that all the proteins are amphoteric compounds, and so their charge is influenced by the surrounding environment. The isoelectric point (**pI**) defines the pH value at which the protein has a neutral charge. For pHs above the

value, the protein has a negative charge, while if the pH environment is below the isoelectric point, the protein has a positive charge (Figure 45). For example, the **pI** of BSA is 4.7- 5.5 [313], so that means that for pHs higher than 6.0 the analyte has negative charge and, in turn, the movement will be directed from the cathode toward the anode. In contrast, the direction is from the anode to the cathode, when the environment is acidic with a pH lower than 5.2.

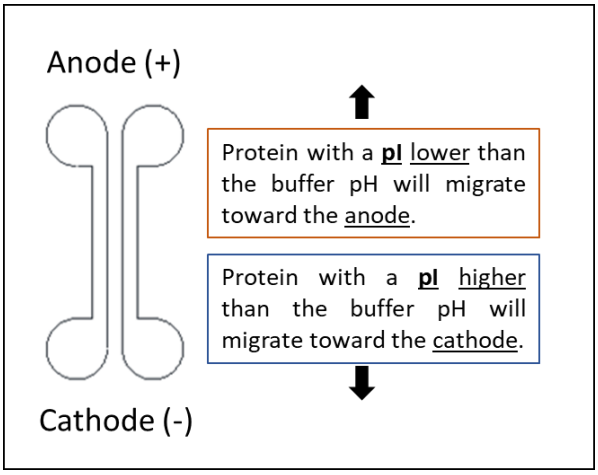

Figure 45 Schematic representation of migration of charged proteins in the chip.

Furthermore, no reducing agents, such as sodium dodecyl sulphate (SDS), are being adopted to conserve the integrity of the analyte. A wash is executed in the followed way. After the channels of the chip are filled with the preferred gels, the chip is mounted in the instrument and the electrodes are fixed. In turn, each reservoir is filled with 40 µl of 10 mM buffered solution at the pH selected for the experiment. At this point, the voltage is applied for 20 minutes. This is the maximum time for which, by applying a voltage of 10/15V in both channels, the buffer can maintain the same pH, or, at least, to not show opposite behaviours, such as move in the opposite direction. The causes for a variation in the buffer and analyte mobilities can be various and all of them must be considered and controlled. Firstly, the power supplies used in this project (PS350, Stanford Research Systems, California, USA) holds the voltage on the set value, but the electric resistance of the total circuit change during the run, due to decreasing of the buffer resistance caused by Joule heating [164]. Secondly, the electrolysis of the water generates OH^- ions at the cathode, and H^+ ions at the anode, causes an alteration in the pH [164]. Consequently, every 20 minutes the voltage is turned off to exchange the buffer in the reservoirs with fresh ones, and eventually a second wash can be performed. So, by

turning off at maximum 20 minutes will also reduce the side effect of the heating, such as damage in the gel structure. In paragraph 5.3.5 further information will be presented.

5.3.1 Voltage and porosity

The *electrophoresis* is an analytical technique in which charged particles migrate under the presence of an external electrical field immersed in a medium in such a way that the positive and the negative carriers will be separated in two different areas [163]. The velocity depends not only on the mass of the molecule, but also on the electrophoretic mobility, which describes the tendency of a molecule to move under the influence of an electrical field. The medium features (porosity, viscosity, etc.) add other factors, such as ion exchange with charged groups or adsorption effect, which may influence the quality and the velocity of the separation.

5.3.2 Instrumental set-up

Generally, a capillary electrophoresis system is composed with a high-voltage power supply, reservoirs filled with buffer and sample solution, a fused silica capillary tube, a detector, and finally an output reading device. The capillary is the connection between the two reservoirs. In those reservoirs, an electrode is immersed, and is connected to one of the two polarities (positive and negative) of the high voltage power supply. By applying a constant voltage between the two electrodes, the induced electric field triggers the migration of the sample through the capillary. The detection is usually performed through a UV-Vis absorbance spectrum detection through the capillary, or fluorescence detection, or via mass spectrometry. Our system differs in some aspect from the typical set-up just described. In Figure 46a and Figure 46.b, it is possible to appreciate the length and width of the channel, which is shorter and wider than a capillary. The chip is made of PMMA, and not silica. The stainless-steel electrodes have been utilised since the material is resistant to a various aggressive chemical reagents [314], and it is cheap. The electrodes are obtained by laser cutting a stainless-steel sheet.

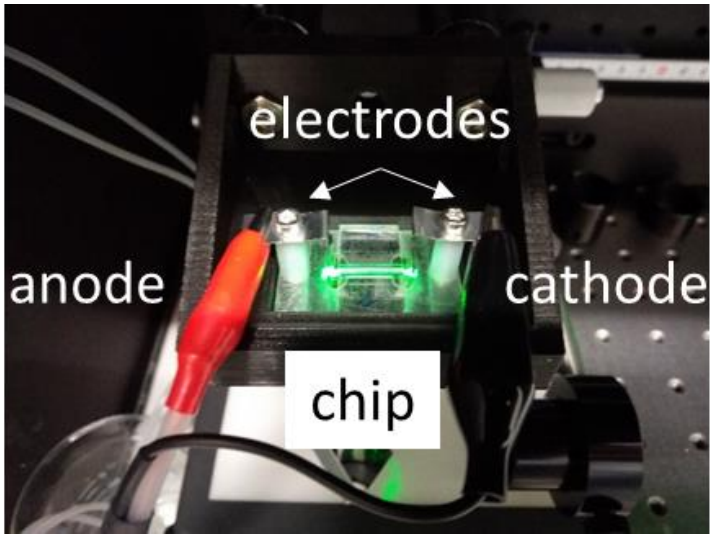

a.

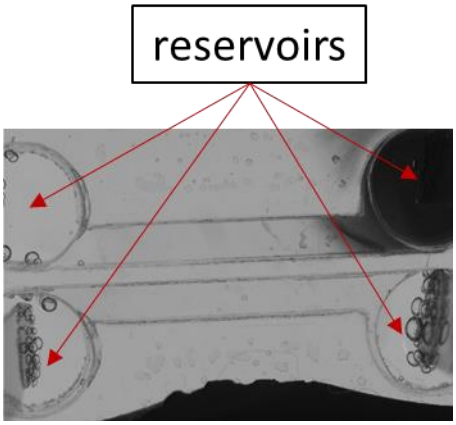

b.

*Figure 46 Microfluidic chip with the electrodes attached and laser beams going through the channels **(a)**. And an image from the top of the chip, to visualise with a camera the movement of solution with dye (black) inside the channels filled with agarose gel **(b)**.*

Finally, the most diverse aspect is the detection method. For initial investigation a colour camera and after that the interferometer have been used. The volume of each reservoir is 40 μl. The acquisition of the analyte movement has been performed in two ways: by calculating the phase difference (PD) from the interference pattern, and by recording a colour image, where thanks to the use of pH sensitive dye, the analyte and different solutions can be distinguished by their different colours. In fact, in Figure 46.b the dye solution is black, whereas the channels filled with agarose gel appear grey. The electro-kinetic system previously described is the one that has been used through all the experiments in this project. Any variation from that will be reported.

5.3.3 Data acquisition and representation (counter plot)

The unit of measurement acquired by the interferometric sensor is the Phase Difference (PD). Through an algorithm, based on Fast Fourier Transform (FFT) and developed in C++, the changes in the interferogram are analysed and transformed into PD variations in real-time. Once the PD values for each area file is recorded, the information is represented in a counter plot where the PD variations (in colour scale) is shown not only as the time of the measurement progresses, but also as the analytes within the channel (spatial information). This is possible thanks to the translation of the interferogram to length representation of the zone of the channel. The variation of PD represents a variation of the refractive index, which in turn, due to a variation of the analyte concentration, as the last increases, also the other parameters increase proportionally.

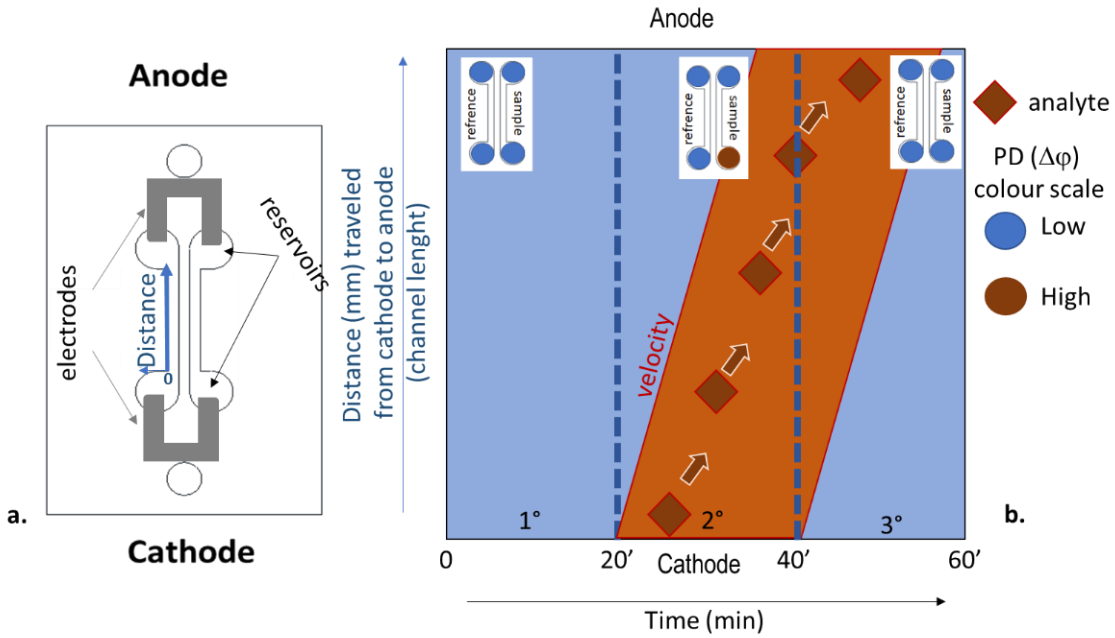

*Figure 47 Schematic representation of channel configuration (it is indicated the axis for the distance) (a) and of the counter plot of the phase difference (b) **distance vs. time**, highlighting the three main steps of the measurement.*

To better interpret the contour plots in two dimensions in the following paragraph, it seems important to explain the counter plot representation step by step by showing a schematic and general plot. The experimental counter plot has been created by using SigmaPlot. The contour plot of the PD in Figure 47.b is a distance vs. time graph, where the colour scale represents the PD value. In the figure 47only two colours are reported, while for the experimental measurements a "rainbow" scale is adopted, where blue is

the lowest value and red the highest ones. The target analyte reported in the schematic plot has a negative charge in the buffer system (the movement is from cathode to anode). In general, in counter plots it is possible to identify three experimental steps.

1° In the first 20 minutes (maximum), buffer is driven in both channels. The PD is low (blue) as there is no difference in solution composition in the two channels.

2° At the 20th minute, the voltage is turned off to change the reservoirs solutions with fresh one. In particular, the sample channel reservoir is filled with analyte solution. This operation usually required two minutes. The voltage is turned on for a further 20 minutes. As the analyte solution travels inside the channel, the PD increases (amber) since the analyte concentration causes a difference of refractive index between the two channels. The average time of the analytes to move from one electrode to the other one is 10 minutes with the voltage used in this project.

3° At the 40th minutes, the voltage is turned off again. All the solutions in the reservoirs are changed with a fresh buffered solution. The voltage is turned on again for last time to wash the sample channel. As the buffer is moving in, the PD returns to its low value, as the analyte is completely removed, and it reaches the other side of the channel.

5.3.4 Data experiments

To test the influence of the voltage on the analyte mobility in 1% (w/v) agarose gel, three different voltages, 10, 20, 30V has been investigated. In this paragraph, the data reported represent the PD variation recorded from the interference pattern.

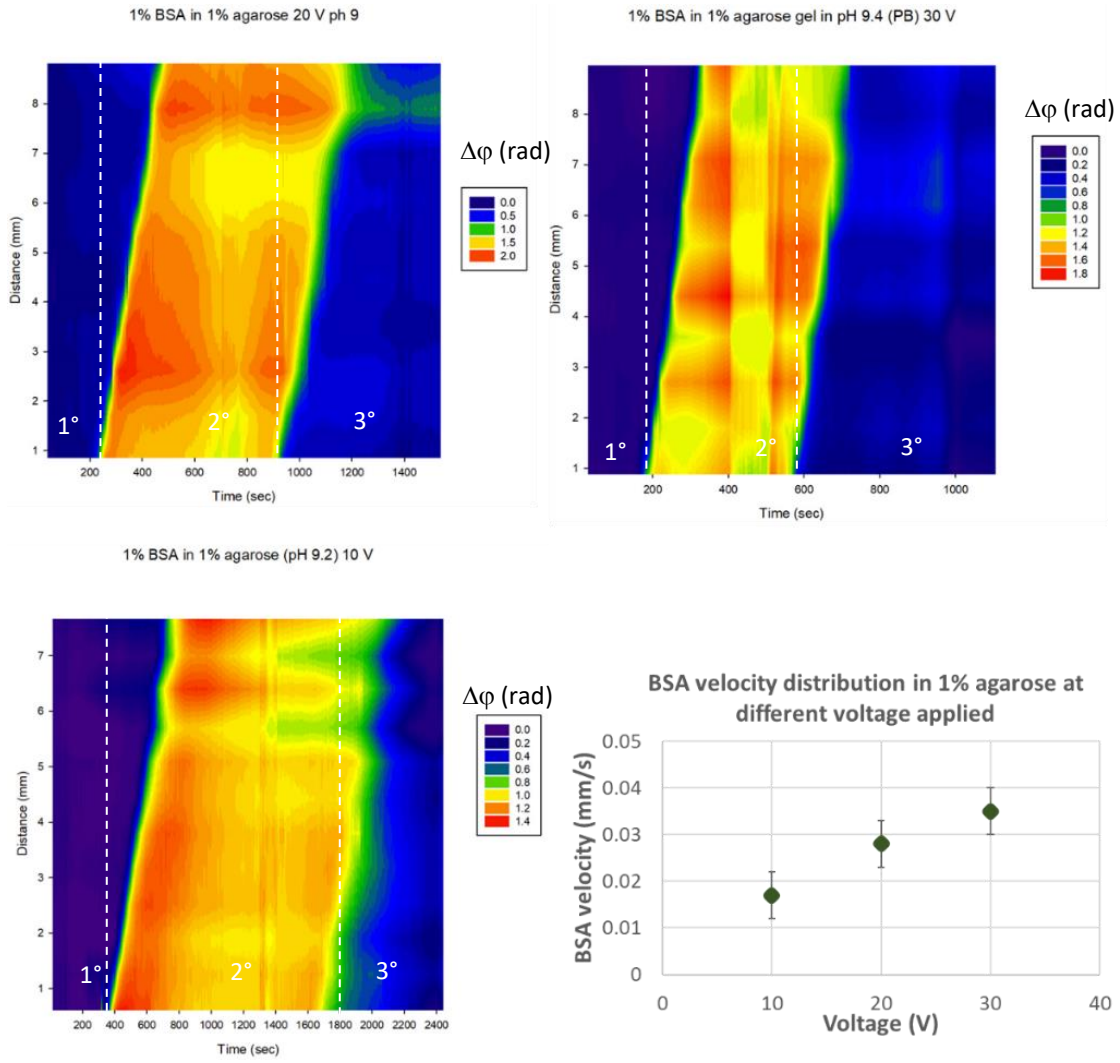

Figure 48 BSA velocity. Counter plot distance versus time for three voltages (20, 30, 10 V) and velocity distribution.

The analyte used is bovine serum albumin (BSA) from Sigma-Aldrich (A215-10g, lyophilized powder, ≥ 96%), and the concentration used was 1% (w/V, 15 μM). The velocity graph in figure 47, was extrapolated by analysing the data in the three counter plots reported in the same figure; by knowing the time required to the analyte to a known distance, the velocity was calculated.

To investigate how the porosity influences the analyte velocity, other two agarose concentration have been tested, 2% and 0.5% reported in Figure 49. As with the case before, 1% BSA has been used as the analyte solution and the 10 V was applied in all cases. From the velocity graph, reported in the same figure, it is possible to observe that, by applying the same voltage, 10 V, the BSA was slower in 2% agarose gel rather than

0.5% agarose gel. The data illustrated in this paragraph have been used as initial study for testing the interferometer sensor integrated with the electro-drive system.

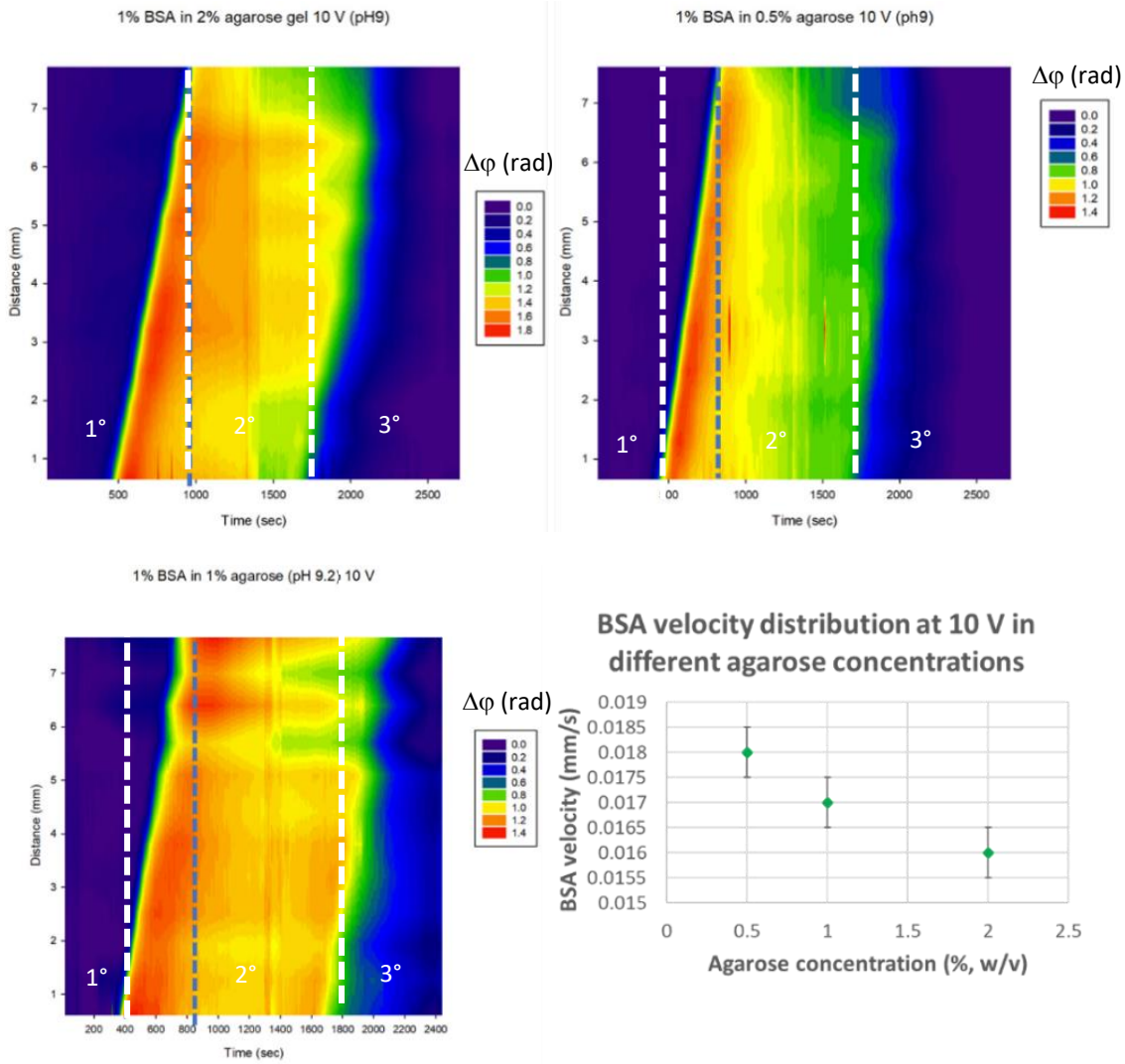

Figure 49 Phase difference values in counter plot distance vs time of 1% BSA in two agarose concentration 2%, 1%, and 0.5%. The dashed lines identify the time when the BSA has been arrived at the opposite site. The time is higher for 2% than 0.5%.

The data helped to better interpretate the distance vs time plot extrapolated, such as how to choose the better colour scale for the PD values. The data on the gel porosity have confirmed that the movement of an analyte, such as BSA, will strongly depends by the gel environment, such as its porosity. A higher agarose concentration means smaller porous through which the analyte is slower compared to a gel with an agarose percentage smaller.

5.3.5 Discussion

Different voltages have been tested not only to verify the different velocity on the analyte (BSA), but also to study some other aspects, such as how long it is possible to apply the same voltage and not observe any effects in the phase difference (PD) detection (due the electrolysis of water in the reservoirs). In other words, which were the electric limitations of the system agarose gel and buffers.

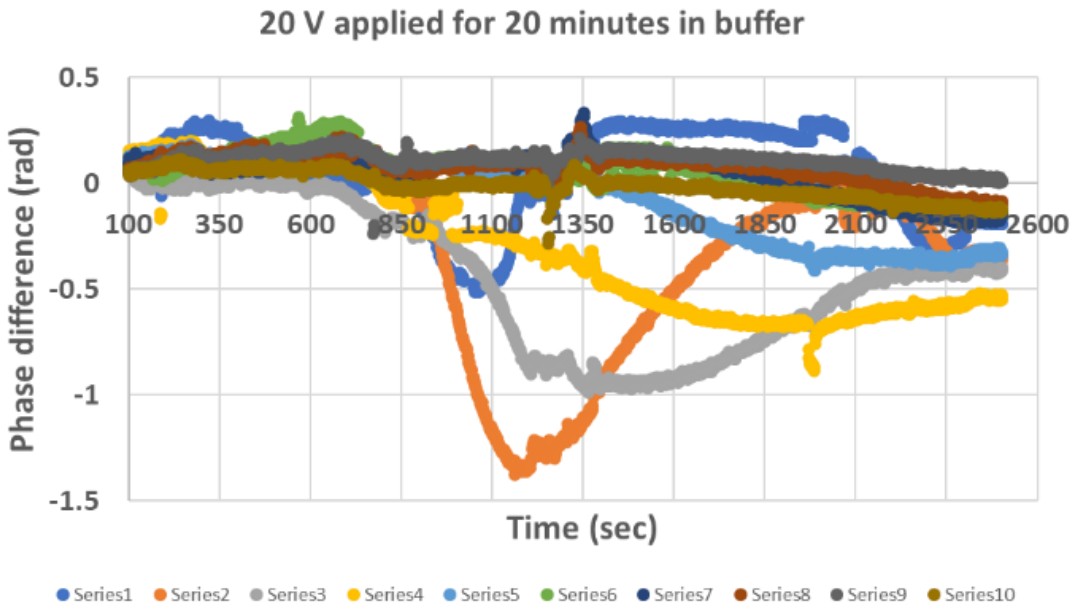

Figure 50 PD values at difference position in the channel, for buffer applied in 1% agarose gel at 20 V for 20 minutes (1200 seconds). Around 850 sec, in some position the PD assumes values quite far from 0 radians.

It was observed that for 10/15 V applied in our system, 20 minutes (1200 seconds) is the maximum time, as Figure 52 illustrates. Around that time interval the PD values start to change drastically. On the other hands, for a 30 V the maximum time was 5 minutes (300 seconds, Figure 51), and 14 minutes (≅ 800 seconds, Figure 50). As it can be possible to observe in both figures 50 and 51 after the maximum time of the voltage application, the PDs of diverse channel areas (the series of colour reported) were not homogeneous, and a lot of jumps are visible in the graph reported. In more particular in figure 50, the PD acquired in the orange box (series 2) is far different from the brown one (series 10).

In other words, for those three voltages a maximum time in which the voltage can be applied continuously was set; after that time interval the PD will suffer noise due some external stimuli, such as Joule effect or fragility of the gel.

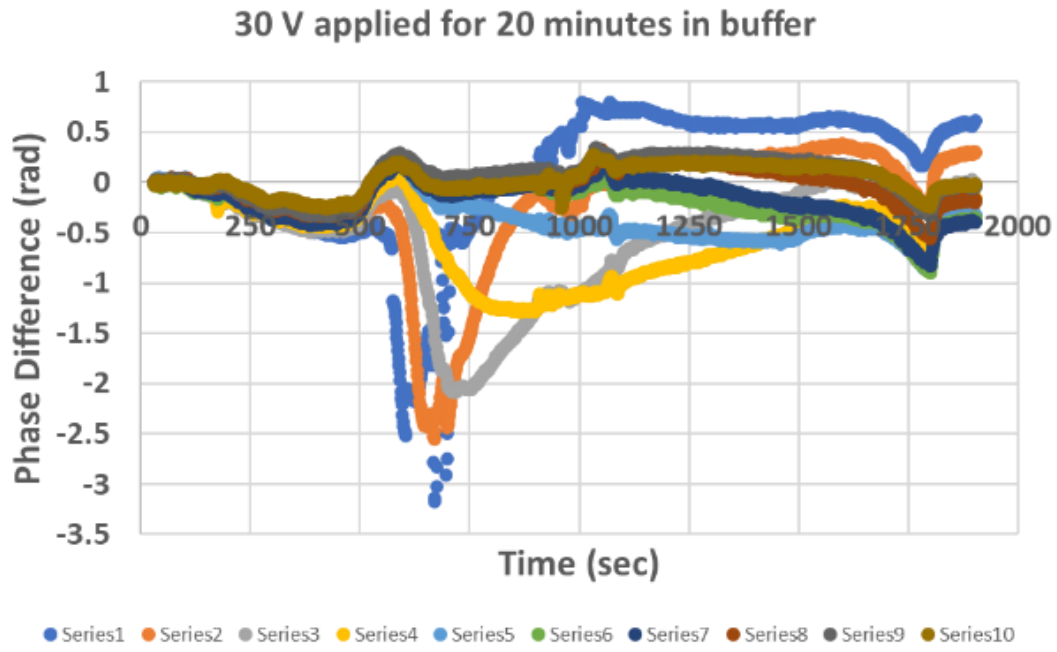

Figure 51 PD values at difference position in the channel, for buffer applied in 1% agarose gel at 30 V for 20 minutes (1200 seconds). Around 600 sec, in some position the PD assumes values quite far from 0 radians.

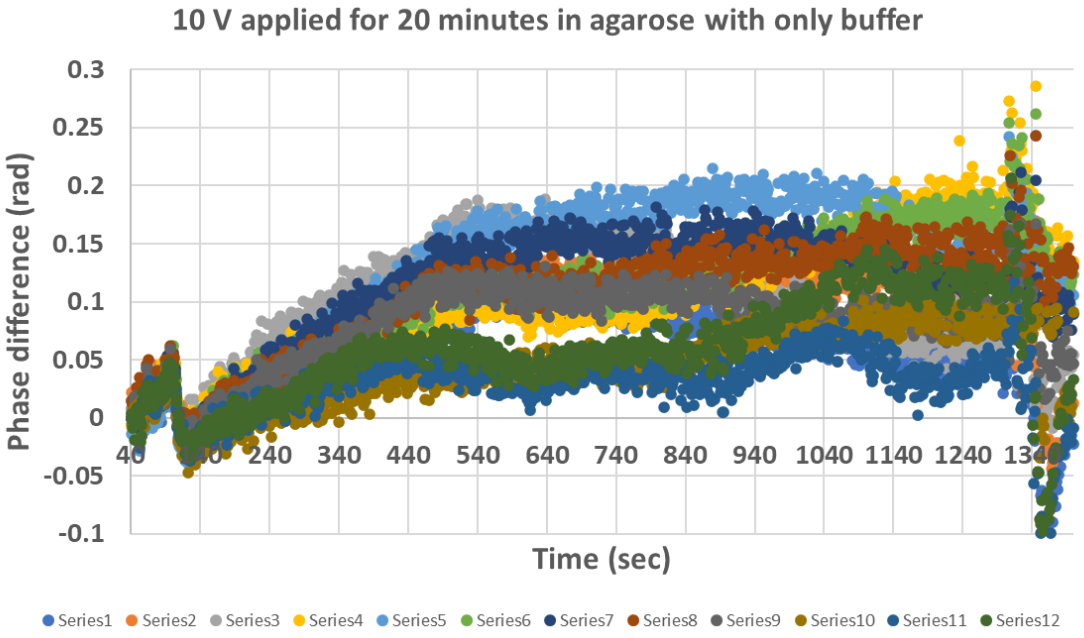

Figure 52 PD values at difference position in the channel, for buffer applied in 1% agarose gel at 10 V for 20 minutes. For all the experiment the PD keep the same value 0.12±0.05 radians.

In conclusion it was preferred to use a voltage below 20 V due the longer time available to acquire the data, in a way that the software could be assisted in the phase difference acquisition.

For this project, the buffers study was addressed on obtain a focusing and a reasonable movement of the analyte. The only instruments used for this study were the interferometer and a colour camera, other types of instrumentations were not used, such as a pH control during or after the experiments, or an electropherogram or other more specific technique generally used electrophoresis. Consequently, a deepening on the buffers system should be considered for reducing noise on the measurement and improve the results.

5.4 pH junction

Subsequently to the electric characterisation of agarose gel and PBS, we move forward to establish the protocol to follow to allow analyte focusing on the middle region of the sample channel. As reference, works on dynamic pH junction ([308],[198], [315]) were studied in a way to translate their conditions in our setup.

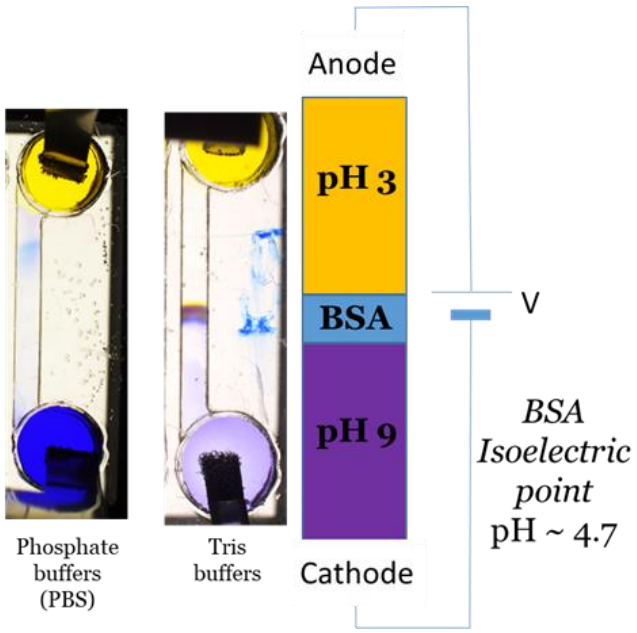

Figure 53 Experimental BSA focusing on a pH junction made with PBS and TRIs buffers. A schematic representation of the pH junction is also reported. The BSA has a blue colour, while acid buffer is yellow, and basic buffer is purple.

This is a technique that is mainly performed in a capillary as a pre-concentration method on a wide range of analytes [209]. It has been described in paragraph 3.2.3 “pH

junction". The technique has been reported for the first time by Aebersold and Morrison in 1990 [202], but the name has been created by Britz-McKibbin and Chen in 2000. They have found that for different analytes the condition of the buffers were different, in particular, they suggest that the pH of the buffer should be selected from a range in which the mobility of the analyte will change more rapidly [316].

Nevertheless, this and their next papers were more experimental with lacking a solid theoretical explanation of the phenomenon. There have been through the years numerous mentions of explanation of the mechanism; in common all of them assert a sophisticated balance of diverse parameters [308].

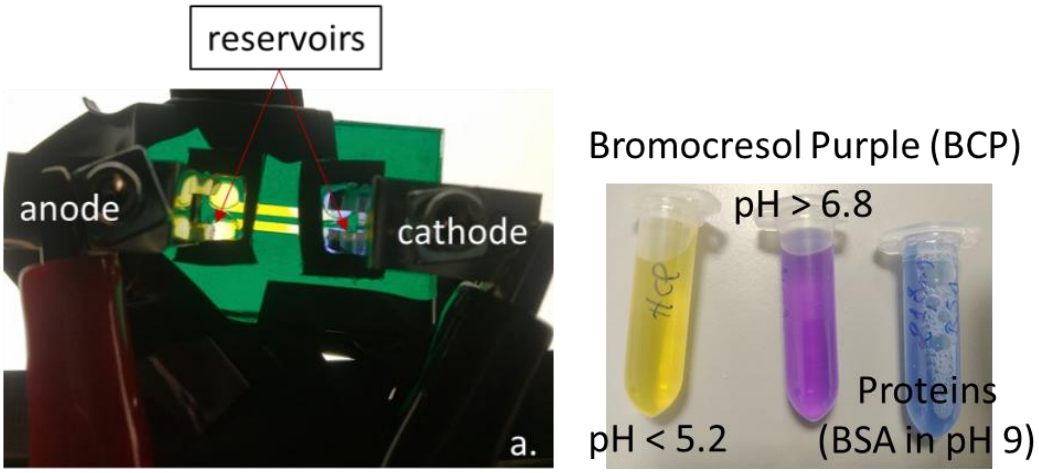

Figure 54 Apparatus to create a pH junction with the use of a pH sensitive dye (a). In b, the colours, due to the BCP dye, represent the basic (purple), acidic (yellow) pH, and the presence of 1% or more BSA in basic solution (blue).

As a proof of the wide conditions used in the literature [317], it is very rare find in it any theoretical explanation of this method [318], Cao with his group has been one of the few that has presented a theoretical explanation on the pH stacking technique [319]. Briefly, the sample solution is introduced in the capillary filled with buffer, called Background electrolyte (BGE), by electrophoresis. As the sample solution moves, it is followed by another buffer, different from BGE, and in turn the analyte is focused at the boundary as the voltage is applied [320]. The focusing is resulting at the interfaces of the two buffers, where the analyte has also a diverse mobility, so that it results in "immobilisation" [301]. A schematic representation of the phenomenon is shown in Figure 53. In the case of the project proposed, the main difference between two buffers

is their pH, chose in a way that the protein (the analyte) has different mobility in them. The sample volume is in most cases not reported, but the volume seems to range from μl to ml [315]. As with any other techniques, the pH junction has some drawbacks, one of which is a low reproducibility factor [306], due to problems that can be various (integrity of capillary, electrolysis, etc.). The detector is usually focus on a very narrow region of the capillary, that is able to acquire any variation, but the short analysing region can be too small for detecting very small concentration [320]. Besides, in the literature it was impossible to find an example of the pH junction performed in a complete hydrogel environment. In most of the cases, a polyacrylamide thin layer is attached to the surface of the capillary or microchannel, to reduce the electroendosmosis effects of the electrophoresis, or the gel has been used as plug that acts as a physical barrier and so it is used for size-exclusion of the molecules [252, 315]. It follows that it was not so straightforward to reproduce the pH junction in our system.

In summary, this electrophoresis technique creates a pH junction by filling the anode reservoir with an acidic solution, whereas the cathode is filled with the alkaline solution. A constant voltage is applied, by connecting the anode to the positive and the cathode to the negative. As the voltage is applied, the charges will start to migrate to the electrode with opposite charge, in a way that in the channel the opposite charge will collide and create a pH junction in the gel. In all the experiments stainless-steel electrode have been adopted. To find out the right conditions of the buffer to create a pH junction, a colour camera, and a colour pH sensitive dye, Bromocresol Purple (BCP) (Sigma-Aldrich, B5880-5g), have been used in parallel to the interferometer, Figure 54. This was a qualitative technique used only to find the right condition of making a pH junction inside the channel. The dye exhibits a yellow colour for pHs lower than 5.2, whereas is purple for pHs above 6.8. An aspect of this dye is that for proteins concentration higher than 1% (w/v) it shows a blue colour [321], as it is visible in Figure 54. Consequently, in pH junction experiments with the colour camera, the blue colour has been interpreted as where the analyte is present.

5.4.1 HCl-NaOH junction

5.4.1.1 Materials

As a first approach to create a pH junction in the channel filled with agarose gel, hydrochloric acid (HCl) and Sodium hydroxide (NaOH) have been selected. The method has been successfully used by Goddard N. et al [322], who have obtained three order of magnitude of protein preconcentration by integrate electrokinetic preconcentration with a HCl-NaOH junction. The main idea was to fill the anode reservoirs with HCl solution (1, 10 and 100 mM), whereas the cathode reservoirs were filled with NaOH solution (1, 10, 100 mM). The difference is due to the diverse RI (the RI between air and the hydrogel is bigger than between water and the hydrogel) in the two areas of the sample channel.

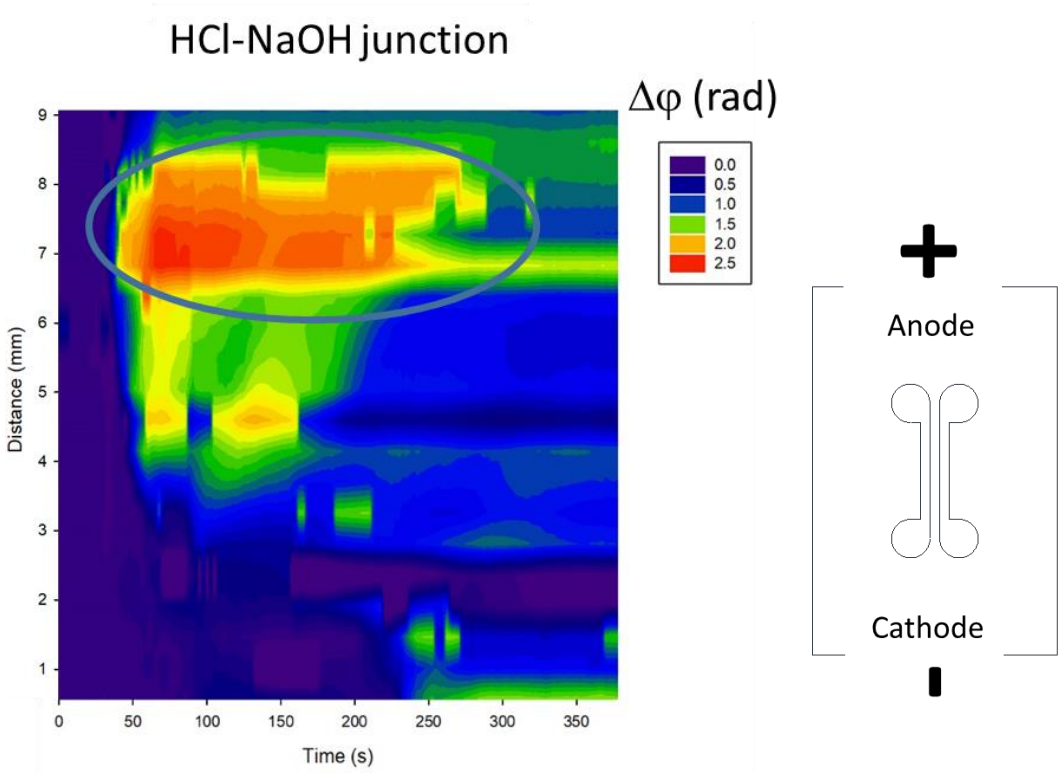

Figure 55 How the PD changes at different regions of the interference pattern along the time of the measurement.

The only successful experiment of focusing BSA in a pH junction in agarose gel is presented in Figure 55. In that plot, the PD changes (in colours scale from 0 to 2.5 rad) along the time (x axis) when a voltage of 60 V is applied around 60 s and is switched off around 290 seconds. On the *y* axis is presented the 20 regions that divide the

interference pattern, translated in length of the channel (distance). The change of the PD is at its maximum at 7 mm distance from cathode for each time interval that the voltage is applied, highlighted by the blue ellipse. This figure represents again a qualitative behaviour of the protein movements in presence of a pH junction made by filling the cathode reservoir with 1 mM solution of hydrochloric acid and the anode with 1 mM of sodium hydroxide for the reference channels. For the sample channel BSA was added to the same solutions at a concentration of 1 mg/ml. This method to create a pH junction with NaOH and HCl was very difficult to achieve. It was not possible to have a clear focusing of the analyte, neither with the interferometer and nor with the camera. For this reason, a second approach has been attempted.

5.4.2 PBS junction

5.4.2.1 Materials

The second approach was to utilise different pHs of Phosphate Buffered Solutions (PBS) at different concentrations, as this system is one of the most used in the literature to create a pH junction. As in the previous method, the anode reservoir was filled with a pH 3.20 solution, whereas the cathode reservoir was filled with either pH 9.2 or near-neutral pH (pH 7.2) solution.

Table 6 Composition of the PBS buffered for the pHs used in the experiments. The composition refers to 100 ml solution of 100 mM strength.

Compound	pH 3.2	pH 5.5	pH 7.2	pH 9.2
NaH_2PO_4	1.37 g	1.57 g	700 mg	11 mg
Na_2HPO_4	0.3 mg	36 mg	1.55 g	2.66 g
Na_3PO_4	/	/	/	2 mg

Additionally, the agarose gel was prepared at four different pHs: pH 3.20, pH 5.5, pH 7.2, and pH 9.2. Furthermore, combinations of different pH strengths have been tested. PBS at four different pHs have been prepared by dissolving the defined amount of Sodium

phosphate monobasic dihydrate (**NaH_2PO_4**, Sigma-Aldrich, BioUltra, for molecular biology, ≥99.0% (T), 71505-250g), Sodium Phosphate dibasic heptahydrate (**Na_2HPO_4**, Sigma-Aldrich, ACS reagent, 98.0-102.0%, S9390-500g) and Sodium Phosphate Tribasic dodecahydrate extra pure (**Na_3PO_4**, Acros Organics, 450660010, 1 kg). The colour camera was used here as qualitative method necessary to find the right conditions for the creation of a pH-junction within the gel (type and strength of the buffer, pHs, etc.).

5.4.2.2 Data

In the following images, it is possible to observe some of the successful BSA focusing with the colour camera. As stated before, for concentration higher than 1% the BSA solution resulted in a blue colour, whereas for acidic conditions the buffer is yellow and for alkaline conditions the buffer colour is purple. The matrix was made of low melting point agarose (LM agarose) (Invitrogen™ UltraPure™ Low Melting Point Agarose) 1% (w/v) concentration.

Figure 56 PBS junction. agarose in pH 3. The BSA focusing is visible in one channel.

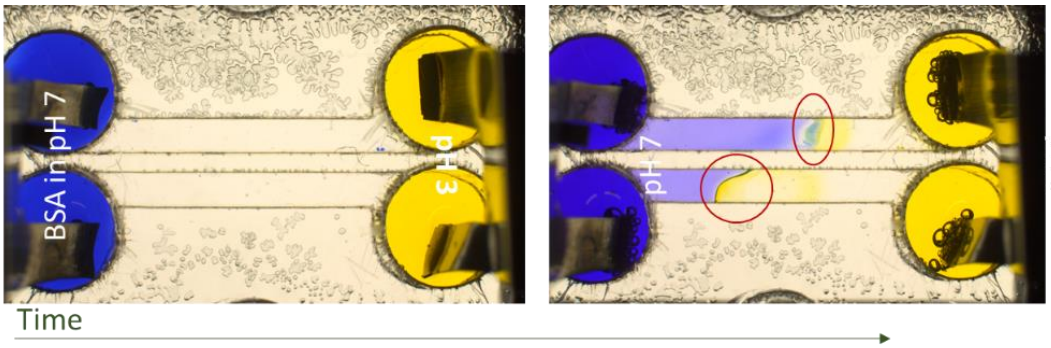

Figure 57 PBS junction. agarose in pH 3. The BSA focusing is visible in both channels.

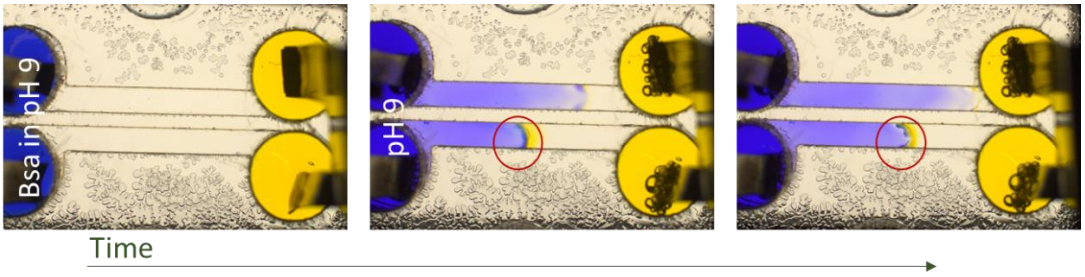

Figure 58 PBS junction. agarose in pH 5. The BSA focusing is visible in one channel

In all the images (Figure 56, Figure 57, Figure 58), it is possible to observe a narrow blue line, highlighted by a red circle, between the regions purple, and yellow, the pH junction. As stated before, the BCP dye is blue when the analyte is present in the solution, so it is possible to state that the blue line is where the BSA has been focused. The focusing was only visible for a range of time between of 2-20 seconds. An important factor was to determine the right condition for the agarose gel. To have a more defined profile for the BSA section, the best results were obtained by preparing the agarose in a pH 5.3 buffer, 10 mM strength, and in 1 mM NaCl solution, while 100 mM strength of pH 3.2 at the anode reservoirs, and 10 mM strength of pH 9.2 and pH 7.2 in the cathode reservoirs and dissolving the BSA in the same alkaline buffer. One last aspect that has been studied was to define the right method and voltage applied to obtain the focusing.

The method extrapolated from all the attempts is the following. The anode was filled with 100 mM PBS pH 3.2, while the cathode reservoir was filled with a BSA solution, containing 10 mM PBS solution (pH 7.2 or pH 9.4 buffer). Then, 20/30 V was applied for 15/20 seconds, then the BSA was removed and substituted with fresh alkaline PBS buffer (10 mM strength). In turn, the same voltage as before was applied for 10 minutes.

5.4.3 Discussion on the pH junction results

The PBS method was more reliable than the HCl-NaOH system. The focusing of BSA resulted in a narrower region, but its profile was not always straight during all the focusing process. Another aspect to evaluate was that, even though the voltage is applied by the same electrodes in both channels, the migration of the analytes and the buffer is not the same in both, as it is visible, for example, in Figure 56 and Figure 57. For that reason, for all the next experiments the voltage has been applied only in the sample channel (Figure 59).

The difference in strength between the anode and the cathode buffers, may be due to the fact that in the anode the electrolysis is faster than in the cathode (galvanic corrosion); so, by increasing the anode strength, the pH junction is more controlled. Another aspect observable in the images in the Figure 57 is the profile of the BSA focusing. It is evident that the profile is not in all cases a straight line, or a slight curve. This could be due to the imperfection of the gel in the edges near the reservoirs. In fact, the gel in the reservoirs is removed by using a pipette tip of 10-100 µl. A more reliable technique should be used to obtain a smooth cut in correspondence of the edges of the channels. Furthermore, it is important to consider that the dye could have influenced the migration and separation of the analytes from the pHs. This should be considered for comparison reasons, as in the next paragraph the experiments were performed without dye. In conclusion, the pH junction procedure established by from the experiments, results to be faster and less complicated as for example the case of P. Britz-McKibbin and D. Chen, where the capillary needed an overnight treatment [316]. The sample volume used in the procedure, is smaller or comparable to some other works [256, 323, 324].

5.5 BSA in pH junction

5.5.1 Description and materials

The key part to establish a pH junction was to define the right contribution of the buffer system.

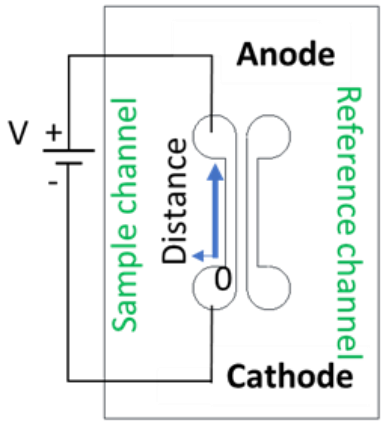

Figure 59 Schematic set-up of the electric circuit. The voltage is applied only in the sample channel.

As stated before, the first buffer system was the PBS, and in Table 6 it is possible to read the composition of all the pHs used in the experiments, for a preparation of 100 ml

solution of 100 mM strength. The experiments were performed by applying the voltage only in the sample channel, as the scheme in Figure 59 shows. From the literature [208], it is evident the difficulty is to determine the right composition of the buffers. Typically, the acidic buffer is in a range between 4.0-6.5, whereas the sample and the buffer (called background electrolyte, BGE) is in the range 8.2-10.0 [208]. The following data mainly represent the measurements made with the interferometer. In the graph the Phase Difference values (PD) are reported. It is important to remember that the analyte concentration is proportional to the PD, therefore as the concentration increases, the PD will follow accordingly.

5.5.2 PBS

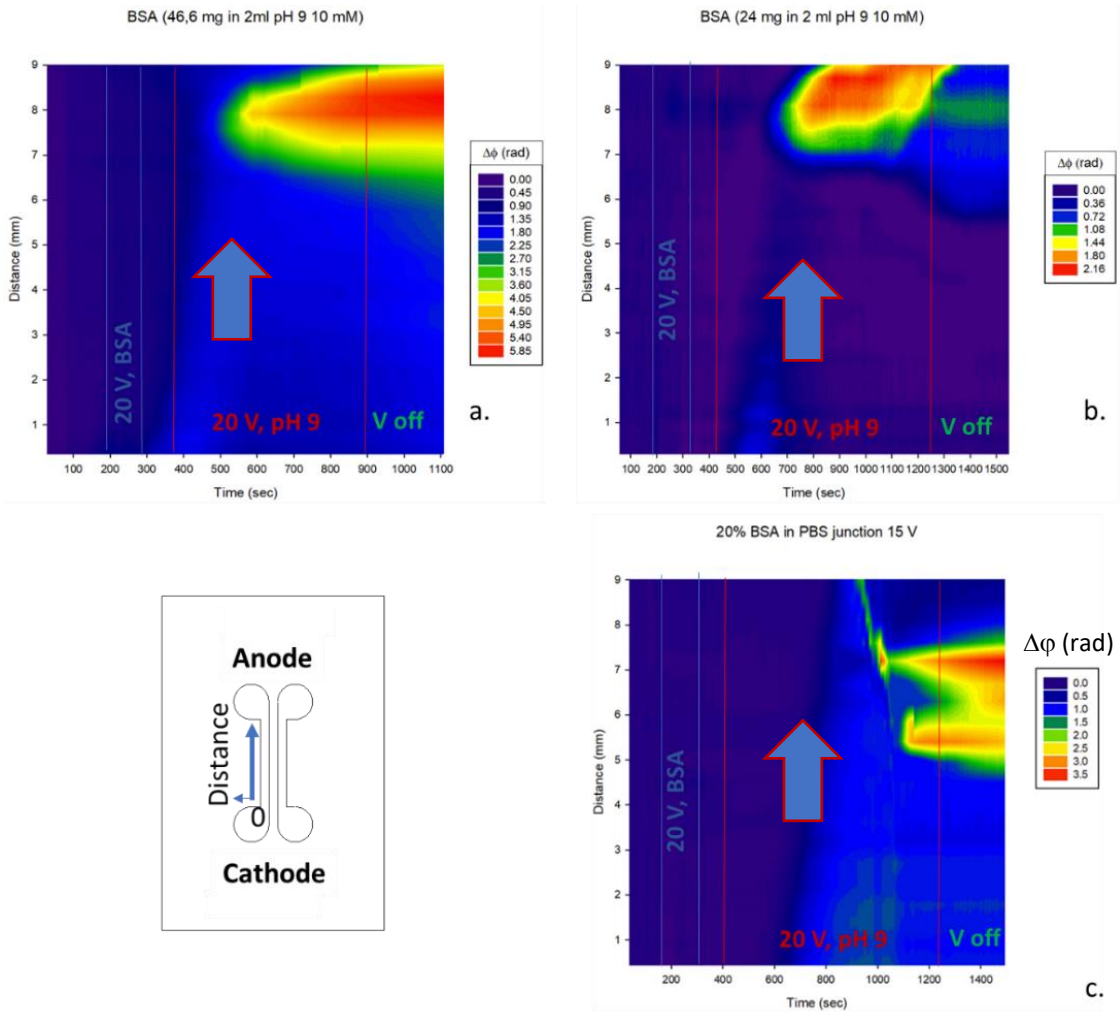

Figure 60 Counter plots of BSA focused on pH junction for three concentrations (w/v): 23% (a), 12% (b), 20% (c).

The data from the interferometer exhibit a good focusing of high BSA concentrations (higher than 10%) (Figure 60) but the same behaviour was not so well observed for lower concentrations. In figure 60 the plots are presented in different PD scale, since here we want to emphasize the focusing of the analyte, since a comparable of the data were not possible. In Figure 61, the focusing of 0.5% BSA is showed for a pH junction. As it is possible to observe, the PD values do not increase, but the BSA movement is visible by the PD value of 0.5 radians circa, which is constant for all the experiment.

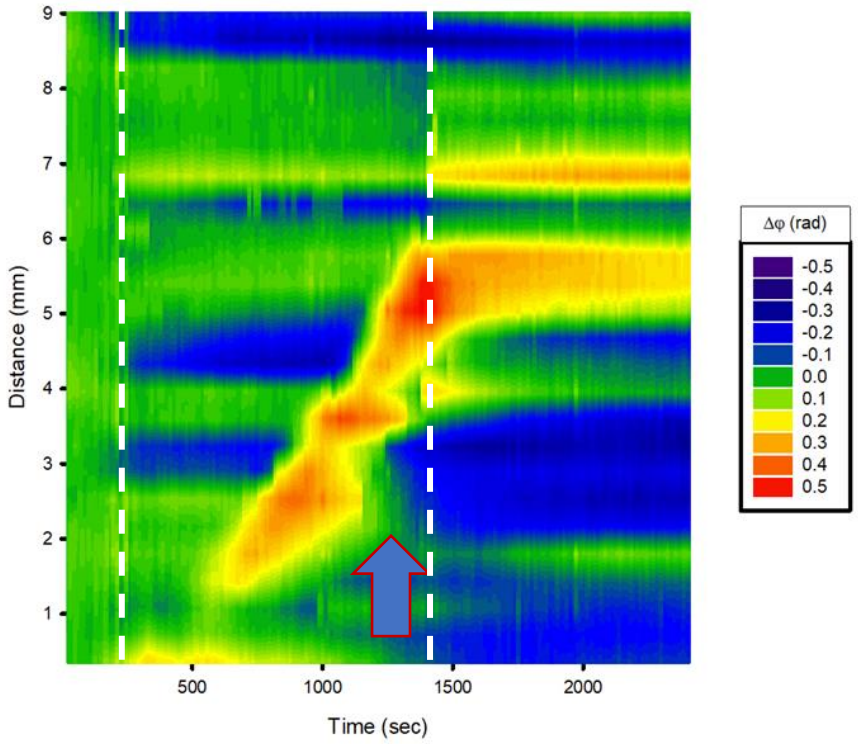

Figure 61 Distance vs time plot of 0.5% BSA in PBS pH junction.

In conclusion, with those experimental conditions it is possible to observe an increasing of the PD value in a small region for high BSA concentrations, but not for smaller concentrations. For this reason, a small modification in agarose gel has been tested.

5.5.2.1 Agarose prepared in pH 5 (10 mM), and NaCl (10 mM) solution

The main difficulty was to reproduce the focusing for BSA concentrations lower than 5%, so an idea was to dissolve the agarose in a solution prepared at pH 5.3 (10 mM, PBS as before) with 10 mM NaCl dissolved. All the other conditions (anode, cathode solutions) were kept the same, so in other words, the Na^+ and Cl^- ions were only present in the agarose gel. In the Figure 62 are reported three counter plots of three BSA

concentrations: 4%, 1%, and 0.4%. For the first two concentrations it is possible to observe an increase in PD value, that can be related to the focusing of the analyte, in the part of the channel nearest the anode. For 4% the PD is 5.7 radians circa, while for 1% the PD is 2.7 radians. To sum up, it is possible to state that by dissolving 10 mM NaCl in the agarose gel it has made it possible to focus smaller BSA concentrations (between 10% and 1%), yet for concentrations smaller than 1% the focusing was still not achieved.

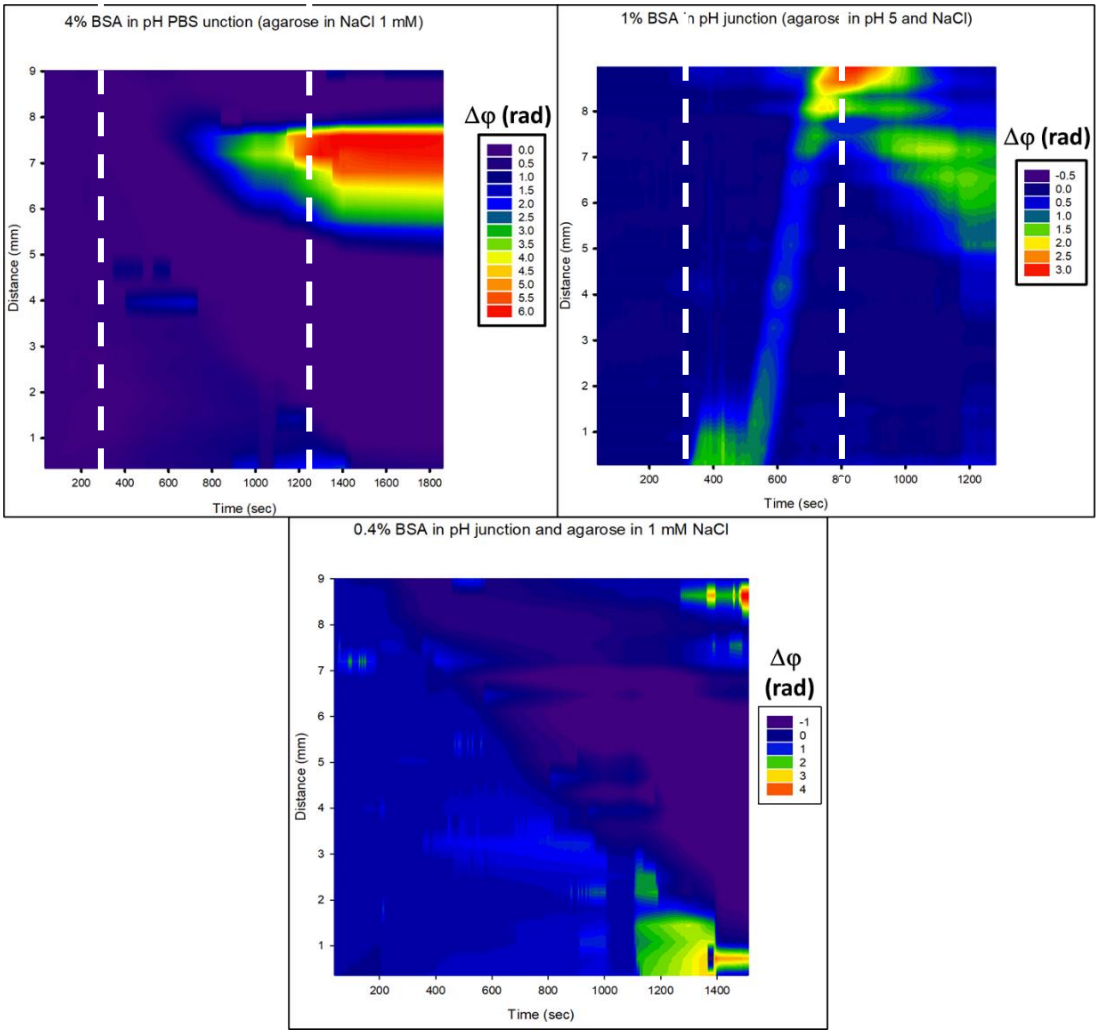

Figure 62 Counter plots of pH junction in PBS, where the agarose gel is prepared in pH 5.3 10 mM, and 10 mM NaCl.

Overall, a new approach was needed to focus lower BSA concentrations. For that reason, a second buffered system, using Tris buffer, has been studied since that has also been used in literature for the pH junction.

5.5.3 Tris junction

As it was difficult to focus a small amount of BSA (lower than 1%) with the pH junction using PBS, the method used for the PBS was applied with the Tris buffer. In Figure 63 it is shown the focusing of the analyte using the colour camera. The pH sensitive compound was the same that was used before.

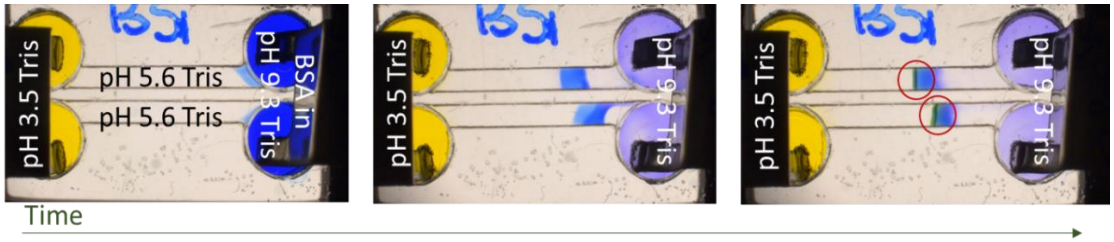

Figure 63 An example with the colour images, how the focusing is happening with Tris buffer system. The red circles represent the regions where the BSA has been focused in both channels.

Principally, this buffer system has been tested with the interferometer for BSA concentration smaller than 1%.

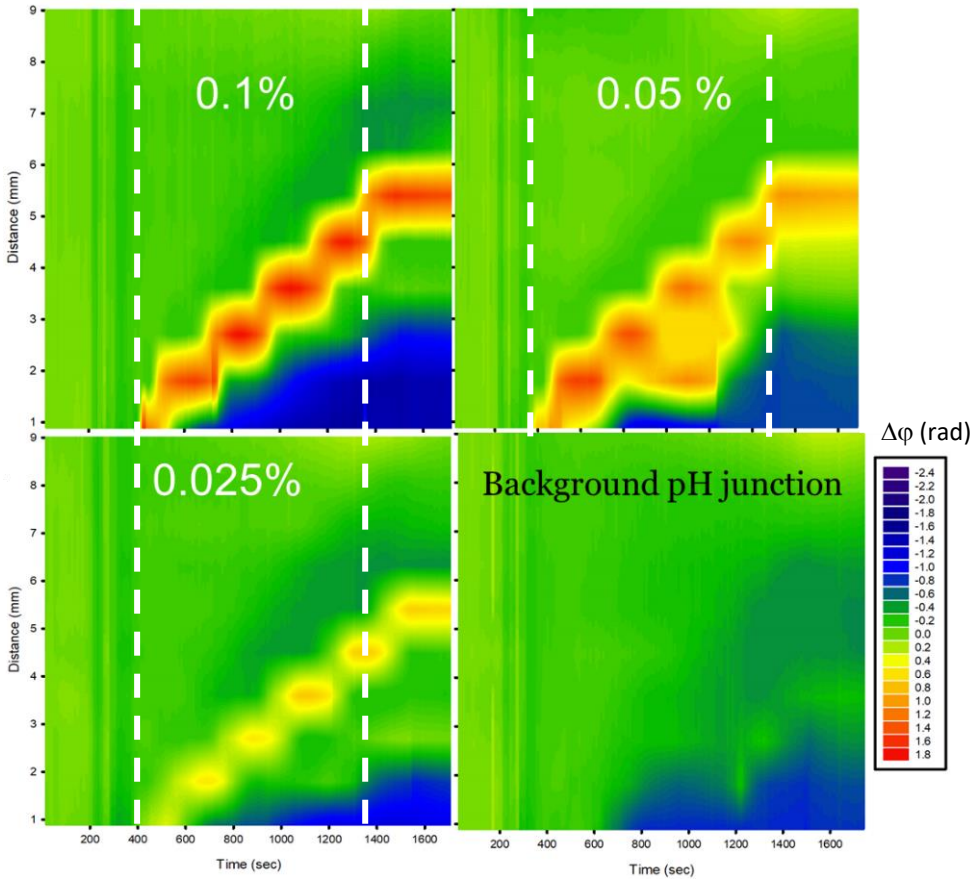

Figure 64 Counter plot of three BSA concentrations in a pH junction Tris buffer, and of the background (due only to the two pHs).

In Figure 64 three counter plots of the PD are shown. They represent the pH junction experiments for three BSA concentrations (0.1%, 0.05%, 0.025%), whereas the fourth plots show the background of the experiment, so the procedure is always in three steps, but in the second one, instead of the analyte solution, pH 9.0 buffer has been used.

5.5.4 Discussion on the BSA focusing by a pH junction

The main difference that seems to characterise the two buffers system is related to the interaction with the analyte, BSA. It seems that the Tris buffer can keep the analyte more contained, so that it is possible to track, not to focus, very small BSA concentrations, such as 0.025%. On the other hand, the pH junction technique seems to work and be more reliable for concentration higher than 10% for both the buffer systems, even though the TRIS buffer pH junction presents a higher reliability. In comparison, the use of NaCl seems to have helped in the focusing technique. The reason could be that Na^+ and Cl^- ions are free to move in the system and could have helped to maintain a more stable electric current, in a way those ions were mainly responsible for the current instead of buffer ions or sample charges.

Regarding the higher consistency of focusing higher analyte concentration (higher than 10%), this could have been justified by thinking that it is easier to maintain close to each other molecules, so that the sample is less prone being “dissolved” by the interaction with the buffers. Even though more than one buffer system has been adopted, it should be pointed out that the choice to not mix different buffer systems was intended to minimise at the starting stage possible artefacts detected by the interferometer. The interferometer is sensitive to every change of refractive index (RI) in the channels, but itself is not specific.

5.6 BSA in one buffer

Another interesting aspect to study is the migration of the analyte from one electrode to the other one through the gel. This was a fundamental aspect that has given the base for the selectivity experiments presented in the sixth chapter. Some of the data and graphs are taken from our paper “*An optofluidic Young interferometer sensor for real-time imaging of refractive index in μTAS applications*” in Sensors and Actuators B:

Chemical journal (2020) [284]. Even in this case, the channel was filled with agarose gel, so the analyte is observed migrating through the gel based on the gel porosity.

5.6.1 Description and chemical materials

The experiments were performed in 1% agarose (LM agarose) gel prepared at the same pH of the BSA solution. BSA and the buffers were prepared as before. The voltage is applied only in the sample channel, while the reference channel is filled with the same agarose prepared for the sample channel. For each sample solution, the measurement was performed as it follows: 10 V was applied for 20 minutes in the channel where the BSA solution had filled one of the reservoirs (anode for pH 3, cathode for pH 9). In turn, fresh buffer was substituted in both the reservoirs and the voltage applied again, as to rinse the agarose gel.

5.6.2 PBS

As it was previously described, for each BSA solutions the phase difference has been measured with the interferometer, as the solution migrates through the gel by electrophoresis. To determine the calibration curve, an average of the PD values in 15 minutes interval has been calculated for each region. The error of each average is the standard deviation.

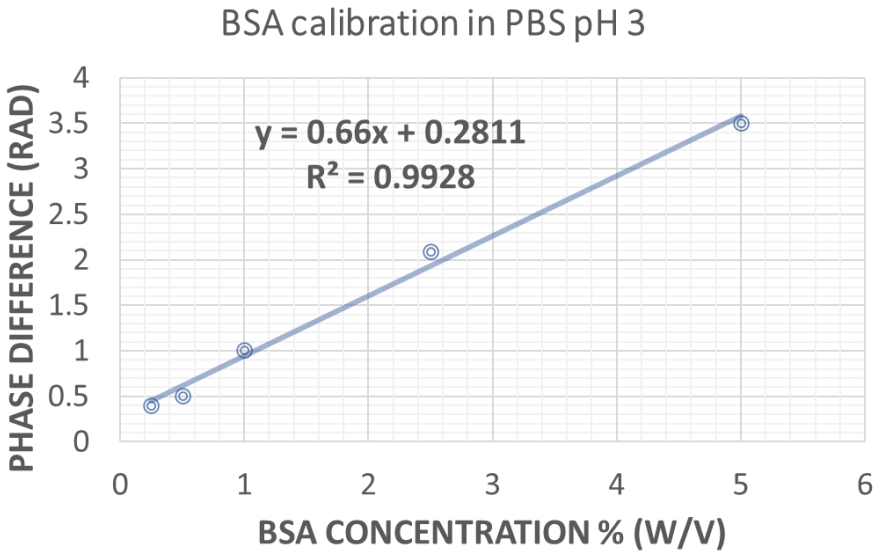

Figure 65 BSA calibration curve in pH 3.2 environment. 10V applied, 10 mM buffer strength.

In both graphs, figure 65 and figure 66, the errors bars are being represented by the diameter since the errors are in the order of 10^{-5} to 10^{-4} radians.

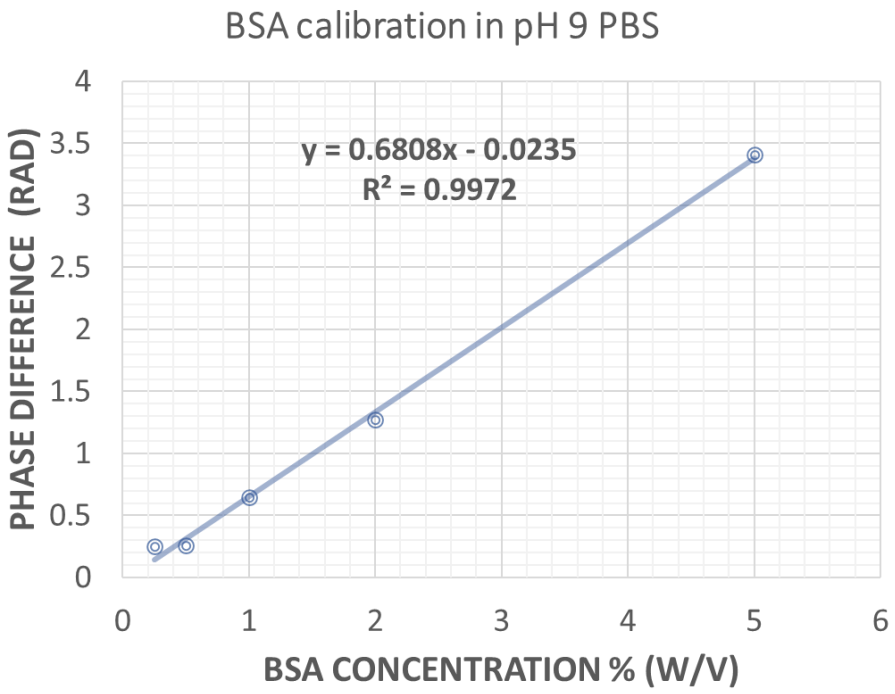

Figure 66 BSA calibration curve in pH 9.2 environment. 10V applied, 10 mM buffer strength.

5.6.3 Tris

More difficult was the calibration of BSA in tris buffer. The interaction between the analyte and the amino groups present in the buffer, may be the cause of the difficulties to drive the analyte through all the channels with consistency. The interaction could cause a setback in the BSA movements, in a way that the analyte seems to not conclude their movement.

5.6.4 Discussion on detection of BSA driven by an electric force

The analyte driving in both environment, acidic and alkaline buffers, has given an understanding of the phase difference linked to the BSA concentration. The two calibration curves of the two pH environments are reported in the graphs in Figure 65 and Figure 66. The calibration of the BSA in the two buffers system has revealed a lower precision than the glycerol measurements illustrated in chapter 4. If the calibration with electrophoresis is compared with the calibration reported in the previous chapter (here

reported again for faster comparison, Figure 31), it should be noted that the calibration curve results to be different, Table 7.

TABLE 7 CALIBRATION CURVES OF BSA IN TWO INSTRUMENT CONFIGURATIONS.

Average calibration between two PBS pHs (Interferometry and Electro-kinetic)	$\Delta\varphi = 0.67c + k_{IE}$	1
Calibration in Interferometry-pump (both channels) (Section 4.3.4)	$\Delta\varphi = 0.55c + k_I$	2

An explanation about this modest difference for the two types of calibration could be due to the diverse procedure. In other words, since in the electric driving, the voltage is applied only in the sample channel, that means that the background due to the buffer is higher than in the case where the solutions are moved in both channels with a pump. Furthermore, as the voltage is applied other ions, other than the analyte or the buffer may be produced, like for example H^+ and OH^- ions from the water electrolysis.

5.7 Comparison between two methods

Both methods, the driving and the focusing of the analyte, have been useful and determinant for the steps in the developing of the biosensor, more specifically for the combination between interferometer and electro-kinetic. While the driving method, illustrate in paragraph 5.6, has supported the determination of the voltage and the buffers properties, the focusing method has also stimulated the studying on the further combination of the interferometer with the electro-kinetic. For example, how to recognise in the counter plot the region where the analyte is focused and how to improve the recognition.

As verification of the focusing (increasing of the PD value for the same BSA concentration), one may think to compare the PD obtained with the driving methods,

with the PD collected with the focusing method. For example, we can start with the PBS. The most successful experiments were the one with agarose gel prepared in a pH 5.3, 1 mM NaCl solution. If the PD values obtained from the plot in Figure 62 for 4% and 1% BSA is compared with the value calculated from the calibration curve, equation 1 (from Figure 65 and Figure 66), than it is possible to see an increasing of the PD value for the same concentration. In a way more convincing, for 4% BSA the PD value from the calibration curve is 2.92±0.05 radians, whereas the value from the focusing is 5.96±0.05 radians (Figure 62). Consequently, the focusing has made possible an increasing of a factor of 2. Same procedure can be done for 1% BSA (w/v), where the PD value from the calibration is 0.94±0.05 radians, whereas in the focusing plot (Figure 62) the PD value obtained is 3.05±0.05 radians. In the last case a factor of 3.2 has been observed. As it possible to see, the incrementing due the focusing is not the same for all the concentrations. This diverse factor could be due to a lack of reproducibility of the procedure, such as human error, preparation of new buffer solutions, and the interconnection between electrophoresis and interferometer.

5.8 Conclusion

After the hydrogel had been chosen, the research was directed to define the right combination of the buffer parameters for driving not only the analyte from one electrode to the other one, but also for focusing it on a narrow area in the chip. Having found the right conditions in both methods, the next step was to improve the steadiness of both methods, but especially for the focusing technique. More than one approach has been adopted to determine the most reliable focusing techniques, nevertheless, a study on the increasing factor was difficult to undertake. This could be a perfect starting point for further experiments with electrophoresis. Another important aspect to evaluate is the lack of reproducibility of the pH junction technique. Both acquisition and buffers system should be investigated, in particular during the analysing of the data, the “corrections” of all the spikes and jumps was intense for these experiments. The high numbers of “jump” in the PD value could also be due to the fact that during one measurement the voltage is turn off and on multiple times, since it will be safer for the researcher changing the solutions in the reservoirs. Maybe a slower variation of the voltage could reduce not only the noise in the acquisition file, but also on the

reproducibility of the experiments. Regarding the experimental preparation, an automated system may reduce the human errors during the change of the solutions.

In conclusion, two were the main aspects to study: the pH junction technique, and the combination between interferometer and electrophoresis techniques. Both the aspects were new in our group, so that the research needed to evaluate both at the same time. This has been resulted in lack of consistency of the technique, which could have been resolved by separated the two investigations. In other words, for the pH junction research well-known techniques (such as electropherogram) should have been used, whereas the improvement of the combination of the interferometer and electrophoresis should have been performed with a more standardized electrophoresis techniques. As both the aspects have been investigated, then more conscious research could be performed.

Chapter 6 Selectivity

6.1 Introduction

In the last decade micro-fluidic chips gel electrophoresis are considered as a valuable alternative to classical native gel electrophoresis or SDS–PAGE techniques for protein separation, due to their reduced dimensions and shorter time measurements [325-329]. Some microfluidic electrophoresis devices are already commercially available [254], such as Protein ScreenTape (Agilent). Typically, in the gel electrophoresis separation techniques, the target analyte is detected by using a labelled dye [330] [331] [205] [332]. The detection methods can be organised in four groups: spectrophotometric techniques, such as fluorescence techniques, mass spectrometry, electrochemical detection [254], and refractive index gradient [333], which are label-free methods. Generally, label-free detection of the analyte is more accurate as it has been explained in the previous chapters. In summary, the artefacts in the measurements, and the time-consuming passages for the labelling are drastically reduced in label-free techniques. While the majority of the experiments reported in literature are principally performed by using labelled techniques [334] [335] (absorption imaging detection, laser-induced fluorescence (LIF)), in the field of microfluidic sensors some examples of label-free approaches, such as the combination of the backscattering and the capillary electrophoresis, can now be found [261].

In this project, we propose a new label-free biosensing technique, in which the microfluidic gel electrophoresis is assembled with an optical interferometric detection. As previously described [284], the interferometer embedded with electrophoresis represents a valuable and innovative sensor that can not only quantify but also potentially monitor in real time the movement of the analyte by tracking the spatial distribution of the refractive index along the microchannel. The main difference between a biosensor and a commonly used sensor resides in the device structure, since in the former a recognition element is chemically fixed within the sensing area. Therefore, the acquired signal relies on the strength of the binding affinity of the recognition biomolecules with the target analyte [22, 31, 44, 75, 336]. The aim of this project is to separate and, by doing so, to identify the target analyte from other

molecules present in the same solution by adding, in the gel matrix, a biorecognition element displaying appropriate binding affinity towards the target. Within this setup, the electrophoresis component of the system is adopted with a modality similar to one of a native gel electrophoresis, in which proteins are analysed in their native folded state [337] [338]. Specifically, the electrophoretic mobility of the proteins is governed not only by their charge, but also by their hydrodynamic size (charge-to-mass ratio) [241]. Since it is widely accepted that a high affinity binding can be considered specific and selective [339, 340], like other before us, here we employ the Streptavidin-Biotin system, the current gold standard, as the proof-of-concept system for our biosensing applications [77]. Additionally, Bovine serum albumin (**BSA**) is here use as a negative control analyte to highlight the selectivity of the sensor.

6.2 Chip designs: Plug and junction configurations.

In the vast literature of the MFE (microfluidic electrophoresis), two main channels are reported within the chip design: one for sample flowing, the other, crossing the previous one, for separation [326]. The main reason for this configuration is that the separation of the target analyte from the solution happens in the crossed region. The chips used here do not have this characteristic and the separation happens in the channel selected for the sample solution, while the other channel is used as reference (Figure 67). In other words, in the reported setup the separation is solely due to the presence of binding sites, rather than complicated channel configurations.

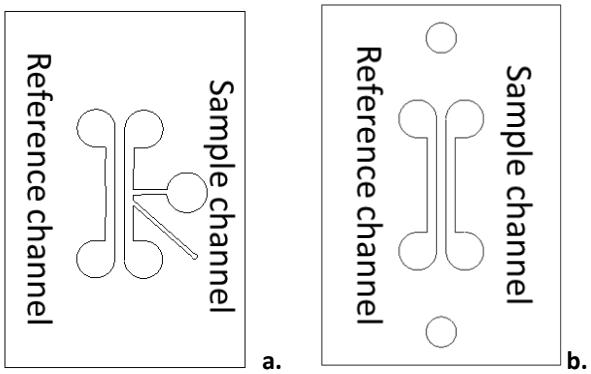

Figure 67 Chip designs for plug (a) and junction (b) configuration.

In the chip configuration here reported, the sample solution flows in the same channel in which the analyte is separated by bioselective binding, while the other channel is used as reference. In this way, the recorded signal is already normalised for reference signal,

as it has been described in the chapter for the instrument description. The design allows to fill the sample channel with two different gels, obtaining to possible configurations: the formation of a gel junction (junction configuration, Figure 67.b), or a plug of functionalised gel between untreated gels (plug configuration, Figure 67.a and Figure 68).

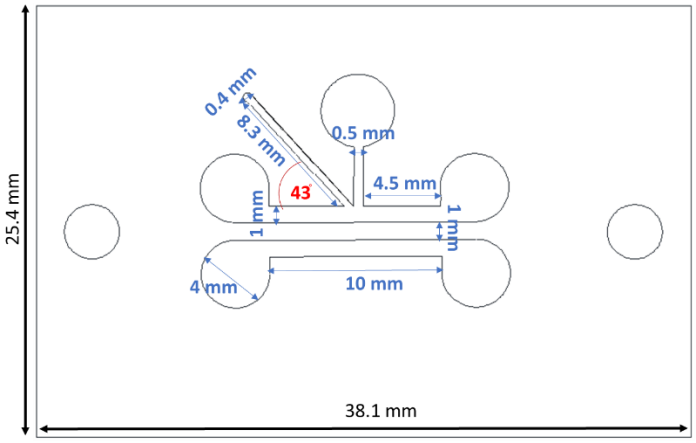

Figure 68 Schematic representation of the plug configuration channels chip with the dimensions reported.

To be able to visualise the different regions in the channels, one gel was prepared in a fluorescent solution, visible by using a fluorescence imaging setup. The preparation protocol and chemicals used are reported below.

6.2.1 Materials and procedure

The hydrogel selected for all the following experiments is agarose gel (BioReagent, for molecular biology, low EEO, CAS number 9012-36-6, 10 g, Sigma-Aldrich) (**HM agarose**), while the fluorescent dye selected for this stage is Fluorescein Sodium Salt (Sigma-Aldrich F6377-100g, used as fluorescent tracer). The agarose powder is thermally sensitive, so it is possible to dissolve it in water at temperature over 70 °C. A 1% (w/v). In our case, the agarose solution was dissolved in deionised water at 120°C and stirred on a hotplate while in a glass vial. After the powder has completely dissolved, the temperature is set to 70°C. In parallel, 1mM Fluorescein solution is prepared in deionised water and covered with aluminium foil, to protect it from the light. A second 1 % (w/v) agarose gel is now prepared starting from the fluorescent solution by covering the vial with aluminium foil and heating it at 120 °C on a hotplate, until the agarose has completely dissolved. At this point, also the second agarose solution is set at 70 °C. At

that temperature, the solution can be pipetted and used to fill the channel of the chip, to obtain a junction or a plug gel.

6.2.2 Fluorescence imaging set-up

In order to obtain further information about the composition and the configuration of the gel, a fluorescence imaging set-up has been designed and incorporated into the interferometer instrument, taking advantage of the camera already present (6.6 Mpixel CMOS camera (PL-B781, Pixelink, Ottawa, Canada). A 470 nm LED light source (excitation emitted) and a wavelength filter with 20 nm wide peak, centred at 520 nm have been added. The excitation light has been set with an incidence angle of 40°, while the reflectance angle (camera position) is set at 0° (perpendicularly to the chip surface), as Figure 69 shows.

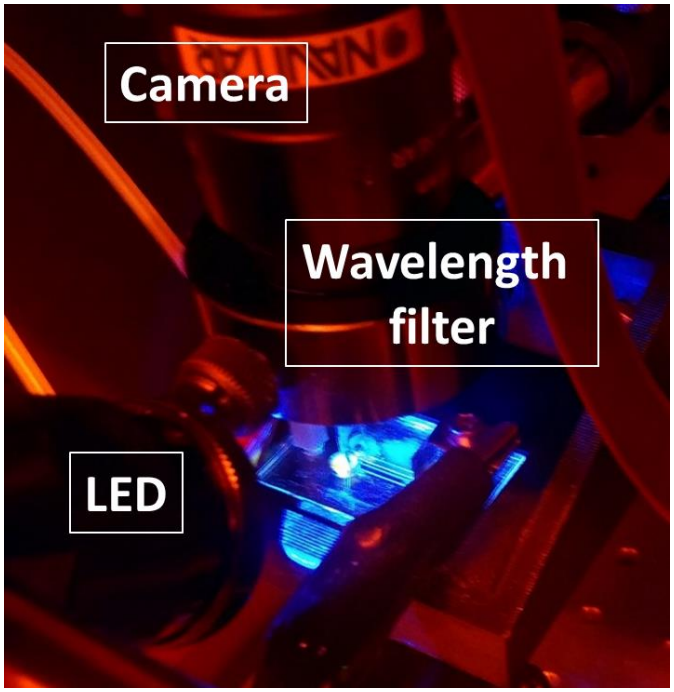

Figure 69 Fluorescence imaging set-up used.

The incidence angle was selected as the best angle at which the surface was illuminated uniformly. Since the emission of the fluorescence dye is spherical, any angles could have been used for the reflection beam, so the most straight forward configuration was selected (camera over the chip). The same apparatus has been adopted for visualising the electro-kinetic movements of other dye solutions, as will be described in the next paragraphs.

6.2.3 Results and discussion

The two chip designs (Figure 67) were developed for two different purposes within the context of interferometric imaging. In the gel junction configuration, for example, one part of the channel is filled with functionalised gel, while the other is filled with untreated gel. Through the interferometer acquisition, it is then possible to track the binding of the target analyte only in the region of the functionalised gel. Instead, in the plug gel configuration (chip), the sensing channel comprises a small region of functionalised gel squeezed between untreated gel. In this case, the phase difference detected by the interferometer has a higher value in the narrower region of the channel where the target analyte will bind on the treated gel. The use of fluorescence imaging has allowed to visualise the intersection between diverse gels inside the same channel. For example, in the fluorescence images below, it is possible to see the fluorescence gel as the functionalised gel, while the "black" one is the untreated agarose gel.

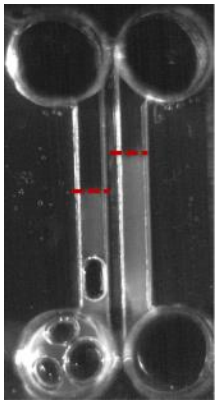

Figure 70 Fluorescence image of junction configuration in both channels of the chip. The red dashed lines show where the intersection between the two gels is.

As it is possible to observe in the Figure 70, the intersection between the two gels (red dashed line) within the two channels is quite different, as they are not aligned. That is because the reproducibility of this configuration is quite poor, since it is performed manually by the researcher by using a pipette. However, the plug configuration resulted to be more reproducible, as it was possible to estimate the dimension of the plug profile by calculating the average value for five different plug length. For each plug profile the l_{plug} considered was the length at half height of the peak. l_{plug} = 3.3±0.6 mm.

In conclusion, both designs have been helpful for obtaining useful information about the functionalisation of the agarose, but in particular the plug configuration has given a

more solid base to prove the selective properties of the sensor, as it will be more evident in the following paragraphs.

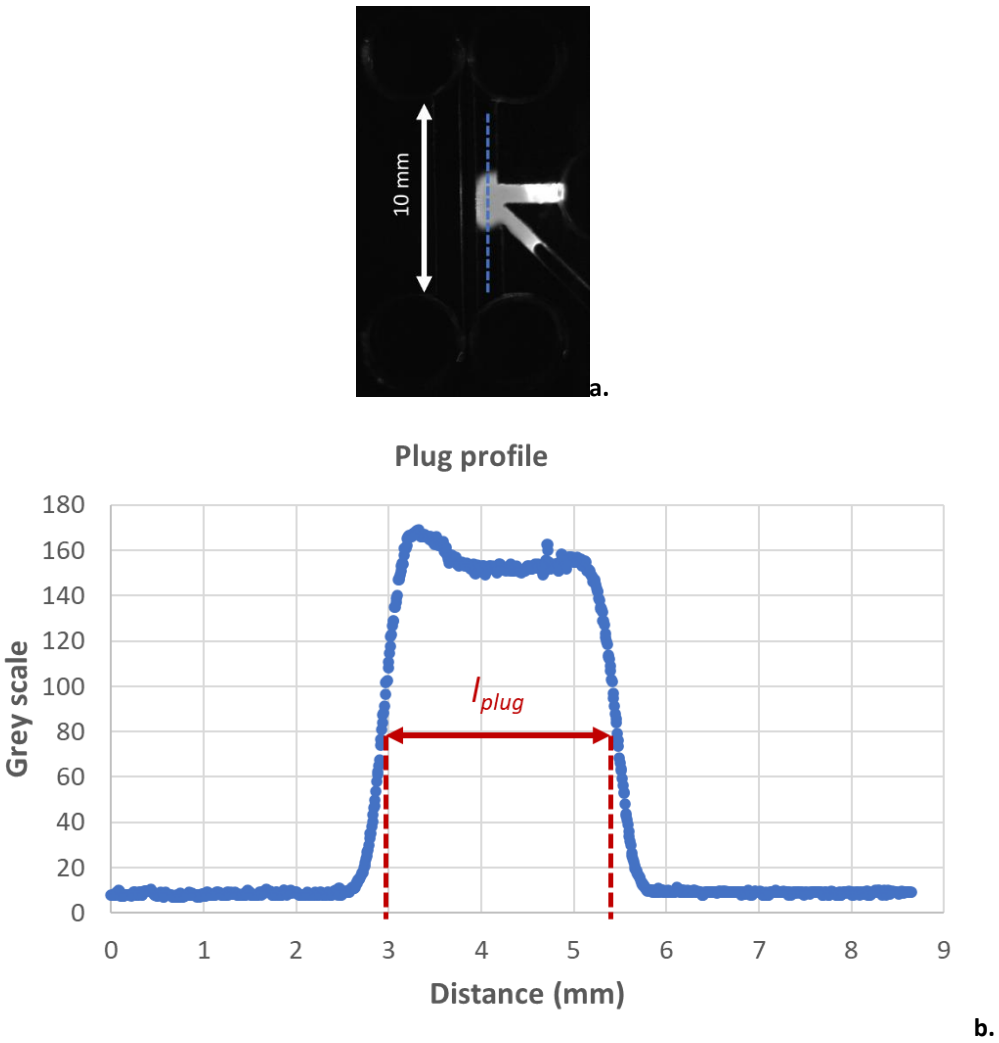

Figure 71 Fluorescent image (a) and profile (b) of one plug gel execution. The blue dashed line in image a represents the length of the profile acquired. In image b, the red dashed lines represent the distance value at half height of the plug profile.

6.3 Agarose oxidation

As the first step of gel functionalisation, the agarose has been oxidised to transform its vicinal hydroxyl groups to aldehyde groups [341], by reaction with sodium metaperiodate (**$NaIO_4$**). To find the best oxidising conditions, a hydrazide has been exploited.

6.3.1 Materials

Agarose (BioReagent, for molecular biology, low EEO, CAS number 9012-36-6, 10 g, Sigma-Aldrich) (**HM agarose**), Sodium Metaperiodate (**$NaIO_4$**) (VWR Chemicals, Sodium periodate ≥99.0%, AnalaR NORMAPUR® ACS, Reag. Ph. Eur. analytical reagent, CAS Number: 7790-28-5), 10 mM Phosphate buffer solution (**PBS**) at pH 5.30 and pH 6.20. Oxidation with periodate is most efficient in acidic conditions [247]. The hydrazide dye is Lucifer Yellow CH (Invitrogen™, Lithium Salt, 25 mg, Catalog number: L453) (**LY**), whose excitation/emission peaks are 428/536 nm, respectively.

6.3.2 Reaction

6.3.2.1 Phosphate buffer solution

In this experimental procedure Phosphate buffered Solution (PBS) has been used. A few attempts were also made in HEPES buffer, no significant results were obtained (data not reported). Other buffers such as Tris or acetate had to be excluded since they contain primary amine or carboxyls groups that quench the hydrazide bonds [247].

Table 8 Quantities used in the preparation of pHs 5.5; 6.4, 7.4 PBS, for 100 ml, 100 mM strength.

Compound	pH 5.5	pH 6.4	pH 7.4
NaH_2PO_4	1.57 g	1.37 g	0.339 g
Na_2HPO_4	0.036 g	0.321 g	2.021 g
Na_3PO_4	/	/	/

A 100 mM stock PBS solution was diluted to a concentration of 10 mM and buffered to three different pH strengths (5.5; 6.4; 7.4) (**Table 8**) using a pHmeter (Hanna instruments HI 2210 pH meter). The buffers were kept in the cupboard and prepared fresh weekly.

6.3.2.2 Agarose oxidation

The hydrazide dye, Lucifer Yellow (LY), has been used to evaluate the formation of aldehyde groups in the oxidised gel. To do so, 2% (w/v) agarose solution was prepared by suspending the agarose powder in pH 5.30 PBS (10 mM) using a hotplate at 120 °C and stirred with a magnetic bar. In parallel, a 40 mM solution of $NaIO_4$ was prepared in

the same buffer (pH 5.30). When the agarose solution is cooled down to 70 °C, the same volume of $NaIO_4$ was added, to reach a final agarose concentration of 1%. The oxidising reaction was left on a hotplate at 70 °C covered with aluminium foil. The solution was then removed from the hotplate and left to cool down at room temperature. Once the gel was solidified, it was washed with pH 5.30 PBS (10 mM) for 4-6 hours and then immersed in pH 6.20 PBS (10 mM) overnight. For the last step, also a pH 7.40 PBS (10 mM) buffer was used. Finally, 10 mM (2mg in 1 ml) Lucifer Yellow solution prepared in pH 7.40 PBS (10 mM) was introduced in the gel by using three different methods: by an electro-kinetic method; by immersing the gel into the dye solution; or by adding the dye solution into the oxidised gel solution. In all cases, the dye was left to react for 2 hours. Adding the dye solution into the gel solution was the method that displayed the highest reproducibility, once the gel has been rinsed in buffer to remove the excess dye.

6.3.3 Results and discussion

To find the right protocol to follow for the functionalisation of agarose gel, the starting point has been to identify the right time reaction for the agarose oxidation. For this purpose, we used the LY dye, which can react and bind to the aldehyde groups of the oxidised agarose gel, and which has been used to evaluate concentration of these functional groups in the gel. To do so, a calibration curve of the hydrazide dye has been extrapolated.

6.3.3.1 Lucifer Yellow calibration

The calibration curve of the LY hydrazide dye has been calculated, by preparing five different dye concentrations (w/v) in pH 7.4 buffer PBS (Figure 72). For each dye concentration (0.1; 0.25; 0.5; 0.75; 1 mM), one channel (10 mm length, 1 mm width and 250 µm height) of the chip was filled with the dye solution while the second channel was filled with buffer only, to act as reference. The image for each dye concentration was recorded using the fluorescence imaging setup described in the previous paragraph. The settings of the camera for the acquisition (exposure time 2000 ms, gain 1, and contrast 1) were kept constant in all cases. The images were analysed by using the ImageJ software. The image was first “despeckled” to remove the background noise; in turn, the grey scale value of the longitudinal profile of the channel has been collected. Then, the average value of the grey scale was calculated by using Excel.

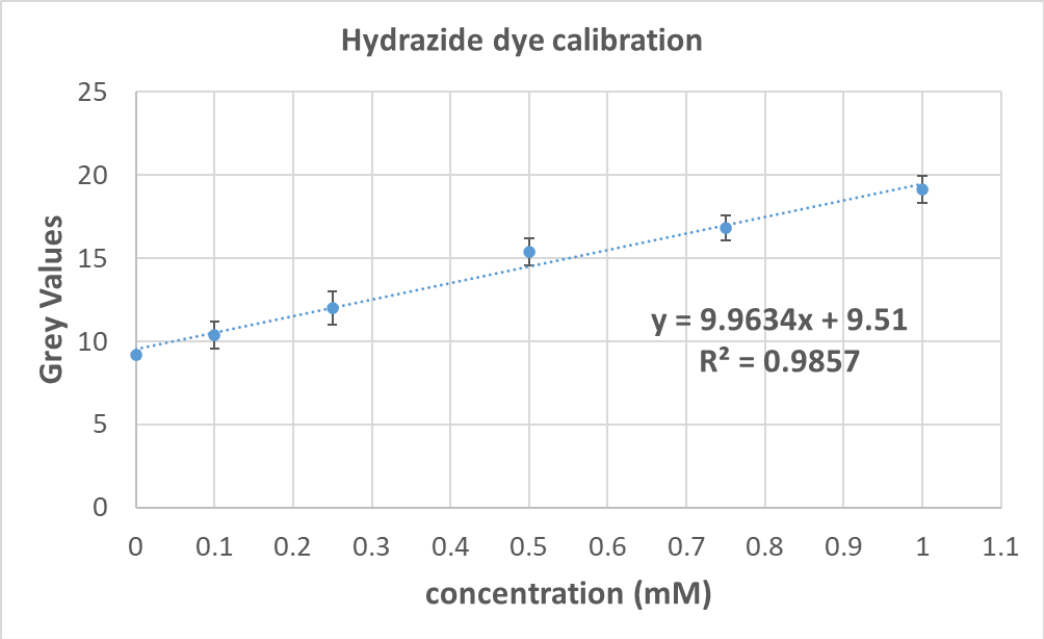

Figure 72 Hydrazide dye (LY) calibration curve (pH 7.4).

Concentration (mM)	Grey Values	Standard deviation errors
0	9.2	0.3
0.1	10.4	0.8
0.25	12.0	1.0
0.5	15.4	0.8
0.75	16.8	0.7
1	19.1	0.8

Figure 73 Values of the LY calibration curve reported in the graph in figure 72.

The grey scale value is reported in Figure 73 and shown in Figure 72 for each concentration. The relationship between the grey scale value and the LY concentration is reported in the graph in Figure 72. The coefficient of determination (R^2) demonstrates the good quality of the calibration.

6.3.3.2 Oxidation time

Different reaction times for the oxidation were studied to identify the condition that could result in a sufficient amount of aldehyde groups and, at the same time, protect the structure of the gel. For reaction times longer than 1 hour, damage was observed in

the gel structure the solution was no longer gelling. Here the data regarding three different oxidation times (30, 45, 60 minutes) are reported. In all three cases, the hydrazide dye solution (1 mM in 10 mM PBS at pH 7.4 PBS) was driven inside the channel by electrophoresis and washed away by using the electro-kinetic approach.

Background/reference signal for the fluorescence images

The reference signal was evaluated by filling half sensor channel with agarose while leaving the other half empty, as the right channel in the fluorescence image in *Figure 74* shows. From the image, the grey scale values of the longitudinal profile were recorded and are reported in *Figure 74*.

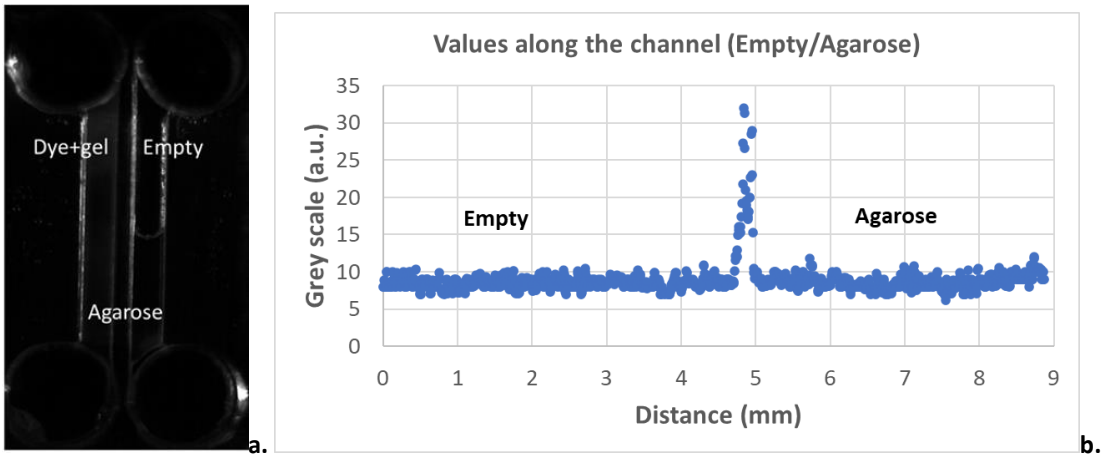

Figure 74 Fluorescence image (a), Grey scale values in the junction between agarose gel and empty channel (b).

The average of the grey scale value in the presence of agarose, or buffer or within empty channel, was the same. This means that in the fluorescent imaging setup also the diffracted light was the same. The peak in the graph at 5 mm represents the diffracted light due the edge of the agarose gel.

30 minutes oxidation time

During a 30 minutes reaction, $NaIO_4$ solution, prepared in 10 mM PBS at pH 5.4 PBS was left to react at 70 °C with 2% (w/v) agarose solution in the same buffer. In Figure 75, the graph reported the grey scale values of the oxidised agarose, whose average value is 8 ±1, comparable to the value of the reference.

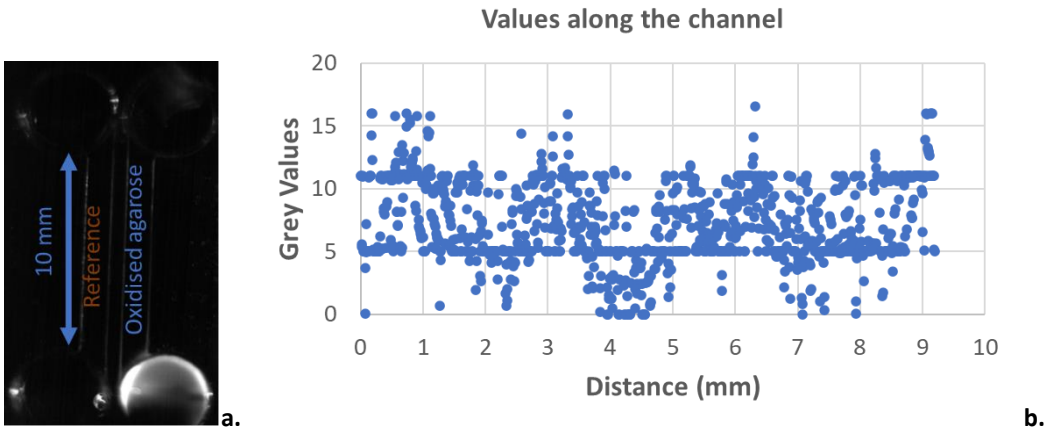

Figure 75 Fluorescence image (a), Grey scale values in the channel filled with oxidised agarose (b).

The hydrazide dye was then driven into the channel at 15 V and left to react for two hours, covered in aluminium foil. After that time (Figure 76.a), the gel was washed using 10 mM PBS buffer at pH 7.40 (Figure 76.b). At this point, the grey scale values were studied and the average value determined (Figure 77).

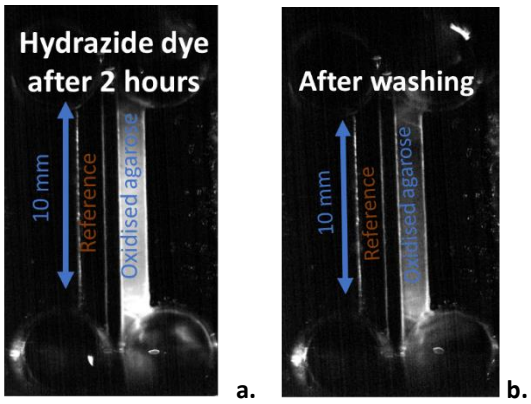

Figure 76 Fluorescence image of oxidised agarose (30 min), after 2 hours dye reaction (a), and after the washing (b).

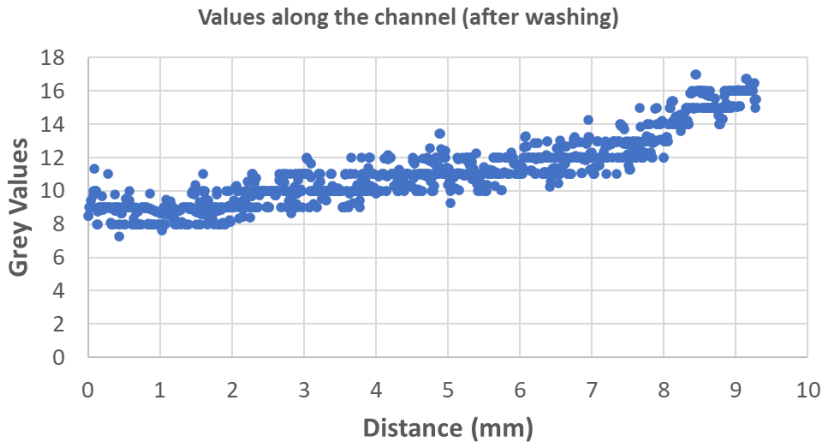

Figure 77 Grey scale values after the washing in the oxidised agarose gel (30 minutes)

The average value was slightly higher than the reference value, and on the calibration curve in Figure 72 corresponds to a concentration of 0.1 mM.

45 minutes

The second reaction time studied was 45 minutes. In Figure 78 is reported the fluorescence image of the chip with one channel filled with agarose oxidised for 45 minutes, while the reference is filled with non-oxidised agarose gel.

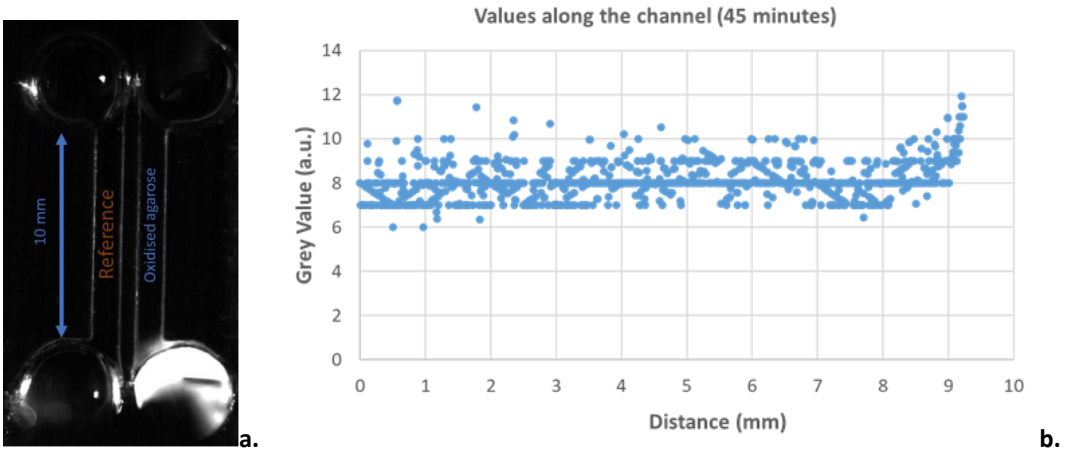

a. **b.**

Figure 78 Fluorescence image (a), Grey scale values in the channel filled with oxidised agarose (45 minutes) (no dye inside. The average represents the background value).

As in the 30 minutes reaction, the grey scale values of the oxidised gel comparable with the average value of the reference. The LY was then driven inside the channel and left react for two hours while covered in aluminium foil.

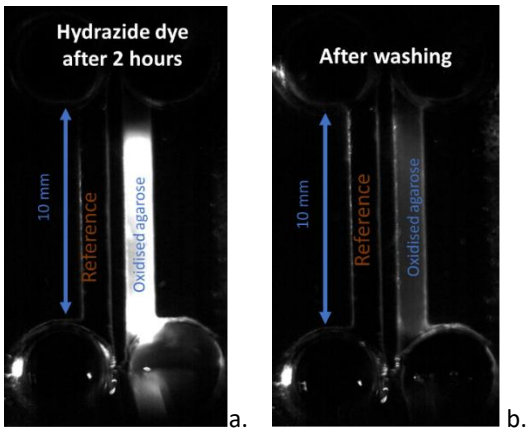

a. b.

Figure 79 Fluorescence image of oxidised agarose (45 min), after 2 hours dye reaction (a), and after the washing (b).

The procedure was the same as described for the 30-minute reaction time. The grey scale values determined after the washing (Figure 79.B), are reported in Figure 80. The average value of the LY dye on the oxidised gel is 18 ± 2, which corresponds to a hydrazide concentration of 0.8 mM.

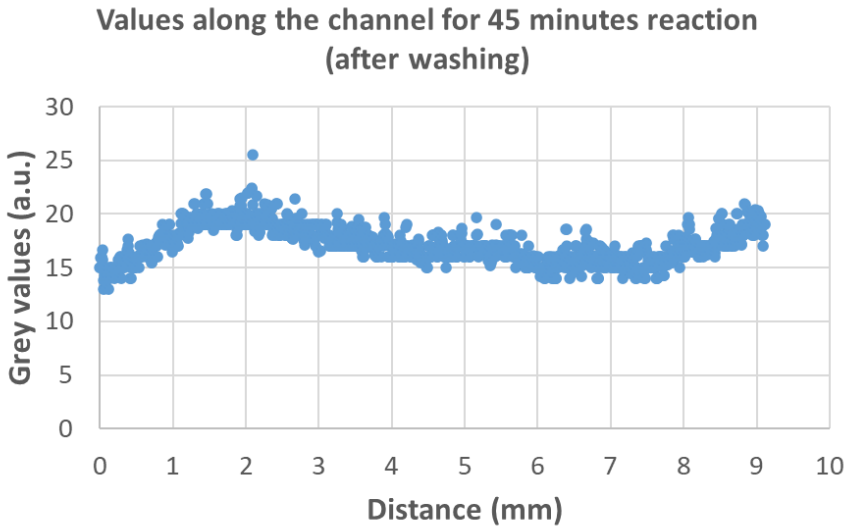

Figure 80 Grey scale values after the washing in the oxidised agarose gel (45 minutes).

60 minutes oxidation time

The last time interval studied was 60 minutes. Also in this case, the grey scale values of the oxidised agarose gel were comparable with the ones of the reference channel (Figure 81.b).

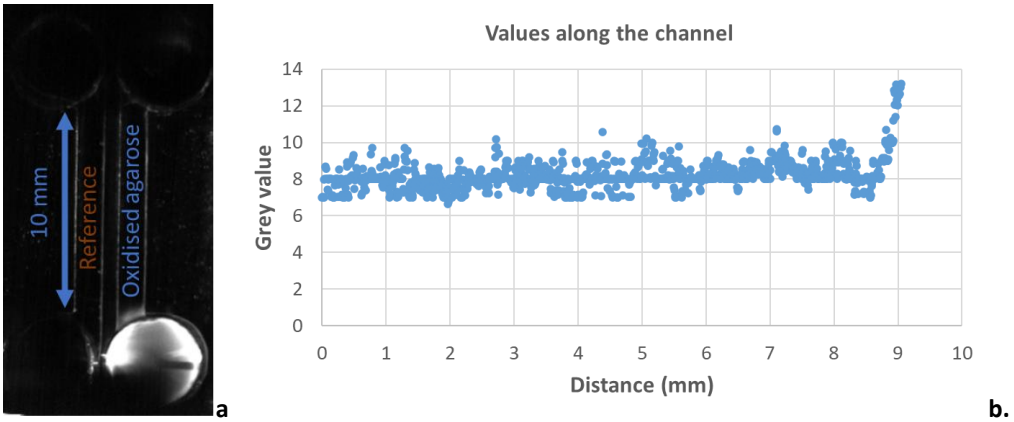

Figure 81 Fluorescence image (a), Grey scale values in the channel filled with oxidised agarose (60 minutes).

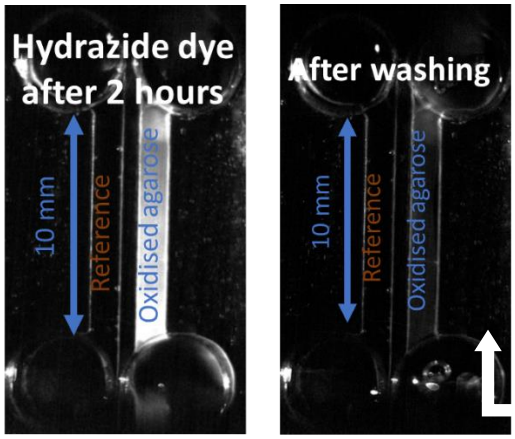

Figure 82 Fluorescence image of oxidised agarose (60 min), after 2 hours dye reaction (a), and after the washing (b).

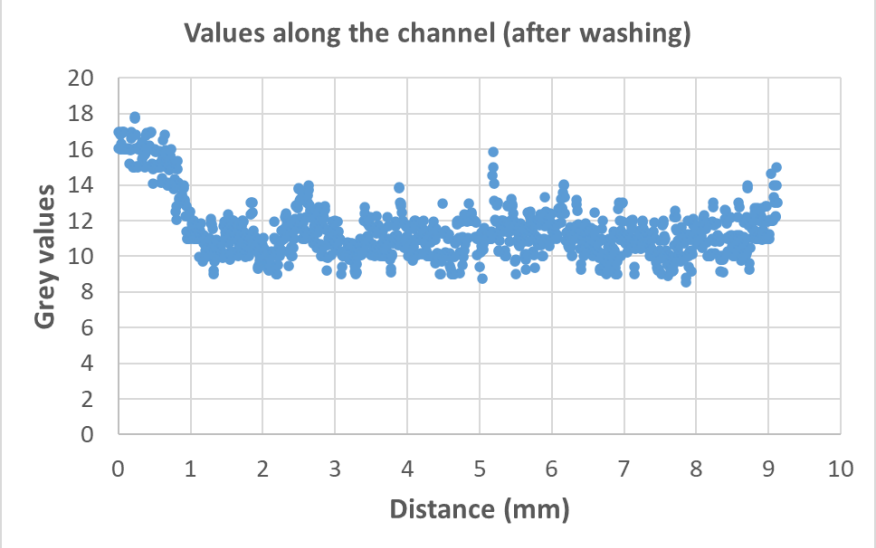

Figure 83 Grey scale values after the washing in the oxidised agarose gel (60 minutes).

Following the same process described for the other reaction times (Figure 82), the grey scale values are reported in Figure 83. The average is 12±3, a lower value compared to that of the 45 minutes. This could be due to the fragility of the gel structure. Since the 45 minutes was shown to give the best combination of hydrazone bonds and structural stability, this reaction time was selected for the next steps. To obtain a more complete view, the hydrazone bonds were quantified also for the case in which the hydrazide dye is added to the gel solution, left to react in solution (70 °C) for two hours and then, rinsed overnight in 10 mM PBS at pH 7.4.

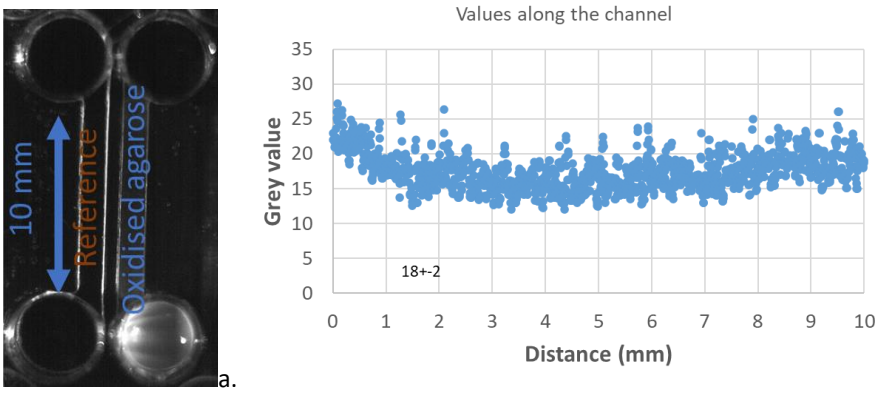

Figure 84 Fluorescence image of the chip filled with agarose oxidised and LY dye (a), and grey scale values (b).

By comparing the grey values of the graph in Figure 84.b with the ones of the graph in Figure 80, the average results appear to be higher in the latter case. This means that the binding of dye might be more efficient when occurring in solution, rather than using the electro-kinetic. This was one of the reasons why all the next steps were preferred to be performed in solution rather than on the gel.

6.4 Agarose functionalisation

To make sure that the Biotin bound correctly on the gel, the binding of another compound was adopted. As the in-solution reaction resulted to be more efficient, this approach was employed to verify that, by melting the gel for longer time, its structure and its interactions were preserved. In this way it was possible to exclude the high temperature as a possible cause of poor binding efficiency on the gel structure. In this perspective, further investigations should be taken, but that is not the scope of this project. Here, the main passages for the agarose functionalisation were applied for the proof of concept.

6.4.1 Materials

The 4,7,10-Trioxa-1,13-tridecanediamine (4246-51-9, 500g, Sigma-Aldrich) **(diamine)** has been used as a cheaper alternative to Biotin. The Fluorescein isothiocyanate isomer I 90% **(FITC)** dye has been selected as the fluorescent dye, capable to the amine groups available in the diamine-functionalised gel.

6.4.2 Reaction

Following the oxidation reaction previously described, the oxidised gel is immersed in a beaker of 10 mM PBS at pH 7.4 PBS and stirred overnight to allow the gel buffer exchange from pH from pH 5.5 to pH 7.4, since neutral alkaline environment are more suited for the diamine reaction. The final diamine concentration for the two compounds in the gel solution was 10 mM. The reaction has been left for 2 hours on a hotplate at 70 °C. After removal from the hotplate, the gel was washed overnight in 10 mM PBS at pH 7.40 PBS (10 mM) in a beaker. After the final wash, 2.7 mM FITC solution prepared in 10 mM PBS buffer at pH 7.4 PBS (10 mM) was added in three different ways: by adding the dye solution on the gel solution (at 70 °C); by immersing the gel in the dye solution; or by electro-kinetic method. Here, the latter application is reported, since it is the same methodology applied for the measurement of the Streptavidin-Biotin binding.

6.4.3 Results and discussion

As stated in the previous paragraphs, the steps described helped to visualise and characterise differently functionalised gels within the channels of the chip. In particular, by analysing the effect of an additional plug of untreated agarose, where the binding with the fluorescent dye does not occur, inserted between functionalised agarose in which the amino group can readily bind the FITC, insert creating a plug of functionalised agarose, where amino groups are available for binding with FITC. In Figure 85.a, a plug of untreated agarose gel is visible between portions of FITC-diamine gel. Firstly, one channel was filled with the two differently functionalised gels, while the other channel was filled only with agarose gel. Then, FITC in pH 7.4 was inserted inside the plug-channel by electro-kinetics, and subsequently washed with PBS at the same pH and strength. The image 85.a has been recorded after the washing step. The FITC is only visible at the two edges of the channel on the right and is labelled “diamine-gel” in the figure 85.a. A expect, the centre of the channel, where only agarose is present, appears dark while (Figure 85.a).

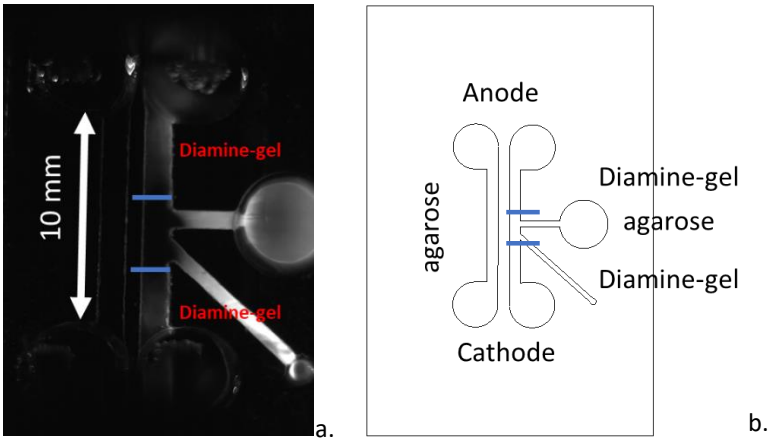

Figure 85 Fluorescence image after the washing (a) and configuration (b) of the plug.

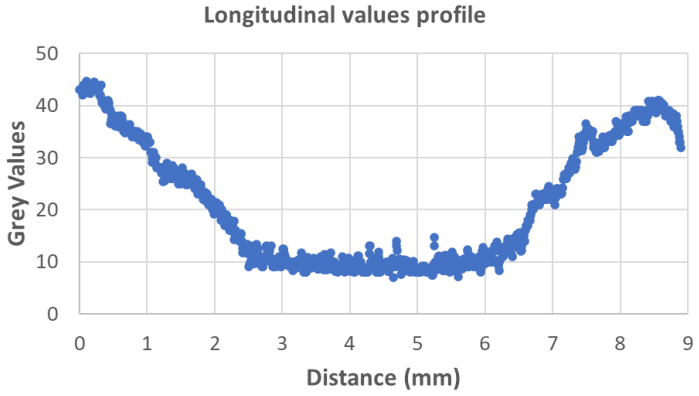

Figure 86 Grey values of the plug profile from the fluorescent image (plug configuration)

Grey values relative so the plug profile is being determined using the software ImageJ and are reported in Figure 86. As depicted in the graph above, the plug of untreated agarose is 3.5 mm long, comparable to l_{plug} average (=3.6±0.4 mm). The values increase towards the edge of the profile due to the presence of FITC.

In conclusion, the oxidised agarose can act as a stable functionalised support, as observed with the diamine functionalisation and the FITC recognition of different areas within the channel. These results provided a solid protocol for the next and final step, in which, instead of the diamine molecules, Biotin Hydrazide will be used, and Streptavidin will be driven into the channel as it has done for FITC.

6.5 Streptavidin-Biotin system

The most commonly employed model in proof-of-concept experiments for the development of new biosensors is the Streptavidin-Biotin system [77, 342]. This system not only display a high association constant rate (whose value is > 10^7 $M^{-1}s^{-1}$)[343], but also, with a dissociation constant of about 1.3 10^{-15} M [77], represents one of the strongest affinities found in nature. Importantly for our application, the interaction affinity is not affected by the ionic strength of the buffer [344], as happens for many other proteins. Hence, we were able to drive the Streptavidin within the biotinylated gel by using buffers and electrophoresis system described above. Because of these characteristics, the Streptavidin-Biotin system represents an exception in the biomolecules field, rather than the rule. For this reason, comparing this system with the binding between other biomolecules might not necessarily be corrected. Nevertheless, the Streptavidin-Biotin pair continues to be used in the development of immunosensor systems [77], because, in the bound state, it still offers unique advantage of displaying higher affinities also towards other molecules, such as antibodies. Streptavidin is a protein originating from bacteria *Streptomyces avidinii*, and is a tetramer composed of four subunits, each of them with equal affinity for Biotin [77, 342]. Consequently, it can be expected that binding will be in a ratio of 1:4 (Streptavidin to Biotin). Below, the protocol and the materials used are described, followed by the experimental data of the interferometric sensor embedded by means of electrokinetic force.

6.5.1 Materials

Invitrogen™ UltraPure™ Low Melting Point Agarose (**LM agarose**), **Streptavidin** (Iba, lyophilized from 25mg/ml solution in pH 6.5 potassium phosphate buffer (10 mM), 0.80 mg/ml, 100mg, 2-0203-100), Agarose (BioReagent, for molecular biology, low EEO, CAS number 9012-36-6, 10 g, Sigma-Aldrich) (HM agarose), Bovine serum Albumin **(BSA)** (lyophilized powder, essentially globulin free, ≥99% (agarose gel electrophoresis, A7638-10G, Sigma-Aldrich). For the functionalisation of the gel Biotin Hydrazide (**BH**) (B7639, 100 mg, Sigma-Aldrich) has been adopted. The chips were routinely regenerated through removal of residual gel and molecules with a solution of 0.1 mM Tween ® 20 (Sigma-Aldrich, for molecular biology, viscous liquid, P9416-25ml) in deionised water, so that damage to the PMMA chip that would have occurred with the use of ethanol.

Phosphate Buffered Solutions (PBS) at five different pH values have been prepared by dissolving the defined amount of Sodium phosphate monobasic dihydrate (**NaH_2PO_4**, Sigma-Aldrich, BioUltra, for molecular biology, ≥99.0% (T), 71505-250g), Sodium Phosphate dibasic heptahydrate (**Na_2HPO_4**, Sigma-Aldrich, ACS reagent, 98.0-102.0%, S9390-500g) and Sodium Phosphate Tribasic dodecahydrate extra pure (**Na_3PO_4**, Acros Organics, 450660010, 1 kg). For pH 3.2, the final pH has been adjusted with hydrochloric acid (HCl) (VWR Chemicals,1 mol/l, mol/l (1 N), Reagent Grade, 7647-01-0). The electrodes are made of stainless steel and have been laser cut from metal foil.

6.5.2 Reaction and methodology

6.5.2.1 Phosphate buffer solution

In this experimental procedure Phosphate buffered Solution (PBS) has been used. Because of the presence in their composition of primary amine or carboxyls groups that could quench the hydrazide bonds, no other buffer, such as Tris or acetate, was employed. The experiments were performed in 10 mM PBS at three different pH (3.2; 7.4; 9.2). The final buffer concentration was reached by diluting it from a 100 mM stock. The buffers were prepared routinely replaced every 3/4 weeks.

Table 9 Quantities used in the preparation of pHs 3.2; 6.4, 7.4 and 9.2 PBS, for 100 ml, 100 mM strength.

Compound	pH 3.2	pH 6.4	pH 7.4	pH 9.2
NaH_2PO_4	1.37 g	1.37 g	339 mg	11 mg
Na_2HPO_4	0.3 mg	321 mg	2.021 g	2.66 g
Na_3PO_4	/	/	/	2 mg

Table 9 reports the quantities weighed to prepare 100 ml of 100 mM buffer at three different pH values. The final pH was measured with pH meter. The stocks were kept in the cupboard and the 10 mM buffers were prepared fresh every week by diluting 10 times the stock solutions.

6.5.2.2 Agarose Biotinylation

The agarose gel, as well other carbohydrates and glycoconjugates can been biotinylated by using Biotin hydrazide [341]. To do so, the gel needs to be oxidised, as it has been described before (Agarose oxidation 6.3), to obtain the aldehyde groups that can react with the hydrazide groups of the biotin hydrazide compound. The agarose used for the biotinylation is **HM agarose**, which was observed to maintain its structure under the multiple heating cycling better than **LM agarose**. The oxidised gel, which was prepared in 10 mM PBS at pH 5.5 was then immersed in a beaker filled with 10 mM of PBS at pH 6.4 and stirred overnight to exchange the buffer for one with a pH more favourable for the hydrazide, which is between 5.5 to 7.4 pH. The gel was then collected and, on the hotplate, heated again at 120 °C. As the gel solution was cooled down to 70 °C, Biotin hydrazide was added with a final concentration of 4 mM. The reaction was left for 2 hours on a hotplate at 70 °C. After removal from the hotplate, at room temperature, the gel was washed overnight in 10 mM PBS buffer at pH 7.4 PBS. At this point, the gel was melted once more, and the solution was pipetted to fill the microfluidic chip, according to the different experimental setup (channel, junction or plug design). This protocol was oprimised from standard procedures developed by Thermofisher and Uptima, for the biotinylation of glycoproteins [247, 345]. Finally, for the selectivity experiments the final wash of the biotinylated gel was performed in three different pH environments, pH 3.2, 7.4 or 9.2, in accordance with the experiment settings.

6.5.2.3 Untreated agarose

The untreated agarose was prepared using standard protocols (paragraph 6.2.1). Both HM agarose and LM agarose, were use as matrix, with different preparations. LM agarose was preparade by dissolving the powder in buffer using a microwave, whereas the HM agarose powder was dissolved on a hotplate at 120°C and stirred with a magnetic bar. After the powder had completely dissolved, both solutions were kept on hotplate at 70 °C. The pH of the buffer was the same for the untreated agarose and for the sample solution. For instance, if the sample was prepared in 10 mM PBS at pH 3.2, also the untreated agarose was prepared at the same pH. As done by other protein analysis [346], the agarose was used at 1% (w/v), a porosity that allows the selected analytes to move through the gel.

6.5.3 Electrophoresis buffers system and methodology

A voltage of 10/15V was applied for 20 minutes to both channels. In these conditions, no pH variation nor phase difference - such as analyte movement in the opposite direction - was detected by the interferometer (paragraph “5.3.1.”). Every 20 minutes, the voltage was turned off to allow for buffer exchange in the reservoirs with fresh solutions, after which a second wash can be performed. Applying the voltage for a maximum of 20 minutes also reduced heating side. For example, it was observed that for pH values 7.4 and 9.2 two washings were required to stabilise both the system and the phase difference signal recorded by the interferometer sensor. Instead, the experiments performed at pH 3.2 required only one washing step. Of note, the biotinylated agarose had always a starting pH of 7.4, irrespective of the final pH value. The isoelectric point (pI) of Streptavidin is at pH 5.2-6.0 [345], which means that, at pH higher than 6.0, the analyte has negative charge, and, in turn, the movement will be directed from the cathode toward the anode. In contrast, the direction of movement is from the anode to the cathode in acidic environment (pH lower than 5.2). BSA was the analyte to be used in the assay as a negative control since it displays no affinity towards biotin [334]. For the pH values selected in this project, streptavidin and BSA will move in the same direction. An important point to highlight is that both streptavidin and BSA have been introduced in the gel without any preceding purification, but they were weighed out and dissolved in the selected buffer.

6.5.4 Experimental steps

In the experiments presented in this chapter, contrarily to the previous one, the voltage was applied to both channels. In general, the experimental procedure is divided in three main steps shown in figure 87 for the sensing channel.

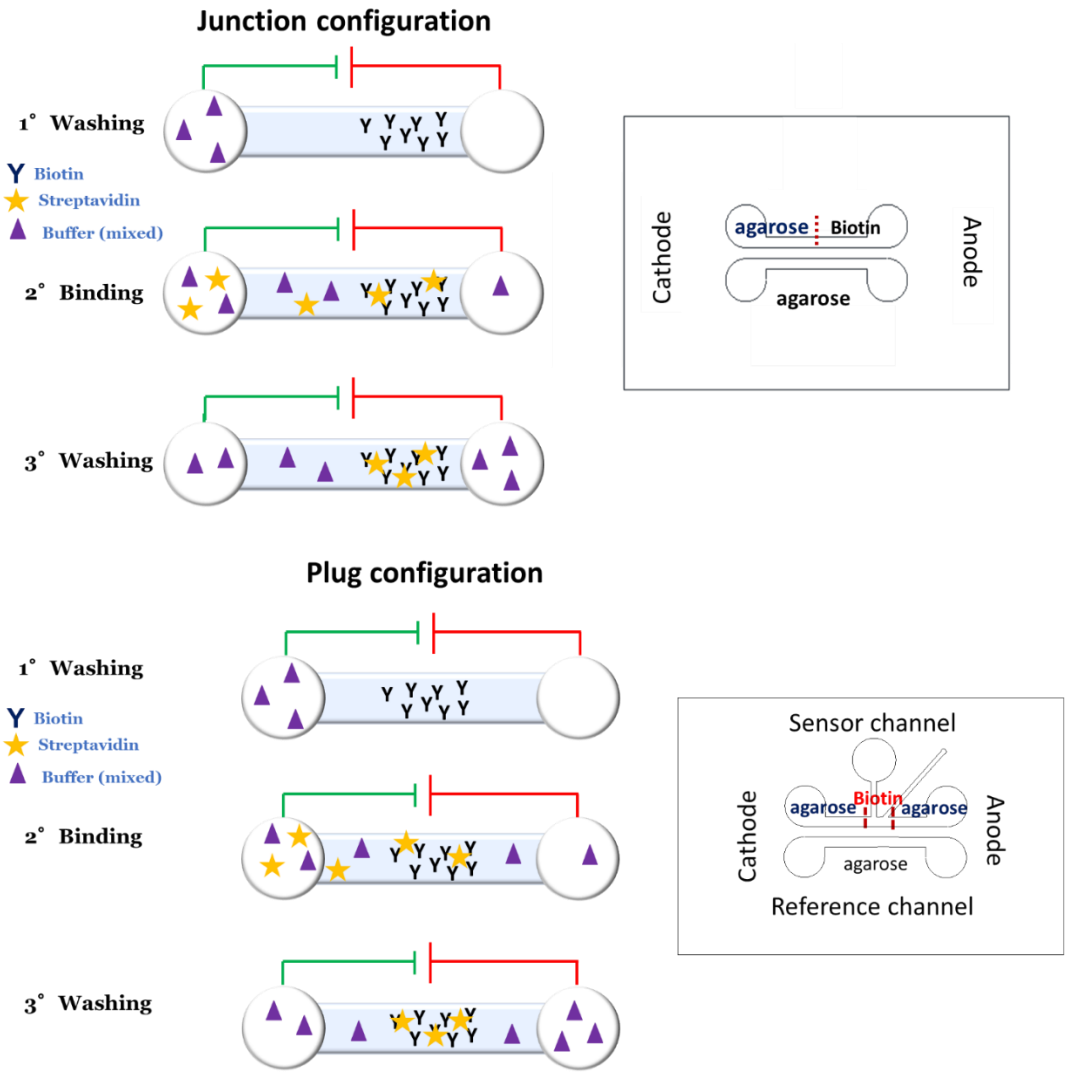

Figure 87 Schematic representation of the experimental steps, for the junction and the plug scenarios.

1° In the first 20 minutes, buffer is driven in both channels filled with gel (untreated agarose for the reference, a unction or a plug gel configuration for the sensing channel).

2° At the 20th minute, the voltage is turned off to change all reservoirs solutions with fresh ones. In particular, one of the sample channel reservoirs is filled with analyte solution (from where the analyte will move), while the other is filled with buffer only. This operation usually required two minutes. The voltage is then turned on for other 20 minutes. As the analyte solution travels inside the channel, the PD increases as the analyte concentration causes a change in refractive index between the two channels.

3° At the 40th minute, the voltage is turned off again. All solutions in the reservoirs are changed with a fresh buffered solution. The voltage is turned on again for the last time to wash the sample channel. As the buffer moves in, the PD turns back to its lower value, as the analyte is completely removed and reaches the other side of the channel. At this stage, if the analyte binds in an area of the sample channel, the PD values will remain high.

The interpretation of the counter plots has been already explained in paragraph 5.3.3. Every step is characterised by complete solutions removal from all the reservoirs and replacement with fresh ones.

6.5.5 Results

The Streptavidin-Biotin system has been studied in two different gel configurations:

1. the junction gel configuration,
2. the plug gel configuration.

The first data here reported represent the streptavidin calibration in untreated agarose, in buffer with 10 V applied for 15 minutes. Then the data for the junction and the plug configuration are reported at different pH environments.

6.5.5.1 Streptavidin calibration

The streptavidin calibration of the interferometric sensor integrated with electrokinetic is shown in Figure 88, while in the following table their values are reported.

It is possible to observe that the phase difference value increased with streptavidin concentration, whose the lowest limit detect is 6 μM without the biorecognition element in the gel. The streptavidin was dissolved in 10 mM PBS at pH 9.2 PBS. Although the coefficient of determination (R^2 =0.91) is slightly low, the calibration curve represented a good starting point to interpret the measurements of the interferometer with biotin-functionalise agarose. The reduced volume prepared for the streptavidin samples was too low (between 50-100 μl) to measure the RI with the refractometer, which would have required a volume above 120 μl.

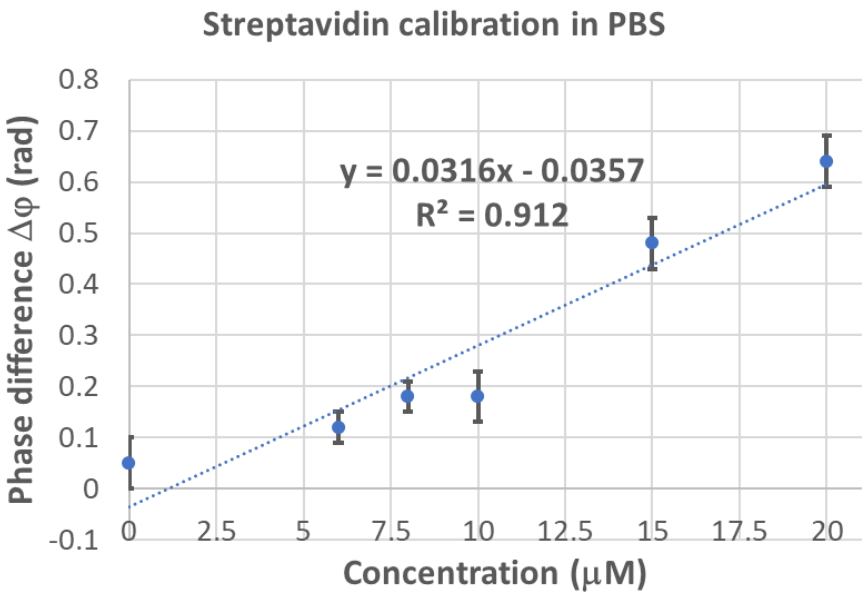

Figure 88 Streptavidin calibration of the interferometric embedded with electro-kinetic. The values and the errors are reported in the table 10.

Table 10 Phase Difference values for the streptavidin concentrations used in the calibration curve.

Concentration (μM)	Phase difference (rad)	Standard errors (rad)
0	0.05	0.05
6	0.12	0.03
8	0.18	0.03
10	0.18	0.05
15	0.48	0.05
20	0.64	0.05

6.5.5.2 Junction configuration

The first gel design configuration presented here is the **junction**, where the sample channel is filled with untreated and biotinylated agarose, while the reference channel is filled only with untreated agarose (Figure 87). The filling was performed by using a 10-100 μl pipette. For this configuration, pH 7.40 was tested. Through this paragraph the position of the biotinylated agarose will be ether near the cathode or near the anode as a further proof that the local PD change correlates to the binding area. The gel junction configuration is represented schematically represents in *Figure 89*, where it is shown that the biotinylated gel occupies the area of the sample channel nearest the cathode.

The counter plot reported in the same figure shows the change of phase difference (colour scale) as function of the time (x axis) and as the solution moves through the channel (y axis). In the case reported in the plot, 10 μM streptavidin prepared in 10 mM PBS at pH 7.4 was driven (from the cathode to the anode) in the gel junction where the biotin concentration was 2 mM. It is possible to distinguish three steps: the starting washing (15 minutes), the streptavidin movement (15 minutes) and finally the rinse of the channel from the unreactive molecules (15 minutes). For each step 15 V were applied.

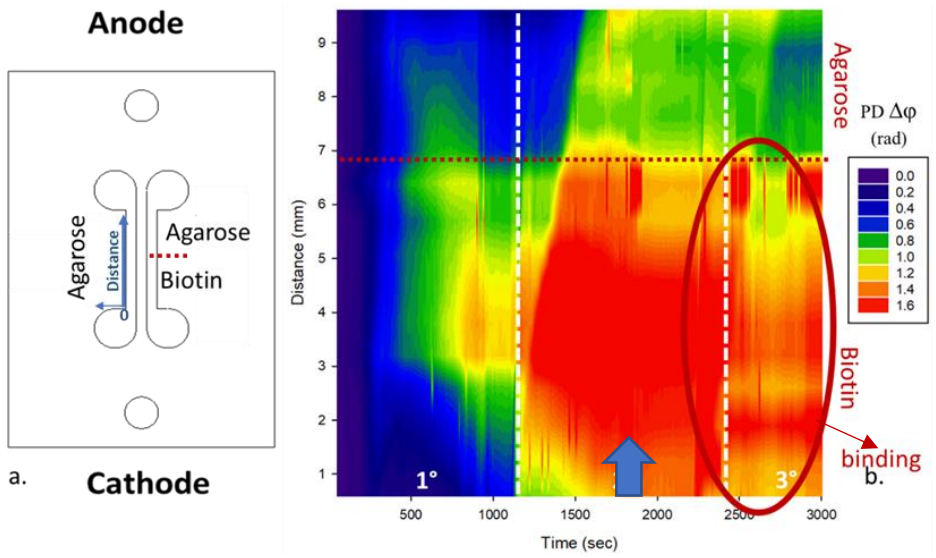

Figure 89 Schematic representation of the junction configuration (a). The Biotin-gel is near the cathode. Counter plot (b) of the Phase Difference variation through the channel as the time going.

For the first step, the PD was quite low, as the pH 7.4 buffer is stabilising the system. For the second step, as the streptavidin is moving through the channel the PD showed an increase, and in particular the value was higher in the first 7 mm.

Around that distance from the cathode, it is possible to identify the intersection between the untreated and biotinylated agarose gels. In fact, during the third step, the final washing, the PD of the area near the anode is decreasing, but the other part of the channel presents the same value as the second step. The increase of PD in the part of the channel where the biotin is present, demonstrate that the streptavidin is binding where the agarose is functionalised with the biotin. As the binding has been proven, it is important to prove the selectivity of the biosensor.

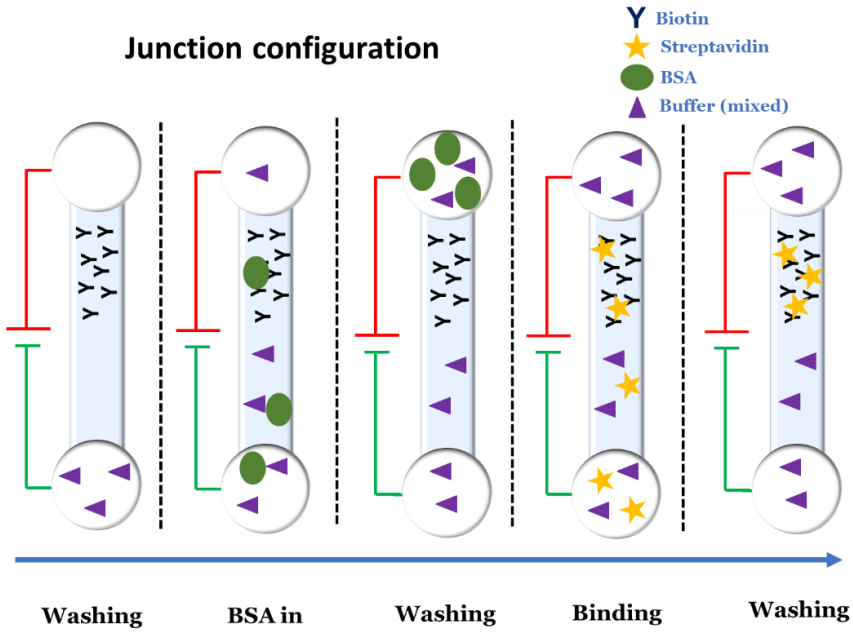

Figure 90 Schematic representation of the steps to prove the selectivity of the sensor.

Hence 7.5 µM BSA solution in pH 7.4 PBS (10 mM) has been tested. In particular, by using the same disposition of the gel junction (biotinylated gel is near the cathode, Figure 91.a), after the initial wash, the BSA has been driven in for 10 minutes, followed by 15 minutes of rinsing, then 10 µM Streptavidin for 10 minutes, and finally two buffer washings (schematic representation illustrated in Figure 90).

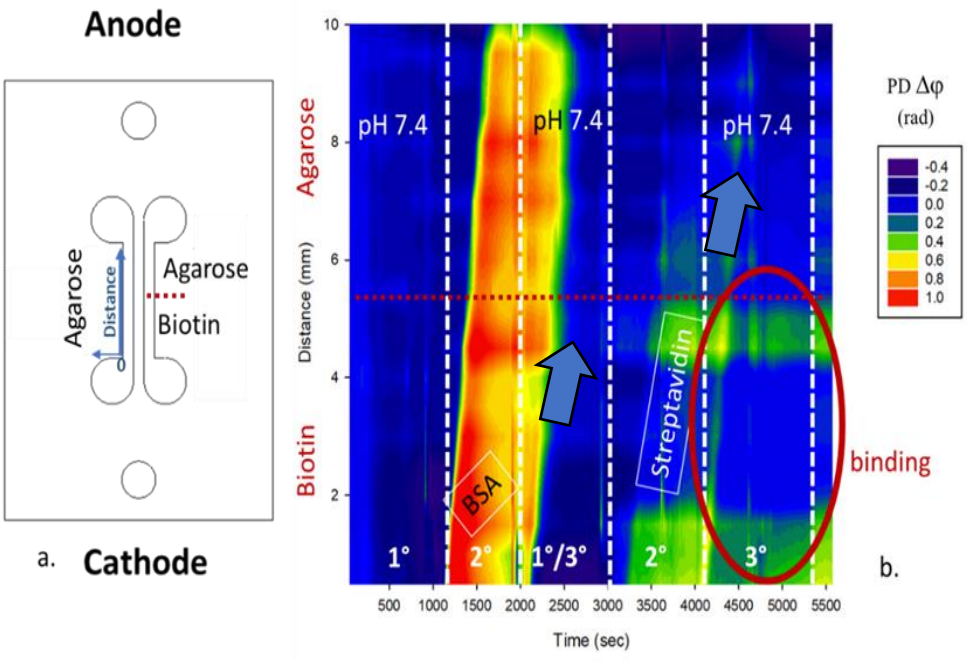

Figure 91 Schematic representation of the chip (a), contour plot showing 7.5 µM BSA, and 10 µM Streptavidin runs in a gel junction configuration (b).

On the counter plot in Figure 91, it is noticeable the PD was low before and after the BSA run, indicated that all the unreactive molecules (BSA) have been completely removed from the gel. Whereas, as the streptavidin moved through the channel (the PD is lower than the BSA, but still comparable with the calibration curve), the PD held a higher value in the area nearest the cathode, where the agarose was functionalised with biotin. Looking at the measurement of the streptavidin run until the end, it was possible to distinguish two areas, but the difference in their PD values was not as pronounced as for the previous case. The main reason was the limited reproducibility of the electrophoresis, where the PD value can oscillated between 0.4 to 1 radian, within a system in which the noise due the buffer causes a PD variation of 0.2-0.3 radians.

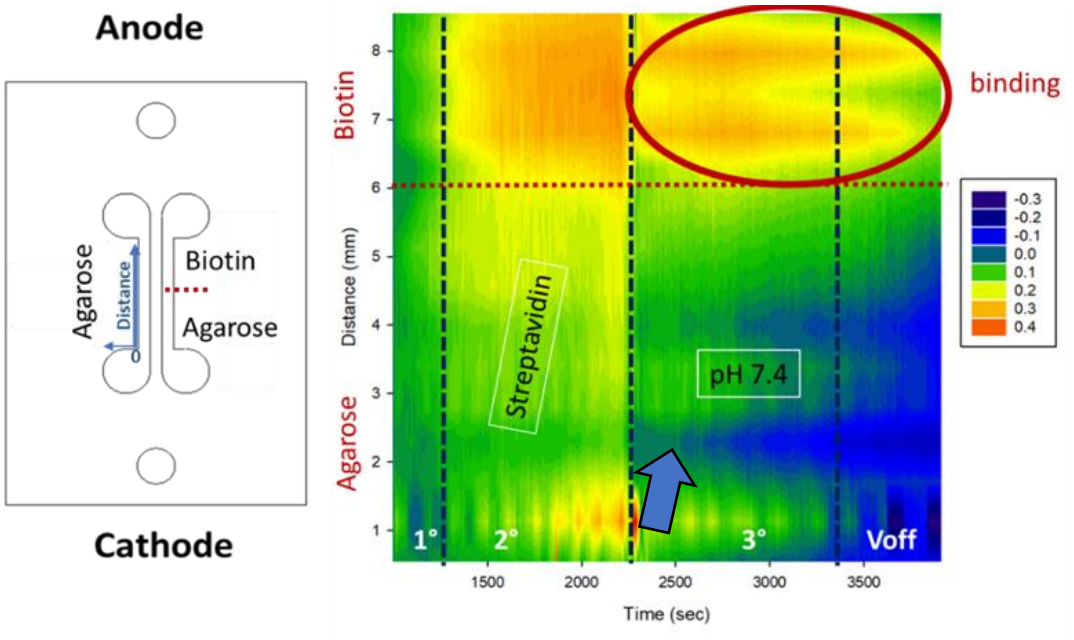

Figure 92 Schematic representation of the chip (a), contour plot showing 8 μM Streptavidin runs in a gel junction configuration (b).

In addition, an opposite configuration has been tested by filling the region of the sensitive channel nearest the anode with biotin-gel, and the rest of the channel with untreated agarose, as the figure 92 shows. The experiment is being realised in10 mM PBS at pH 7.4. In the graph in Figure 92, the conditions were 4 mM Biotin-gel and 8 μM streptavidin. The first visible step on the counter plot represents the streptavidin run (20 minutes), followed by buffer rinsing (20 minutes). During the last 3 minutes the voltage was turned off. Also in this case, it was possible to observe an increment of the PD in the region nearest the anode, particularly during the washing, as expecting from

the binding of the streptavidin to the biotin in the area going from 6 mm to 8.8 mm, exactly where the biotin-gel was.

As in the previous configuration, the selectivity was tested by driving in a mixed solution (3.75 μM BSA, 5 μM streptavidin) (Figure 93). Two starting washings were performed at 15 V, and at 3000 seconds the mixed solution was driven in at the same voltage for 20 minutes.

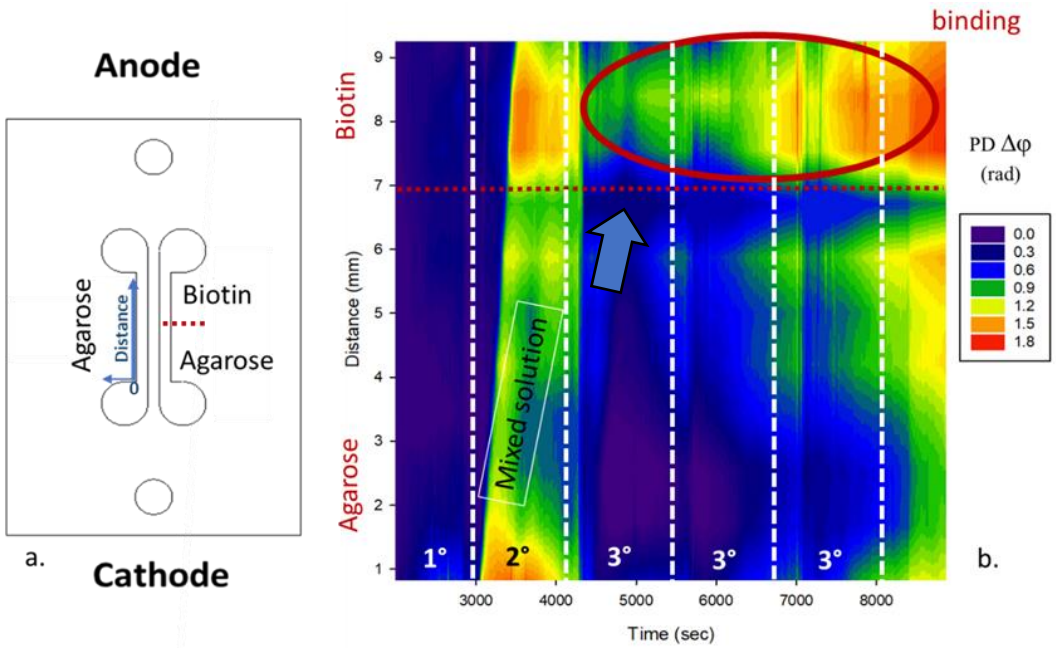

Figure 93 Schematic draw of gel configuration (a) and counter plot of the mixed solution (3.75 μM BSA, 5 μM streptavidin) in gel junction.

After that, three washing steps performed at 10 mM PBS at pH 7.4 were performed. In the counter plot it was possible to observe a higher value of the PD in the area between 7 and 9.2 mm, rather than in the one between 0 mm and 6 mm. Also in this case, the difference between two regions was not so as pronounced, but still significant. The junction configuration was tested with 10 mM PBS buffer at pH 9.2 (Figure 94). In the case reported here, the Biotin gel (2mM) was near the anode, while the other part of the channels was filled with untreated agarose.

In the complete counter plot Figure 94, it is noticeable that before and after the BSA (15 μM) run the PD had lower values, compared to the streptavidin (20 μM) run. The washing showed a higher PD value in the region nearest the anode, as it can be appreciated in the second counter plot, reporting the final part of the measurement. From 6 mm to 8.8 mm the PD values were higher than the zone between 0 mm and 6

mm. In conclusion, the use of a pH 9.2 did not improve the detection on the target analyte.

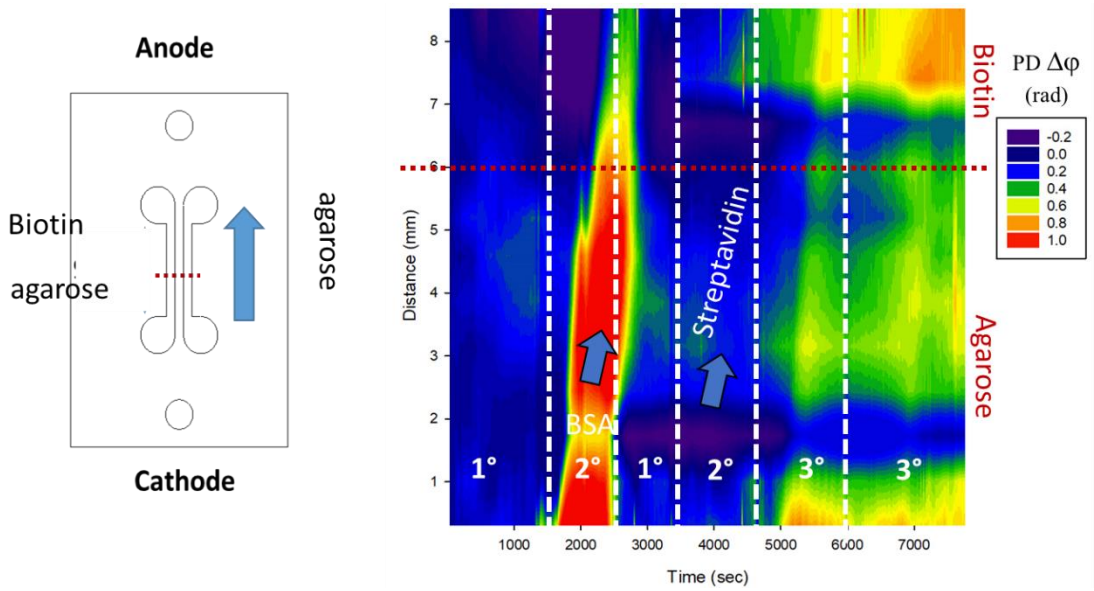

Figure 94 Schematic draw of gel configuration (a), 3.75 μM BSA, 5 μM streptavidin in gel junction (b).

6.5.5.3 Plug configuration.

Since the measurement in the gel junction configuration had poor reproducibility both in terms of PD values and recognition of the gel junction, the plug configuration was employed. This configuration should narrow and confine the functionalised gel area, allowing for a more accurate interpretation of the interferometer measurements (schematic representation is illustrated in Figure 87). The filling was performed by using a 10-100 μl pipette. Of notice, two similar configurations are possible for the plug design (Figure 95).

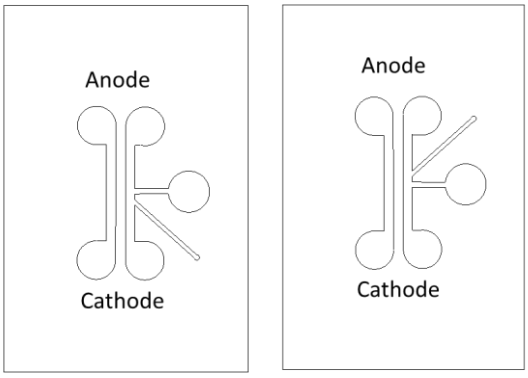

Figure 95 Two possible orientation of the plug configuration.

Firstly, a control measurement was conducted by driving 20 μM streptavidin, prepared in 10 mM PBS pH 7.4, into the sample channel filled with untreated agarose. As expected, after the streptavidin run, it was not possible to observe a particular region with higher PD (Figure 96). Below, the experiment performed in 10 mM PBS pH 7.4 is shown. The counter plot represents the run of 20 μM streptavidin (20 minutes at 15 V) in a plug-chip, followed by two washing steps (Figure 96).

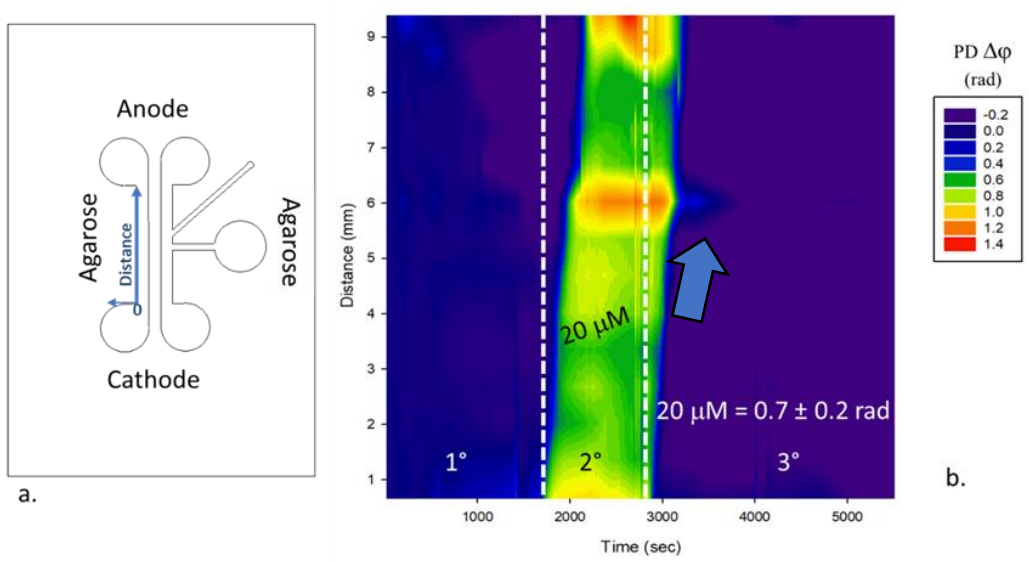

Figure 96 Control measurement. 20 μM Streptavidin in agarose gel in plug chip.

The first example of the Streptavidin binding on a biotin-plug gel is reported in Figure 97, where 8 μM streptavidin was driven in a 4 mM Biotin-gel plug.

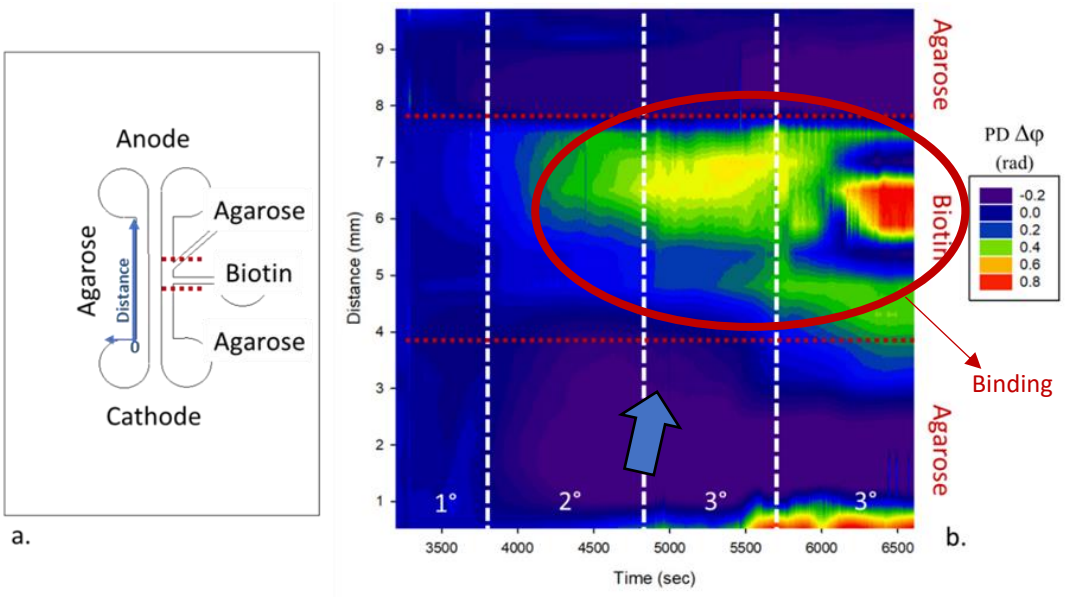

Figure 97 Schematic representation of the chip (a), contour plot showing 8 μM Streptavidin runs in a gel plug configuration (b).

The streptavidin run (15 V for 20 minutes) induced very small variations of the PD (around 0.15 mm, comparable with the calibration curve), in respect to the one observed in the two washing steps (20 minutes each) in the area between 5 mm to 8 mm (area inside the red circle), the zone that corresponds to the plug region (3.6±0.4mm, paragraph 6.2.3). This could be a hint at the possible binding of the streptavidin to the biotin, although the values of PD were very low.

Despite these difficulties, the selectivity has been tested also in this configuration and at this pH, Figure 98, represents the initial washing, followed by the 7.5 μM BSA run (20 V for 20 minutes), followed by a rinse (20 V for 20 minutes), 20 μM streptavidin (20 V for 15 minutes), and two final washing steps (20 minutes each, at the same voltage). There are several interesting results reported in the graph, as they are discussed below.

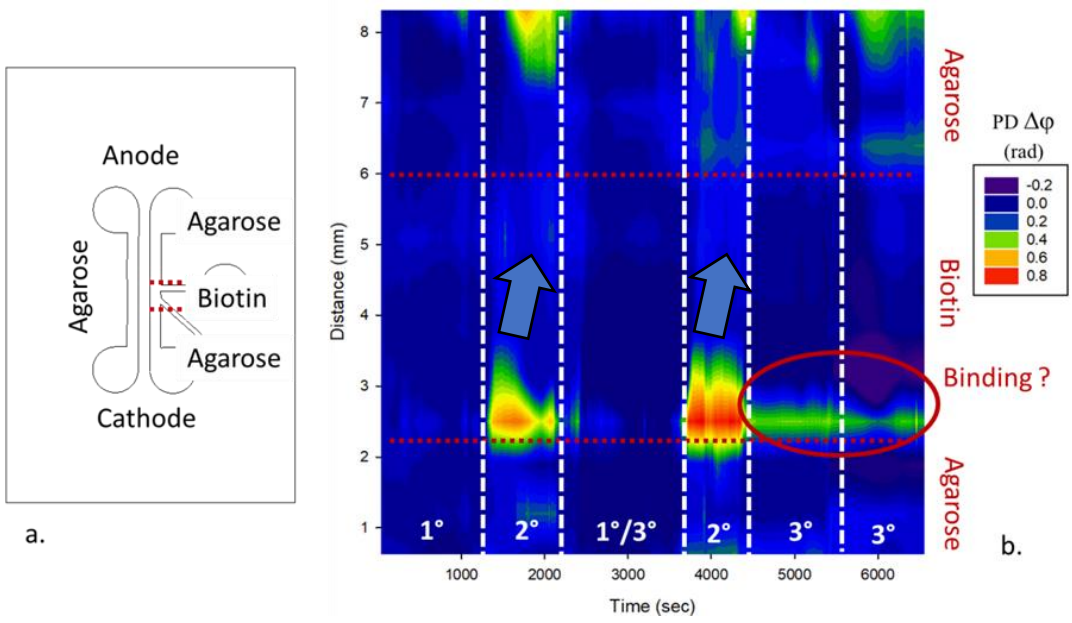

Figure 98 Schematic representation of the chip (a), contour plot showing 7.5 μM BSA, and 20 μM Streptavidin runs in a gel plug configuration (b).

An interesting point is that neither streptavidin nor BSA induced a homogeneous variation of the PD during the run from one electrode to the other. An increasing of PD was appreciable for both molecules between 2 mm and 4 mm. Intriguingly, the plug area starts from the same distance. Consequently, an increased PD for BSA and streptavidin could have been caused by the passage of the sample in two different gels. The increasing of PD around that area could be due to the intersection between the two gels with different characteristics. Furthermore, analysing the measurement for the

streptavidin run until the end, it is possible to notice a more substantial increase of the PD during the run and a decrease after the two washing steps, however still a higher variation compared to the difference between the top and the bottom of the channel. In this instance, the binding was visible only in some part of the plug (the area is only 1.5 mm long, instead of 3.6 mm), but the sensor was still able to distinguish the two analytes. Since no good reproducibility was achievable, different pH values have been tested. The second buffer employed was 10 mM PBS at a pH of 9.2. Since the pI of the two analytes (BSA and Streptavidin) is around 4-5 pH, the hypothesis was to increase the alkalinity of the environment. The example reported in Figure 99 shows the run of 15 μM BSA (15 V for 15 minutes) followed by a buffer rinsing (pH 9.2, 15 V for 20 minutes), and by the addition of 20 μM streptavidin, followed by a final washing step.

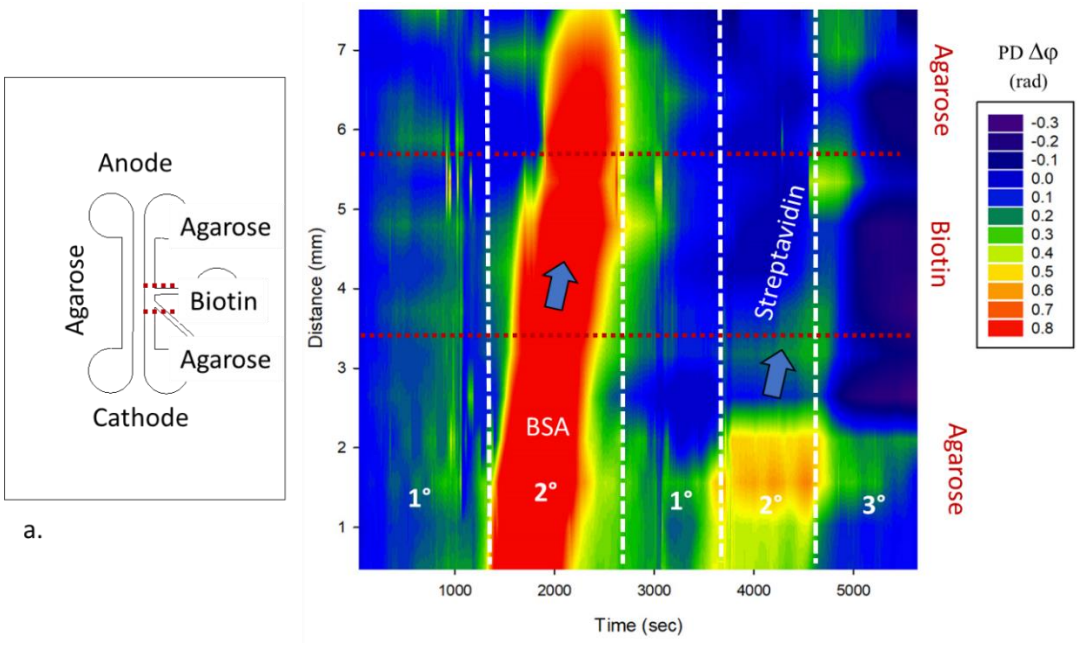

Figure 99 Schematic representation of the chip (a), contour plot showing 15 μM BSA, and 20 μM Streptavidin runs in a gel plug configuration (b).

Unlike the case of pH 7.4, the BSA run caused a more homogeneous modification of the PD along the channel, however the rinsing step presented some unexpected inconsistencies. Similarly, to the example before, the streptavidin run seemed to stop at the edges between the plug and the untreated agarose (2-3 mm distance). However, in the plug configuration the streptavidin-biotin biding in pH 9.2 caused a decrease of the PD, rather than an increase.

Hence, it was thought to test the system in acidic environment, since the affinity between the two molecules is such that it may not be influenced by pH variation.

The following experiment refer to 20 μM streptavidin in 2 mM biotin-gel plug in a pH 3.2 buffer system (Figure 100). After the first washing to stabilise the system and the application of 10 V for 20 minutes (not reported in the plot), the streptavidin run was much more easily tracked compare with the previous two pH values tested.

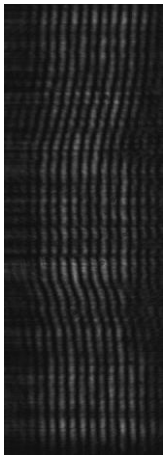

Interference Pattern where is evident the plug

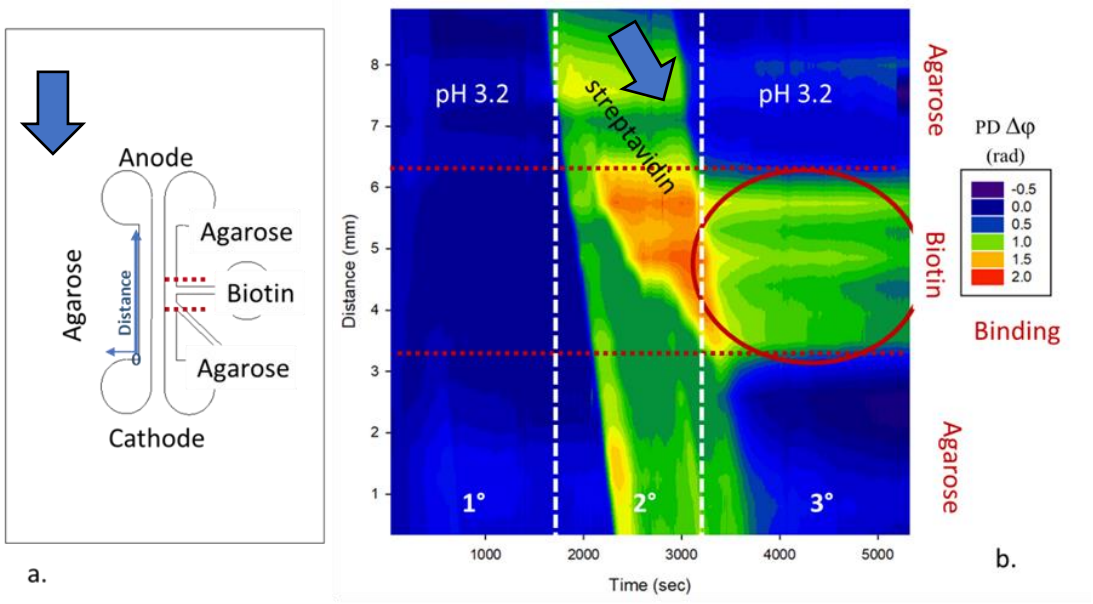

*Figure 100 Schematic representation of the chip (a), contour plot showing 20 μM Streptavidin runs in a gel plug configuration, 2mM Biotin gel plug (b). Interference pattern in the plug configuration at **pH 3.**2. On the left is also reported the interference pattern recorded.*

As the solution approached the plug, an increase of PD is visible but, unlike before, the area was more compatible with the plug region. More importantly, the PD values in the central area remain higher than the values at the bottom and the top of the chip during

the buffer rinsing. Furthermore, it was possible to observe a small decrease of PD as the target solution passes through the plug, as a confirmation that part of the analyte is binding on the plug and, consequently, the concentration of the sample in solution was lower than the starting one. In contrast with all the previous measurements, it appeared evident that, in this different setting, the binding was more easily trackable. As a further proof, Figure 100 shows how, in the interference pattern, it was straightforward to distinguish the shift of the fringes in the central area, corresponding to the plug region. As shown in the previous cases, the selectivity has been tested by running BSA and streptavidin both separately (Figure 101) and together (Figure 102).

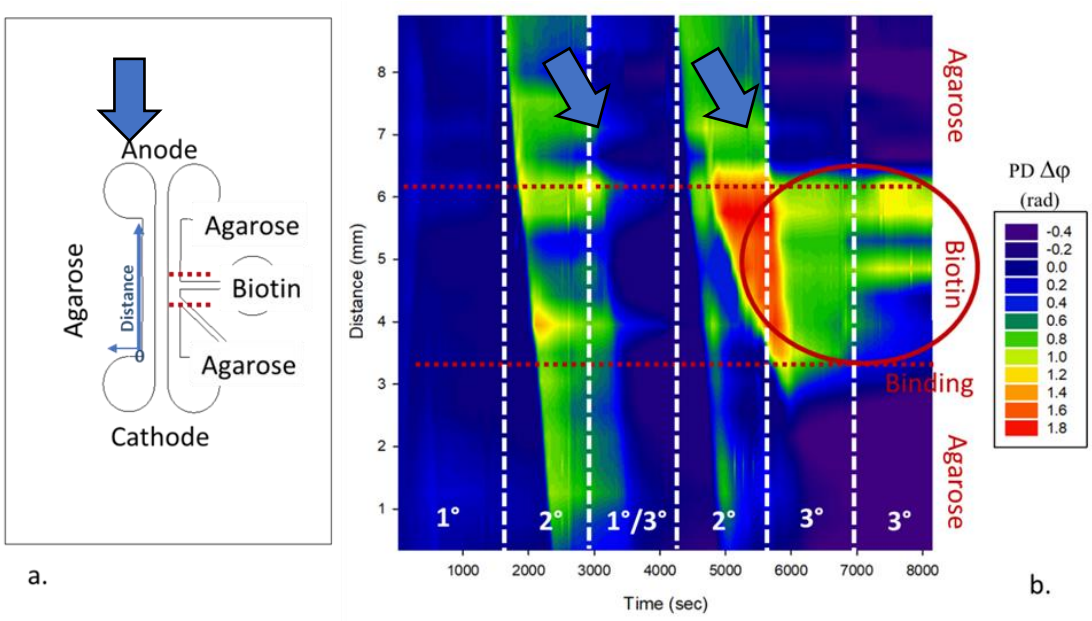

Figure 101 Schematic representation of the chip (a), contour plot showing 15 μM BSA, and 20 μM Streptavidin runs in a gel plug configuration (b).

In the counter plot in Figure 101, after the 15 μM BSA run, wash step with a pH 3.2 buffer removed all unreacted molecules. After the 20 μM streptavidin run, the two rinsing steps highlighted the contrast in PD values of the central part (plug region) with the other two areas of the channel.

The same plot shows that the PD induced by the streptavidin run presented a higher value in the plug zone and a strong decreasing immediately after the plug. In the plot reported in Figure 102, both of analytes were dissolved in the same pH solution (7.5 μM BSA and 10 μM streptavidin, in pH 3.2).

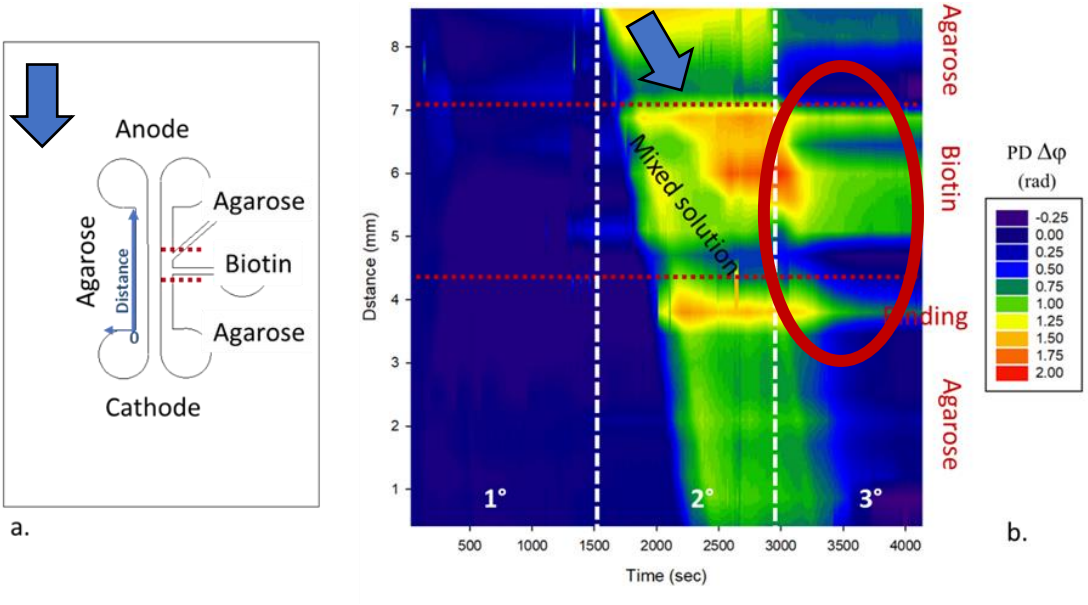

Figure 102 Schematic representation of the chip (a), contour plot showing mixed solution (7.5 μM BSA, and 10 μM Streptavidin) runs in a gel plug configuration (b).

Similarly, to the previous plot, in these experiments the binding sites are visible in the area between 4 mm and 7 mm. Furthermore, the decreasing of PD after the interaction of the plug resulted less pronounced, since the solution was composed of BSA, rather than streptavidin only.

To confirm the quite good reproducibility, further investigation was attempted.

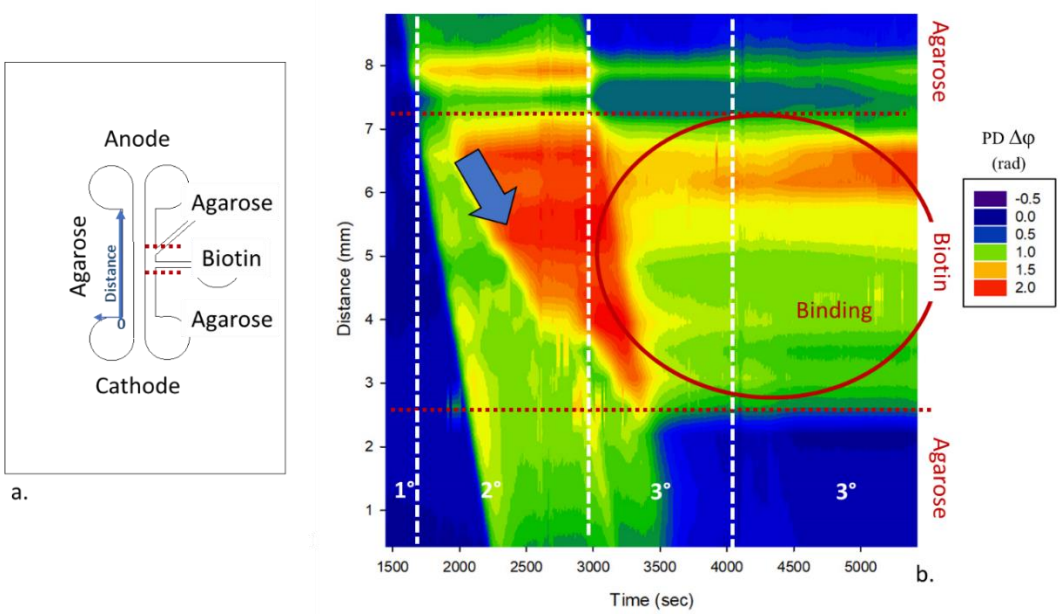

Figure 103 Schematic representation of the chip (a), contour plot showing 20 μM Streptavidin runs in a gel plug configuration, 1mM biotin plug gel (b).

The 2 mM Biotin-gel was diluted in untreated agarose (pH 3.2) with 1:2 ratio, to obtain a 1 mM biotin-gel. The streptavidin binding on 1 mM biotin plug is showed in Figure 103 Comparing the PD value during the washing reported in the plot of Figure 100 ($\Delta\varphi\sim$ 1 rad) with the value in plot of Figure 103 ($\Delta\varphi\sim$ 1 rad), it is possible to notice that decreasing the biotin concentration on the gel support did not induced a significant decrease of the PD value. Instead of reducing the binding sites on the agarose gel, the streptavidin concentration has been decreased and the system was tested for the concentrations 2 μM, 200 nM and 20 nM. Regrettably, the results with the latter two concentrations (200 nM and 20 nM) were not distinguishable and are not here reported.

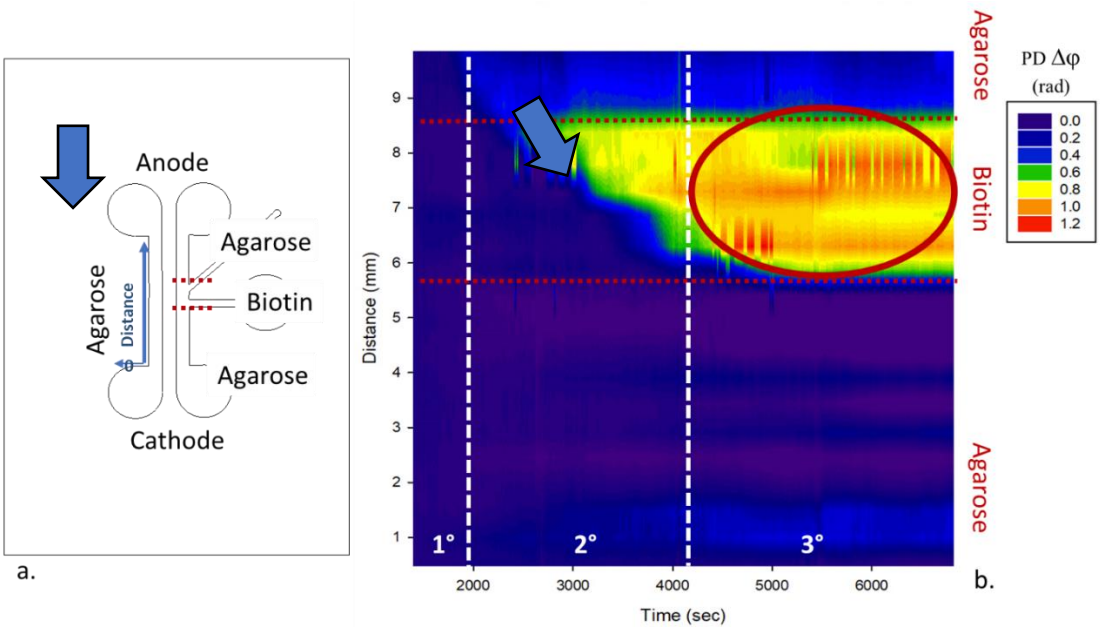

Figure 104 Schematic representation of the chip (a), contour plot showing 2 μM Streptavidin run in a gel plug configuration (b).

The 2 μM streptavidin run is reported in Figure 104, where the PD values of the streptavidin was 0.10 radians (slightly visible in the top part of the plot) but, as the solution passed through the plug, the PD increased and remained constant after the two washing steps (pH 3.2 buffer, 10 V 15 minutes each). The 2μM streptavidin represent the lowest concentration detectable by the instrument.

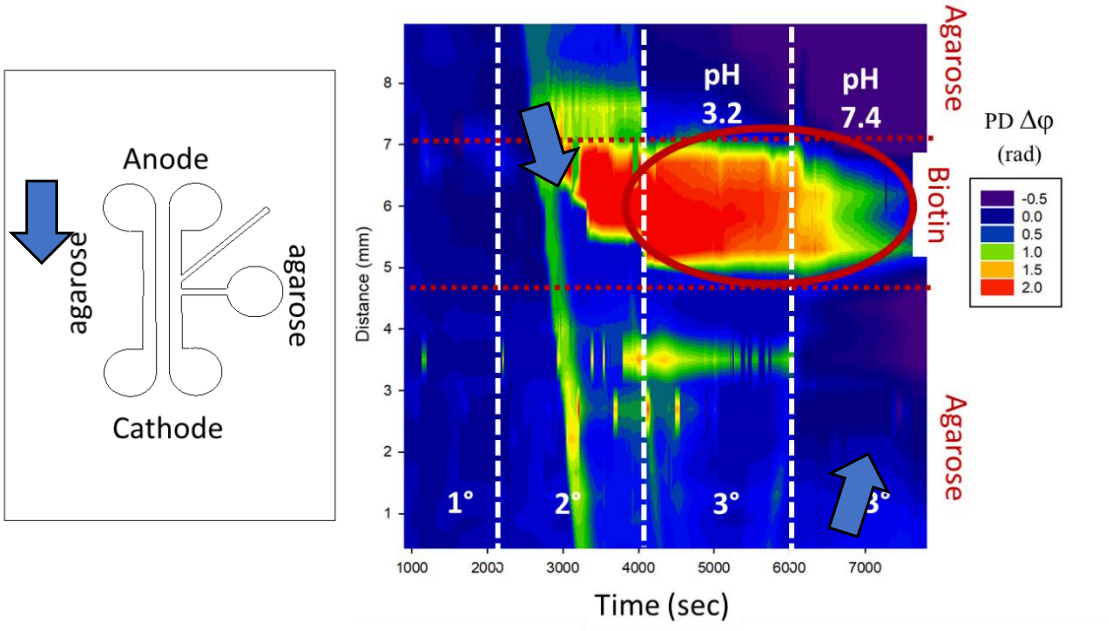

Figure 105 Schematic representation of the plug chip (a), counter plot of 20 μM streptavidin run in 2 mM Biotin gel plug followed by a wash of pH 3.2 and a wash of pH 7.4.

Finally, as it was evident that at pH 3.2 the interferometer was able to track the streptavidin binding better than neutral or alkaline environment, instead of running two washings with the same pH, in the following plot (Figure 105) only the first rinsing was performed at pH 3.2, while the final washing was done at pH 7.4. As it is possible to note, until 6000 seconds the plug region could be tracked. However, after that time, when the pH 7.4 was used, the PD decreased. This last experiment suggests that reproducibility and the possibility to distinguish different regions within the gel might be influenced by the pH of the surroundings.

6.5.6 Comments and discussion

Someone could notice that the concentrations used for Streptavidin, BSA in the pH 7.4 and 9.2 scenarios were not always the same. This is because their concentrations were ranged between 4 μM and 20 μM for the Streptavidin, while the BSA was ranged between, values that are tracked by the interferometer. Then, for calibration reasons, the same conditions were repeated more times and the results, here not all of them showed, were not comparable between each other. The plots reported here are the ones more significant out of the experiments performed and are the one that required

few external interventions during the analysing process. This aspect reflects the difficulty to obtain a good reproducibility. Every combination of all the variables were performed two or three times, even the same day, but the results were not comparable. The causes have already been presented (acquisition, buffers steps).

Nevertheless, it is evident that the reproducibility and the clarity of the data are better for the pH 3.2 environment, rather than for the other basic environments tested. In all the measurements performed in the acid environment it is clear a local increase of the PD corresponding exactly on the plug area, where the biotin-gel is present. One hypothesis of the lack of reproducibility in the other two pHs tested could be the high S/N ratio due to a difference in electric current in the system. Since, each electrode is connected with both channels, the sensing system can be compared to an electric circuit where the resistances are connected in parallel (Figure 106). The currents, i_1 and i_2, are equal only if both the resistances are also equal. In the sensing system here presented, this is not possible, since in the sensing channel there are the recognition elements and the target analytes, which are absent in the reference channel.

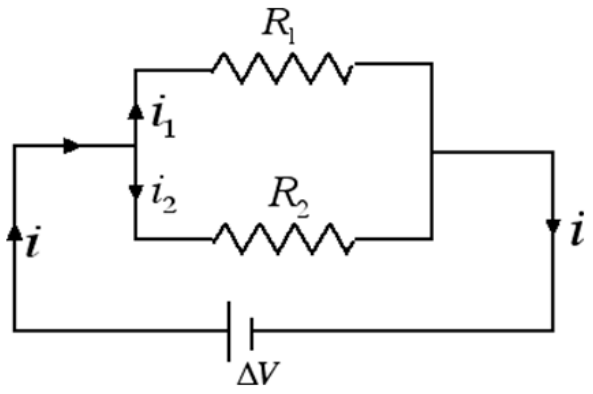

Figure 106 Schematic representation of the electric circuit of the channels system, where R_1 and R_2 represent the electric resistance of the sensing and reference channels, respectively. While i_1 and i_2 are their currents.

The difference in resistance is very small, but it may become more relevant in some buffered surrounds, such as the neutral and the alkaline here presented, where the ions are represented principally by NaH_2PO_4, Na_2HPO_4 and Na_3PO_4, whereas HCl molecules are a further source of ions in pH 3.2 buffer. The consequences of a larger difference in currents in the two channels may translate into the interferometric system as a difference in refractive index in the two channels, and so in turn causes noise in the PD

acquisition. If that is the case, to reduce this noise a solution could be to fill the reference channel as the sensing channel.

The HCl molecules may be the reason for the lower electric current recorded in the acidic surrounding experiments. In turn, that could translate into a lower noise of the buffer background, which then allowed a better tracking of the streptavidin binding. From the control experiments of the three pH buffers, is evident that the most stable is the pH 3.2.

The second hypothesis is that at pH 3.2 the streptavidin experiences a denaturation which causes protein aggregation, thus making the analyte more compact, but still reactive with the biotin. As mentioned before, the affinity of the Streptavidin-Biotin system is so strong it is able to endure in extreme pHs. The aggregation behaviour could cause the higher variation of PD recorded in the acidic system, since it may result in a more compact shape than in other pHs environment, consequently generating an increase in the refractive index and, in turn, the phase difference result to be distinguished more visibly by the interferometer. In other words, in equal biotin and streptavidin concentrations, the binding could be more visible in acidic surroundings due to the compactness of the streptavidin, rather in neutral or basic environments. One hypothesis does not exclude the other one and further investigation are needed, such as the ionic strength of the buffer and its influence in the acquisition of the PD, as it has been reported to cause screening effects in electrochemical sensors [344] [347].

Conclusion and final remarks

Through all the previous chapters, the background, the steps pursued, the challenges and the achievements for the development of a biosensor have been described. The interferometer has been characterised with its low and high limit of detection, showing a RIU sensitivity competitive with other optical sensors in the literature. Overall, the data presented here suggests that the interferometric biosensor embedded with electro-kinetic is capable to recognise the target analyte from other molecules in solution, but still requires further works to improve the imaging of the PD spatial variation, and to provide more reproducible data. Regarding the sensor sensitivity, the refractive index resolution of our interferometer is 2.04×10^{-6} RIU, which is give quite competitive with other optical interferometric sensors (table 2, chapter 2). The lowest protein concentration detectable is 0.21% for BSA, which corresponds to 3.15 μM. From the study of the PD at diverse channel heights, even though the 3 mm height produce the best sensitivity, for all the following experiments and the BSA run a 250 μm height has been adopted, since for electrophoresis studies, a higher channel would have caused more thermal noises (Joule effects).

An improvement of the algorithm could address this aspect by reducing the human rectification to settle the data. The software should discriminate better between the real shift of the fringes and the noise from the image of the interference pattern. The algorithm should be implemented in such a way that it can discriminate at least three different peaks that correspond to three constructive fringes. So that the PD value acquired by FFT could be extrapolated by confronting the three values, one for each fringe tracked. Furthermore, a modification of the channel dimensions, such as increase the height of the channel (the optical path) and a reduction of the length, will improve the limit of detection. As it was explained in chapter 4, this way was not undertaken for this project, since the main aim was to prove the combination of two techniques, rather than improve every aspect of the sensing instrumentation. By observing the **Table 2**, it is evident that the optical path of our instrument is much smaller than most of the interferometer presented in the table. So, as the experimental data have demonstrated

for longer optical path (paragraph 4.3.3.1), by increasing the height of the channel the sensitivity will improve.

Moreover, further investigation into the buffer systems will help to reduce the S/N ratio. A further aspect for the improvement of the sensor are the buffer conditions. By changing the type of buffers (PBS, Tris), the pH and their strengths, the results of the pH junction or the Streptavidin binding on Biotin-gel were studied and achieved. However, a more in-depth study on the buffer electric propriety should reduce the background noise during the interferometer acquisition. A parallel study using an electropherogram or by recording automatically the current and the voltage during the experiments, could boost an improvement on this aspect, as they will contribute to control on those variables.

The next development process should also include the antigen-protein binding. This will universally recognise the instrument as a biosensor, since the final stage of the development includes the measurement of the target analyte from real sample, such as blood or saliva. By adding in the gel matrix antibodies (such as Protein A) the instrument can immobilise the target analyte (which identify a specific diseases), and so being potentially adopted in point-of-care field.

Furthermore, the detection of local binding could be expanded, it opens the option for exploration of multi-detection of the instrument. The next steps should investigate this aspect, by filling the channel with a sequence of different functionalisation gels, so that different regions of the channel will correspond to region with different analyte bindings.

The improvement of each aspect is important in the development of all biosensors. The conversion of this proof-of-concept study to a practical could be the next step that the research should take. In conclusion, even if the project is on the initial steps, we can say that the proof-of-principle has been demonstrated, and all the future challenges have been discussed.

References

1. IUPAC. *https://goldbook.iupac.org/B00663.html*.
2. Battersby, B.J., A. Chen, D. Kozak, and M. Trau, *7 - Biosensors for disease biomarker detection*, in *Biosensors for Medical Applications*, S. Higson, Editor. 2012, Woodhead Publishing. p. 191-216.
3. Ziegler, C., *Cantilever-based biosensors.* Analytical and bioanalytical chemistry, 2004. **379**(7-8): p. 946-959.
4. Webb, A. and P. Townsend, *Refractive index profiles induced by ion implantation into silica.* Journal of Physics D: Applied Physics, 1976. **9**(9): p. 1343.
5. Länge, K., B.E. Rapp, and M. Rapp, *Surface acoustic wave biosensors: a review.* Analytical and bioanalytical chemistry, 2008. **391**(5): p. 1509-1519.
6. Josse, F., F. Bender, and R.W. Cernosek, *Guided shear horizontal surface acoustic wave sensors for chemical and biochemical detection in liquids.* Analytical chemistry, 2001. **73**(24): p. 5937-5944.
7. Karp, F.B., N.A. Bernotski, T.I. Valdes, K.F. Bohringer, and B.D. Ratner, *Foreign body response investigated with an implanted biosensor by in situ electrical impedance spectroscopy.* IEEE Sensors Journal, 2008. **8**(1): p. 104-112.
8. Höök, F., J. Vörös, M. Rodahl, R. Kurrat, P. Böni, J.J. Ramsden, M. Textor, N.D. Spencer, P. Tengvall, J. Gold, and B. Kasemo, *A comparative study of protein adsorption on titanium oxide surfaces using in situ ellipsometry, optical waveguide lightmode spectroscopy, and quartz crystal microbalance/dissipation.* Colloids and Surfaces B: Biointerfaces, 2002. **24**(2): p. 155-170.
9. Martins, T.D., A.C.C. Ribeiro, H.S. de Camargo, P.A. da Costa Filho, H.P.M. Cavalcante, and D.L. Dias, *New insights on optical biosensors: techniques, construction and application*, in *State of the Art in Biosensors-General Aspects*. 2013, InTech.
10. Ciminelli, C., C.M. Campanella, F. Dell'Olio, C.E. Campanella, and M.N. Armenise, *Label-free optical resonant sensors for biochemical applications.* Progress in Quantum Electronics, 2013. **37**(2): p. 51-107.
11. Fan, X.D., I.M. White, S.I. Shopova, H.Y. Zhu, J.D. Suter, and Y.Z. Sun, *Sensitive optical biosensors for unlabeled targets: A review.* Analytica Chimica Acta, 2008. **620**(1-2): p. 8-26.
12. Luan, E., H. Yun, M. Ma, D.M. Ratner, K.C. Cheung, and L. Chrostowski, *Label-free biosensing with a multi-box sub-wavelength phase-shifted Bragg grating waveguide.* Biomedical Optics Express, 2019. **10**(9): p. 4825-4838.
13. Chen, A. and S. Chatterjee, *Nanomaterials based electrochemical sensors for biomedical applications.* Chemical Society Reviews, 2013. **42**(12): p. 5425-5438.
14. Market, B. *https://www.marketsandmarkets.com/Market-Reports/biosensors-market-798.html*.
15. Yetisen, A.K., I. Naydenova, F. da Cruz Vasconcellos, J. Blyth, and C.R. Lowe, *Holographic sensors: three-dimensional analyte-sensitive nanostructures and their applications.* Chemical reviews, 2014. **114**(20): p. 10654-10696.
16. Cunningham, B.T., *Label-free optical biosensors: An introduction.* Label-Free Biosensors: Techniques and Applications, 2009. **1**.
17. Luan, E., H. Shoman, D.M. Ratner, K.C. Cheung, and L. Chrostowski, *Silicon photonic biosensors using label-free detection.* Sensors, 2018. **18**(10): p. 3519.
18. Crespi, A., Y. Gu, B. Ngamsom, H.J. Hoekstra, C. Dongre, M. Pollnau, R. Ramponi, H.H. van den Vlekkert, P. Watts, and G. Cerullo, *Three-dimensional Mach-Zehnder*

interferometer in a microfluidic chip for spatially-resolved label-free detection. Lab on a Chip, 2010. **10**(9): p. 1167-1173.
19. Fernández Gavela, A., D. Grajales García, J.C. Ramirez, and L.M. Lechuga, *Last advances in silicon-based optical biosensors.* sensors, 2016. **16**(3): p. 285.
20. Syahir, A., K. Usui, K.-y. Tomizaki, K. Kajikawa, and H. Mihara, *Label and Label-Free Detection Techniques for Protein Microarrays.* Microarrays, 2015. **4**(2): p. 228.
21. Angelopoulou, M., S. Kakabakos, and P. Petrou, *Label-free biosensors based onto monolithically integrated onto silicon optical transducers.* Chemosensors, 2018. **6**(4): p. 52.
22. Cooper, M.A., *Label-free biosensors: techniques and applications*. 2009: Cambridge University Press.
23. Myers, F.B. and L.P. Lee, *Innovations in optical microfluidic technologies for point-of-care diagnostics.* Lab on a Chip, 2008. **8**(12): p. 2015-2031.
24. Petrou, P., E. Makarona, S. Kakabakos, G. Koukouvinos, K. Misiakos, and I. Raptis, *Chapter 10 - Interferometry-Based Immunoassays*, in *Handbook of Immunoassay Technologies*, S.K. Vashist and J.H.T. Luong, Editors. 2018, Academic Press. p. 241-271.
25. Chen, P., N.-T. Huang, M.-T. Chung, T.T. Cornell, and K. Kurabayashi, *Label-free cytokine micro- and nano-biosensing towards personalized medicine of systemic inflammatory disorders.* Advanced Drug Delivery Reviews, 2015. **95**: p. 90-103.
26. Grieshaber, D., R. MacKenzie, J. Vörös, and E. Reimhult, *Electrochemical biosensors-sensor principles and architectures.* Sensors, 2008. **8**(3): p. 1400-1458.
27. Putzbach, W. and N.J. Ronkainen, *Immobilization techniques in the fabrication of nanomaterial-based electrochemical biosensors: A review.* Sensors, 2013. **13**(4): p. 4811-4840.
28. Pirzada, M. and Z. Altintas, *Recent progress in optical sensors for biomedical diagnostics.* Micromachines, 2020. **11**(4): p. 356.
29. Daghestani, H.N. and B.W. Day, *Theory and applications of surface plasmon resonance, resonant mirror, resonant waveguide grating, and dual polarization interferometry biosensors.* Sensors (Basel, Switzerland), 2010. **10**(11): p. 9630-9646.
30. Makarona, E., P. Petrou, S. Kakabakos, K. Misiakos, and I. Raptis, *Point-of-Need bioanalytics based on planar optical interferometry.* Biotechnology Advances, 2016. **34**(3): p. 209-233.
31. Borisov, S.M. and O.S. Wolfbeis, *Optical biosensors.* Chemical reviews, 2008. **108**(2): p. 423-461.
32. Weng, L., Y. Lu, L. Shi, X. Zhang, L. Zhang, X. Guo, and J. Xu, *In situ investigation of drug diffusion in hydrogels by the refractive index method.* Analytical chemistry, 2004. **76**(10): p. 2807-2812.
33. Gauglitz, G., *Critical assessment of relevant methods in the field of biosensors with direct optical detection based on fibers and waveguides using plasmonic, resonance, and interference effects.* Analytical and Bioanalytical Chemistry, 2020. **412**(14): p. 3317-3349.
34. Gallegos, D., K.D. Long, H. Yu, P.P. Clark, Y. Lin, S. George, P. Nath, and B.T. Cunningham, *Label-free biodetection using a smartphone.* Lab on a Chip, 2013. **13**(11): p. 2124-2132.
35. Zarei, M., *Portable Biosensing Devices for Point-of-Care Diagnostics: Recent Developments and Applications.* TrAC Trends in Analytical Chemistry, 2017.
36. Busch, K., G. Von Freymann, S. Linden, S. Mingaleev, L. Tkeshelashvili, and M. Wegener, *Periodic nanostructures for photonics.* Physics reports, 2007. **444**(3): p. 101-202.

37. Fan, X., I.M. White, S.I. Shopova, H. Zhu, J.D. Suter, and Y. Sun, *Sensitive optical biosensors for unlabeled targets: A review.* analytica chimica acta, 2008. **620**(1): p. 8-26.
38. Lova, P., C. Bastianini, P. Giusto, M. Patrini, P. Rizzo, G. Guerra, M. Iodice, C. Soci, and D. Comoretto, *Label-free vapor selectivity in poly (p-phenylene oxide) photonic crystal sensors.* ACS applied materials & interfaces, 2016. **8**(46): p. 31941-31950.
39. Lee, K. and S.A. Asher, *Photonic crystal chemical sensors: pH and ionic strength.* Journal of the American Chemical Society, 2000. **122**(39): p. 9534-9537.
40. Cunningham, B., P. Li, B. Lin, and J. Pepper, *Colorimetric resonant reflection as a direct biochemical assay technique.* Sensors and Actuators B: Chemical, 2002. **81**(2): p. 316-328.
41. Pal, S., A.R. Yadav, M.A. Lifson, J.E. Baker, P.M. Fauchet, and B.L. Miller, *Selective virus detection in complex sample matrices with photonic crystal optical cavities.* Biosensors and Bioelectronics, 2013. **44**: p. 229-234.
42. Block, I.D., L.L. Chan, and B.T. Cunningham, *Photonic crystal optical biosensor incorporating structured low-index porous dielectric.* Sensors and Actuators B: Chemical, 2006. **120**(1): p. 187-193.
43. Scullion, M.G., T.F. Krauss, and A. Di Falco, *Slotted photonic crystal sensors.* Sensors, 2013. **13**(3): p. 3675-3710.
44. Chen, C. and J. Wang, *Optical biosensors: an exhaustive and comprehensive review.* Analyst, 2020. **145**(5): p. 1605-1628.
45. Choi, E., Y. Choi, Y.H.P. Nejad, K. Shin, and J. Park, *Label-free specific detection of immunoglobulin G antibody using nanoporous hydrogel photonic crystals.* Sensors and Actuators B: Chemical, 2013. **180**: p. 107-113.
46. Maeng, B., Y. Park, and J. Park, *Direct label-free detection of Rotavirus using a hydrogel based nanoporous photonic crystal.* RSC advances, 2016. **6**(9): p. 7384-7390.
47. Inan, H., M. Poyraz, F. Inci, M.A. Lifson, M. Baday, B.T. Cunningham, and U. Demirci, *Photonic crystals: emerging biosensors and their promise for point-of-care applications.* Chemical Society Reviews, 2017. **46**(2): p. 366-388.
48. Whelan, R.J. and R.N. Zare, *Surface plasmon resonance detection for capillary electrophoresis separations.* Anal Chem, 2003. **75**(6): p. 1542-7.
49. Murray, W.A. and W.L. Barnes, *Plasmonic Materials.* Advanced Materials, 2007. **19**(22): p. 3771-3782.
50. Homola, J., *Surface plasmon resonance sensors for detection of chemical and biological species.* Chemical reviews, 2008. **108**(2): p. 462-493.
51. Kussrow, A., C.S. Enders, and D.J. Bornhop, *Interferometric methods for label-free molecular interaction studies.* Analytical chemistry, 2011. **84**(2): p. 779-792.
52. Estevez, M.-C., M. Alvarez, and L.M. Lechuga, *Integrated optical devices for lab-on-a-chip biosensing applications.* Laser & Photonics Reviews, 2012. **6**(4): p. 463-487.
53. Gupta, R. and N.J. Goddard, *Leaky waveguides (LWs) for chemical and biological sensing−A review and future perspective.* Sensors and Actuators B: Chemical, 2020. **322**: p. 128628.
54. Pal, A.K., N.J. Goddard, H.J. Dixon, and R. Gupta, *A Self-Referenced Diffraction-Based Optical Leaky Waveguide Biosensor Using Photofunctionalised Hydrogels.* Biosensors (Basel), 2020. **10**(10).
55. Zinoviev, K.E., A.B. Gonzalez-Guerrero, C. Dominguez, and L.M. Lechuga, *Integrated Bimodal Waveguide Interferometric Biosensor for Label-Free Analysis.* Journal of Lightwave Technology, 2011. **29**(13): p. 1926-1930.
56. Levy, R. and S. Ruschin, *Design of a Single-Channel Modal Interferometer Waveguide Sensor.* Sensors Journal, IEEE, 2009. **9**: p. 146-1.

57. Dostalek, J., J. Čtyroký, J. Homola, E. Brynda, M. Skalský, P. Nekvindova, J. Špirková, J. Škvor, and J. Schröfel, *Surface plasmon resonance biosensor based on integrated optical waveguide.* Sensors and actuators B: Chemical, 2001. **76**(1): p. 8-12.
58. Kumar, M., A. Kumar, and R. Dwivedi, *Ultra high sensitive integrated optical waveguide refractive index sensor based on multimode interference.* Sensors and Actuators B: Chemical, 2016. **222**: p. 556-561.
59. Panzner, B., A. Jöstingmeier, and A. Omar. *A novel multimodal waveguide technique for the broadband characterization of dielectric material parameters*. in *Systems, Signals and Devices (SSD), 2012 9th International Multi-Conference on*. 2012. IEEE.
60. Osterfeld, M., H. Franke, and C. Feger, *Optical gas detection using metal film enhanced leaky mode spectroscopy.* Applied Physics Letters, 1993. **62**(19): p. 2310-2312.
61. Kozma, P., F. Kehl, E. Ehrentreich-Förster, C. Stamm, and F.F. Bier, *Integrated planar optical waveguide interferometer biosensors: A comparative review.* Biosensors and Bioelectronics, 2014. **58**(Supplement C): p. 287-307.
62. Lenney, J.P., N.J. Goddard, J.C. Morey, R.D. Snook, and P.R. Fielden, *An electro-osmotic flow system with integrated planar optical waveguide sensing.* Sensors and Actuators B: Chemical, 1997. **39**(1): p. 212-217.
63. Horváth, R., H.C. Pedersen, N. Skivesen, D. Selmeczi, and N.B. Larsen, *Optical waveguide sensor for on-line monitoring of bacteria.* Optics letters, 2003. **28**(14): p. 1233-1235.
64. Ji, L., X. Sun, G. He, Y. Liu, X. Wang, Y. Yi, C. Chen, F. Wang, and D. Zhang, *Surface plasmon resonance refractive index sensor based on ultraviolet bleached polymer waveguide.* Sensors and Actuators B: Chemical, 2017. **244**: p. 373-379.
65. Kang, M.K., J. Lee, A.H. Nguyen, and S.J. Sim, *Label-free detection of ApoE4-mediated β-amyloid aggregation on single nanoparticle uncovering Alzheimer's disease.* Biosensors and Bioelectronics, 2015. **72**: p. 197-204.
66. Skivesen, N., A. Têtu, M. Kristensen, J. Kjems, L.H. Frandsen, and P.I. Borel, *Photonic-crystal waveguide biosensor.* Optics Express, 2007. **15**(6): p. 3169-3176.
67. Ymeti, A., J.S. Kanger, R. Wijn, P.V. Lambeck, and J. Greve, *Development of a multichannel integrated interferometer immunosensor.* Sensors and Actuators B: Chemical, 2002. **83**(1): p. 1-7.
68. Kim, D.-K., K. Kerman, M. Saito, R.R. Sathuluri, T. Endo, S. Yamamura, Y.-S. Kwon, and E. Tamiya, *Label-free DNA biosensor based on localized surface plasmon resonance coupled with interferometry.* Analytical Chemistry, 2007. **79**(5): p. 1855-1864.
69. Hariharan, P. *Basics of Interferometry*. 1992.
70. Brandenburg, A., *Differential refractometry by an integrated-optical Young interferometer.* Sensors and Actuators B: Chemical, 1997. **39**(1): p. 266-271.
71. Zhou, C., M.K. Hedayati, and A. Kristensen, *Multifunctional waveguide interferometer sensor: simultaneous detection of refraction and absorption with size-exclusion function.* Optics Express, 2018. **26**(19): p. 24372-24383.
72. Guo, Y., J.Y. Ye, C. Divin, B. Huang, T.P. Thomas, J. Baker, James R, and T.B. Norris, *Real-time biomolecular binding detection using a sensitive photonic crystal biosensor.* Analytical chemistry, 2010. **82**(12): p. 5211-5218.
73. Bastos, A.R., C.M.S. Vicente, R. Oliveira-Silva, N.J.O. Silva, M. Tacão, J.P.D. Costa, M. Lima, P.S. André, and R.A.S. Ferreira, *Integrated Optical Mach-Zehnder Interferometer Based on Organic-Inorganic Hybrids for Photonics-on-a-Chip Biosensing Applications.* Sensors (Basel), 2018. **18**(3).
74. Arshavsky-Graham, S., N. Massad-Ivanir, E. Segal, and S. Weiss, *Porous silicon-based photonic biosensors: Current status and emerging applications.* Analytical Chemistry, 2018. **91**(1): p. 441-467.

75. Conroy, P.J., S. Hearty, P. Leonard, and R.J. O'Kennedy, *Antibody production, design and use for biosensor-based applications.* Seminars in Cell & Developmental Biology, 2009. **20**(1): p. 10-26.
76. Charles, P.T., E.R. Goldman, J.G. Rangasammy, C.L. Schauer, M.-S. Chen, and C.R. Taitt, *Fabrication and characterization of 3D hydrogel microarrays to measure antigenicity and antibody functionality for biosensor applications.* Biosensors and Bioelectronics, 2004. **20**(4): p. 753-764.
77. Hermanson, G.T., *Chapter 11 - (Strept)avidin–Biotin Systems*, in *Bioconjugate Techniques (Third Edition)*, G.T. Hermanson, Editor. 2013, Academic Press: Boston. p. 465-505.
78. Hoffmann, C., K. Schmitt, A. Brandenburg, and S. Hartmann, *Rapid protein expression analysis with an interferometric biosensor for monitoring protein production.* Analytical and Bioanalytical Chemistry, 2007. **387**(5): p. 1921-1932.
79. Schneider, B.H., J.G. Edwards, and N.F. Hartman, *Hartman interferometer: versatile integrated optic sensor for label-free, real-time quantification of nucleic acids, proteins, and pathogens.* Clinical chemistry, 1997. **43**(9): p. 1757-1763.
80. Stamm, C. and W. Lukosz, *Integrated optical difference interferometer as biochemical sensor.* Sensors and Actuators B: Chemical, 1994. **18**(1-3): p. 183-187.
81. Maxwell, J.C., *VIII. A dynamical theory of the electromagnetic field.* Philosophical Transactions of the Royal Society of London, 1865. **155**: p. 459-512.
82. Niklasson, G.A., C.G. Granqvist, and O. Hunderi, *Effective medium models for the optical properties of inhomogeneous materials.* Applied Optics, 1981. **20**(1): p. 26-30.
83. Mistrik, J., S. Kasap, H.E. Ruda, C. Koughia, and J. Singh, *Optical Properties of Electronic Materials: Fundamentals and Characterization*, in *Springer Handbook of Electronic and Photonic Materials*, S. Kasap and P. Capper, Editors. 2017, Springer International Publishing: Cham. p. 1-1.
84. Bruggeman, D.A.G., *Berechnung verschiedener physikalischer Konstanten von heterogenen Substanzen. I. Dielektrizitätskonstanten und Leitfähigkeiten der Mischkörper aus isotropen Substanzen.* Annalen der Physik, 1935. **416**(7): p. 636-664.
85. Garnett, J.C.M. and J. Larmor, *Colours in metal glasses and in metallic films.* Proceedings of the Royal Society of London, 1904. **73**(488-496): p. 443-445.
86. Garnett, J.C.M. and J. Larmor, *VII. Colours in metal glasses, in metallic films, and in metallic solutions.—II.* Philosophical Transactions of the Royal Society of London. Series A, Containing Papers of a Mathematical or Physical Character, 1906. **205**(387-401): p. 237-288.
87. Burggraf, N., B. Krattiger, N. F. de Rooij, A. Manz, and A. J. de Mello, *Holographic refractive index detector for application in microchip-based separation systems.* Analyst, 1998. **123**(7): p. 1443-1447.
88. Dunn, R.C., *High-Speed Capillary Electrophoresis Using a Thin-Wall Fused-Silica Capillary Combined with Backscatter Interferometry.* Analytical Chemistry, 2020. **92**(11): p. 7540-7546.
89. Lai, Y., J.L. Gabayno, M. Cadatal-Raduban, K. Yamanoi, T. Shimizu, and N. Sarukura, *Direct measurement of refractive index and dispersion of optical glass by dual-prism configuration with imaging spectrograph.* Japanese Journal of Applied Physics, 2019. **58**(9): p. 096503.
90. Anghinolfi, L., *Self-organized arrays of gold nanoparticles: morphology and plasmonic properties*. 2012: Springer Science & Business Media.
91. Young, T., *I. The Bakerian Lecture. Experiments and calculations relative to physical optics.* Philosophical Transactions of the Royal Society of London, 1804. **94**: p. 1-16.

92. Chaussard, F., H. Rigneault, and C. Finot, *Two-wave interferences space-time duality: Young slits, Fresnel biprism and Billet bilens.* Optics Communications, 2017. **397**: p. 31-38.
93. Jackson, D.P., N. Ferris, R. Strauss, H. Li, and B.J. Pearson, *Subtleties with Young's double-slit experiment: Investigation of spatial coherence and fringe visibility.* American Journal of Physics, 2018. **86**(9): p. 683-689.
94. Hariharan, P., *Basics of interferometry*. 2010: Elsevier.
95. Hariharan, P. and P. Hariharan, *2 - Interference: A Primer*, in *Basics of Interferometry (Second Edition)*, P. Hariharan and P. Hariharan, Editors. 2007, Academic Press: Burlington. p. 3-12.
96. Brandenburg, A., R. Krauter, C. Künzel, M. Stefan, and H. Schulte, *Interferometric sensor for detection of surface-bound bioreactions.* Applied Optics, 2000. **39**(34): p. 6396-6405.
97. Born, M. and E. Wolf, *Principles of Optics: Electromagnetic Theory of Propagation, Interference and Diffraction of Light*. 7 ed. 1999, Cambridge: Cambridge University Press.
98. Van Altena, W.F., *Astrometry for astrophysics: methods, models, and applications*. 2013: Cambridge University Press.
99. Pearson, B.J., N. Ferris, R. Strauss, H. Li, and D.P. Jackson, *Measurements of slit-width effects in Young's double-slit experiment for a partially-coherent source.* OSA Continuum, 2018. **1**(2): p. 755-763.
100. Wang, Z. and D.J. Bornhop, *Dual-capillary backscatter interferometry for high-sensitivity nanoliter-volume refractive index detection with density gradient compensation.* Analytical chemistry, 2005. **77**(24): p. 7872-7877.
101. Lukosz, W., *Principles and sensitivities of integrated optical and surface plasmon sensors for direct affinity sensing and immunosensing.* Biosensors and Bioelectronics, 1991. **6**(3): p. 215-225.
102. Zinoviev, K., L.G. Carrascosa, J. Sánchez del Río, B. Sepulveda, C. Domínguez, and L.M. Lechuga, *Silicon photonic biosensors for lab-on-a-chip applications.* 2008.
103. Angelopoulou, M., S. Kakabakos, and P. Petrou, *Label-Free Biosensors Based onto Monolithically Integrated onto Silicon Optical Transducers.* Chemosensors, 2018. **6**(4).
104. Maldonado, J., M.C. Estévez, A. Fernández-Gavela, J.J. González-López, A.B. González-Guerrero, and L.M. Lechuga, *Label-free detection of nosocomial bacteria using a nanophotonic interferometric biosensor.* Analyst, 2020. **145**(2): p. 497-506.
105. Kozma, P., F. Kehl, E. Ehrentreich-Förster, C. Stamm, and F.F. Bier, *Integrated planar optical waveguide interferometer biosensors: A comparative review.* Biosensors and Bioelectronics, 2014. **58**: p. 287-307.
106. Brandenburg, A. and R. Henninger, *Integrated optical Young interferometer.* Applied optics, 1994. **33**(25): p. 5941-5947.
107. Brandenburg, A., *Differential refractometry by an integrated-optical Young interferometer.* Sensors and Actuators B: Chemical, 1997. **39**(1-3): p. 266-271.
108. Cross, G.H., Y. Ren, and N.J. Freeman, *Young's fringes from vertically integrated slab waveguides: applications to humidity sensing.* Journal of applied physics, 1999. **86**(11): p. 6483-6488.
109. Cross, G.H., A. Reeves, S. Brand, M.J. Swann, L.L. Peel, N.J. Freeman, and J.R. Lu, *The metrics of surface adsorbed small molecules on the Young's fringe dual-slab waveguide interferometer.* Journal of Physics D: Applied Physics, 2003. **37**(1): p. 74.
110. Ymeti, A., J.S. Kanger, R. Wijn, P.V. Lambeck, and J. Greve. *Building of a Highly Sensitive Two-Channel Integrated Optical Young Interferometer as the First Step Towards Constructing an Integrated Multichannel Interferometer Immunosensor*. 2001. Dordrecht: Springer Netherlands.

111. Ymeti, A., J.S. Kanger, J. Greve, P.V. Lambeck, R. Wijn, and R.G. Heideman, *Realization of a multichannel integrated Young interferometer chemical sensor.* Applied optics, 2003. **42**(28): p. 5649-5660.
112. Ymeti, A., J. Greve, P.V. Lambeck, T. Wink, S.W. van Hövell, T.A. Beumer, R.R. Wijn, R.G. Heideman, V. Subramaniam, and J.S. Kanger, *Fast, ultrasensitive virus detection using a young interferometer sensor.* Nano letters, 2007. **7**(2): p. 394-397.
113. Schmitt, K., B. Schirmer, C. Hoffmann, A. Brandenburg, and P. Meyrueis, *Interferometric biosensor based on planar optical waveguide sensor chips for label-free detection of surface bound bioreactions.* Biosensors and Bioelectronics, 2007. **22**(11): p. 2591-2597.
114. Hradetzky, D., C. Mueller, and H. Reinecke, *Interferometric label-free biomolecular detection system.* Journal of Optics A: Pure and Applied Optics, 2006. **8**(7): p. S360-S364.
115. Hiltunen, M., J. Hiltunen, P. Stenberg, S. Aikio, L. Kurki, P. Vahimaa, and P. Karioja, *Polymeric slot waveguide interferometer for sensor applications.* Optics Express, 2014. **22**(6): p. 7229-7237.
116. Ahmadi, L., M. Hiltunen, P. Stenberg, J. Hiltunen, S. Aikio, M. Roussey, J. Saarinen, and S. Honkanen, *Hybrid layered polymer slot waveguide Young interferometer.* Optics Express, 2016. **24**(10): p. 10275-10285.
117. Qi, Z.-m., S. Zhao, F. Chen, R. Liu, and S. Xia, *Performance investigation of an integrated Young interferometer sensor using a novel prism-chamber assembly.* Optics Express, 2010. **18**(7): p. 7421-7426.
118. Wong, W.R. and P. Berini, *Integrated multichannel Young's interferometer sensor based on long-range surface plasmon waveguides.* Optics express, 2019. **27**(18): p. 25470-25484.
119. Divitt, S., M. Frimmer, T.D. Visser, and L. Novotny, *Modulation of optical spatial coherence by surface plasmon polaritons.* Optics Letters, 2016. **41**(13): p. 3094-3097.
120. Kalbarczyk, A., L. Jaroszewicz, N. Bennis, M. Chrusciel, and P. Marc, *The Young Interferometer as an Optical System for a Variable Depolarizer Characterization.* Sensors, 2019. **19**: p. 3037.
121. Makarona, E., A. Salapatas, I. Raptis, P. Petrou, S. Kakabakos, E. Stavra, A. Malainou, and K. Misiakos, *Broadband Young interferometry for simultaneous dual polarization bioanalytics.* Journal of the Optical Society of America B, 2017. **34**(8): p. 1691-1698.
122. Gupta, R., E. Labella, and N.J. Goddard, *An Optofluidic Young Interferometer Sensor for Real-Time Imaging of Refractive Index in µTAS Applications.* Sensors and Actuators B: Chemical, 2020: p. 128491.
123. Wang, M., S. Uusitalo, C. Liedert, J. Hiltunen, L. Hakalahti, and R. Myllylä, *Polymeric dual-slab waveguide interferometer for biochemical sensing applications.* Applied optics, 2012. **51**(12): p. 1886-1893.
124. Wang, M., J. Hiltunen, C. Liedert, L. Hakalahti, and R. Myllylä, *An integrated Young interferometer based on UV-imprinted polymer waveguides for label-free biosensing applications.* Journal of the European Optical Society-Rapid publications, 2012. **7**.
125. Aikio, S., M. Zeilinger, J. Hiltunen, L. Hakalahti, J. Hiitola-Keinänen, M. Hiltunen, V. Kontturi, S. Siitonen, J. Puustinen, P. Lieberzeit, and P. Karioja, *Disposable (bio)chemical integrated optical waveguide sensors implemented on roll-to-roll produced platforms.* RSC Advances, 2016. **6**(56): p. 50414-50422.
126. Dullo, F.T., M. Ingvaldsen, J. Jágerská, S.K. Jacobsen, and O.G. Hellesø, *Temperature Sensitivity of a Waveguide Young Interferometer.* IEEE Photonics Technology Letters, 2016. **28**: p. 1205-1208.
127. Carnal, O. and J. Mlynek, *YOUNGS DOUBLE-SLIT EXPERIMENT WITH ATOMS - A SIMPLE ATOM INTERFEROMETER.* Physical Review Letters, 1991. **66**(21): p. 2689-2692.

128. Heideman, R.G., R.P.H. Kooyman, and J. Greve, *Development of an optical waveguide interferometric immunosensor.* Sensors and Actuators B: Chemical, 1991. **4**(3): p. 297-299.
129. Heideman, R., R. Kooyman, and J. Greve, *Performance of a highly sensitive optical waveguide Mach-Zehnder interferometer immunosensor.* Sensors and Actuators B: Chemical, 1993. **10**(3): p. 209-217.
130. Heideman, R.G. and P.V. Lambeck, *Remote opto-chemical sensing with extreme sensitivity: Design, fabrication and performance of a pigtailed integrated optical phase-modulated Mach-Zehnder interferometer system*. Vol. 61. 1999. 100-127.
131. Brosinger, F., H. Freimuth, M. Lacher, W. Ehrfeld, E. Gedig, A. Katerkamp, F. Spener, and K. Cammann, *A label-free affinity sensor with compensation of unspecific protein interaction by a highly sensitive integrated optical Mach–Zehnder interferometer on silicon.* Sensors and Actuators B: Chemical, 1997. **44**(1): p. 350-355.
132. Schipper, E., A. Brugman, C. Domínguez, L.M. Lechuga, R. Kooyman, and J. Greve, *The realization of an integrated Mach-Zehnder waveguide immunosensor in silicon technology.* Sensors and Actuators B: Chemical, 1997. **40**(2-3): p. 147-153.
133. Prieto, F., B. Sepúlveda, A. Calle, A. Llobera, C. Domınguez, and L.M. Lechuga, *Integrated Mach–Zehnder interferometer based on ARROW structures for biosensor applications.* Sensors and actuators B: Chemical, 2003. **92**(1-2): p. 151-158.
134. Sepúlveda, B., J.S. Del Rio, M. Moreno, F.J. Blanco, K. Mayora, C. Domínguez, and L.M. Lechuga, *Optical biosensor microsystems based on the integration of highly sensitive Mach–Zehnder interferometer devices.* Journal of Optics A: Pure and Applied Optics, 2006. **8**(7): p. S561.
135. Tung, K., W. Wong, and E. Pun, *Polymeric optical waveguides using direct ultraviolet photolithography process.* Applied Physics A, 2005. **80**(3): p. 621-626.
136. Bruck, R., E. Melnik, P. Muellner, R. Hainberger, and M. Lämmerhofer, *Integrated polymer-based Mach-Zehnder interferometer label-free streptavidin biosensor compatible with injection molding.* Biosensors and Bioelectronics, 2011. **26**(9): p. 3832-3837.
137. Sepúlveda, B., G. Armelles, and L. Lechuga, *Magneto-optical phase modulation in integrated Mach–Zehnder interferometric sensors.* Sensors and Actuators A: Physical, 2007. **134**(2): p. 339-347.
138. Berini, P., *Bulk and surface sensitivities of surface plasmon waveguides.* New Journal of Physics, 2008. **10**(10): p. 105010.
139. Lee, D.E., Y.J. Lee, E. Shin, and S.-H. Kwon, *Mach-Zehnder interferometer refractive index sensor based on a plasmonic channel waveguide.* Sensors, 2017. **17**(11): p. 2584.
140. Yang, X., M. Zhou, S. Li, Z. Liu, J. Yang, H. Xu, T. Yuan, X. Qi, H. Li, and L. Yuan, *On-line dynamic detection in the electrophoretic separation by tapered optical fiber interferometer.* Sensors and Actuators B: Chemical, 2016. **242**.
141. Misiakos, K., I. Raptis, E. Makarona, A. Botsialas, A. Salapatas, P. Oikonomou, A. Psarouli, P. Petrou, S. Kakabakos, and K. Tukkiniemi, *All-silicon monolithic Mach-Zehnder interferometer as a refractive index and bio-chemical sensor.* Optics Express, 2014. **22**(22): p. 26803-26813.
142. Gajos, K., M. Angelopoulou, P. Petrou, K. Awsiuk, S. Kakabakos, W. Haasnoot, A. Bernasik, J. Rysz, M.M. Marzec, K. Misiakos, I. Raptis, and A. Budkowski, *Imaging and chemical surface analysis of biomolecular functionalization of monolithically integrated on silicon Mach-Zehnder interferometric immunosensors.* Applied Surface Science, 2016. **385**: p. 529-542.
143. Gajos, K., A. Budkowski, P. Petrou, V. Pagkali, K. Awsiuk, J. Rysz, A. Bernasik, K. Misiakos, I. Raptis, and S. Kakabakos, *Protein adsorption/desorption and antibody*

binding stoichiometry on silicon interferometric biosensors examined with TOF-SIMS. Applied Surface Science, 2018. **444**: p. 187-196.
144. Sun, L.-P., T. Huang, Z. Yuan, M. Yang, Y. Huang, P. Xiao, and B.-O. Guan, *Ultrasensitive Optofluidic Interferometer for Online Monitoring of Photocatalytic Reactions.* Journal of Lightwave Technology, 2019. **37**(21): p. 5435-5441.
145. Guan, Y., Q. Chen, X. Zhang, Y. Peng, and J. Xu, *Investigation of the gelation process by in-situ interferometry.* Macromolecular rapid communications, 2000. **21**(14): p. 998-1001.
146. Bornhop, D.J., J.C. Latham, A. Kussrow, D.A. Markov, R.D. Jones, and H.S. Sørensen, *Free-Solution, Label-Free Molecular Interactions Studied by Back-Scattering Interferometry.* Science, 2007. **317**(5845): p. 1732.
147. Bornhop, D.J. and N.J. Dovichi, *Simple nanoliter refractive index detector.* Analytical Chemistry, 1986. **58**(2): p. 504-505.
148. Kammer, M.N., A.K. Kussrow, I.R. Olmsted, and D.J. Bornhop, *A Highly Compensated Interferometer for Biochemical Analysis.* ACS Sensors, 2018. **3**(8): p. 1546-1552.
149. Dunn, R.C., *Compact, inexpensive refractive index detection in femtoliter volumes using commercial optical pickup technology.* Analytical Methods, 2019. **11**(17): p. 2303-2310.
150. Blanco, F.J., M. Agirregabiria, J. Berganzo, K. Mayora, J. Elizalde, A. Calle, C. Domínguez, and L.M. Lechuga, *Microfluidic-optical integrated CMOS compatible devices for label-free biochemical sensing.* Journal of Micromechanics and Microengineering, 2006. **16**(5): p. 1006.
151. Khan, M. and S.-Y. Park, *Liquid crystal-based biosensor with backscattering interferometry: A quantitative approach.* Biosensors and Bioelectronics, 2017. **87**: p. 976-983.
152. Brynda, E., M. Houska, A. Brandenburg, and A. Wikerstål, *Optical biosensors for real-time measurement of analytes in blood plasma.* Biosensors and Bioelectronics, 2002. **17**(8): p. 665-675.
153. Aikio, S., M. Zeilinger, J. Hiltunen, L. Hakalahti, J. Hiitola-Keinänen, M. Hiltunen, V. Kontturi, S. Siitonen, J. Puustinen, and P. Lieberzeit, *Disposable (bio) chemical integrated optical waveguide sensors implemented on roll-to-roll produced platforms.* RSC advances, 2016. **6**(56): p. 50414-50422.
154. Heideman, R.G., R.P.H. Kooyman, and J. Greve, *Immunoreactivity of adsorbed anti human chorionic gonadotropin studied with an optical waveguide interferometric sensor.* Biosensors and Bioelectronics, 1994. **9**(1): p. 33-43.
155. Lenferink, A.T., E. Schipper, and R.J.R.o.s.i. Kooyman, *Improved detection method for evanescent wave interferometric chemical sensing.* 1997. **68**(3): p. 1582-1586.
156. Maldonado, J., A.B. González-Guerrero, C. Domínguez, and L.M. Lechuga, *Label-free bimodal waveguide immunosensor for rapid diagnosis of bacterial infections in cirrhotic patients.* Biosensors and Bioelectronics, 2016. **85**(Supplement C): p. 310-316.
157. Dante, S., D. Duval, B. Sepúlveda, A.B. González-Guerrero, J.R. Sendra, and L.M. Lechuga, *All-optical phase modulation for integrated interferometric biosensors.* Optics express, 2012. **20**(7): p. 7195-7205.
158. Mariani, S., L. Pino, L.M. Strambini, L. Tedeschi, and G. Barillaro, *10 000-Fold Improvement in Protein Detection Using Nanostructured Porous Silicon Interferometric Aptasensors.* ACS Sensors, 2016. **1**(12): p. 1471-1479.
159. Kammer, M.N., A.K. Kussrow, R.L. Webster, H. Chen, M. Hoeksema, R. Christenson, P.P. Massion, and D.J. Bornhop, *Compensated Interferometry Measures of CYFRA 21–1 Improve Diagnosis of Lung Cancer.* ACS combinatorial science, 2019. **21**(6): p. 465-472.
160. Markov, D., D. Begari, and D.J. Bornhop, *Breaking the 10-7 Barrier for RI Measurements in Nanoliter Volumes.* Analytical Chemistry, 2002. **74**(20): p. 5438-5441.

161. Dante, S., D. Duval, D. Fariña, A.B. González-Guerrero, and L.M. Lechuga, *Linear readout of integrated interferometric biosensors using a periodic wavelength modulation.* Laser & Photonics Reviews, 2015. **9**(2): p. 248-255.
162. Ghiglia, D.C. and M.D. Pritt. *Two-Dimensional Phase Unwrapping: Theory, Algorithms, and Software*. 1998.
163. Andrews, A.T., *Electrophoresis: theory, techniques, and biochemical and clinical applications*. 1986: Clarenden Press.
164. *Protein Electrophoresis: Applications Guide*. 1994: Hoefer Scientific Instruments.
165. Westermeier, R., T. Naven, and H.R. Höpker, *Proteomics in Practice: A Guide to Successful Experimental Design*. 2008: Wiley.
166. Magdeldin, S., *Gel electrophoresis: Principles and basics*. 2012: BoD–Books on Demand.
167. García-Descalzo, L., E. García-López, A. Alcázar, F. Baquero, and C. Cid, *Gel electrophoresis of proteins.* Gel Electrophoresis/Book, 2012. **1**: p. 57-68.
168. Duarte, L.M., R.C. Moreira, and W.K. Coltro, *Nonaqueous electrophoresis on microchips: A review.* Electrophoresis, 2019.
169. Copper, C.L., *Capillary electrophoresis: Part I. Theoretical and experimental background.* Journal of chemical education, 1998. **75**(3): p. 343.
170. Schmitt-Kopplin, P. and A. Fekete, *The CE Way of Thinking*, in *Capillary Electrophoresis: Methods and Protocols*, P. Schmitt-Kopplin, Editor. 2008, Humana Press: Totowa, NJ. p. 611-629.
171. Huck, C.W. and G.K. Bonn, *Analysis of proteins by capillary electrophoresis*, in *Capillary Electrophoresis*. 2008, Springer. p. 507-540.
172. Ramsey, J.M., S.C. Jacobson, and M.R. Knapp, *Microfabricated chemical measurement systems.* Nature Medicine, 1995. **1**(10): p. 1093-1095.
173. Mark, D., S. Haeberle, G. Roth, F. Von Stetten, and R. Zengerle, *Microfluidic lab-on-a-chip platforms: requirements, characteristics and applications*, in *Microfluidics based microsystems*. 2010, Springer. p. 305-376.
174. Štěpánová, S. and V. Kašička, *Recent applications of capillary electromigration methods to separation and analysis of proteins.* Analytica chimica acta, 2016. **933**: p. 23-42.
175. Kim, J.-B., P. Britz-McKibbin, T. Hirokawa, and S. Terabe, *Mechanistic study on analyte focusing by dynamic pH junction in capillary electrophoresis using computer simulation.* Analytical chemistry, 2003. **75**(16): p. 3986-3993.
176. Hsu, W.-L., D.W. Inglis, M.A. Startsev, E.M. Goldys, M.R. Davidson, and D.J.E. Harvie, *Isoelectric Focusing in a Silica Nanofluidic Channel: Effects of Electromigration and Electroosmosis.* Analytical Chemistry, 2014. **86**(17): p. 8711-8718.
177. Heaney, A. and D.L. Weller, *Isoelectric pH of hemoglobin and cytochrome c by electrofocusing.* Journal of Chemical Education, 1970. **47**(10): p. 724.
178. Kolin, A., *Separation and Concentration of Proteins in a pH Field Combined with an Electric Field.* Journal of Chemical Physics, 1954. **22**: p. 1628-1629.
179. Luner, S.J. and A. Kolin, *A new approach to isoelectric focusing and fractionation of proteins in a pH gradient.* Proceedings of the National Academy of Sciences of the United States of America, 1970. **66**(3): p. 898-903.
180. Startsev, M.A., D.W. Inglis, M.S. Baker, and E.M. Goldys, *Nanochannel pH gradient electrofocusing of proteins.* Analytical chemistry, 2013. **85**(15): p. 7133-7138.
181. Righetti, P.G. and C. Gelfi, *Immobilized pH gradients for isoelectric focusing. III. Preparative separations in highly diluted gels.* Journal of biochemical and biophysical methods, 1984. **9**(2): p. 103-119.
182. Righetti, P.G. and J.W. Drysdale, *Isoelectric focusing in gels.* Journal of Chromatography A, 1974. **98**(2): p. 271-321.

183. Svensson, H., *Isoelectric fractionation, analysis, and characterization of ampholytes in natural pH gradients. I. The differential equation of solute concentrations at a steady state and its solution for simple cases.* Acta Chem. Scand, 1961. **15**(2).
184. Li, G.-Q., H.-G. Li, F.-F. Dong, Y.-F. Bi, Q. Zhang, F.-Z. Kong, X.-P. Liu, S. Saud, H. Xiao, F. Luo, Y. Peng, H.-J. Lu, L.-Y. Fan, Y.-X. Wang, and C.-X. Cao, *Isoelectric focusing array with immobilized pH gradient and dynamic scanning imaging for diabetes diagnosis.* Analytica Chimica Acta, 2019. **1063**: p. 178-186.
185. Görg, A., W. Postel, and S. Günther, *Two-dimensional electrophoresis. The current state of two-dimensional electrophoresis with immobilized pH gradients.* Electrophoresis, 1988. **9**(9): p. 531-546.
186. Sommer, G.J., J. Mai, A.K. Singh, and A.V. Hatch, *Microscale isoelectric fractionation using photopolymerized membranes.* Analytical chemistry, 2011. **83**(8): p. 3120-3125.
187. Righetti, P.G., K. Ek, and B. Bjellqvist, *Polymerization kinetics of polyacrylamide gels containing immobilized pH gradients for isoelectric focusing.* Journal of Chromatography A, 1984. **291**: p. 31-42.
188. Magdeldin, S., Y. Zhang, B. Xu, Y. Yoshida, and T. Yamamoto, *Two-dimensional polyacrylamide gel electrophoresis–a practical perspective.* Gel Electrophoresis-Principles and Basics, 2012: p. 91-116.
189. Herzog, C., E. Beckert, and S. Nagl, *Rapid Isoelectric Point Determination in a Miniaturized Preparative Separation Using Jet-Dispensed Optical pH Sensors and Micro Free-Flow Electrophoresis.* Analytical Chemistry, 2014. **86**(19): p. 9533-9539.
190. Dawod, M., N.E. Arvin, and R.T. Kennedy, *Recent advances in protein analysis by capillary and microchip electrophoresis.* Analyst, 2017. **142**(11): p. 1847-1866.
191. Łapińska, U., K.L. Saar, E.V. Yates, T.W. Herling, T. Müller, P.K. Challa, C.M. Dobson, and T.P.J. Knowles, *Gradient-free determination of isoelectric points of proteins on chip.* Physical Chemistry Chemical Physics, 2017. **19**(34): p. 23060-23067.
192. Nagl, S., *Micro free-flow isoelectric focusing with integrated optical pH sensors.* Engineering in Life Sciences, 2018. **18**(2): p. 114-123.
193. Yu, H., Y. Lu, Y. Zhou, F.-b. Wang, F.-y. He, and X.-H. Xia, *A simple, disposable microfluidic device for rapid protein concentration and purification via direct-printing.* Lab on a chip, 2008. **8**: p. 1496-501.
194. Fritsch, R.J. and I. Krause, *ELECTROPHORESIS*, in *Encyclopedia of Food Sciences and Nutrition (Second Edition)*, B. Caballero, Editor. 2003, Academic Press: Oxford. p. 2055-2062.
195. Haglund, H., *Isotachophoresis.* Science Tools, 1970. **17**(1): p. 2-13.
196. Hsu, W.-L., D.J.E. Harvie, M.R. Davidson, H. Jeong, E.M. Goldys, and D.W. Inglis, *Concentration gradient focusing and separation in a silica nanofluidic channel with a non-uniform electroosmotic flow.* Lab on a Chip, 2014. **14**(18): p. 3539-3549.
197. Breadmore, M.C., W. Grochocki, U. Kalsoom, M.N. Alves, S.C. Phung, M.T. Rokh, J.M. Cabot, A. Ghiasvand, F. Li, and A.I. Shallan, *Recent advances in enhancing the sensitivity of electrophoresis and electrochromatography in capillaries and microchips (2016–2018).* Electrophoresis, 2019. **40**(1): p. 17-39.
198. Breadmore, M.C., R.M. Tubaon, A.I. Shallan, S.C. Phung, A.S. Abdul Keyon, D. Gstoettenmayr, P. Prapatpong, A.A. Alhusban, L. Ranjbar, and H.H. See, *Recent advances in enhancing the sensitivity of electrophoresis and electrochromatography in capillaries and microchips (2012–2014).* Electrophoresis, 2015. **36**(1): p. 36-61.
199. Garcia-Schwarz, G. and J.G. Santiago, *Integration of On-Chip Isotachophoresis and Functionalized Hydrogels for Enhanced-Sensitivity Nucleic Acid Detection.* Analytical Chemistry, 2012. **84**(15): p. 6366-6369.
200. Rogacs, A., L.A. Marshall, and J.G. Santiago, *Purification of nucleic acids using isotachophoresis.* Journal of Chromatography A, 2014. **1335**: p. 105-120.

201. Eid, C. and J. Santiago, *Isotachophoresis applied to biomolecular reactions.* Lab on a Chip, 2018. **18**(1): p. 11-26.
202. Aebersold, R. and H.D. Morrison, *Analysis of dilute peptide samples by capillary zone electrophoresis.* Journal of Chromatography A, 1990. **516**(1): p. 79-88.
203. Britz-McKibbin, P. and D.D.Y. Chen, *Selective Focusing of Catecholamines and Weakly Acidic Compounds by Capillary Electrophoresis Using a Dynamic pH Junction.* Analytical Chemistry, 2000. **72**(6): p. 1242-1252.
204. Zhang, Z., Y. Qu, and N.J. Dovichi, *Capillary zone electrophoresis-mass spectrometry for bottom-up proteomics.* TrAC Trends in Analytical Chemistry, 2018. **108**: p. 23-37.
205. Šlampová, A., Z. Malá, and P. Gebauer, *Recent progress of sample stacking in capillary electrophoresis (2016–2018).* Electrophoresis, 2019. **40**(1): p. 40-54.
206. Cao, C.-X., Y.-Z. He, M. Li, Y.-T. Qian, M.-F. Gao, L.-H. Ge, S.-L. Zhou, L. Yang, and Q.-S. Qu, *Stacking ionizable analytes in a sample matrix with high salt by a transient moving chemical reaction boundary method in capillary zone electrophoresis.* Analytical chemistry, 2002. **74**(16): p. 4167-4174.
207. Booker, C.J., S. Sun, S. Woolsey, J.S. Mejia, and K.K.-C. Yeung, *Removal of sample background buffering ions and myoglobin enrichment via a pH junction created by discontinuous buffers in capillary electrophoresis.* Journal of Chromatography A, 2011. **1218**(33): p. 5705-5711.
208. Kazarian, A.A., E.F. Hilder, and M.C. Breadmore, *Online sample pre-concentration via dynamic pH junction in capillary and microchip electrophoresis.* Journal of separation science, 2011. **34**(20): p. 2800-2821.
209. Zhu, G., L. Sun, and N.J. Dovichi, *Dynamic pH junction preconcentration in capillary electrophoresis-electrospray ionization-mass spectrometry for proteomics analysis.* Analyst, 2016. **141**(18): p. 5216-5220.
210. Nesbitt, C.A., J.T.-M. Lo, and K.K.-C. Yeung, *Over 1000-fold protein preconcentration for microliter-volume samples at a pH junction using capillary electrophoresis.* Journal of Chromatography A, 2005. **1073**(1-2): p. 175-180.
211. Jurcic, K., C.A. Nesbitt, and K.K.-C. Yeung, *Characterization of discontinuous buffer junctions using pH indicators in capillary electrophoresis for protein preconcentration.* Journal of Chromatography A, 2006. **1134**(1-2): p. 317-325.
212. Hou, M., M. Zhang, L. Chen, K. Gong, C. Pan, and Y. Wang, *Amplification of lysozyme signal detected in capillary electrophoresis using mixed polymer brushes coating with switchable properties.* Talanta, 2019. **202**: p. 426-435.
213. Britz-McKibbin, P., G.M. Bebault, and D.D. Chen, *Velocity-difference induced focusing of nucleotides in capillary electrophoresis with a dynamic pH junction.* Analytical chemistry, 2000. **72**(8): p. 1729-1735.
214. Arnett, S.D. and C.E. Lunte, *Enhanced pH-mediated stacking of anions for CE incorporating a dynamic pH junction.* Electrophoresis, 2007. **28**(20): p. 3786-3793.
215. Sonker, M., R. Knob, V. Sahore, and A.T. Woolley, *Integrated electrokinetically driven microfluidic devices with pH-mediated solid-phase extraction coupled to microchip electrophoresis for preterm birth biomarkers.* Electrophoresis, 2017. **38**(13-14): p. 1743-1754.
216. Bisswanger, H., *Enzyme assays.* Perspectives in Science, 2014. **1**(1-6): p. 41-55.
217. Lee, S.V. and A.R. Bahaman, *Discriminatory power of agarose gel electrophoresis in DNA fragments analysis.* Gel Electrophoresis-Principles and Basics, 2012.
218. Yılmaz, M., C. Ozic, and İ. Gok, *Principles of nucleic acid separation by agarose gel electrophoresis.* Gel Electrophoresis–Principles and Basics, 2012. **33**.
219. Desmarais, W.T., D.L. Bienvenue, K.P. Bzymek, R.C. Holz, G.A. Petsko, and D. Ringe, *The 1.20 Å resolution crystal structure of the aminopeptidase from Aeromonas proteolytica complexed with tris: a tale of buffer inhibition.* Structure, 2002. **10**(8): p. 1063-1072.

220. Lide, D.R., *CRC handbook of chemistry and physics: a ready-reference book of chemical and physical data*. 1995: CRC press.
221. Kavoosi, G. and S.K. Ardestani, *Gel electrophoresis of protein–from basic science to practical approach.* Gel Electrophoresis–Principles and Basics, 2012: p. 69.
222. Ou, X., P. Chen, X. Huang, S. Li, and B.F. Liu, *Microfluidic chip electrophoresis for biochemical analysis.* Journal of separation science, 2020. **43**(1): p. 258-270.
223. Calo, E. and V.V. Khutoryanskiy, *Biomedical applications of hydrogels: A review of patents and commercial products.* European Polymer Journal, 2015. **65**: p. 252-267.
224. Lloyd, A.W., R.G.A. Faragher, and S.P. Denyer, *Ocular biomaterials and implants.* Biomaterials, 2001. **22**(8): p. 769-785.
225. Hoffman, A.S., *Hydrogels for biomedical applications.* Advanced drug delivery reviews, 2012. **64**: p. 18-23.
226. Peppas, N.A., *Biomedical applications of hydrogels handbook*. 2010: Springer Science & Business Media.
227. Rosiak, J.M. and F. Yoshii, *Hydrogels and their medical applications.* Nuclear Instruments and Methods in Physics Research Section B: Beam Interactions with Materials and Atoms, 1999. **151**(1): p. 56-64.
228. Pal, A.K., E. Labella, N.J. Goddard, and R. Gupta, *Photofunctionalizable Hydrogel for Fabricating Volume Optical Diffractive Sensors.* Macromolecular Chemistry and Physics, 2019. **220**(16): p. 1970031.
229. Jung, I.Y., J.S. Kim, B.R. Choi, K. Lee, and H. Lee, *Hydrogel based biosensors for in vitro diagnostics of biochemicals, proteins, and genes.* Advanced healthcare materials, 2017. **6**(12): p. 1601475.
230. Mateescu, A., Y. Wang, J. Dostalek, and U. Jonas, *Thin hydrogel films for optical biosensor applications.* Membranes, 2012. **2**(1): p. 40-69.
231. Naghash, H.J. and O. Okay, *Formation and structure of polyacrylamide gels.* Journal of applied polymer science, 1996. **60**(7): p. 971-979.
232. Omidian, H. and K. Park, *Introduction to Hydrogels*, in *Biomedical Applications of Hydrogels Handbook*, R.M. Ottenbrite, K. Park, and T. Okano, Editors. 2010, Springer New York: New York, NY. p. 1-16.
233. Alvarado, A.G., J. Cortés, L.A. Pérez-Carrillo, M. Rabelero, J. Arellano, J.C. Sánchez-Díaz, J.E. Puig, and M. Arellano, *Temperature and pH-Responsive Polyacrylamide/Poly (Acrylic Acid) Interpenetrating Polymer Network Nanoparticles.* Journal of Macromolecular Science, Part B, 2016. **55**(11): p. 1086-1098.
234. Li, W., H. Zhao, P. Teasdale, R. John, and S. Zhang, *Synthesis and characterisation of a polyacrylamide–polyacrylic acid copolymer hydrogel for environmental analysis of Cu and Cd.* Reactive and Functional Polymers, 2002. **52**(1): p. 31-41.
235. Abe, Z., H. Tanaka, and M. Sumimoto, *Copolymerization of acrylamide and allylamine.* Journal of Polymer Science: Polymer Chemistry Edition, 1978. **16**(1): p. 305-308.
236. Zhao, Q., J. Sun, Y. Lin, and Q. Zhou, *Study of the properties of hydrolyzed polyacrylamide hydrogels with various pore structures and rapid pH-sensitivities.* Reactive and Functional polymers, 2010. **70**(9): p. 602-609.
237. Yang, S., J. Liu, C.S. Lee, and D.L. DeVoe, *Microfluidic 2-D PAGE using multifunctional in situ polyacrylamide gels and discontinuous buffers.* Lab on a Chip, 2009. **9**(4): p. 592-599.
238. Pervez, S., M.A. Nawaz, A. Aman, S. Qayyum, F. Nawaz, and S.A.U. Qader, *Agarose Hydrogel Beads: An Effective Approach to Improve the Catalytic Activity, Stability and Reusability of Fungal Amyloglucosidase of GH15 Family.* Catalysis Letters, 2018. **148**(9): p. 2643-2653.
239. Zucca, P., R. Fernandez-Lafuente, and E. Sanjust, *Agarose and its derivatives as supports for enzyme immobilization.* Molecules, 2016. **21**(11): p. 1577.

240. Cooke, M.E., S.W. Jones, B. Ter Horst, N. Moiemen, M. Snow, G. Chouhan, L.J. Hill, M. Esmaeli, R.J. Moakes, and J. Holton, *Structuring of hydrogels across multiple length scales for biomedical applications.* Advanced Materials, 2018. **30**(14): p. 1705013.
241. Drabik, A., A. Bodzoń-Kułakowska, and J. Silberring, *7 - Gel Electrophoresis*, in *Proteomic Profiling and Analytical Chemistry (Second Edition)*, P. Ciborowski and J. Silberring, Editors. 2016, Elsevier: Boston. p. 115-143.
242. Bernal, C., K. Rodríguez, and R. Martínez, *Integrating enzyme immobilization and protein engineering: An alternative path for the development of novel and improved industrial biocatalysts.* Biotechnology Advances, 2018. **36**(5): p. 1470-1480.
243. Mateo, C., J.M. Palomo, M. Fuentes, L. Betancor, V. Grazu, F. López-Gallego, B.C.C. Pessela, A. Hidalgo, G. Fernández-Lorente, R. Fernández-Lafuente, and J.M. Guisán, *Glyoxyl agarose: A fully inert and hydrophilic support for immobilization and high stabilization of proteins.* Enzyme and Microbial Technology, 2006. **39**(2): p. 274-280.
244. Blanco, R.M. and J. Guisán, *Stabilization of enzymes by multipoint covalent attachment to agarose-aldehyde gels. Borohydride reduction of trypsin-agarose derivatives.* Enzyme and Microbial Technology, 1989. **11**(6): p. 360-366.
245. Guisán, J., *Aldehyde-agarose gels as activated supports for immobilization-stabilization of enzymes.* Enzyme and Microbial Technology, 1988. **10**(6): p. 375-382.
246. Hermanson, G.T., *Chapter 3 - The Reactions of Bioconjugation*, in *Bioconjugate Techniques (Third Edition)*, G.T. Hermanson, Editor. 2013, Academic Press: Boston. p. 229-258.
247. Inc., T.F.S. *Instruction, EZ-Link® HydrazideBiotins*. [cited 2011 June 2021]; Available from: https://www.thermofisher.com/document-connect/document-connect.html?url=https%3A%2F%2Fassets.thermofisher.com%2FTFS-Assets%2FLSG%2Fmanuals%2FMAN0011178_EZ_Hydrazide_Biotins_UG.pdf&title=VXNlciBHdWlkZTogIEVaLUxpbmsgSHlkcmF6aWRlIEJpb3RpbnM=.
248. Li, Y., X. Feng, W. Du, Y. Li, and B.-F. Liu, *Ultrahigh-throughput approach for analyzing single-cell genomic damage with an agarose-based microfluidic comet array.* Analytical chemistry, 2013. **85**(8): p. 4066-4073.
249. Ou, G., X. Feng, W. Du, X. Liu, and B.-F. Liu, *Recent advances in microchip electrophoresis for amino acid analysis.* Analytical and bioanalytical chemistry, 2013. **405**(25): p. 7907-7918.
250. Horsman, K.M., J.M. Bienvenue, K.R. Blasier, and J.P. Landers, *Forensic DNA analysis on microfluidic devices: a review.* Journal of forensic sciences, 2007. **52**(4): p. 784-799.
251. Yamamoto, S., F. Okada, M. Kinoshita, and S. Suzuki, *On-line microchip electrophoresis-mediated preconcentration of cationic compounds utilizing cationic polyacrylamide gels fabricated by in situ photopolymerization.* Analyst, 2018. **143**(18): p. 4429-4435.
252. Dhopeshwarkar, R., L. Sun, and R.M. Crooks, *Electrokinetic concentration enrichment within a microfluidic device using a hydrogel microplug.* Lab on a Chip, 2005. **5**(10): p. 1148-1154.
253. Yamamoto, S., M. Himeno, M. Kobayashi, M. Akamatsu, R. Satoh, M. Kinoshita, R. Sugiura, and S. Suzuki, *Microchip electrophoresis utilizing an in situ photopolymerized Phos-tag binding polyacrylamide gel for specific entrapment and analysis of phosphorylated compounds.* Analyst, 2017. **142**(18): p. 3416-3423.
254. Rodríguez-Ruiz, I., V. Babenko, S. Martínez-Rodríguez, and J.A. Gavira, *Protein separation under a microfluidic regime.* Analyst, 2018. **143**(3): p. 606-619.
255. Fang, Q., G.-M. Xu, and Z.-L. Fang, *A high-throughput continuous sample introduction interface for microfluidic chip-based capillary electrophoresis systems.* Analytical chemistry, 2002. **74**(6): p. 1223-1231.

256. Tentori, A.M., A.J. Hughes, and A.E. Herr, *Microchamber integration unifies distinct separation modes for two-dimensional electrophoresis.* Analytical chemistry, 2013. **85**(9): p. 4538-4545.
257. Demierre, N., T. Braschler, P. Linderholm, U. Seger, H. Van Lintel, and P. Renaud, *Characterization and optimization of liquid electrodes for lateral dielectrophoresis.* Lab on a Chip, 2007. **7**(3): p. 355-365.
258. Chen, J., Y. Zhou, D. Wang, F. He, V.M. Rotello, K.R. Carter, J.J. Watkins, and S.R. Nugen, *UV-nanoimprint lithography as a tool to develop flexible microfluidic devices for electrochemical detection.* Lab on a Chip, 2015. **15**(14): p. 3086-3094.
259. Yamamoto, S., S. Hirakawa, and S. Suzuki, *In situ fabrication of ionic polyacrylamide-based preconcentrator on a simple poly (methyl methacrylate) microfluidic chip for capillary electrophoresis of anionic compounds.* Analytical chemistry, 2008. **80**(21): p. 8224-8230.
260. Das, C., J. Zhang, N.D. Denslow, and Z.H. Fan, *Integration of isoelectric focusing with multi-channel gel electrophoresis by using microfluidic pseudo-valves.* Lab on a Chip, 2007. **7**(12): p. 1806-1812.
261. Wu, J. and M. Gu, *Microfluidic sensing: state of the art fabrication and detection techniques.* Journal of biomedical optics, 2011. **16**(8): p. 080901.
262. Xiao, D., T.V. Le, and M.J. Wirth, *Surface modification of the channels of poly (dimethylsiloxane) microfluidic chips with polyacrylamide for fast electrophoretic separations of proteins.* Analytical chemistry, 2004. **76**(7): p. 2055-2061.
263. Bi, H., S. Meng, Y. Li, K. Guo, Y. Chen, J. Kong, P. Yang, W. Zhong, and B. Liu, *Deposition of PEG onto PMMA microchannel surface to minimize nonspecific adsorption.* Lab on a Chip, 2006. **6**(6): p. 769-775.
264. Liu, J., T. Pan, A.T. Woolley, and M.L. Lee, *Surface-modified poly (methyl methacrylate) capillary electrophoresis microchips for protein and peptide analysis.* Analytical chemistry, 2004. **76**(23): p. 6948-6955.
265. He, M. and A.E. Herr, *Microfluidic Polyacrylamide Gel Electrophoresis with in Situ Immunoblotting for Native Protein Analysis.* Analytical Chemistry, 2009. **81**(19): p. 8177-8184.
266. Forrer, K., S. Hammer, and B. Helk, *Chip-based gel electrophoresis method for the quantification of half-antibody species in IgG4 and their by-and degradation products.* Analytical biochemistry, 2004. **334**(1): p. 81-88.
267. Sommer, G.J., A.K. Singh, and A.V. Hatch, *On-chip isoelectric focusing using photopolymerized immobilized pH gradients.* Analytical chemistry, 2008. **80**(9): p. 3327-3333.
268. Yamauchi, K.A., A.M. Tentori, and A.E. Herr, *Arrayed isoelectric focusing using photopatterned multi-domain hydrogels.* ELECTROPHORESIS, 2018. **39**(8): p. 1040-1047.
269. Albrecht, J.W. and K.F. Jensen, *Micro freef-low IEF enhanced by active cooling and functionalized gels.* Electrophoresis, 2006. **27**(24): p. 4960-4969.
270. Herzog, C., E. Poehler, A.J. Peretzki, S.M. Borisov, D. Aigner, T. Mayr, and S. Nagl, *Continuous on-chip fluorescence labelling, free-flow isoelectric focusing and marker-free isoelectric point determination of proteins and peptides.* Lab on a Chip, 2016. **16**(9): p. 1565-1572.
271. Riddick, L. and W.C. Brumley, *Capillary Electrophoresis With Laser-Induced Fluorescence*, in *Capillary Electrophoresis: Methods and Protocols*, P. Schmitt-Kopplin, Editor. 2008, Humana Press: Totowa, NJ. p. 119-134.
272. Wang, J., Y. Zhang, Y. Okamoto, N. Kaji, M. Tokeshi, and Y. Baba, *Online transient isotachophoresis concentration by the pseudo-terminating electrolyte buffer for the*

separation of DNA–aptamer and its thrombin complex in poly (methyl methacrylate) microchip. Analyst, 2011. **136**(6): p. 1142-1147.
273. Yu, H., Y. Lu, Y.-g. Zhou, F.-b. Wang, F.-y. He, and X.-h. Xia, *A simple, disposable microfluidic device for rapid protein concentration and purificationvia direct-printing.* Lab on a Chip, 2008. **8**(9): p. 1496-1501.
274. Guo, X., M.B. Chan-Park, S.F. Yoon, J.-h. Chun, L. Hua, and N.S.K. Sze, *UV Embossed Polymeric Chip for Protein Separation and Identification Based on Capillary Isoelectric Focusing and MALDI-TOF-MS.* Analytical Chemistry, 2006. **78**(10): p. 3249-3256.
275. Adamski, K., W. Kubicki, and R. Walczak, *3D printed electrophoretic lab-on-chip for DNA separation.* Procedia Engineering, 2016. **168**: p. 1454-1457.
276. Piacentini, N., G. Mernier, R. Tornay, and P. Renaud, *Separation of platelets from other blood cells in continuous-flow by dielectrophoresis field-flow-fractionation.* Biomicrofluidics, 2011. **5**(3): p. 034122.
277. Goddard, N.J. and R. Gupta, *Speed and sensitivity–Integration of electrokinetic preconcentration with a leaky waveguide biosensor.* Sensors and Actuators B: Chemical, 2019. **301**: p. 127063.
278. Roper, M.G., J.G. Shackman, G.M. Dahlgren, and R.T. Kennedy, *Microfluidic Chip for Continuous Monitoring of Hormone Secretion from Live Cells Using an Electrophoresis-Based Immunoassay.* Analytical Chemistry, 2003. **75**(18): p. 4711-4717.
279. Pirmoradian, M., J. Astorga-Wells, and R.A. Zubarev, *Multijunction capillary isoelectric focusing device combined with online membrane-assisted buffer exchanger enables isoelectric point fractionation of intact human plasma proteins for biomarker discovery.* Analytical chemistry, 2015. **87**(23): p. 11840-11846.
280. Olsen, K.G., D.J. Ross, and M.J. Tarlov, *Immobilization of DNA hydrogel plugs in microfluidic channels.* Analytical chemistry, 2002. **74**(6): p. 1436-1441.
281. Han, C.M., E. Katilius, and J.G. Santiago, *Increasing hybridization rate and sensitivity of DNA microarrays using isotachophoresis.* Lab on a Chip, 2014. **14**(16): p. 2958-2967.
282. Chong, K.C., L.Y. Thang, J.P. Quirino, and H.H. See, *Monitoring of vancomycin in human plasma via portable microchip electrophoresis with contactless conductivity detector and multi-stacking strategy.* Journal of Chromatography A, 2017. **1485**: p. 142-146.
283. Li, S., D. Zhang, Q. Zhang, Y. Lu, N. Li, Q. Chen, and Q. Liu, *Electrophoresis-enhanced localized surface plasmon resonance sensing based on nanocup array for thrombin detection.* Sensors and Actuators B: Chemical, 2016. **232**: p. 219-225.
284. Gupta, R., E. Labella, and N.J. Goddard, *An optofluidic Young interferometer sensor for real-time imaging of refractive index in µTAS applications.* Sensors and Actuators B: Chemical, 2020. **321**: p. 128491.
285. Young, T., *I. The Bakerian Lecture. Experiments and calculations relative to physical optics.* Philosophical Transactions of the Royal Society of London: p. 1 - 16.
286. Fresnel, A., *Œuvres complètes d'Augustin Fresnel, Imprimerie impériale, Paris, 1866–1870.* (The 150th anniversary of his death, J. Appl. Spectrosc. 27): p. 825–830.
287. Billet, F., *Traité d'optique physiqu.* Mallet-Bachelier Libraire, Paris Annales de Chimie et de Physique, 1858. **LXIV**
288. Scientific, B. *https://www.3bscientific.com/PhysicsExperiments/UE4030300_EN.pdf*.
289. Leon, S.C., *Broad source fringe formation with a Fresnel biprism and a Mach-Zehnder interferometer.* Appl Opt, 1987. **26**(24): p. 5259-65.
290. Ladino, A.I., J. Mendoza-Hernández, M.L. Arroyo-Carrasco, R. Salas-Montiel, M. García-Méndez, V. Coello, and R. Tellez-Limon, *Large depth of focus plasmonic metalenses based on Fresnel biprism.* AIP Advances, 2020. **10**(4): p. 045025.
291. Sabatyan, A. and S.A. Hoseini, *Fresnel biprism as a 1D refractive axicon.* Optik, 2013. **124**(21): p. 5046-5048.

292. Hariharan, P. and P. Hariharan, *4 - Source-Size and Spectral Effects*, in *Basics of Interferometry (Second Edition)*, P. Hariharan and P. Hariharan, Editors. 2007, Academic Press: Burlington. p. 23-30.
293. Hariharan, P. and P. Hariharan, *6 - The Laser as a Light Source*, in *Basics of Interferometry (Second Edition)*, P. Hariharan and P. Hariharan, Editors. 2007, Academic Press: Burlington. p. 39-48.
294. Kreis, T., *Handbook of holographic interferometry: optical and digital methods*. Vol. Chapter 5, Quantitative Determination of the Interference Phase 2006: John Wiley & Sons. 222-225.
295. Mark, D., S. Haeberle, G. Roth, F. von Stetten, and R. Zengerle, *Microfluidic lab-on-a-chip platforms: requirements, characteristics and applications.* Chem Soc Rev, 2010. **39**(3): p. 1153-82.
296. Kerwin, B.A., *Polysorbates 20 and 80 used in the formulation of protein biotherapeutics: structure and degradation pathways.* J Pharm Sci, 2008. **97**(8): p. 2924-35.
297. Zhao, H., Patrick H. Brown, and P. Schuck, *On the Distribution of Protein Refractive Index Increments.* Biophysical Journal, 2011. **100**(9): p. 2309-2317.
298. Khago, D., J.C. Bierma, K.W. Roskamp, N. Kozlyuk, and R.W. Martin, *Protein refractive index increment is determined by conformation as well as composition.* Journal of physics. Condensed matter : an Institute of Physics journal, 2018. **30**(43): p. 435101-435101.
299. Velasco-Garcia, M. *Optical biosensors for probing at the cellular level: a review of recent progress and future prospects*. in *Seminars in cell & developmental biology*. 2009. Elsevier.
300. Olsen, K.G., D.J. Ross, and M.J.J.A.c. Tarlov, *Immobilization of DNA hydrogel plugs in microfluidic channels.* 2002. **74**(6): p. 1436-1441.
301. Landers, J.P., *Handbook of capillary and microchip electrophoresis and associated microtechniques*. 2007: CRC press.
302. Kašička, V., *Recent developments in capillary and microchip electroseparations of peptides (2015–mid 2017).* Electrophoresis, 2018. **39**(1): p. 209-234.
303. Malá, Z. and P. Gebauer, *Recent progress in analytical capillary isotachophoresis.* Electrophoresis, 2019. **40**(1): p. 55-64.
304. Kašička, V., *Recent developments in capillary and microchip electroseparations of peptides (2017–mid 2019).* Electrophoresis, 2020. **41**(1-2): p. 10-35.
305. Breadmore, M.C., A. Wuethrich, F. Li, S.C. Phung, U. Kalsoom, J.M. Cabot, M. Tehranirokh, A.I. Shallan, A.S. Abdul Keyon, and H.H. See, *Recent advances in enhancing the sensitivity of electrophoresis and electrochromatography in capillaries and microchips (2014–2016).* Electrophoresis, 2017. **38**(1): p. 33-59.
306. Schaeper, J.P. and M.J. Sepaniak, *Parameters affecting reproducibility in capillary electrophoresis.* ELECTROPHORESIS: An International Journal, 2000. **21**(7): p. 1421-1429.
307. Tsai, C.H., R.J. Yang, C.H. Tai, and L.M. Fu, *Numerical simulation of electrokinetic injection techniques in capillary electrophoresis microchips.* electrophoresis, 2005. **26**(3): p. 674-686.
308. Kazarian, A.A., E.F. Hilder, and M.C. Breadmore, *Online sample pre-concentration via dynamic pH junction in capillary and microchip electrophoresis.* J Sep Sci, 2011. **34**(20): p. 2800-21.
309. Ghosal, S., *Effect of analyte adsorption on the electroosmotic flow in microfluidic channels.* Analytical chemistry, 2002. **74**(4): p. 771-775.
310. Tavakoli, J. and Y. Tang, *Hydrogel Based Sensors for Biomedical Applications: An Updated Review.* Polymers, 2017. **9**(8): p. 364.

311. Shi, Q. and G. Jackowski, *One-dimensional polyacrylamide gel electrophoresis.* Gel electrophoresis of proteins: A practical approach, 1998. **3**: p. 1-52.
312. Reddy, P. and R. Nomula, *Gel-Electrophoresis and Its Applications*. 2012.
313. Shouren, G., K. Kojio, A. Takahara, and T. Kajiyama, *Bovine serum albumin adsorption onto immobilized organotrichlorosilane surface: Influence of the phase separation on protein adsorption patterns.* Journal of Biomaterials Science, Polymer Edition, 1998. **9**(2): p. 131-150.
314. Tomov, T. and I. Tsoneva, *Are the stainless steel electrodes inert?* Bioelectrochemistry, 2000. **51**(2): p. 207-9.
315. Fu, L.M., H.H. Hou, P.H. Chiu, and R.J. Yang, *Sample preconcentration from dilute solutions on micro/nanofluidic platforms: A review.* Electrophoresis, 2018. **39**(2): p. 289-310.
316. Britz-McKibbin, P. and D.D. Chen, *Selective focusing of catecholamines and weakly acidic compounds by capillary electrophoresis using a dynamic pH junction.* Anal Chem, 2000. **72**(6): p. 1242-52.
317. Lin, C.-C., J.-L. Hsu, and G.-B. Lee, *Sample preconcentration in microfluidic devices.* Microfluidics and Nanofluidics, 2011. **10**(3): p. 481-511.
318. Zhang, Q., Z. Guo, F. Luo, H. Xiao, W. Liu, L. Fan, and C. Cao, *Model, Simulation, and Experiments on Moving Exchange Boundary via Ligand and Quantum Dots in Chip Electrophoresis.* Analytical Chemistry, 2021. **93**(13): p. 5360-5364.
319. Cao, C.-X., L.-Y. Fan, and W. Zhang, *Review on the theory of moving reaction boundary, electromigration reaction methods and applications in isoelectric focusing and sample pre-concentration.* Analyst, 2008. **133**(9): p. 1139-1157.
320. Quirino, J.P. and S. Terabe, *Sample stacking of cationic and anionic analytes in capillary electrophoresis.* Journal of Chromatography A, 2000. **902**(1): p. 119-135.
321. Kurzweilová, H. and K. Sigler, *Fluorescent staining with bromocresol purple: a rapid method for determining yeast cell dead count developed as an assay of killer toxin activity.* Yeast, 1993. **9**(11): p. 1207-11.
322. Goddard, N.J. and R. Gupta, *Speed and sensitivity – Integration of electrokinetic preconcentration with a leaky waveguide biosensor.* Sensors and Actuators B: Chemical, 2019. **301**: p. 127063.
323. Heo, J. and R.M. Crooks, *Microfluidic Biosensor Based on an Array of Hydrogel-Entrapped Enzymes.* Analytical Chemistry, 2005. **77**(21): p. 6843-6851.
324. Wang, Y., W. Yuan, M. Kimber, M. Lu, and L. Dong, *Rapid differentiation of host and parasitic exosome vesicles using microfluidic photonic crystal biosensor.* ACS sensors, 2018. **3**(9): p. 1616-1621.
325. Hou, C. and A.E. Herr, *Microfluidic integration of Western blotting is enabled by electrotransfer-assisted sodium dodecyl sulfate dilution.* Analyst, 2013. **138**(1): p. 158-63.
326. Dorfman, K.D., S.B. King, D.W. Olson, J.D.P. Thomas, and D.R. Tree, *Beyond Gel Electrophoresis: Microfluidic Separations, Fluorescence Burst Analysis, and DNA Stretching.* Chemical Reviews, 2013. **113**(4): p. 2584-2667.
327. Wu, D., J. Qin, and B. Lin, *Electrophoretic separations on microfluidic chips.* Journal of Chromatography A, 2008. **1184**(1): p. 542-559.
328. Forrer, K., S. Hammer, and B. Helk, *Chip-based gel electrophoresis method for the quantification of half-antibody species in IgG4 and their by- and degradation products.* Analytical Biochemistry, 2004. **334**(1): p. 81-88.
329. Ou, X., P. Chen, X. Huang, S. Li, and B.-F. Liu, *Microfluidic chip electrophoresis for biochemical analysis.* Journal of Separation Science, 2020. **43**(1): p. 258-270.

330. Butler, J.M., *Chapter 6 - Capillary Electrophoresis: Principles and Instrumentation*, in *Advanced Topics in Forensic DNA Typing: Methodology*, J.M. Butler, Editor. 2012, Academic Press: San Diego. p. 141-165.
331. Borecki, M., M.L. Korwin-Pawlowski, M. Beblowska, J. Szmidt, and A. Jakubowski, *Optoelectronic Capillary Sensors in Microfluidic and Point-of-Care Instrumentation.* Sensors, 2010. **10**(4): p. 3771-3797.
332. Yang, Y., Y. Chen, H. Tang, N. Zong, and X. Jiang, *Microfluidics for biomedical analysis.* Small methods, 2020. **4**(4): p. 1900451.
333. Mao, Q. and J. Pawliszyn, *Capillary isoelectric focusing with whole column imaging detection for analysis of proteins and peptides.* Journal of Biochemical and Biophysical Methods, 1999. **39**(1): p. 93-110.
334. Goodridge, L., C. Goodridge, J. Wu, M. Griffiths, and J. Pawliszyn, *Isoelectric point determination of norovirus virus-like particles by capillary isoelectric focusing with whole column imaging detection.* Analytical chemistry, 2004. **76**(1): p. 48-52.
335. Liu, Z., T. Lemma, and J. Pawliszyn, *Capillary Isoelectric Focusing Coupled with Dynamic Imaging Detection: A One-Dimensional Separation for Two-Dimensional Protein Characterization.* Journal of proteome research, 2006. **5**: p. 1246-51.
336. Williams, E.H., A.V. Davydov, A. Motayed, S.G. Sundaresan, P. Bocchini, L.J. Richter, G. Stan, K. Steffens, R. Zangmeister, and J.A. Schreifels, *Immobilization of streptavidin on 4H–SiC for biosensor development.* Applied surface science, 2012. **258**(16): p. 6056-6063.
337. Yoon, K.Y., W.S. Tan, B.T. Tey, K.W. Lee, and K.L. Ho, *Native agarose gel electrophoresis and electroelution: A fast and cost-effective method to separate the small and large hepatitis B capsids.* Electrophoresis, 2013. **34**(2): p. 244-53.
338. Garfin, D.E., *Gel electrophoresis of proteins.* Essential cell biology, 2003. **1**(7): p. 197-268.
339. Raducanu, V.-S., M. Tehseen, A. Shirbini, D.-V. Raducanu, and S.M. Hamdan, *Two chromatographic schemes for protein purification involving the biotin/avidin interaction under native conditions.* Journal of Chromatography A, 2020. **1621**: p. 461051.
340. Eaton, B.E., L. Gold, and D.A. Zichi, *Let's get specific: the relationship between specificity and affinity.* Chemistry & biology, 1995. **2**(10): p. 633-638.
341. Diamandis, E.P. and T.K. Christopoulos, *The biotin-(strept)avidin system: principles and applications in biotechnology.* Clin Chem, 1991. **37**(5): p. 625-36.
342. Lowe, B.M., K. Sun, I. Zeimpekis, C.-K. Skylaris, and N.G. Green, *Field-effect sensors – from pH sensing to biosensing: sensitivity enhancement using streptavidin–biotin as a model system.* Analyst, 2017. **142**(22): p. 4173-4200.
343. Duan, X., Y. Li, N.K. Rajan, D.A. Routenberg, Y. Modis, and M.A. Reed, *Quantification of the affinities and kinetics of protein interactions using silicon nanowire biosensors.* Nat Nanotechnol, 2012. **7**(6): p. 401-7.
344. Lloret, N., R.S. Frederiksen, T.C. Møller, N.I. Rieben, S. Upadhyay, L. De Vico, J.H. Jensen, J. Nygård, and K.L. Martinez, *Effects of buffer composition and dilution on nanowire field-effect biosensors.* Nanotechnology, 2012. **24**(3): p. 035501.
345. Uptima, I. *Hydrazide-Biotin Carbohyhydrate-reactive activated biotins*. Available from: https://www.interchim.fr/ft/7/78631A.pdf.
346. Li, C. and T. Arakawa, *Agarose native gel electrophoresis of proteins.* International Journal of Biological Macromolecules, 2019. **140**: p. 668-671.
347. Stern, E., R. Wagner, F.J. Sigworth, R. Breaker, T.M. Fahmy, and M.A. Reed, *Importance of the Debye screening length on nanowire field effect transistor sensors.* Nano letters, 2007. **7**(11): p. 3405-3409.